Cruise Report:
IBRV *Araon* ARA05B, July30-August25, 2014
Bering Sea US EEZ, Chukchi/Beaufort/East Siberian Seas, MIZ Ice Camp

Sung-Ho Kang, Chief Scientist
Korea Polar Research Institute (KOPRI)

Korea Polar Research Institute

Report Editors:
Sung-Ho Kang[1]*, Craig Lee[2], Eun Jin Yang[1], Jung Ho Hyung[3], Tae Wan Kim[1], Koji Shimasa[4], Sang Heon Lee[5], Phil Hwang[6], Jingping Zhao[7], Mary Jane Perry[8], Byoung Woong An[9], Joo-Hong Kim[1], Martin Doble[10], Jin Young Jung[1], James Stokel[11], Kyoung-Ho Cho[1], Shawn Gallaher[11], Eurico D'Sa[12]

[1]Korea Polar Research Institute (KOPRI)
[2]University of Washington (UW)
[3]Hanyang University (HU)
[4]Tokyo University of Marine Science and Technology (TUMST)
[5]Pusan National University (PNU)
[6]The Scottish Association for Marine Science (SAMS)
[7]Ocean University of China (OUC)
[8]University of Maine (UM)
[9]Finnish Meteorological Institute (FMI)
[10]Laboratoire d'Océonographie de Villefranche (LOV)
[11]Naval Graduate School (NPS)
[12]Louisiana State University (LSU)

***e-mail: shkang@kopri.re.kr**
Telephone: +82 32.760.5332
Korea Polar Research Institute (KOPRI)
Songdo Miraero 26, Yeonsu-gu
Incheon 406-840
Korea

Editor's Note: All data and summaries provided herein are subject to revision or correction and should be treated as unpublished data with intellectual property reserved to the scientist contributing to the report. Please contact the individuals listed as having responsibility for each report section for additional information or Dr. Sung-Ho Kang (shkang@kopri.re.kr), the chief scientist of 2014 Araon Arctic Cruise. Report prepared August 2014, Chukchi Sea, the Arctic.

Contents

IBRV *Araon* Arctic Cruise ARA05B
July30 - August25, 2014

Summary:

Araon Cruise (ARA05B) departed Nome, Alaska on July 31, 2014 and returned to Barrow on August24, 2014. With funding provided by the Ministry of Oceans and Fisheries (MOF) and by Korea Polar Research Institute (KOPRI), the aim of the cruise was to investigate the structure and processes in the water column and subsurface (sediment) around the Bering/Chukchi/Beaufort/East Siberian Seas in rapid transition. The research effort was the jointly conducted research cruise of the Korea-Polar Ocean in Rapid Transition (K-PORT) Program with support from the MOF and the KOPRI and the Marginal Ice Zone (MIZ) Program with support from the US ONR (Ocean Naval Research). Because of high demand for berth space, ship time, and helicopter time on the Arctic cruise aboard Araon in 2014, special efforts were made to accommodate two main projects compatible with the use of the ship during the K-PORT study, and the 2 projects are outlined below. In addition to science programs, additional efforts were made to communicate scientific efforts and research issues by providing berth space for a writer that undertook interviews during the scientific work.

Acknowledgements:

We thank the IBRV *Araon* crew, officers and commanding officer onboard Araon for well-executed hard work and flexibility under cold and often difficult conditions. We wish to specifically thank the experienced Marine Science Technician team aboard the ship which was invaluable in facilitating the research operations. Maritime Helicopters team and Umiaq polar bear guards from Barrow also contributed significantly to completing successfully the science mission objectives.

Core Projects:

K-PORT (Korea-Polar Ocean in Rapid Transition) Program: Ministry of Oceans and Fisheries (MOF), KOPRI Project No. PM13020, PI: Sung-Ho Kang, KOPRI

MIZ (Marginal Ice Zone) Program: US Ocean Naval Research, PI: Craig Lee, University of Washington

Cruise Participants:

1. Dr. Sung-Ho KANG, Korea Polar Research Institute (KOPRI) (shkang@kopri.re.kr)
2. Dr. Craig LEE, University of Washington (craig@apl.washington.edu)
3. Dr. Eun Jin YANG, Korea Polar Research Institute (KOPRI) (ejyang@kopri.re.kr)
4. Dr. Jung-Ho HYUN, Hanyang University (hyunjh@hanyang.ac.kr)
5. Dr. Tae Wan KIM, Korea Polar Research Institute (KOPRI) (twkim@kopri.re.kr)
6. Dr. Koji SHIMADA, Tokyo University of Marine Science and Technology (TUMSAT), Japan (koji@kaiyodai.ac.jp)
7. Dr. Sang Heon LEE, Pusan National University (sanglee@pusan.ac.kr)
8. Dr. Phil HWANG, The Scottish Association for Marine Science (SAMS), Scottish Marine Institute, UK (phil.hwang@sams.ac.uk)
9. Dr. Jinping ZHAO, Ocean University of China (OUC), China (jpzhao@ouc.edu.cn)
10. Dr. Mary Jane PERRY, University of Maine (perrymj@maine.edu)
11. Dr. Byoung Woong AN, Finnish Meteorological Institute (byoung.woong.an@fmi.fi)
12 .Dr. Joo-Hong KIM, Korea Polar Research Institute (KOPRI) (joo-hong.kim@kopri.re.kr)
13. Dr. Martin DOBLE, Laboratoire d'Océanographie de Villefranche, (doble@obs-vlfr.fr)
14. Dr. Jin Young JUNG, Korea Polar Research Institute (KOPRI),(jinyoungjung@kopri.re.kr)
15. Dr. James STOKEL, Naval Postgraduate School, (stockel@nps.edu)
16. Dr. Kyoung-Ho CHO, Korea Polar Research Institute (KOPRI), (kcho@kopri.re.kr)
17. Dr. Shawn GALLAHER, Naval Postgraduate School, (sggallah1@nps.edu)
18. Dr. Eurico D'SA, Louisiana State University, (ejdsa@lsu.edu)
19. Dr. Byeong Deok YEA, Korea Maritime &Ocean University, (byea@kmou.ac.kr)
20. Dr. Jeff PIETRO, Woods Hole Institute of Oceanography (WHOI), (jpietro@whoi.edu)
21. Dr. Hyoung Sul LA, Korea Polar Research Institute (KOPRI), (hsla@kopri.re.kr)
22. Mr. Dong Seob SHIN, Korea Polar Research Institute (KOPRI) (dsshin@kopri.re.kr)
23. Dr. Doo Byoul LEE, Korea Polar Research Institute (KOPRI), (copepod@kopri.re.kr)
24. Dr. Hyoung Min JOO, Korea Polar Research Institute (KOPRI), (hmjoo77@kopri.re.kr)
25. Dr. Sun Yong HA, Korea Polar Research Institute (KOPRI), (sundragon@kopri.re.kr)
26. Dr. Chang-Uk HYUN, Korea Polar Research Institute (KOPRI),(cuhyun@kopri.re.kr)
27. Ms. Eri YOSHIZAWA, Tokyo University of Marine Science and Technology (TUMSAT), Japan (eri.yoshizawa075@gmail.com)
28. Mr. Jun Oh MIN, Korea Polar Research Institute (KOPRI) (jomin@kopri.re.kr)
29. Mr. Chan Yeong GANG, Korea Polar Research Institute, (changyoung85@kopri.re.kr)
30. Mr. Hyoung Jun KIM, Korea Polar Research Institute (KOPRI), (jun7100@kopri.re.kr)
31. Mr. Seokkyoung CHOI, Araon Doctor, (onlycsk@naver.com)
32. Mr. Howard REED, Maritime Helicopters, (reedhoward03@gmail.com)
33. Mr. Eric RICHARD, Maritime Helicopters, (cp@maritimehelicopters.com)
34. Mr. David GUY, Maritime Helicopters (safety@maritimehelicopters.com)
35. Mr. Reynold AVEOGANNA, Polar Bear Guard, Umiaq, 8525254(local phone)
36. Mr. Gordon BROWER II, Polar Bear Guard, Umiaq, (ikpikpukpik@hotmail.com)
37. Mr. Christopher KOONALOAK, Polar Bear Guard, Umiaq, (braaap_421@hotmail.com)
38. Mr. Vladimir PISAREV, Ice Navigator, Russia (irishka-4ever@mail.ru)
39. Mr. Leonid TUYNO, Ice Pilot, FESCO, Russia, (lftuyno@outlook.com)
40. Mr. Youngho KO, Pohang Institute of Science and Technology(sldla@postech.ac.kr)

41. Mr. Goan Woo KIM, Pusan National University, (goanwoo7@pusan.ac.kr)
42. Mr. Dongwoo KIM, Korea Maritime &Ocean University, (kimduocean@naver.com)
43. Ms. Bomina KIM, Hanyang University, (bomina0315@hanyang.ac.kr)
44. Mr. Su Hwan KIM, Korea Polar Research Institute (KOPRI),(idsuhwan@kopri.re.kr)
45. Mr. Hong Lyun PARK, Korea Polar Research Institute,(parkhonglyun@kopri.re.kr)
46. Ms. Min Young BANG, Korea Polar Research Institute (KOPRI),(alsdud0623@kopri.re.kr)
47. Ms. Ho Jung SONG, Pusan National University, (strawpirate@pusan.ac.kr)
48. Mr. Yoon-Yong YANG, Korea Polar Research Institute (KOPRI) (tazmenia@kopri.re.kr)
49. Ms. Jin Ah OH, Korea Polar Research Institute (KOPRI),(jaoh@kopri.re.kr)
50. Mr. Jae Hyung LEE, (Pusan National University), (tlyljh78@pusan.ac.kr)
51. Mr. Ho Jun RHEE, Hankuk University of Foreign Studies, (lunari1202@gmail.com)
52. Mr. Sehyun JANG, Pohang Institute of Science and Technology (sehyun@postech.ac.kr)
53. Mr. Kwang Ho JIN, Korea Polar Research Institute (KOPRI),(khjin@kopri.re.kr)
54. Mr. Jin Yeol CHOI, Inha University, (cjy13@inha.edu)

2014 ARAON ARCTIC CRUISE

ARA05B (31ST JULY – 25TH AUGUST)

KOPRI

Sung-Ho KANG
KOPRI
shkang@kopri.re.kr

Craig LEE
University of Washington
craig@apl.washington.edu

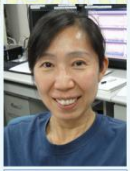

Eun Jin YANG
KOPRI
ejyang@kopri.re.kr

Jung Ho HYUN
Hanyang University
hyunjh@hanyang.ac.kr

Tae Wan KIM
KOPRI
twkim@kopri.re.kr

Koji SHIMADA
TUMSAT, Japan
koji@kaiyodai.ac.jp

Sang Heon LEE
Pusan Nat. University
sanglee@pusan.ac.kr

Phil HWANG
SAMS, UK
phil.hwang@sams.ac.uk

Jinping ZHAO
Ocean Unvi. of China
jpzhao@ouc.edu.cn

Mary Jane PERRY
University of Maine
perrymj@maine.edu

Byoung Woong AN
Finnish Met. Institute
byoung.woong.an@fmi.fi

Joo-Hong KIM
KOPRI
joo-hong.kim@kopri.re.kr

Martin DOBLE
LOV, France
doble@obs-vlfr.fr

Jin Young JUNG
KOPRI
jinyoungjung@kopri.re.kr

James STOKEL
Naval Postgraduate School
stockel@nps.edu

Kyoung-Ho CHO
KOPRI
kcho@kopri.re.kr

Shawn GALLAHER
Naval Postgraduate School
sggallah1@nps.edu

Eurico D'SA
Louisiana Stat. Univ.
ejdsa@lsu.edu

Byeong Deok YEA
Korea Mari&Ocean Univ.
byea@kmou.ac.kr

Jeff PIETRO
WHOI
jpietro@whoi.edu

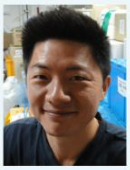

Hyoung Sul LA
KOPRI
hsla@kopri.re.kr

Dong Seob SHIN
KOPRI
dsshin@kopri.re.kr

Doo Byoul LEE
KOPRI
copepod@kopri.re.kr

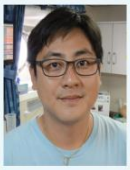

Hyoung Min JOO
KOPRI
hmjoo77@kopri.re.kr

Sun Yong HA
KOPRI
sundragon@kopri.re.kr

Chang-Uk HYUN
KOPRI
cuhyun@kopri.re.kr

Eri YOSHIZAWA
TUMSAT, Japan
eri.yoshizawa075@gmail.com

Jun Oh MIN
KOPRI
jomin@kopri.re.kr

Chan Yeong GANG
KOPRI
changyoung85@kopri.re.kr

Hyoung Jun KIM
KOPRI
jun7100@kopri.re.kr

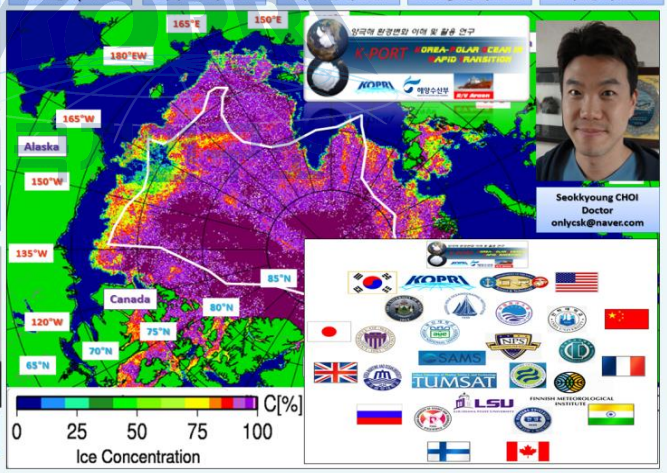

Seokkyoung CHOI
Doctor
onlycsk@naver.com

Howard REED
Maritime Helicopter
reedhoward03@gmail.com

Reynold AVEOGANNA
Polar Bear Guard, Umiaq
8525254(local phone)

Gordon BROWER II
Polar Bear Guard, Umiaq
ikpikpukpik@hotmail.com

Christopher KOONALOAK
Polar Bear Guard, Umiaq
braaap_421@hotmail.com

Eric RICHARD
Maritime Helicopters
cp@maritimehelicopters.com

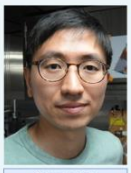

Youngho KO
POSTECH
sldla@postech.ac.kr

Goan Woo KIM
Pusan Nat. University
goanwoo7@pusan.ac.kr

Dongwoo KIM
Korea Mar.&Ocean Univ.
kimduocean@naver.com

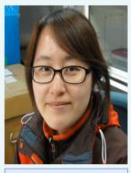

Bomina KIM
Hanyang University
bomina0315@hanyang.ac.kr

Su Hwan KIM
KOPRI
idsuhwan@kopri.re.kr

Hong Lyun PARK
KOPRI
parkhonglyun@kopri.re.kr

Vladimir PISAREV
Ice Pilot, FESCO, Russia
irishka-4ever@mail.ru

Leonid TUYNO
Ice Pilot, FESCO, Russia
lftuyno@outlook.com

David GUY
Maritime Helicopters
safety@maritimehelicopters.com

Min Young BANG
KOPRI
alsdud0623@kopri.re.kr

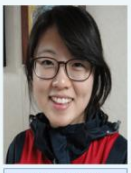

Ho Jung SONG
Pusan Nat. University
strawpirate@pusan.ac.kr

Yoon-Yong YANG
KOPRI
tazmenia@kopri.re.kr

Jin Ah OH
KOPRI
jaoh@kopri.re.kr

Jae Hyung LEE
Pusan Nat. University
tlyljh78@pusan.ac.kr

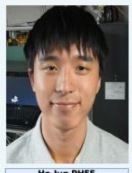

Ho Jun RHEE
Hankuk University Of Foreign Studies
lunari1202@gmail.com

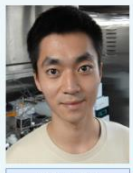

Sehyun JANG
POSTECH
sehyun@postech.ac.kr

Kwang Ho JIN
KOPRI
khjin@kopri.re.kr

Jin Yeol CHOI
Inha University
cjy13@inha.edu

=

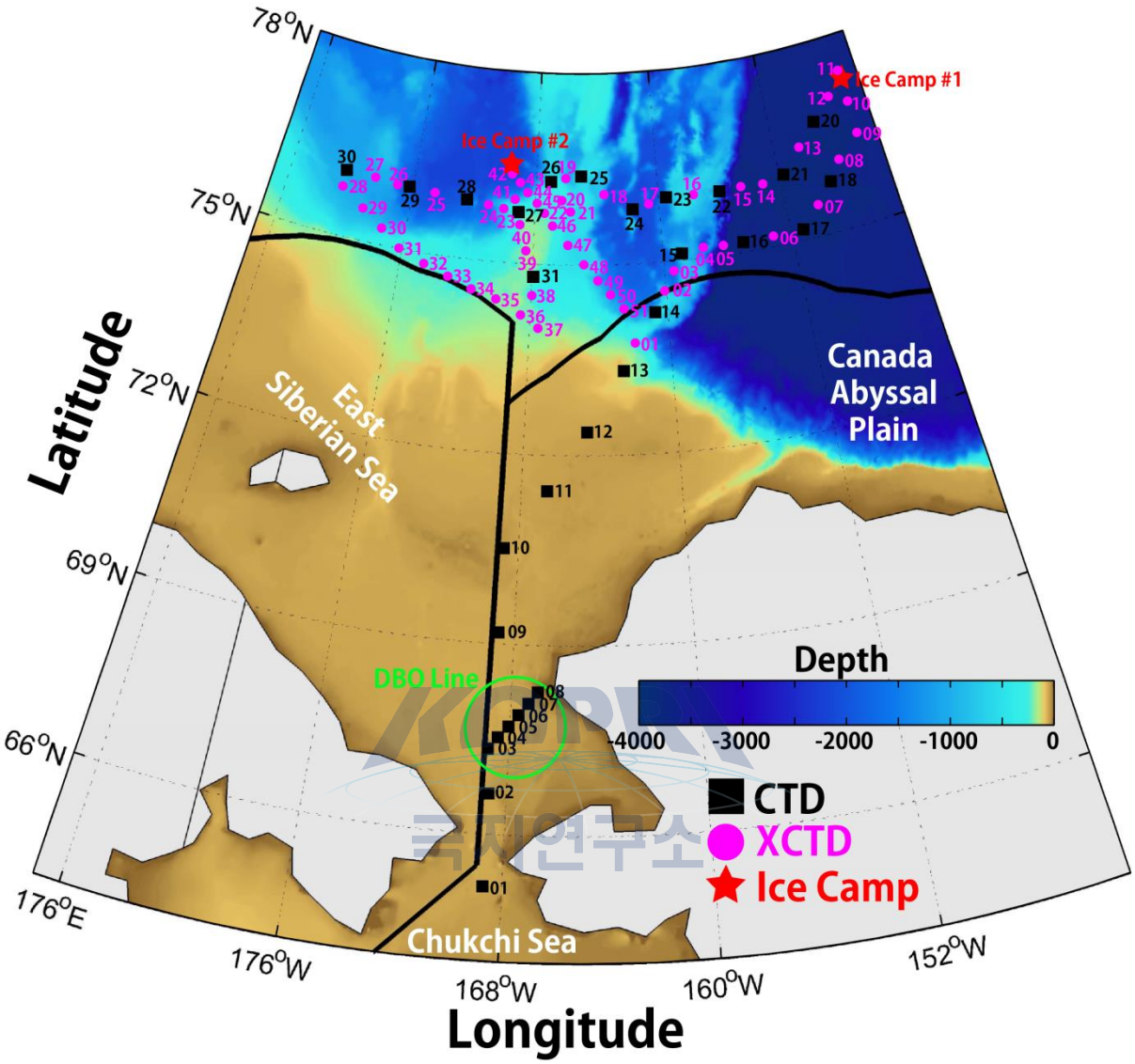

Map of 2014 Araon Arctic Cruise study area. CTD, XCTD, MOORING, SEA-ICE camp, Helicopter Survey stations.

2014 Araon Arctic Cruise

Araon Arctic Cruise (ARA05B) departed Nome, Alaska on July 31, 2014 and returned to Barrow on August24, 2014. With funding provided by the Ministry of Oceans and Fisheries (MOF) and by Korea Polar Research Institute (KOPRI), the aim of the cruise was to investigate the structure and processes in the water column and subsurface (sediment) around the Bering/Chukchi/Beaufort/East Siberian Seas in rapid transition. The research effort was thejointlyconducted research cruise of the Korea-Polar Ocean in Rapid Transition (K-PORT) Programwith support from the MOF and the KOPRI and the Marginal Ice Zone (MIZ) Program with support from the US ONR (Ocean Naval Research).Total of 54 scientists have participated from 10 countries (Korea, US, China, Japan, Canada, Russia, U.K., France, India, Finland) representing 17 different universities and research organizations. Because of high demand for berth space, ship time, and helicopter time on the Arctic cruise aboard Araon in 2014, special efforts were made to accommodate two main projects compatible with the use of the ship during the K-PORT study.

Araon data were collected on the physical, biological, chemical, and biogeochemical properties of ocean waters and sea-ice in the shelf, slope and deep-sea regions of the Bering/Chukchi/Beaufort/East Siberian Seas. Profiles of water temperature and salinity were obtained with CTD, and an underway XCTD system. Additional sensors on the CTD profiler were collected in situ data on phytoplankton concentrations (fluorometer), optical clarity (transmissometer), dissolved oxygen and photoactive radiation. A rosette sampler was used with the CTD to obtain water samples from discrete depths for a broad suite of biological and geochemical parameters, some for onboard analysis, others to be stored for later analysis in shore-based laboratories. Both bio-acoustic backscatter data and depth-varying current information were collected using a Acoustic Doppler Current Profiler (ADCP) deployed under the ship at most of the science stations. Data were also collected from the ship-mounted transducer along the ship track to evaluate the possibility of using these data for bottom classification purposes. Plankton samples were obtained in vertical hauls by phyto- and bongo-nets lowered to 200 m.

Survey components:

- Water Column (WC) components
  -Water column observations of biota
  -Pelagic ecosystems observations
  -Nutrients and productivity
  -Bio-geochemical measurements
- Underway collection of meteorological and near-surface seawater
- Meteorological data from ship sensors
- On-shore calibration of instrument compasses
- XCTD (expendable temperature, salinity and depth profiler) casts
- CTD/rosette casts for hydrograph and geochemistry (ecosystem, nutrients, salinity, and barium)
- Deploy oceanographic moorings
- Seaglider and SWIFT float deployments
- Sea-ice (ICE) observations through regular visual observations from bridge and automated fixed-camera photos.
- Arctic Sea-ice camp operation
  - Sea-ice physic and dyanmic
  - Sea-ice biogeochemisty
  - Sea-ice biota
  - Buoy deployment
  -Helicopter surbey
  -Melt pond ecosystem

Chapter 1. Atmospheric observation

Joo-Hong Kim and Kwang-Ho Jin

Korea Polar Research Institute, Incheon 406-840, Korea (joo-hong.kim@kopri.re.kr, khkin@kopri.re.kr)

1.1. Introduction

The Arctic Ocean has dramatically opened during the summer melting seasons of recent decades with the unprecedented reduction of sea ice due to global warming, at least over the past thousand years (Kinnard *et al.*, 2011). Although the total volume of Arctic sea ice is negligibly small due to its thin thickness compared with the overlying atmosphere and the underlying ocean, its role on radiative balance is very crucial. Its high albedo hinders solar radiation from being absorbed at the surface, forming cold temperature over the ice-covered region, provided that the warming effect by horizontal warm air advection is negligible. Therefore the reduction of the ice-covered region is related to the warming of the polar atmosphere, particularly the thin atmospheric low boundary layer (Serreze *et al.*, 2011). The role of sea ice in controlling the atmospheric temperature in the Arctic indicates that sea ice affects the overall meridional temperature gradient, the main factor defining general circulation in the Northern Hemisphere.

Conversely, Arctic sea ice is also highly influenced by the atmospheric and oceanic environments. The atmosphere and ocean dynamically affect the sea ice melting rate by fracturing it through winds and waves, and transporting it to warmer or colder areas. Also they thermodynamically drive sea ice melting/growth by changing the ice temperature through the accumulation/loss of heat in the form of both radiative and turbulent fluxes. These dynamical and thermodynamical influences on sea ice are modulated by the large-scale climate system.

Semiletov *et al.* (2007) suggested that melting ponds and open channels may change the dynamics of carbon cycle between the atmosphere and the ocean in the Arctic Ocean. Arctic sea ice has shown a pronounced decrease during recent decades and the record-breaking

small ice coverage was observed in 2012 summer. However, its impact on global climate through the modification in energy and carbon cycles over the Arctic sea is not clarified yet. In addition, transport of anthropogenic light absorbing carbonaceous particles from lower latitudes is found responsible for the Arctic warming. Aerosols change radiative budget by scattering/absorbing incoming solar light and forming clouds by acting as cloud condensation nuclei (CCN). For instance, black carbon (BC) which absorbs solar radiation has the second largest influence on global warming following greenhouse gases (Jacobson, 2002).

Arctic clouds themselves are also especially important, given their strong influence on the surface energy budget (Curry *et al.*, 1996). Arctic clouds make winter surface cooling and summer surface heating lessen by tens of watts per square meter (Curry *et al.*, 1996; Vavrus and Waliser, 2008). Therefore, Arctic clouds are the highly influential component that controls the growth and decay of sea ice. Therefore, the recent decline of Arctic sea ice can be understood as the result from the complex interaction of the whole climate systems centered on Arctic sea ice. As a result, understanding and predicting the future status of Arctic sea ice under global warming requires an efficient combined network of observation, theory and numerical simulation, connecting various scale physical systems.

All of those facts emphasize the continuous, on-site observations of atmospheric parameters in the Arctic Ocean. However, the polar weather is cold and harsh even during summertime, so autonomous platforms measuring atmospheric properties (e.g., air temperature, humidity, pressure, wind, gases, particles, turbulent fluxes, etc.) in the Arctic often suffer from malfunction arising from freezing, which means a difficulty in maintaining them without regular management by humans. Alternatively, ship-base observations of the Arctic atmosphere can provide invaluable records along the cruise track with regular management when malfunction is detected. In 2014 summer, the Korean ice-breaking research vessel (IBRV) *Araon* voyaged the Bering/Beaufort/Chukchi Seas from 31 July through 24 August and supported 6-day sea ice camp in the Beaufort Sea (period: August 8-14, location: 77.4°N, 146.1°W). Various atmospheric properties were observed during the cruise. In this report, we overview the meteorological instruments aboard IBRV *Araon* and deliver some results of observations.

1.2. Atmospheric Observations

1.2.1. Overview

Atmospheric observations on IBRV *Araon* include the basic meteorological parameters (e.g., air temperature, humidity, pressure and wind), radiative fluxes (e.g., net shortwave and longwave radiations), greenhouse gases (e.g., carbon dioxide and water vapor) and aerosols. She is also equipped with an eddy covariance system to measure scalar turbulent fluxes at air-sea interface. For aerosol observation, the light scattering coefficient, number concentration, and mass of the Arctic aerosols are measured including the concentration of black carbon.

Because all the observations are almost continuous during the cruise, precious observational data can be acquired along the cruise track. However, it is challenging to maintain the best performance of the instruments due to harsh weather condition in the Arctic Ocean. Especially, the eddy covariance system is a very delicate instrument that often malfunctions caused by freezing and raindrop. The overview of atmospheric observations is summarized in Fig. 1.2.

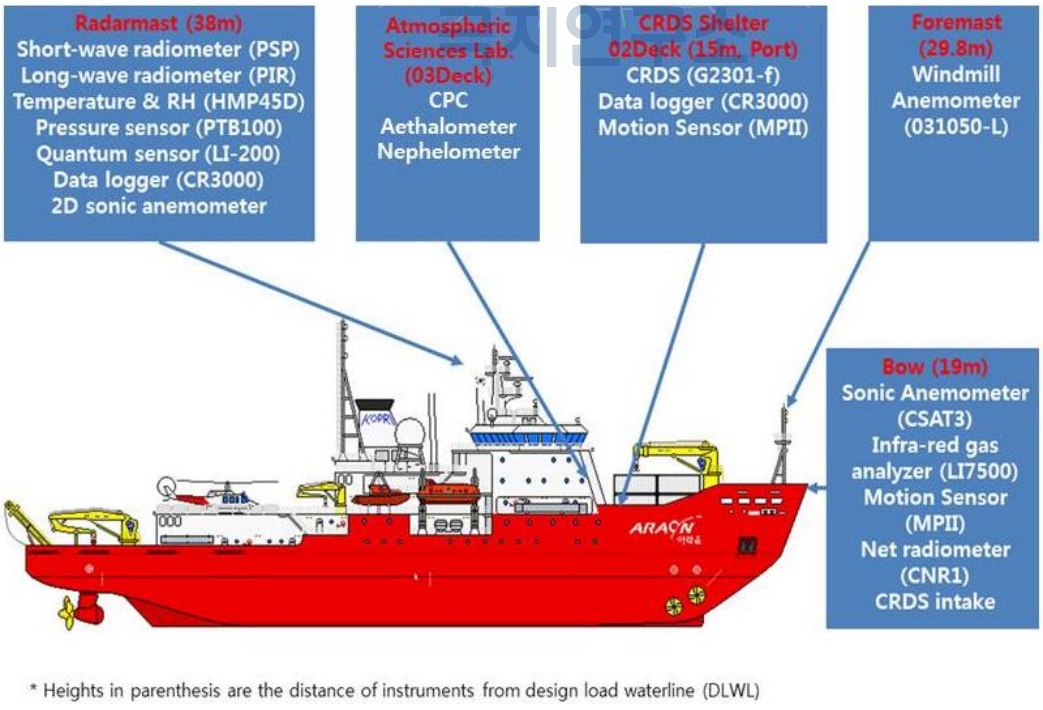

Fig. 1.1. Overview of atmospheric observations on IBRV *Araon* (Updated from 2013 ARA04C cruise report).

1.2.2. Foremast and Bow

At the top of the foremast (the height of 29.8 meters above the water surface), there is a windmill anemometer (05103-L, RMYoung, USA) which measures the speed and direction of winds (Fig. 1.2). The data logger (CR3000, Campbell Scientific) installed in the shelter of a wave-scanned cavity ring-down spectroscopy (CRDS, G2301-f, Picarro Inc., USA) analyzer (on 02Deck) collects wind data from wind vane anemometer every 10 seconds, which is to calculate 30 minute-averaged wind speed and relative wind direction. The relative wind regime is corrected to a true value by considering the vessel's heading direction and speed.

Fig. 1.2. Windmill anemometer at the foremast.

At the ship bow, the eddy covariance system measures turbulent fluxes of scalars (i.e., temperature, water vapor, and carbon dioxide). The system consists of sonic

anemometer (CSAT3, Campbell Scientific, Inc.) and two gas analyzers (Fig. 1.3). One is the infrared gas analyzer (LI7500, Li-cor, USA) measuring molar density of carbon dioxide and water vapor at a high sampling rate, which is installed next to the sonic anemometer. The other is the wave-scanned cavity ring-down spectroscopy (CRDS) analyzer in the shelter on 02Deck, which is tube-connected with the CRDS intake next to the LI7500 at the bow (Fig. 1.4). Thus the air samples should travel through the tube (3/8 inch) to reach the CRDS analyzer. The flow rate of sampled air in the tube should be maintained to ensure turbulent flows [Hong *et al*., 2000]. In order to capture chaotic eddy motions, these instruments sample at high rate, i.e., 10 Hz. The data logger in the CRDS shelter collects the data, and the desktop computer in the Atmospheric Sciences Laboratory receives and monitors the data in real-time. Fig. 1.5 shows the schematic of signal flows of the eddy covariance system. Note that the raw dataset should go through several steps of correction (i.e., post-processes) in terms of density, frequency-response, and motion after the cruise.

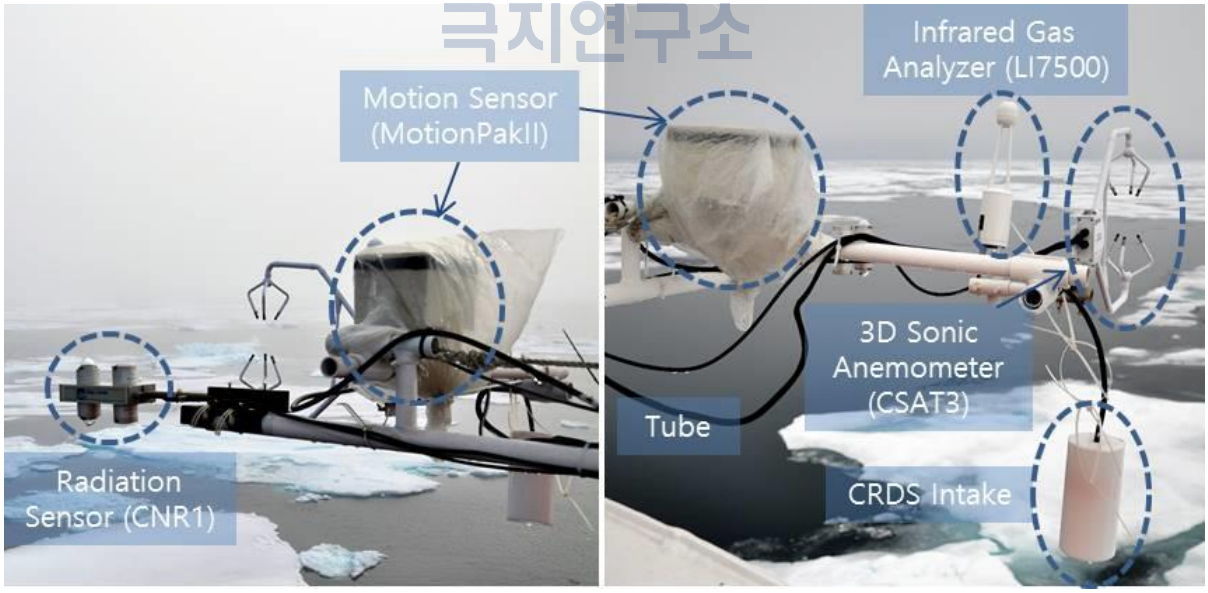

Fig. 1.3. Instruments at the bow.

Fig. 1.4. Cavity ring-down spectroscopy (CRDS) analyzer in the 02Deck shelter (Adapted from 2013 ARA04C cruise report).

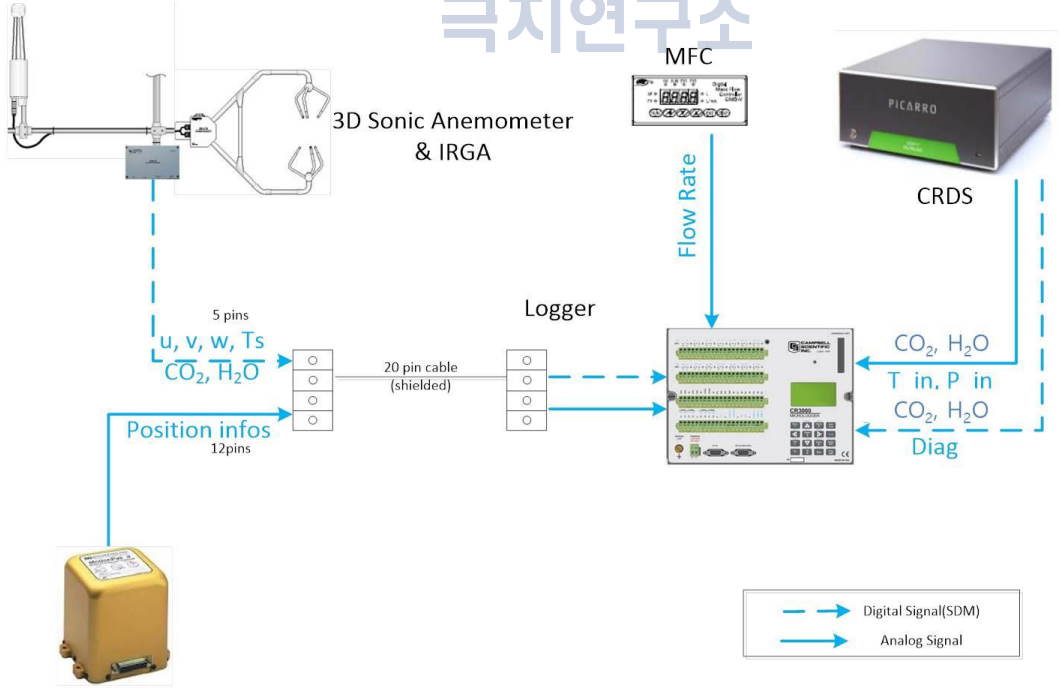

Fig. 1.5. Schematic of signal flows of the eddy covariance system (Updated from 2013 ARA04C cruise report).

As a component of the eddy covariance system, two motion sensors (MotionPakII, BEI, USA) are installed. One is fixed next to the sonic anemometer to monitor the motion the sensors themselves (Fig. 1.3). The other is placed in the CRDS shelter to monitor vibration of the ship as a reference. Motion data will be used to correct apparent wind regime due to movement and vibration of ship with ship navigation data. Along with the eddy covariance system, net radiometer (CNR1, Kipp & Zonen, Netherlands) is also installed at the bow (Fig. 1.3). The CNR1 measures four components of radiation, i.e., incoming shortwave and longwave and outgoing shortwave and longwave. Radiation data are also saved in the data logger in the CRDS shelter.

1.2.3. Radarmast

Meteorological observations on the radarmast include air temperature and relative humidity (HMP45D, Vaisala, Finland), air pressure (PTB100, Vaisala) and downward shortwave (PSP, Eppley, USA) and longwave radiation (PIR, Eppley) (Figure 6). The height of measurement is 38 meters above the water surface. The data logger (CR3000, Campbell Scientific, Inc., USA) scans each sensor every 10 seconds and saves the average of scans every 10 minute. The desktop computer in the Atmospheric Sciences Laboratory retrieves the data from the data logger on a regular basis. The data are announced in real-time via web-based monitoring software (Fig. 1.7).

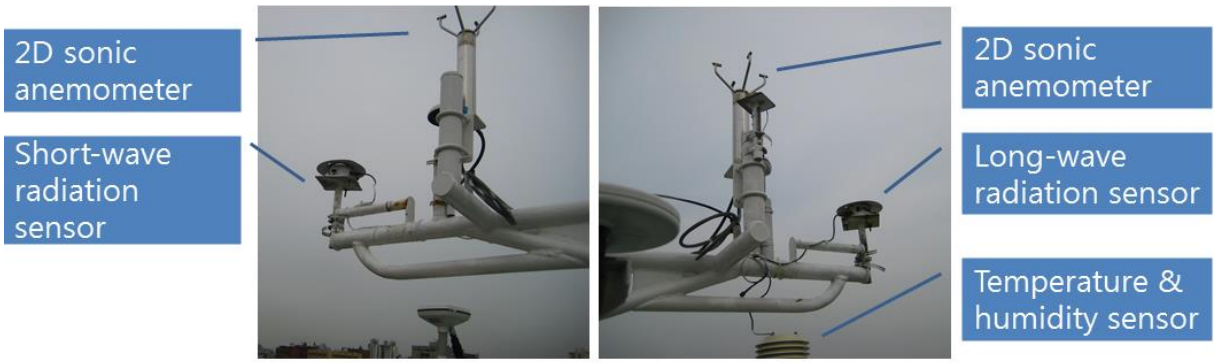

Fig. 1.6. Instruments at the radarmast. Note that 2D sonic anemometers provide wind information for the cruise only (Adapted from 2013 ARA04C cruise report).

Fig. 1.7. Webpage for announcing meteorological data at the radarmast (internal IP address: http://192.168.0.23/), but the wind speed data come from the foremast windmill anemometer.

1.2.4. Atmospheric Sciences Laboratory

The aethalometer (AE, Magee Scientific, USA) collects the sample (w/ the flow rate of 5 LPM) on a quartz fiber filter tape, performs a continuous optical analysis for the quantification of black carbon emitted from the combustion, and yields the mass concentration (ng/m^3) of black carbon (up-left panel in Fig. 1.8). The number concentrations (#/cm^3) of aerosols are determined in real-time by using two condensation particle counters (CPC, CPC 3772 and CPC 3776, TSI, USA, bottom-left panel in Fig. 1.8). The nephelometer (3563, TSI, USA) measures the angular integral of light scattering that yields the quantity called the scattering coefficient, used in the Beer-Lambert Law to calculate total light extinction (right panel in Fig. 1.8).

Fig. 1.8. Aerosol measuring instruments: (Up-left) Aethalometer, (Bottom-left) Condensation Particle Counters (CPC3772 and CPC3776), and (Right) Nephelometer.

1.3. Observed Results

1.3.1. Air temperature

Fig. 1.9 shows the records of air temperature measured by two different sensors aboard IBRV *Araon*. Note that temperatures measured by CSAT3 are slightly higher than those by HMP45D not only due to the height difference (19 meters vs. 38 meters), but also because the former is virtual temperature including the effect of humidity. On the second and third days of cruise (August 1-2, UTC), IBRV *Araon* entered the Arctic Circle (north of 66°N) and continued cruising to the north. Air temperature dropped quickly up to -4°C from August 2

to 4 while the vessel voyaged northeastward through the Chukchi Sea, gradually rose to above freezing level between August 4 to 6 as the vessel entered a different weather regime, and fluctuated between -4°C and 1°C with an apparent diurnal cycle at the location of sea ice camp during August 8-14. The weather was generally clear in the middle of the camp, but on the last day (August 13-14, UTC), it became cloudy and foggy (Fig. 1.10). After the camp, the vessel headed to the southwest and west till August 17, during which she crossed the Northwind ridge and reached the Chukchi Plateau approximately along 76°N. The weather was kept clear till August 16, which means that the same weather regime continued though the vessel moved almost 600 km to the southwest. After August 17, however, the weather quickly changed, became foggy and rainy, and the clouds overcast the sky, during which the vessel was crossing the ice covered region of the Chukchi Abyssal Plain.

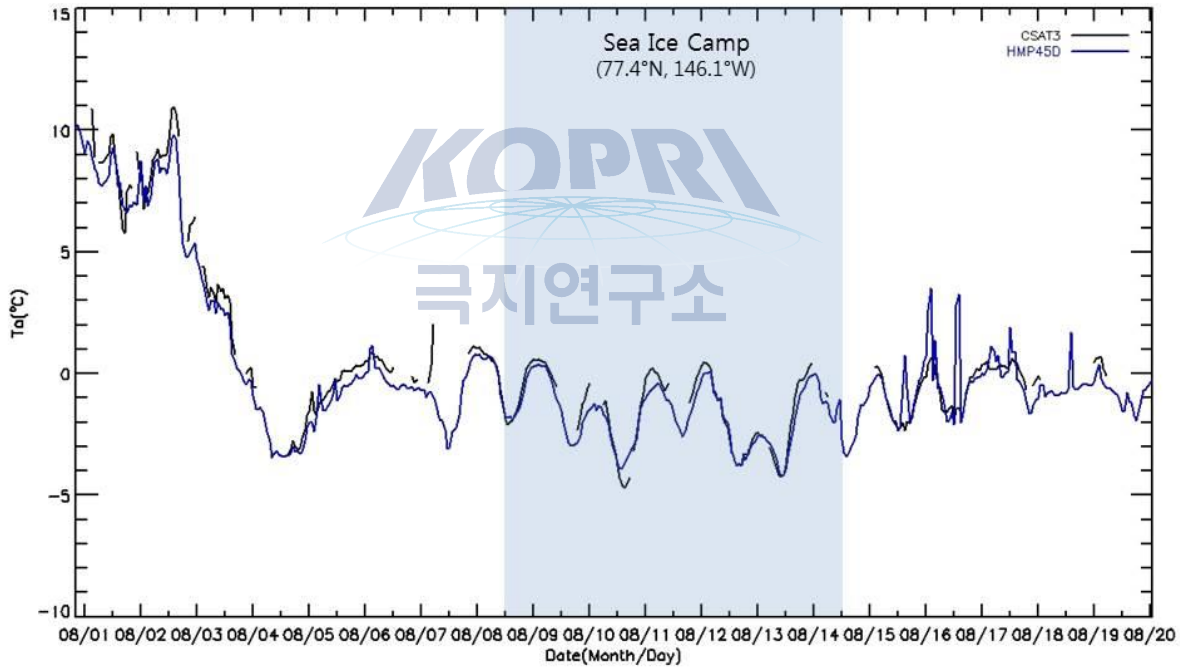

Fig. 1.9. Air temperature: (black) CSAT3 at the bow, (blue) HMP45D at the radarmast. The vessel was anchored to sea ice in the Beaufort Sea (approximately 77.4°N, 146.1°W) during the period of sea ice camp (August 8-14). Missing and erroneous values are omitted for CSAT3, but further quality control is still needed.

Fig. 1.10. Sky pictures during the period of sea ice camp.

1.3.2. Air Pressure

The time series of air pressure measured by two different sensors are shown in Fig. 1.11. Although their temporal variations are nearly similar, the pressure values measured by LI7500 at the bow are higher by 4-5 hPa than those measured by PT100 at the radarmast. Probably the pressure measurement of LI7500 is not well calibrated as it is not needed to calculate the mass density of carbon dioxide and water vapor [LI-COR Environmental Division, 2004]. Air pressure went up till the beginning of sea ice camp, reaching 1026 hPa (PT100). Thus the weather was very clear on the first day of camp (Fig. 1.10). This was expectable because, in a climatological sense, the Beaufort Sea area is governed by the anticyclonic weather regime with clear weather. The short pressure drop from August 4 through August 6 occurred when IBRV *Araon* was passing from the Northwind Ridge to the Beaufort Sea. The weather was cloudy at that time. At the camp site, air pressure gradually dropped with time, implying the high was retreating. The weather was getting cloudier and finally totally overcast on the final date. A short revert to the higher state was observed just after the camp while moving to the southwest, but again dropped quickly as the vessel moved away from the high pressure regime.

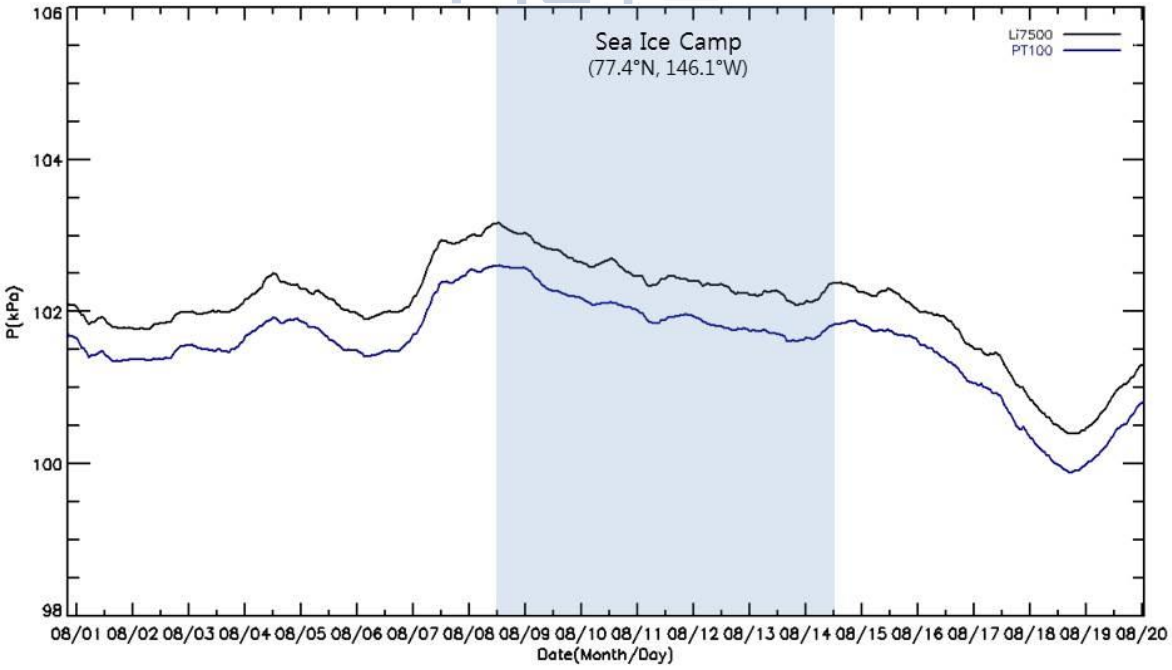

Fig. 1.11. Air pressure: (black) LI7500 at the bow, (blue) PT100 at the radarmast.

1.3.3. Wind

The time series of wind speeds and directions on the radarmast are demonstrated in Fig. 1.12. Here wind direction is not relative but true after applying correction by vessel's heading direction. At the beginning of the cruise, strong westerlies were followed by weak winds whose directions highly fluctuated with time. From the middle of August 2 to the end of August 4 while IBRV *Araon* voyaged northeastward through the Chukchi Sea, the cold northeasterlies with moderate wind speeds blew. These northeasterlies along with the quick drop of air temperature (Fig. 1.9) implies a cold advection during this period.

The cold northeasterlies abruptly changed to the southwesterlies on August 5 while she traveled from the Northwind Ridge to the Beaufort Sea. At the same time, air temperature rose (Fig. 1.9), pressure dropped (Fig. 1.11), and sky was cloudy. All of these conditions indicate that she was at the southern fringe of a low pressure system. The wind regime again changed to the strong northeasterlies from the second half of August 6 to early August 8 while she headed for the sea ice camp located toward the northeast. Air pressure rose again to the highest level 12 UTC August 8 (Fig. 1.11). A high pressure center seemed to pass north of the vessel, inducing surface northeasterlies along the cruise track.

While staying at the camp during August 8-14, the wind speed was generally moderate between 2 and 8 m s^{-1}, and the wind direction periodically changed between northerlies and northwesterlies, which appeared as a diurnal cycle of wind direction like a land-sea breeze. For a couple of days, *Araon* was situated in a region of prevailing northwesterlies with a higher pressure to the west. The fact that air pressure slightly increased on August 15 while she traveled southwestward after the camp may reflect the higher pressure to the west. One day later and onwards (from August 16), the winds got stronger and became easterlies with foggy, cloudy, and rainy weather during which she crossed the Northwind Ridge, Chukchi Plateau, and Chukchi Abyssal Plain approximately along 76°N.

After finishing the cruise, the spatial patterns of temperature, pressure and wind are needed to be analyzed to verify our interpretation based on time series. The global reanalysis data will be acquired and analyzed over the Pacific Arctic region, and also can be compared with the ship observations.

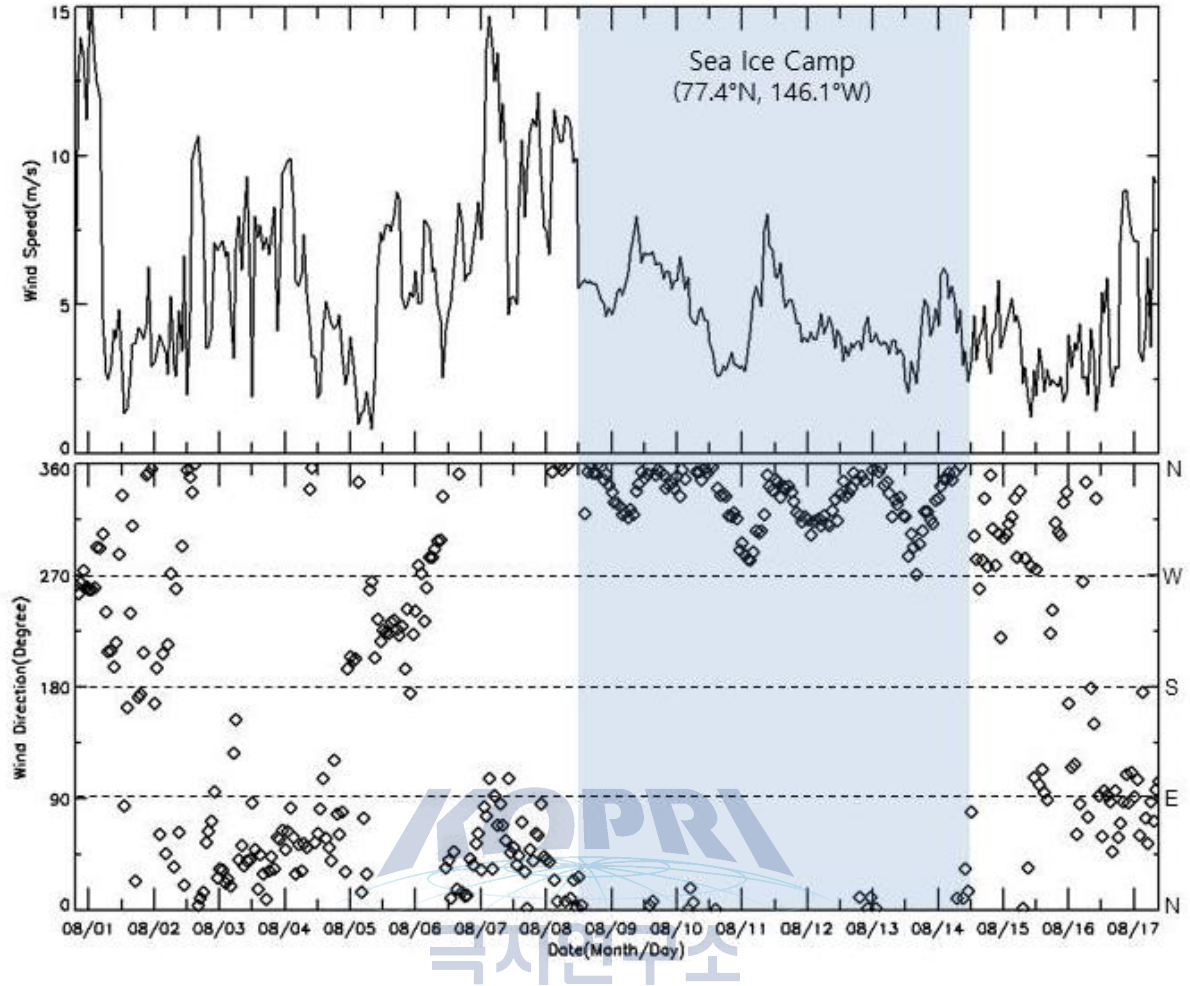

Fig. 1.12. (Top) Wind speed [m s^{-1}] from DaDis data. (Bottom) Compass wind direction using DaDis (wind direction relative to vessel's heading direction) and Gyro Compass (vessel's heading direction) data: 0-90 deg: N-E regime, 90-180 deg: S-E regime, 180-270 deg: S-W regime, and 270-360: N-W regime.

1.3.4. Radiation

Fig. 1.13 displays the time series of net shortwave radiation (NetRS), net longwave radiation (NetRL), and their summation, i.e., net total radiation (Rnet). NetRS shows an apparent diurnal cycle associated with the diurnal variation of solar zenith angle. The peak value almost reached 580 W m^{-2} on 01 UTC August 2 when the vessel was passing by a sunny region, around the latitude of 67°N. As the vessel migrated to the north, the daytime peak value of NetRS became lower due to the increase of solar zenith angle. This effect of latitude can be fairly compared among clear days only (e.g., 22 UTC August 4 near 74°N, 22 UTC

August 7 near 76.8°N, 21 UTC August 10 near 77.4°N, 00 UTC August 15 near 76.8°N, and 00 UTC August 16 and 17 near 76°N). Needless to say, the clouds and fogs were critical for NetRS. The amplitude of NetRL was also an indication of the existence of clouds and fogs. On clear days, NetRL reached -60 W m^{-2} (negative upward), implying strong longwave cooling. By contrast, the existence of clouds and fogs reduced longwave cooling (almost zero or positive NetRL) due to their blanket effects. The temporal variation of Rnet was almost synchronous with that of NetRS, indicating that it is NetRS that dominates the radiation budget in the Arctic summertime.

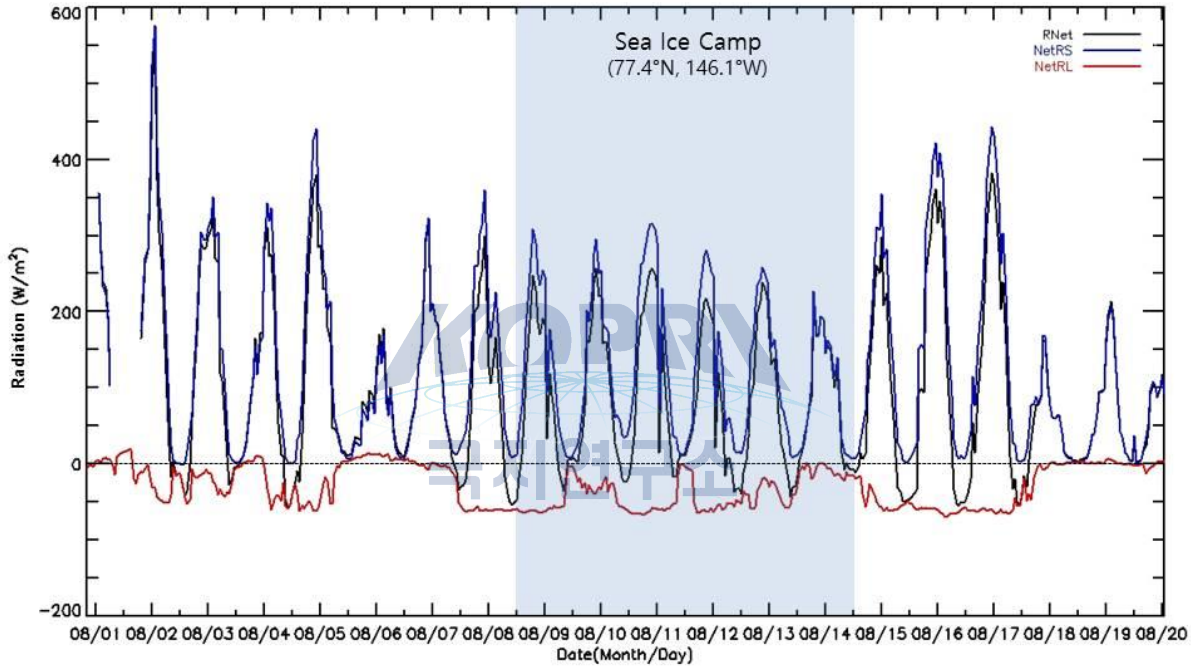

Fig. 1.13. Net radiations [W m^{-2}]: (black) Net total radiation, (blue) Net shortwave radiation, (red) Net longwave radiation. Positive sign denotes downward direction. Missing and erroneous values are omitted.

1.3.5. Humidity and Water Vapor

On the radarmast of IBRV *Araon*, relative humidity (RH) of air was continuously measured by HMP45D during the cruise (Fig. 1.14). For most of the time, RH was kept 100 % regardless of the weather condition. Low air temperature below freezing temperature made the air less capable of containing water vapor, easily rendering the air into a saturation state

even during clear days. Compared with RH records in the 2013 Arctic cruise (ARA04C), the environment was generally more humid during the 2014 cruise. Need to check whether the vapor amount was larger this year. On the other hand, RH dropped down during warm and clear days. However, several sharp drops after the camp seemed to arise from an instrument error, seeing that HMP45D air temperature showed an anomalous short-term peak of warming that cannot be natural (Fig. 1.9).

Two sensors measured water vapor (H_2O): LI7500 and CRDS. LI7500 and CRDS recorded mass density and mole fraction, respectively. Like CSAT3 air temperature data, LI7500-measured H_2O mass density data also have lots of missing due to the vulnerability of the instrument to the wetness and freezing. Around the beginning of the cruise (southward of 70°N), H_2O amount was larger by a factor of two than that for the rest time northward of 72°N. When LI7500 was in a fine condition (e.g., during sunny days or just after management), H_2O mass density mostly fluctuated around 5 g m^{-3}. Mass densities deviated largely from this value are not credible. CRDS continuously measured H_2O mole fraction without malfunction. Temporal variation of mole fraction is very similar to that of air temperature (Fig. 1.9 vs. Fig. 1.14). Air temperature and pressure are required to calculate H_2O mole fraction from its number density [mmol m^{-3}] [LI-COR Environmental Division, 2004]. Therefore the similarity between the time series of mole fraction and air temperature reflects the sensitivity of H_2O mole fraction to air temperature. Like air temperature, H_2O mole fraction has an apparent signal of diurnal cycle.

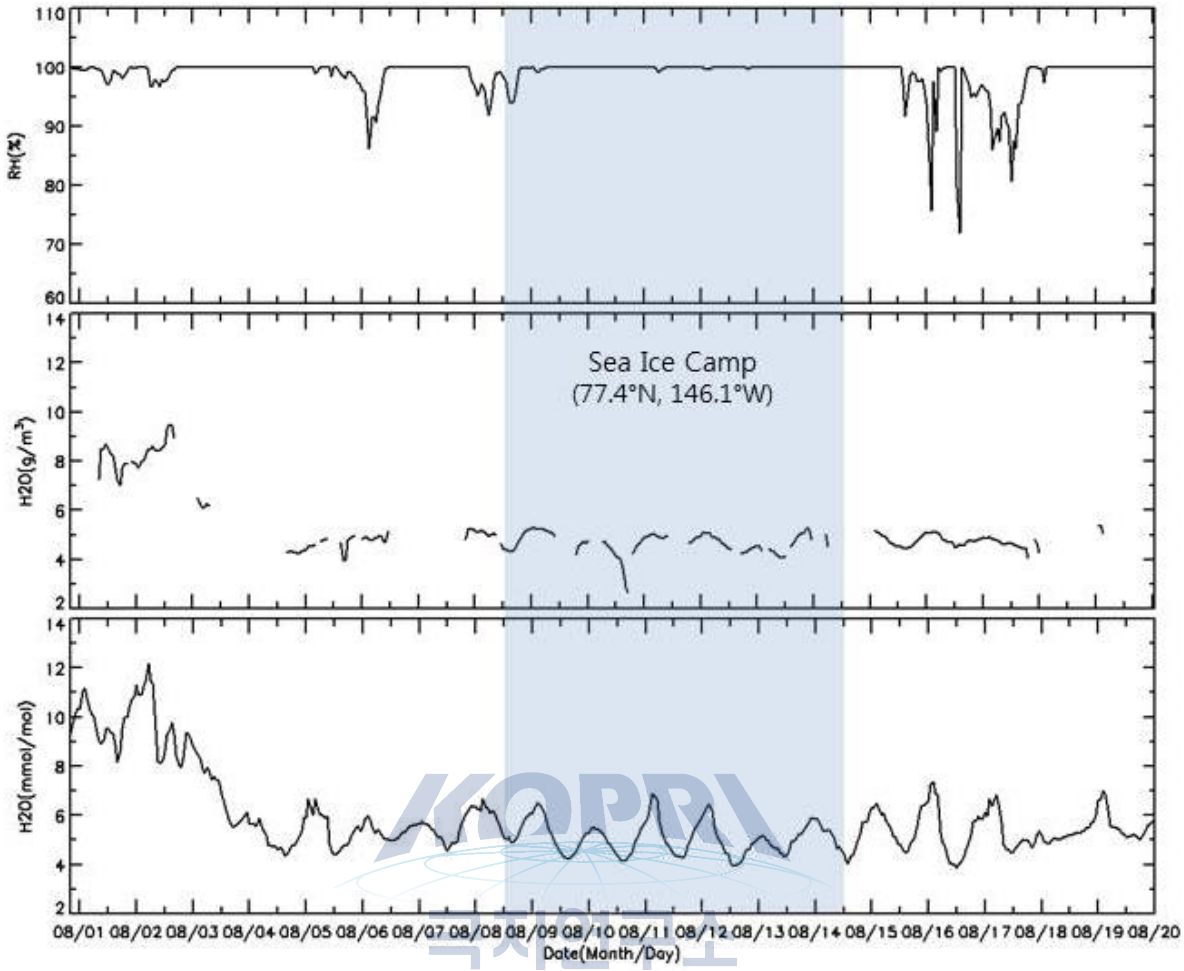

Fig. 1.14. (Top) Relative humidity [%] measured by HMP45D at the radarmast. (Middle) Water vapor mass density [g m^{-3}] measured by LI7500. Missing and erroneous values are omitted for LI7500, but further quality control is still needed. (Bottom) Water vapor mole fraction [mmol mol^{-1}] measured by CRDS.

1.3.6. Carbon dioxide

Two time series of carbon dioxide (CO_2) are shown in Fig. 1.15. Like H_2O, two sensors measured CO_2: LI7500 and CRDS. LI7500-measured CO_2 mass density data also have lots of missing with the same reason as LI7500-measured H_2O mass density data. Around the beginning of the cruise (southward of 70°N), CO_2 mass density was lower than 735 mg m^{-3}, but it increased to 750-760 mg m^{-3} in the middle of the cruise. CO_2 mass density decreased after sea ice camp while moving to the west, by the reason that we don't know. On the

other hand, CRDS recorded CO_2 concentration [ppm] continuously. Concentration data also show a jump of the mean between 70°N and 72°N. After the jump, CO_2 concentration fluctuated with the center close to 388 ppm. This value was almost same as that reported in ARA04C.

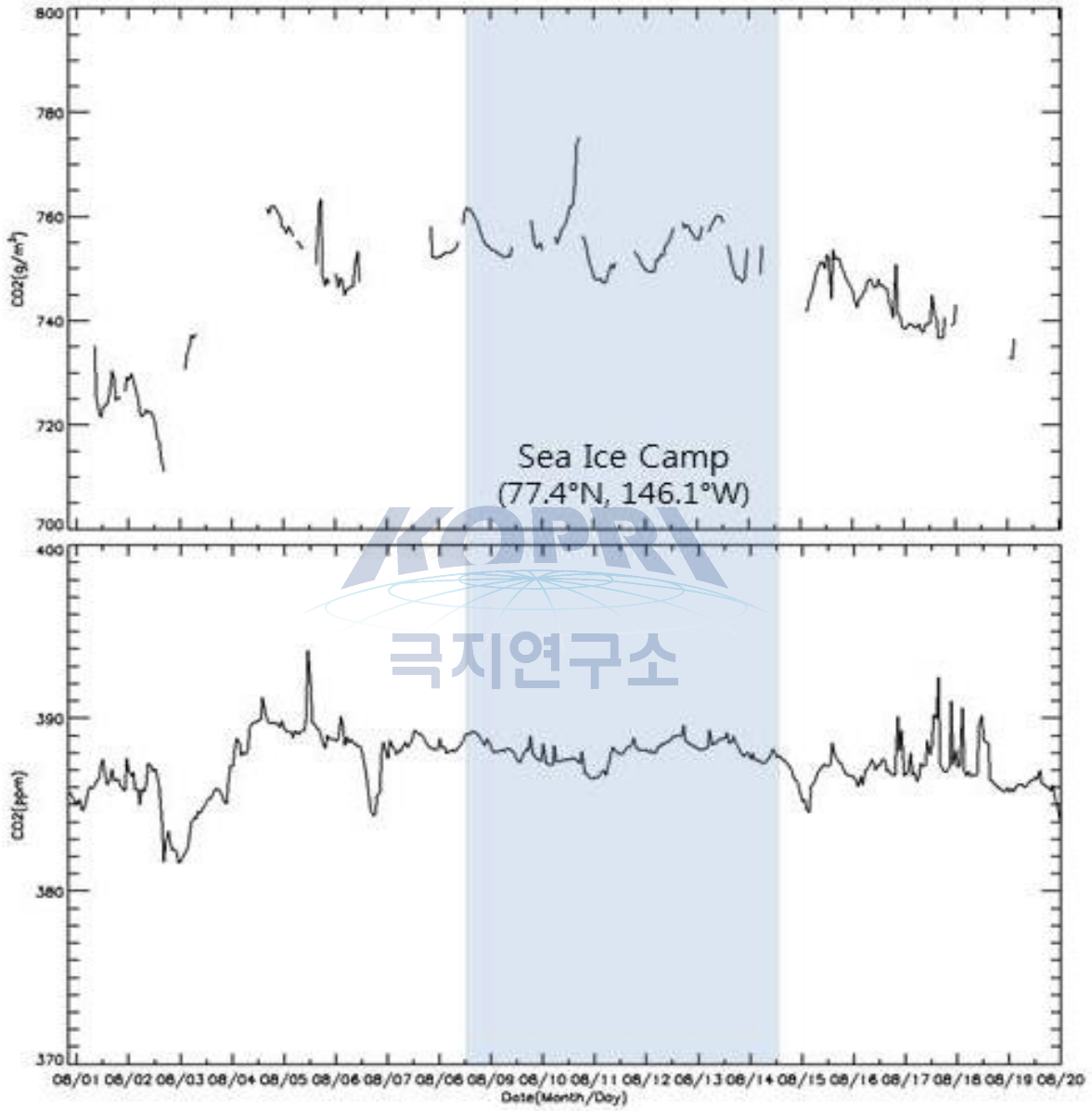

Fig. 1.15. Carbon dioxide: (Top) Mass density [mg m^{-3}] measured by LI7500, (Bottom) Concentration [ppm] measured by CRDS.

1.3.7. Aerosols

The aethalometer, CPC, and nephelometer continuously measured various aerosol

properties. In this report, the mass density [ng m^{-3}] of black carbon (BC) aerosol measured by the aethalometer is demonstrated (Fig. 1.16). However, other data will be processed after the cruise. In the figure, a notable feature is the increase of BC mass density during the two periods; i.e., August 5-6 and August 16-19. Almost certainly, this was due to the BCs originated from vessel's combustion. During the first period, southwesterlies blew while the vessel headed northeastward, whereas during the second period, easterlies blew while the vessel headed westward (Fig. 1.12). Thus tail-winds blew during the two periods, so that the BCs from the vessel's funnel could have a higher change to flow into the intake installed at the front outside of the Atmospheric Sciences Laboratory.

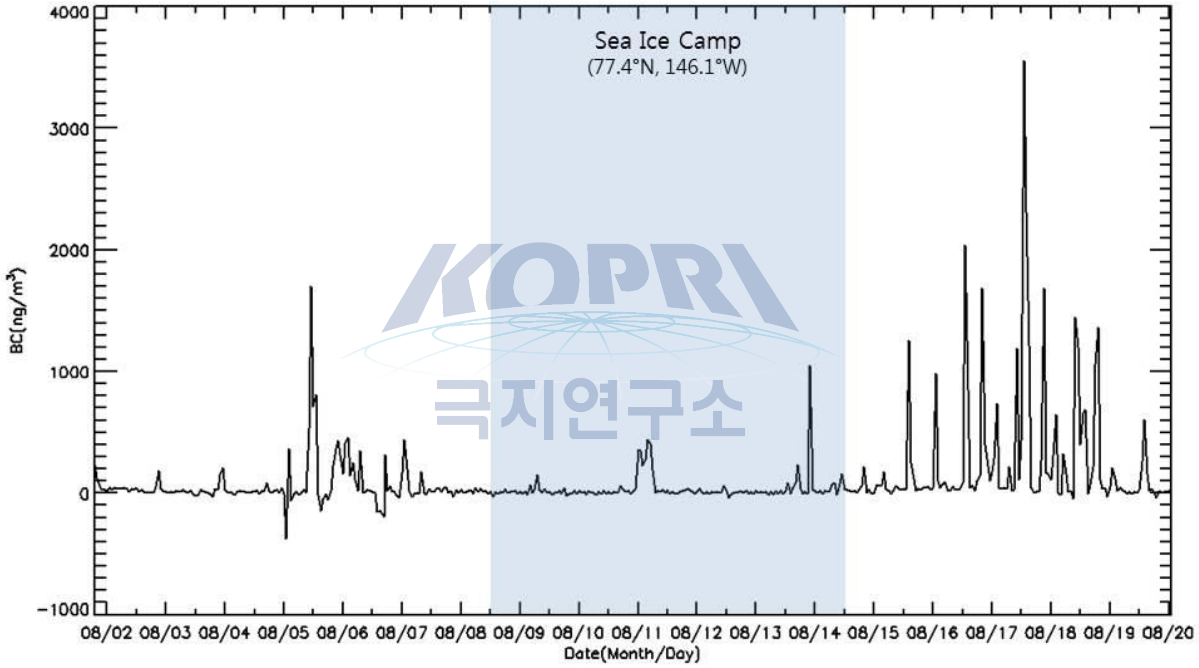

Fig. 1.16. Mass density [ng m^{-3}] of black carbon aerosol measured by aethalometer.

1.3.8. Turbulent fluxes

The eddy covariance system directly measures the air-sea turbulent fluxes of momentum and sensible and latent heat. The new movable platform of the eddy covariance system was installed at the bow in June 2013 and has been running since then. The motion sensor, measuring three-directional accelerations and angular rates, is needed for the calibration of biases of eddy covariance flux measurements due to the ship motion. One

motion sensor is installed near CSAT3 to capture its motion. After the cruise, the motion correction will be applied every 30 minutes [Miller *et al*., 2008], and the corrected data will be saved for a further analysis. Since the calculation of eddy fluxes is a time-consuming process integrating eddy covariance measurements, motion information and navigation data (i.e., course and speed of the vessel), it remains as a post-cruise work.

Just for the purpose of exhibition, the sensible and latent heat fluxes and frictional velocity are displayed in Fig. 1.17. Based on a simple quality control (QC), apparent missing and erroneous data were omitted in the figure. However, more than 50% of measurements are expected to be filtered out during strict QC after the cruise. So we do not interpret these results.

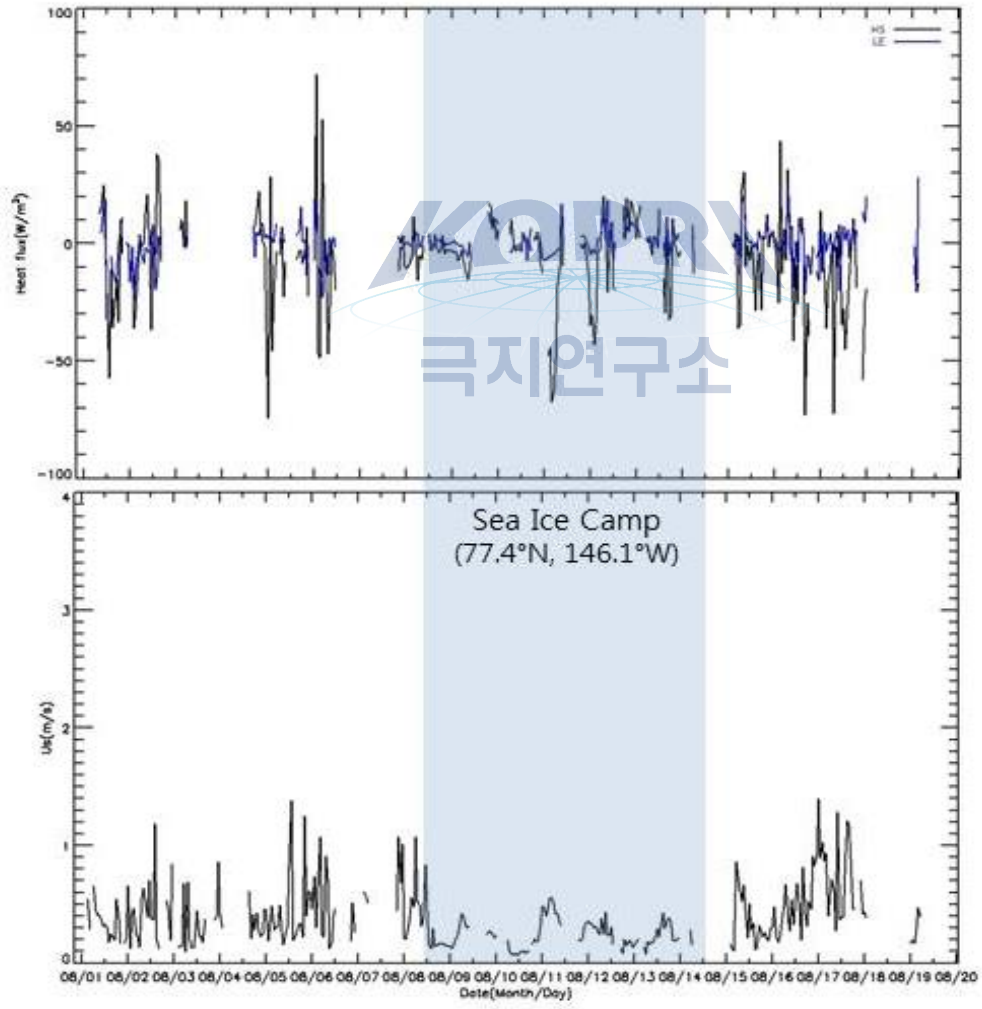

Fig. 1.17. (Top) Turbulent fluxes [W m^{-2}]: (black) sensible heat flux, (blue) latent heat flux. (Bottom) Frictional velocity [m s^{-1}]. Both measured by CSAT3.

1.4. Summary and Concluding remarks

Various atmospheric properties were observed using multiple instruments aboard IBRV *Araon* during her 2014 Arctic cruise to the Bering/Beaufort/Chukchi Seas. She also supported 6-day sea ice camp in the Beaufort Sea (period: August 8-14, location: 77.4°N, 146.1°W). Observed parameters include air temperature, air pressure, wind speed and direction, radiation, humidity, water vapor and carbon dioxide, aerosols, and air-sea turbulent fluxes. While some measurements were stably done during the cruise, others were not due to the harsh weather condition in the Arctic Ocean. For example, the eddy covariance system including CSAT3 and LI7500 frequently fell in malfunction, but it was difficult to manage it immediately while the vessel was moving. The regular managements (e.g., lens cleaning, ice removing, etc.) were done after the vessel stopped for the oceanographic survey and sea ice work. Log of events describing the works of management is given in Appendix A.

Post-process works are needed for some data that include any wind information. The navigation data are needed to get true compass wind direction and speed. The motion sensor and navigation data together can correct the biases of eddy covariance fluxes. The motion correction for the fluxes will be done after the cruise.

Although lots of data are needed strict QC, this report showed basic time series of most data measured during the cruise after simple QC by removing the apparently unphysical values. As discussed in Section 3, the physical meteorological variables (e.g., air temperature, pressure, radiation, and wind) could be reasonably interpreted with the aid of the real environmental information (e.g., weather and location) collected by on-board researchers. All collected data are invaluable for the researches on the Pacific Arctic Sector.

References

Curry, J. A., W. B. Rossow, D. Randall, and J. L. Schramm (1996), Overview of Arctic cloud and radiation characteristics. *J. Climate*, 9, 1731–1764.

Hong, J, J. Kim, T. Choi, J. Yun and B. Tanner (2000), On the effect of tube attenuation on measuring water vapor flux using a closed-path hygrometer. *Korean J. Agricultural and Forest Meteorology*, 2(3), 80–86.

Jacobson, M. Z. (2002), Control of fossil-fuel particulate black carbon and organic matter, possibly the most effective method of slowing global warming. *J. Geophys. Res.*, 107(19).

Kinnard, C., C. M. Zdanowicz, D. A. Fisher, E. Isaksson, A. de Vernal, and L. G. Thompson (2011), Reconstructed changes in Arctic sea ice over the past 1,450 years, *Nature*, 479(7374), 509–512.

LI-COR Environmental Division (2004), *LI-7500 CO_2/H_2O Analyzer: Instruction Manual*. LI-COR, Inc., 155pp.

Miller, S. D., T. S. Hristov, J. B. Edson, and C. A. Friehe (2008), Platform motion effects on measurements of turbulence and air-sea exchange over the open ocean. *J. Atmos. & Ocean. Tech.*, 25(9), 1683–1694.

Semiletov, I. P., I. I. Pipko, I. Repina, N. E. Shakhova (2007), Carbonate chemistry dynamics and carbon dioxide fluxes across the atmosphere–ice–water interfaces in the Arctic Ocean: Pacific sector of the Arctic. J. Marine Systems, 66, 204–226.

Serreze, M. C., A. P. Barrett, and J. J. Cassano (2011), Circulation and surface controls on the lower tropospheric air temperature field of the Arctic. *J. Geophys. Res.*, 116, D07104, doi:10.1029/2010JD015127.

Vavrus, S., and D. Waliser (2008), An improved parameterization for simulating Arctic cloud amount in the CCSM3 climate model. *J. Climate*, 21, 5673–5687.

Appendix A. Log of events

Date & Time (UTC)	Event
2014.07.31 18:00	Install CSAT3(SN:2337), LI7500(SN:0790), CNR1 at bow
2014.07.31 18:30	CRDS power on
2014.07.31 23:00	Install spectral radiometer at bow((Eurico D'Sa)
2014.07.31 23:50	CNR1 re-wiring
2014.08.01 17:45	CNR1 re-wiring
2014.08.01 18:00	Aethalometer, CPC3772, CPC3776, Nephelometer power on
2014.08.02 21:10-21:35	CNR1, LI7500 lens cleaning
2014.08.03 18:00	Enter the ices zone
2014.08.04 13:05-14:10	Remove the ice on CNR1, CSAT3, LI7500
2014.08.06 04:00-04:21	CNR1, CSAT3, LI7500 lens cleaning
2014.08.06 18:35-19:05	Remove the ice on CNR1, CSAT3, LI7500
2014.08.06 22:45-22:53	CNR1, CSAT3, LI7500 lens cleaning
2014.08.06 23:10-23:14	CNR1, CSAT3, LI7500 lens cleaning
2014.08.07 00:40-00:53	CNR1, CSAT3, LI7500 lens cleaning
2014.08.09 17:30-18:00	Remove the ice on CNR1, CSAT3, LI7500
2014.08.10 04:45-05:10	Remove the ice on CNR1, CSAT3, LI7500
2014.08.10 17:25-17:40	Remove the ice on CNR1, CSAT3, LI7500
2014.08.10 22:00-22:30	Climb the radar mast to check HMP45D(remove the ice)
2014.08.11 17:25-17:50	Remove the ice on CNR1, CSAT3, LI7500
2014.08.12 15:50-16:20	Remove the ice on CNR1, CSAT3, LI7500
2014.08.12 19:00-19:20	Climb the radar mast to check HMP45D
2014.08.13 01:00-04:20	Remove the ice on CNR1, CSAT3, LI7500
2014.08.13 12:20-12:43	Remove the ice on CNR1, CSAT3, LI7500
2014.08.14 00:00-00:15	CNR1, CSAT3, LI7500 lens cleaning
2014.08.14 01:15-01:21	CNR1, CSAT3, LI7500 lens cleaning
2014.08.14 02:15-02:20	CNR1, CSAT3, LI7500 lens cleaning
2014.08.14 03:30-03:35	CNR1, CSAT3, LI7500 lens cleaning

Date & Time (UTC)	Event
2014.08.15 00:25-00:45	Remove the ice on CNR1, CSAT3, LI7500
2014.08.17 20:10-20:37	Remove the ice on CNR1, CSAT3, LI7500
2014.08.18 02:20-02:40	Remove the ice on CNR1, CSAT3, LI7500
2014.08.18 22:45-23:00	Remove the ice on CNR1, CSAT3, LI7500
2014.08.18 23:55-23:59	CNR1, CSAT3, LI7500 lens cleaning
2014.08.19 03:10-03:15	CNR1, CSAT3, LI7500 lens cleaning

Chapter 2. Hydrographic Survey

Kyoung-Ho Cho[1], Tae Wan Kim[1] and Chan-Yeong Gang[1]

[1]Korea Polar Research Institute, Incheon, Korea (kcho@kopri.re.kr; twkim@kopri.re.kr; chanyoung85@kopri.re.kr)

Koji Shimada[2] and Eri Yoshizawa[2]

[2]Tokyo University of Marine Science and Technology, Tokyo, Japan (koji@kaiyodai.ac.jp; m103046@kaiyodai.ac.jp)

Jinping Zhao[3]

[3]Ocean University of China, Qingdao, China (jpzhao@ouc.edu.cn)

2.1 Introduction

The Arctic Ocean has warmed over the past few decades (Polyakov et al., 2007; Steele et al., 2008). Most of the Arctic Ocean peripheral seas may be vulnerable to overall warming trends in global climate changes (Solomon et al., 2007). Especially, change in extent and thickness of Arctic sea ice is recognized as a key indicator of Arctic climate change (Shimada et al., 2006). In oceanographic point of view, it is important to identify what forcings drive sea ice reduction in the Arctic Ocean. Increase in temperature of warm waters entrained from the Atlantic Ocean and the Pacific Ocean may be contributing to sea ice melt (Polyakov et al., 2010; Shimada et al., 2006). One of the reasons for rapid reduction of Arctic sea ice is associated with increase in heat transport of summer waters and vertical fluxes of heat and momentum on atmosphere-ice-ocean interfaces (Carmack and Melling, 2011).

In the Pacific sector which covers the Beaufort, Chukchi, East Siberian and Laptev Seas, most of heating during summer comes from ocean surface heat flux and lateral heat flux convergence (Steele et al., 2010). It is well-known that there are relatively warm Pacific-origin summer halocline waters which passes through the Bering Strait and reaches the vicinity of the Chukchi Sea (Shimada et al., 2001; Steele et al., 2004). This Pacific-origin summer waters (PSWs) tend to be redistributed to the Beaufort Sea along the Alaskan coast

and to the vicinity of the Chukchi Borderland (i.e., the Northwind Ridge and Chukchi Plateau) and Mendeleev Ridge. PSW's pathways around this region appear to be spread by the combined effects of local bathymetry, freshwater runoff, and variation of basin-scale oceanic gyre related to sea ice motion. The PSWs can be also recognized with shallow temperature maximum on the basis of salinity range: surface mixed layer water (S < 30 psu), eastern Chukchi summer water (31 < S < 32 psu), and western Chukchi summer water (S > 32 psu) (Shimada et al., 2001).

Halocline structure in the water column of the western Canada Basin presents a complicated layering of different water masses. This halocline structure is spatially non-uniform and depends on the pathways of Pacific-origin summer/winter waters (Shimada et al., 2005). Additionally, a near-surface temperature maximum (NSTM) at typical depths (25-35 m) forms when sufficient solar radiation warms the upper ocean. The NSTM has warmed and expanded northward and bot the NSTM and the summer halocline formed at successively shallower depths (Jackson et al., 2010). The horizontal heat transport and heat release of the summer halocline water and its pathway variation may play a significant role in understanding not only temporal and spatial changes of the halocline structure in the western Canada Basin and the Chukchi Borderland but rapid sea ice reduction in the Pacific sector of the Arctic Ocean.

We, therefore, conduct 25-day Arctic Ocean expedition in summer of 2014 (ARA05B) using the ice breaker R/V Araon to fulfill three scientific goals: (1) to investigate the temporal and spatial changes of the halocline structure of the water column in the western Canada Basin, (2) to understand the variation of the summer halocline water's pathways and its relationship with sea ice reduction, and (3) to represent the pattern of ocean circulation in the Chukchi Borderland for 2014 summertime.

2.2 Materials and Methods

2.2.1 CTD Casting

An intensive oceanographic survey was conducted at 32 hydrographic stations (total 111 casts) in the western Canada Basin and the Chukchi Borderland during the period of July

31 to August 24, 2014 (Fig. 2.1). Along the transects of hydrographic stations (Table 2.1 and Appendix I), vertical profiles of temperature, conductivity, fluorescence, turbidity, transmissivity, and dissolved oxygen and water samples were obtained from the hydro-casts of a SBE32 carousel water sampler equipped with a SBE9plus CTD profiler, a transmissometer, PAR, fluorometer, scattering sensor, altimeter and SBE43 dissolved oxygen sensor, and 24 position rosette with 10-liter Nisken bottles (Fig. 2.2(a)). During the CTD upcasting, water samples were collected at several depths for biochemical analyses. For the precise reading, the salinities of collected water samples were further analyzed by an Autosal salinometer (Guildline, 8400B). The measurement was performed when the temperature of water samples was stabilized to a laboratory temperature, usually within 24-48 h after the collection.

To increase the spatial resolution for temperature and salinity, the expendable CTD (XCTD, Fig. 2.2(b)) probes were released at 46 stations determined in consideration of local bathymetry and distance between hydrographic stations (see Fig. 2.1 and Appendix II). XCTD is designed to sample the temperature and salinity fields of the upper ocean (up to 1100 m depth) from a vessel underway routinely and precisely.

2.2.2 Ocean Current Measurement

A 300 kHz RDI lowered Acoustic Doppler Current Profiler (LADCP) was amounted on the CTD/Rosette frame to measure a full-depth profile of ocean current (Fig. 2.2(c)). Using the conventional “shear method” for processing (e.g., Fischer and Visbeck, 1993), overlapping profiles of vertical shear of horizontal velocity were averaged and gridded to form a full-depth shear profile. The bin size was chosen as 5 m and the number of bins was 20. On the cruise track, a shipboard ADCP with an Ocean Surveyor 38 kHz phased array (OS38) was continuously operated to measure ocean currents up to 1200 m water depth under good weather condition in its deep-profiling mode.

2.2.3 Mooring Observation

One mooring (CPS14) was deployed in the essential location where the summer halocline water is redistributed to the Chukchi Borderland at 74^{o}48.0369'N and

167°53.8962'W. This mooring is comprised of one upward looking ADCP (Work Horse 600 kHz with bottom tracking option), one downward looking ADCP (Work Horse 300 kHz with bottom tracking option), 3 CTD sensors (SBE37SM), one CT sensor (SBE37SM), one pressure sensor (JFE advantec DEFI), 25 temperature loggers (SBE56) and one acoustic releaser (ORE/EdgeTech PORT) (Fig. 2.3). These sensors were distributed from the surface mixed layer to the bottom of the Pacific-origin water layer to investigate the influence of PSW on the formation of sea ice.

Unfortunately, due to heavy sea ice condition, we were unable to recover the mooring array (CP13) deployed during the 2013 Arctic Ocean summer cruise. The mooring array contains one ADCP (Work Horse 600 kHz with bottom tracking option), 2 CTD sensors (SBE37), 2 pressure sensors (JFE advantec DEFI), 14 temperature loggers (SBE56) and one acoustic releaser (ORE/EdgeTech PORT). This mooring was deployed in the shallow area on the Northern Chukchi Plateau at 77° 28.3353′ N and 164° 07.0789′ W to examine the influence of the Pacific-origin water on the sea ice behavior. This mooring array is scheduled to be recovered during the Arctic Ocean expedition next year.

2.3 Sea Ice Camp Activities

2.3.1 OUC's Activity: by Jinping Zhao

Scientific Goals

The main purpose in participating this cruise is to conduct the field observation for CTD and ADCP on the ice camp. With these data, the downward flux for momentum transfer will be analyzed to study the mixing produced by ice drag stress and stratification. The other goal is to track the variation of the geostrophic current during the drifting of the ice camp. Time series data are necessary for these studies.

Instruments

ADCP: The RDI-300kHz Lowered Acoustic Doppler Current Profiler (LADCP, Fig. 2.4(a)) is used to measure the current on the ice camp. The measurement range of the LADCP is

110-160m, speed scope is ±10m/s, measuring accuracy is ±1%(FS) or ±0.1 cm/s, sensitivity is 0.1 cm/s. The resolution of the compass and tilt sensors are 0.1º, and the accuracy of them are all ±0.1°.

CTD: The CTD is RBRconcerto, a product of RBR company (Figs. 2.4(b) and 2.4(c)). The maximum sampling frequency is 6 Hz. This CTD with pressure control function, which can sampling in a given pressure condition and is suitable to an automatic sampling. A winch is adopted to carry out the autonomous profiling with the CTD. The deploy rope length and waiting time of the winch can be set before starting the autonomous mode. The winch then goes down to the maximum rope length with a fixed speed about 0.4 m/sec. It then waits and starts to lift until it is recalled.

Buoy for Sea Ice Lateral Melting: A ball-shape drifting buoy is used to link with 5 laser sensors to test the measurement for sea ice lateral melting (Figs. 2.4(d) and 2.4(e)). The laser ranging system is for deployment in the shallow sea water to measure the distance change from the wall of sea ice. The ranging accuracy is 0.1 cm.

Field Observations

On the ice camp, by collaboration with Dr. Koji Shimada, we decide to assemble two ADCP to measure a deeper current profile. The LADCP was deployed at the depth of 70m to measure downward. The sampling time span is 4 seconds, with 2 seconds interval from the upper ADCP. The first deployment position is the same as the location of TUMSAT (Table 2.3(a)).

CTD is deployed on the afternoon of August 8. The first profile is at local time 14:57 of August 8. The last profile is at local time 13:15 of August 13. The planned deployment frequency is about every two hours. Because the belt of the winch was broken on the second day, the profile was operated by hand for about 3-4 times per day. The maximum depth is more than 300m. Total 18 profiles' data are collected as shown in Fig. 2.5.

Data

All the data need to be analyzed after the cruise. The files of these data are listed in Table 2.2.

Acknowledgement

I greatly appreciate that the Korea Polar Research Institute provides us the opportunity in its 2014 Arctic Cruise. I appreciate the help from Sung-Ho Kang, Tae-Wan Kim, Byoung-Woong An, Phil Hwang, Jeff Pietro, Craig Lee, Hyoung-Sul La, Joo-Hong Kim, Kyoung-Ho Cho, Dong-Seob Shin, Reynold Aveoganna, Eric Richard, Su-Hwan Kim, and many other scientists and crew members.

2.3.2 TUMSAT's Activity: by Koji Shimada and Eri Yoshizawa

Recent rapid sea ice reduction is associated with the underlying ocean stratification and upward heat flux from warm water such as PSW and NSTM. The heat flux is not constant but is affected by the small scale fluctuations of sea ice motions. To understand the condition for substantial heat release from the ocean, variations of vertical mixing in surface layers dominated by oscillatory Ekman spiral. The structure of the spiral is strongly controlled by the vertical eddy viscosity arising from internal wave braking. Here we monitor temperatures and horizontal velocities using ice moored temperature logger (SBE56), MicroCAT (SBE37) and ADCP (WHS300KHz and WHS600KHz) at two sites during the first Ice Camp and at one site during the second Ice Camp. One LADCP (WH300KHz, Zhao) was mounted at the bottom end of the line for the first camp nearby Araon to measure velocities from surface to 200m deep in the Pacific Winter Water layer. Distributions of sensors are listed in Table 2.3(a) and (b). CTD profiling measurements down to 50m deep are also performed using SBE19 plus V2 at the ice camp nearby Araon for the first ice camp and second ice camp (Fig. 2.6). Sampling intervals are 30 min to 120 min.

Melt pond survey using 21 temperature loggers (SBE56) and two MicroCATs (SBE37) was performed on August 12 and 13 (LST). The sensors for this measurement were the same as in the Ice Mooring 2 (50 km northwest from Araon) (Table 2.3(c)).

2.3.3 KOPRI's Activity: by Kyoung-Ho Cho, Tae-Wan Kim, and Chan-Yeong Gang

During the first sea ice camp at Station 19 from August 8 to 13, we conducted every 2-hr ship-based CTD castings to examine temporal variation of halocline structure in the

upper ocean (up to 500 m depth). Water velocities were measured with LADCP.

2.4 Preliminary Results

2.4.1 T-S Diagram

During the expedition, 32 CTD stations and 51 XCTD stations were selected. Using deep downcasting data at each CTD station, we plotted the potential temperature (T)–salinity (S) diagram (Fig. 2.7). It shows that the study area is occupied by six distinct water masses: (1) Surface mixed layer water (SMLW); (2) Pacific summer water (PSW); (3) Pacific winter water (PWW); (4) Atlantic water (AW); (5) Alaskan coastal water (ACW); and (6) East Siberian Sea winter shelf water (ESWW). SMLW has the lowest salinity (down to about 26 psu) due to sea ice melting and fresh water input. PSW is relatively warm, fresh water mass presenting temperature maximum layer at 40~60 m depth. Its salinity is in the range of 30-31 psu, and temperature is around -0.2~0.3 ℃. PWW, a layer of relatively fresh (i.e., buoyant), cold water, lies immediately above the warm AW that is the water mass with the highest temperature and highest salinity. PWW plays a role in shielding the exchange of heat flux between overlying PSW and underlying AW (Fig. 2.8).

.

2.4.2 Vertical Structure of Water Masses

Warm Alaskan coastal water exists near the entrance of the Chukchi Sea within US EEZ (Fig. 2.9). The Pacific summer water (PSW) appears to be mixed with relatively colder and fresher water masses and then PSW's temperature maximum hardly existed. Fresh runoff or sea ice melting water would have an influence on PSW. However, ACW was clearly represented in the vicinity of the Bering Strait. At transect of St. 20 to St. 30, PSW clearly expands to the west and its thickness becomes decreased (Fig. 2.9).

2.4.3 Short Science Report of Koji Shimada

Recent rapid sea ice reduction is not spatially uniform but is from Chukchi Borderland region consisting of the Chukchi Plateau and Northwind Ridge. In the summer of 2014 during the expedition, the maximum sea ice retreat was observed in the Chukchi Plateau (Fig. 2.10) where the major northward pathway of PSW into the Canada Basin (Fig.

2.11). From the hydrographic survey, in this area temperature of PSW was substantially lower than the surrounding area (Fig. 2.11(b)). This suggests that the huge amount heat release affecting less ice formation during winter occurred in this area. Then the sea ice thickness at the melt onset in this area would be thinner than that in the surrounding area, and resulted in earlier disappearance of sea ice (Fig. 2.10).

In this summer, remarkable features in spreading pathway of PWW were observed. From 2011 to 2013, PWW reach northern Chukchi Sea via Herald Canyon, and turned its direction to east along the about 100-150m iso-bathymetries. PWW reached the Canada Basin via the Hanna Canyon at the southern end of the Northwind Ridge (Fig. 2.12(a)). In this year, PWW was rarely found in this region, but was distributed along the western frank of the Chukchi Plateau (Fig. 2.12(b)). Nearly the same pattern as in 2014 was observed in 2008. In these two years, sea ice motion in the preceding winter was substantially larger than the other year. The strengthened clockwise upper ocean circulation, westward currents along the northern shelf slope of the Chukchi Sea, overcame the east ward buoyancy driven-currents.

In the former Araon expeditions (2011-2013), extra warm Fram Strait Branch of Atlantic Water [FSBAW] (>0.8 ℃) was mainly observed in the Makarov Basin (Fig. 2.13(a)). This warm anomaly has propagated into the Chukchi Abyssal Plain in 2014 (Fig. 2.13(b)). Joint effects of the large amplitude seafloor topography of the Chukchi Plateau and the strong surface forcing by sea ice motion prevented the penetration of the extra warm FSBAW into the east of the Chukchi Plateau. The warm anomaly will propagate along the northern rim of the Chukchi Plateau and Northwind Ridge into the Beaufort Sea.

2.4.4 Observations from Sea Ice Camps

ADCP observations during the first ice camp and the second ice camp were shown in Fig. 2.14 and Fig. 2.15, respectively. The colored values are velocity magnitude relative to sea ice motion at each ice camp site. Black areas in Fig. 2.14 represent low correlation between water velocity and sea ice motion. That means that turbulence is relatively strong. It appears to be coincided with large inertial motion of the sea ice (Fig. 2.16).

2.5 Summary and Future Work

We conducted a hydrography survey during the period of July 31 to August 24, 2014. The 32 CTD stations and 51 XCTD stations were selected to observe the property of water masses. Two sea ice camps were held in the western Canada Basin and the west side of the Mendeleev Ridge. Some preliminary conclusions made from the ARA05B scientific cruise can be summarized as follows:

1) In the summer of 2014 during the expedition, the maximum sea ice retreat was observed in the Chukchi Plateau where the major northward pathway of PSW into the Canada Basin. From the hydrographic survey, in this area temperature of PSW was substantially lower than the surrounding area. This suggests that the huge amount heat release affecting less ice formation during winter occurred in this area.

2) In this year, PWW was rarely found in this region, but was distributed along the western frank of the Chukchi Plateau. Nearly the same pattern as in 2014 was observed in 2008. In these two years, sea ice motion in the preceding winter was substantially larger than the other year. The strengthened clockwise upper ocean circulation, westward currents along the northern shelf slope of the Chukchi Sea, overcame the east ward buoyancy driven-currents.

3) Within US EEZ, there are four distinct water masses in the Chukchi Sea within US EEZ: surface mixed layer water (SMLW), Pacific winter water (PWW), Atlantic water (AW), and Alaskan coastal water (ACW). The Pacific summer water (PSW) appears to be mixed with relatively colder and fresher water masses and then PSW's temperature maximum hardly existed. Fresh runoff or sea ice melting water would have an influence on PSW. However, ACW was clearly represented in the vicinity of the Bering Strait.

As a future work, several analyses need to be done as follows:

1) The current field to be derived by LADCP and vessel-mounted ADCP data will directly provide an implication of pathways and spatial distribution of Pacific-origin warm water.

2) As a further analysis, the current velocity field to be derived by LADCP and vessel-mounted ADCP data will directly provide an implication of pathways and spatial distribution

of Pacific-origin warm water.

3) Furthermore, the heat flux calculation will contribute to understanding of thermodynamic processes in the vicinity of the Chukchi Borderland.

References

Carmack, E. and H. Melling, 2011. Warmth from the deep. *Nature Geoscience*, 4, 7-8.

Fischer, J. and M. Visbeck, 1993. Deep velocity profiling with self-contained ADCPs. *Journal of Atmospheric and Oceanic Technology*, 10, 764-773.

Jackson, J.M., E.C. Carmack, F.A. McLanghlin, S.E. Allen, and R.G. Ingram, 2010. Identification, characterization, and change of the near-surface temperature maximum in the Canada Basin, 1993-2008. *Journal of Geophysical Research*, 115, C05021, doi:10.1029/2009JC005265.

Polyakov et al., 2007. Observational program tracks Arctic Ocean transition to a warmer state, *EOS Trans. AGU*, 88, 398-399, doi:10.1029/2007EO400002.

Polyakov et al., 2010. Arctic Ocean warming contributes to reduced polar ice cap. *Journal of Physical Oceanography*, 40, doi:10.1175/2010JPO4339.

Shimada, K., E.C. Carmack, K. Hatakeyama, and T. Takizawa, 2001. Varieties of shallow temperature maximum waters in the western Canadian Basin of the Arctic Ocean. *Geophysical Research Letters*, 28(18), 3441-3444.

Shimada, K., M. Itoh, S. Nishino, F. McLaughlin, E. Carmack, and A. Proshutinsky, 2005. Halocline structure in the Canada Basin of the Arctic Ocean. *Geophysical Research Letters*, 32, L03605, doi:10.1029/2004GL021358.

Shimada, K., T. Kamoshida, M. Itoh, S. Nishino, E. Carmack, F. McLaughlin, S. Zimmermann, and A. Proshutinsky, 2006. Pacific Ocean flow: Influence on catastrophic reduction of sea ice cover in the Arctic Ocean. *Geophysical Research Letters*, 33, doi:1029/2005GL025624.

Solomon, S., D. Qin, M. Manning, R.B. Alley, T. Berntsen, et al., 2007. Technical Summary. In: *Climate Change 2007: The Physical Science Basis. Contribution of Working Group I to the Fourth Assessment Report of the Intergovernmental Panel on Climate Change*. (Eds.) S. Solomon, D. Qin, M. Manning, Z. Chen, M. Marquis, et al., Cambridge, UK/New York, Cambridge University Press.

Steele, M., J. Morison, W. Ermold, I. Rigor, M. Ortmeyer, and K. Shimada, 2004. Circulation of summer Pacific halocline water in the Arctic Ocean. *Journal of Geophysical Research*, 109, C02027, doi:10.1029/2003JC002009.

Steele, M., W. Ermold, and J. Zhang, 2008. Arctic Ocean surface warming trends over the past 100 years. *Geophysical Research Letters*, 35, L02614, doi:10.1029/2007GL031651.

Steele, M., J. Zhang, and W. Ermold, 2010. Mechanisms of summertime upper Arctic Ocean warming and the effect on sea ice melt. *Journal of Geophysical Research*, 115, C11004, doi:10.1029/2009JC005849.

Table 2.1. A list of hydrographic CTD stations for ARA05B 2014 Arctic Ocean cruise.

Station	Start Time (UTC)		Latitude		Longitude		Depth(m)
	YY-MM-DD	hh:nn:ss	Deg.	Min.	Deg.	Min.	
ARA05B01CTD1	2014-08-01	09:39:19	65N	10.398	-168W	41.441	40
ARA05B02CTD1	2014-08-01	17:56:17	66N	37.794	-168W	41.256	33
ARA05B02CTD2	2014-08-01	19:00:00	66N	37.789	-168W	41.244	33
ARA05B03CTD1	2014-08-01	23:52:57	67N	19.999	-168W	49.987	40
ARA05B03CTD2	2014-08-02	01:00:00	67N	19.999	-168W	49.991	41
ARA05B04CTD1	2014-08-02	02:54:29	67N	30.997	-168W	26.003	41
ARA05B05CTD1	2014-08-02	04:44:59	67N	42.007	-168W	2.006	41
ARA05B05CTD2	2014-08-02	05:49:46	67N	42.008	-168W	2.009	40
ARA05B06CTD1	2014-08-02	07:36:43	67N	52.987	-167W	38.029	53
ARA05B07CTD1	2014-08-02	10:00:00	68N	4.003	-167W	14.003	42
ARA05B08CTD1	2014-08-02	12:20:18	68N	15.008	-166W	50.010	29
ARA05B08CTD2	2014-08-02	13:18:30	68N	14.995	-166W	49.988	23
ARA05B09CTD1	2014-08-02	19:17:22	69N	9.998	-168W	39.979	40
ARA05B09CTD2	2014-08-02	20:45:43	69N	9.968	-168W	40.019	42
ARA05B10CTD1	2014-08-03	04:44:45	70N	29.995	-168W	40.010	33
ARA05B10CTD2	2014-08-03	05:46:00	70N	29.995	-168W	40.010	31
ARA05B11CTD1	2014-08-03	11:40:48	71N	25.800	-166W	40.597	39
ARA05B11CTD2	2014-08-03	12:38:12	71N	25.800	-166W	40.597	38
ARA05B12CTD1	2014-08-03	21:10:16	72N	21.597	-164W	41.207	42
ARA05B12CTD2	2014-08-03	22:00:00	72N	21.595	-164W	41.210	41
ARA05B13CTD1	2014-08-04	12:15:28	73N	18.729	-162W	38.598	96
ARA05B13CTD2	2014-08-04	13:45:45	73N	18.515	-162W	38.584	77
ARA05B14CTD1	2014-08-04	22:36:27	74N	13.184	-160W	42.427	546
ARA05B14CTD2	2014-08-05	00:12:00	74N	13.261	-160W	42.073	100
ARA05B14CTD3	2014-08-05	01:59:40	74N	13.332	-160W	41.972	100
ARA05B15CTD1	2014-08-05	12:52:10	75N	51.139	-158W	7.255	829
ARA05B15CTD2	2014-08-05	16:25:37	75N	5.864	-158W	49.466	837
ARA05B15CTD3	2014-08-05	18:14:14	75N	6.193	-158W	53.920	301
ARA05B16CTD1	2014-08-06	03:58:32	75N	9.051	-154W	59.945	3831
ARA05B16CTD2	2014-08-06	08:13:28	75N	9.469	-154W	59.351	101
ARA05B17CTD1	2014-08-06	17:53:37	75N	9.788	-151W	14.491	3827
ARA05B17CTD2	2014-08-07	00:11:20	75N	9.368	-151W	16.451	89
ARA05B17CTD3	2014-08-07	01:00:00	75N	9.314	-151W	17.418	101
ARA05B18CTD1	2014-08-07	10:56:29	75N	47.379	-148W	47.688	1001
ARA05B19CTD1	2014-08-09	04:58:26	77N	36.020	-146W	7.255	201
ARA05B19CTD2	2014-08-09	19:00:00	77N	33.499	-146W	11.525	200
ARA05B19CTD3	2014-08-09	21:00:00	77N	32.851	-146W	9.679	203
ARA05B19CTD4	2014-08-09	22:55:00	77N	31.900	-146W	10.348	203
ARA05B19CTD5	2014-08-10	00:57:45	77N	31.229	-146W	13.451	203
ARA05B19CTD6	2014-08-10	02:56:39	77N	31.141	-146W	17.169	202
ARA05B19CTD7	2014-08-10	04:56:36	77N	31.559	-146W	18.744	201

ARA05B19CTD8	2014-08-10	06:56:56	77N	31.933	-146W	17.500	200
ARA05B19CTD9	2014-08-10	08:57:40	77N	31.812	-146W	14.756	202
ARA05B19CTD10	2014-08-10	10:56:00	77N	31.252	-146W	13.698	202
ARA05B19CTD11	2014-08-10	12:59:48	77N	30.748	-146W	15.220	200
ARA05B19CTD12	2014-08-10	14:56:16	77N	30.790	-146W	17.772	201
ARA05B19CTD13	2014-08-10	16:58:59	77N	31.262	-146W	18.481	201
ARA05B19CTD14	2014-08-10	18:57:20	77N	31.526	-146W	16.491	201
ARA05B19CTD15	2014-08-10	20:57:26	77N	31.214	-146W	13.463	201
ARA05B19CTD16	2014-08-10	22:56:29	77N	30.443	-146W	12.181	201
ARA05B19CTD17	2014-08-11	00:58:00	77N	29.822	-146W	12.975	199
ARA05B19CTD18	2014-08-11	02:57:18	77N	29.671	-146W	13.918	201
ARA05B19CTD19	2014-08-11	04:58:16	77N	29.800	-146W	13.102	200
ARA05B19CTD20	2014-08-11	06:56:33	77N	29.711	-146W	10.280	503
ARA05B19CTD21	2014-08-11	08:56:51	77N	29.124	-146W	8.153	201
ARA05B19CTD22	2014-08-11	10:55:49	77N	28.072	-146W	8.417	200
ARA05B19CTD23	2014-08-11	12:55:55	77N	27.330	-146W	11.355	200
ARA05B19CTD24	2014-08-11	14:57:28	77N	27.191	-146W	14.705	201
ARA05B19CTD25	2014-08-11	16:58:35	77N	27.490	-146W	15.398	502
ARA05B19CTD26	2014-08-11	18:57:34	77N	27.550	-146W	13.306	501
ARA05B19CTD27	2014-08-11	20:57:41	77N	27.101	-146W	10.772	201
ARA05B19CTD28	2014-08-11	22:57:56	77N	26.370	-146W	9.629	201
ARA05B19CTD29	2014-08-12	00:59:26	77N	25.800	-146W	10.758	505
ARA05B19CTD30	2014-08-12	02:57:42	77N	25.755	-146W	12.316	201
ARA05B19CTD31	2014-08-12	04:56:38	77N	25.965	-146W	12.200	200
ARA05B19CTD32	2014-08-12	06:58:24	77N	26.037	-146W	10.361	500
ARA05B19CTD33	2014-08-12	08:57:14	77N	25.733	-146W	8.339	201
ARA05B19CTD34	2014-08-12	10:56:00	77N	25.279	-146W	7.744	201
ARA05B19CTD35	2014-08-12	12:56:33	77N	24.923	-146W	8.653	501
ARA05B19CTD36	2014-08-12	14:57:33	77N	24.868	-146W	10.085	201
ARA05B19CTD37	2014-08-12	16:59:00	77N	25.045	-146W	10.684	200
ARA05B19CTD38	2014-08-12	18:57:28	77N	25.069	-146W	10.016	501
ARA05B19CTD39	2014-08-12	20:58:30	77N	24.810	-146W	9.454	200
ARA05B19CTD40	2014-08-12	22:56:23	77N	24.363	-146W	9.638	201
ARA05B19CTD41	2014-08-13	00:57:26	77N	24.023	-146W	11.239	201
ARA05B19CTD42	2014-08-13	02:57:55	77N	23.945	-146W	13.012	200
ARA05B19CTD43	2014-08-13	04:57:20	77N	24.056	-146W	13.538	200
ARA05B19CTD44	2014-08-13	07:00:00	77N	24.082	-146W	12.803	200
ARA05B19CTD45	2014-08-13	09:00:00	77N	23.960	-146W	11.630	203
ARA05B19CTD46	2014-08-13	11:00:00	77N	23.592	-146W	10.709	201
ARA05B19CTD47	2014-08-13	12:58:47	77N	23.229	-146W	10.654	201
ARA05B19CTD48	2014-08-13	14:55:11	77N	22.950	-146W	10.828	201
ARA05B19CTD49	2014-08-13	16:59:20	77N	22.798	-146W	10.255	200
ARA05B19CTD50	2014-08-13	20:00:00	77N	22.353	-146W	8.498	201
ARA05B19CTD51	2014-08-14	08:00:00	77N	17.912	-146W	17.210	3791
ARA05B20CTD1	2014-08-14	23:32:53	76N	45.659	-148W	54.229	1001

ARA05B21CTD1	2014-08-15	13:26:28	76N	3.997	-151W	41.666	3822
ARA05B22CTD1	2014-08-16	00:28:00	76N	0.031	-156W	0.041	1251
ARA05B22CTD2	2014-08-16	03:00:00	76N	0.073	-155W	59.827	101
ARA05B23CTD1	2014-08-16	12:24:00	76N	0.014	-159W	30.031	1490
ARA05B23CTD2	2014-08-16	14:33:18	76N	0.030	-159W	30.323	101
ARA05B24CTD1	2014-08-16	19:22:25	75N	50.924	-161W	42.160	2092
ARA05B24CTD2	2014-08-16	22:21:50	75N	50.893	-161W	42.030	117
ARA05B24CTD3	2014-08-16	23:58:58	75N	50.864	-161W	43.063	101
ARA05B25CTD1	2014-08-17	07:14:00	76N	23.182	-164W	59.426	506
ARA05B25CTD2	2014-08-17	08:32:14	76N	23.118	-164W	59.471	103
ARA05B26CTD1	2014-08-17	12:47:00	76N	17.959	-167W	0.106	376
ARA05B26CTD2	2014-08-17	14:27:40	76N	18.517	-167W	1.148	82
ARA05B27CTD1	2014-08-18	02:29:53	75N	48.056	-169W	0.773	275
ARA05B27CTD2	2014-08-18	03:48:55	75N	48.056	-169W	0.774	100
ARA05B28CTD1	2014-08-18	09:32:44	75N	55.159	-172W	23.524	1910
ARA05B28CTD2	2014-08-18	12:45:29	75N	54.997	-172W	24.157	100
ARA05B28CTD3	2014-08-18	13:36:58	75N	54.838	-172W	24.558	76
ARA05B29CTD1	2014-08-18	22:57:13	75N	58.628	-176W	11.804	1945
ARA05B29CTD2	2014-08-19	01:59:58	75N	58.423	-176W	11.653	106
ARA05B30CTD1	2014-08-19	11:58:49	76N	1.646	179E	34.134	1150
ARA05B30CTD2	2014-08-19	13:40:59	76N	1.603	179E	33.857	101
ARA05B30CTD3	2014-08-19	15:41:22	76N	1.688	179E	33.618	98
ARA05B31CTD1	2014-08-21	03:05:07	74N	48.036	-167W	53.886	181
ARA05B32CTD2	2014-08-23	03:14:14	76N	31.344	-169W	48.025	2190
ARA05B32CTD3	2014-08-23	05:49:46	76N	31.404	-169W	47.352	101

Table 2.2. All data files in 2014 Korea Arctic cruise provided by OUC (Dr. Jinping Zhao)

Instrument	Deployed time/UTC		Depth/m	File name
	Date	Time		
ADCP	08-08	21:20	70	_RDI_005.000
CTD	08-08	22:57	194	060018_20140809_0814
	08-09	00:56	293	060018_20140809_1114
	08-09	03:25	293	060018_20140810_0748
	08-09	05:18	293	
	08-10	04:53	293	060018_20140810_1347
	08-11	03:30	293	
	08-11	07:40	293	060018_20140811_0040
	08-11	09:50	293	
	08-12	03:30	182	060018_20140811_1229
	08-12	16:30	295	060018_20140812_0114
	08-12	21:50	136	060018_20140812_0617
	08-13	03:25	305	060018_20140812_1222
	08-13	16:40	297	060018_20140813_0234
	08-13	21:35	122	060018_20140813_0900
	08-13	23:35	122	
	08-14	04:05	141	060018_20140813_1231
	08-14	16:38	155	060018_20140814_0119
	08-14	21:15	181	060018_20140814_0551

Table 2.3. Sea ice camp log records for (a) first ice camp, (b) second ice camp, and (c) melt pond survey.

(a) First Ice Camp

Ice Mooring 1 (nearby Araon)

[*1)] Distance from under sea ice[m]	Sensor Type	Serial #
0	WHS300 [*2)] WHS600	20653 17731
1	*SBE37*	11710
2	SBE56	3254
4	SBE56	3255
6	SBE56	3256
8	SBE56	3257
10	SBE56	3258
12	SBE56	3259
14	SBE56	3260
16	SBE56	3261
18	SBE56	3262
20	SBE56	3263
22	SBE56	3264
24	SBE56	3265
26	SBE56	3266
30	SBE56	3267
34	SBE56	3268
38	SBE56	3269
42	SBE56	3270
46	SBE56	3271
50	SBE56	3272
54	SBE56	3361
58	SBE56	3362
62	*SBE37*	8886
74	[*3)] WH300 [LADCP]	Zhao

Ice Mooring 2 (50km northwest from Araon)

[*4)] Distance from under sea ice[m]	Sensor Type	Serial #
0	WHS600	17731
1	*SBE37*	8935
2	SBE56	3225
4	SBE56	3226
6	SBE56	3227
8	SBE56	3228
10	SBE56	3229
12	SBE56	1112
14	SBE56	1113
16	SBE56	1114
18	SBE56	1115
20	SBE56	1178
22	SBE56	1179
24	SBE56	1180
26	SBE56	1181
30	SBE56	1197
34	SBE56	1198
38	SBE56	1199
42	SBE56	1201
46	SBE56	1202
50	SBE56	1203
54	SBE56	1204
58	SBE56	1205
62	*SBE37*	8887

[*1)] Sea ice thickness is 0.94 m.

[*2)] WHS600 (#17731) nearby Araon is deployed from Aug. 12, 21:30 to Aug. 13, 21: 48 (UTC).

[*3)] WH300 [LADCP] nearby Araon at 74 m deep is provided by Jinping Zhao.

[*4)] Sea ice thickness is 1.68 m.

(b) Second Ice Camp

[*1)] Distance from ice surface (Top) [m]	Sensor Type	Serial #	owner
2	WHS600	15957	KOPRI
3	SBE56	1112	TUMSAT
5	*SBE37*	12267	KOPRI
	SBE56	1113	TUMSAT
7	SBE56	1114	TUMSAT
9	SBE56	1115	TUMSAT
11	SBE56	1178	TUMSAT
13	SBE56	1179	TUMSAT
15	*SBE37*	12266	KOPRI
	SBE56	1180	TUMSAT
17	SBE56	1181	TUMSAT
19	SBE56	1197	TUMSAT
21	SBE56	1198	TUMSAT
23	SBE56	1199	TUMSAT
25	*SBE37*	12268	KOPRI
	SBE56	1201	TUMSAT
27	SBE56	1202	TUMSAT
29	SBE56	1203	TUMSAT
31	SBE56	1204	TUMSAT
33	SBE56	1205	TUMSAT
35	*SBE37*	12269	KOPRI
	SBE56	3362	TUMSAT

[*1)] Sea ice thickness is 1.69 m.

(c) Melt pond survey

Location: MP-17, 18, 20, 22, nearby SBE19 site, *1) nearby ITP site

*1) Distance from under sea ice[m]	Sensor Type	Serial #
1 (top)	SBE56	1178
2	SBE56	1179
3	SBE56	1180
4	SBE56	1181
5	SBE56	1112
6	SBE56	1113
7	SBE56	1114
8	SBE56	1115
9	SBE56	3225
10	SBE56	3226
Near surface	*SBE37*	8935

*4) Distance from under sea ice[m]	Sensor Type	Serial #
11	SBE56	3227
12	SBE56	3228
13	SBE56	3229
14	SBE56	1197
15	SBE56	1198
16	SBE56	1199
17	SBE56	1201
18	SBE56	1202
19	SBE56	1203
20	SBE56	1204
21(bottom)	SBE56	1205
Near bottom	*SBE37*	8887

*1) one day survey (Aug. 12-13, 2014, LST)

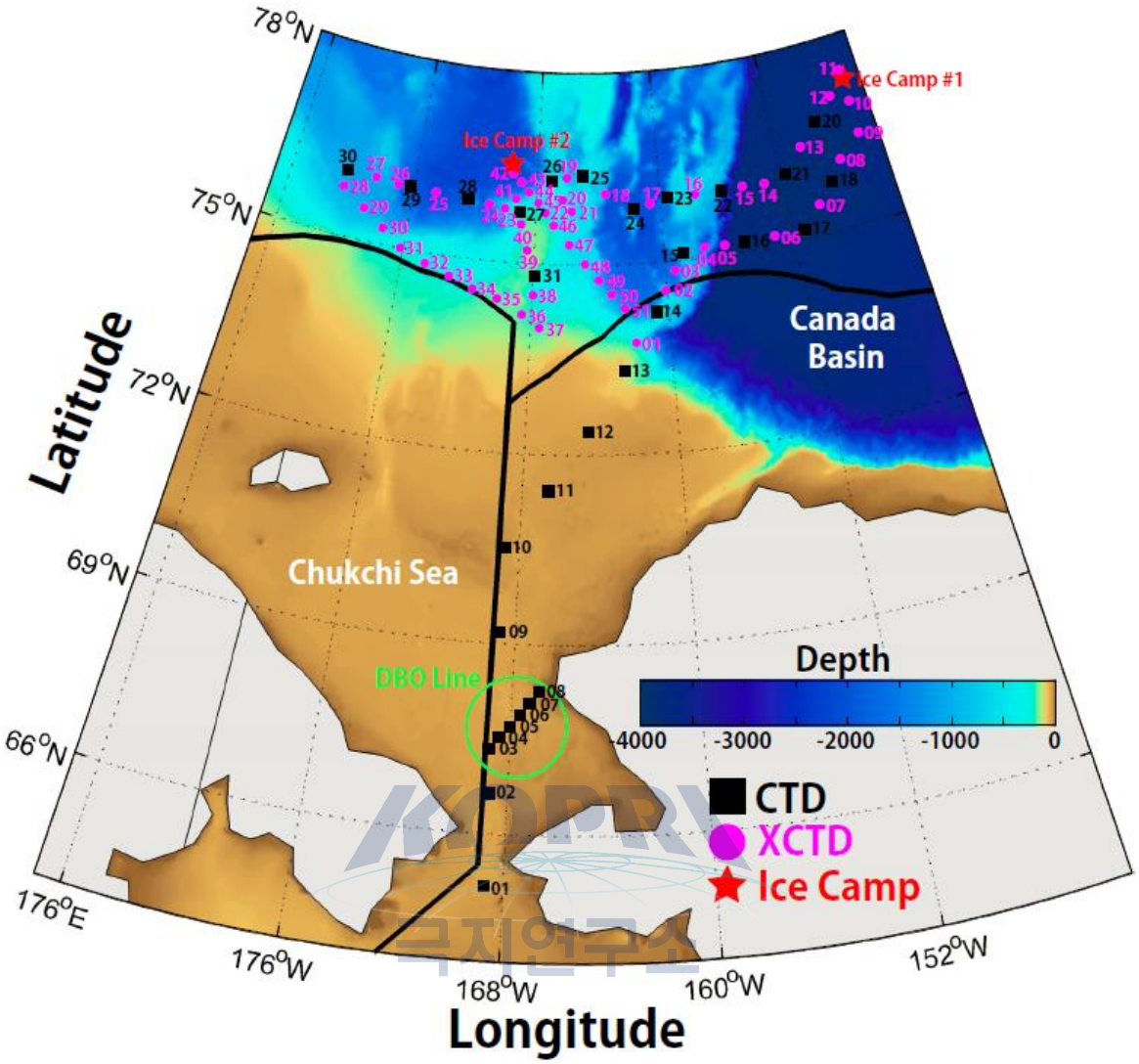

Fig. 2.1. A station map of ARA05B Arctic cruise with color-mapped bathymetry. Black squares are CTD stations and pink dots are XCTD stations. Red stars represent the sea ice camp locations. Mooring station is marked with a red square. Black solid lines denote Russian EEZ and US EEZ lines.

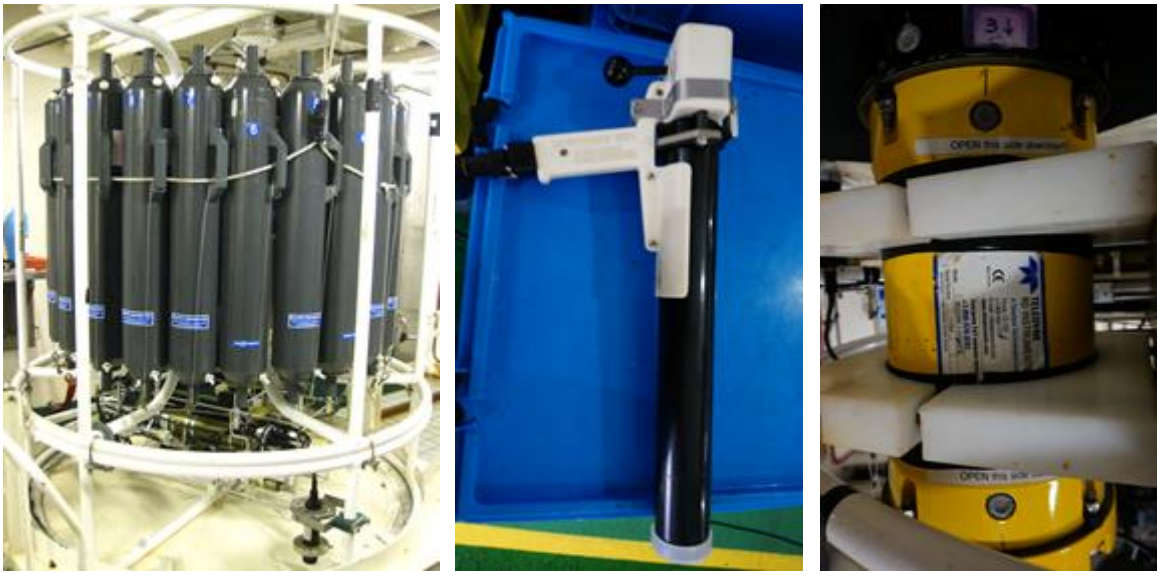

(a) (b) (c)

Fig. 2.2. Hydrographic observation equipment: (a) SBE32 with a SBE9plus CTD profiler and rosette water sampler, (b) expendable CTD, and (c) RDI lowered ADCP.

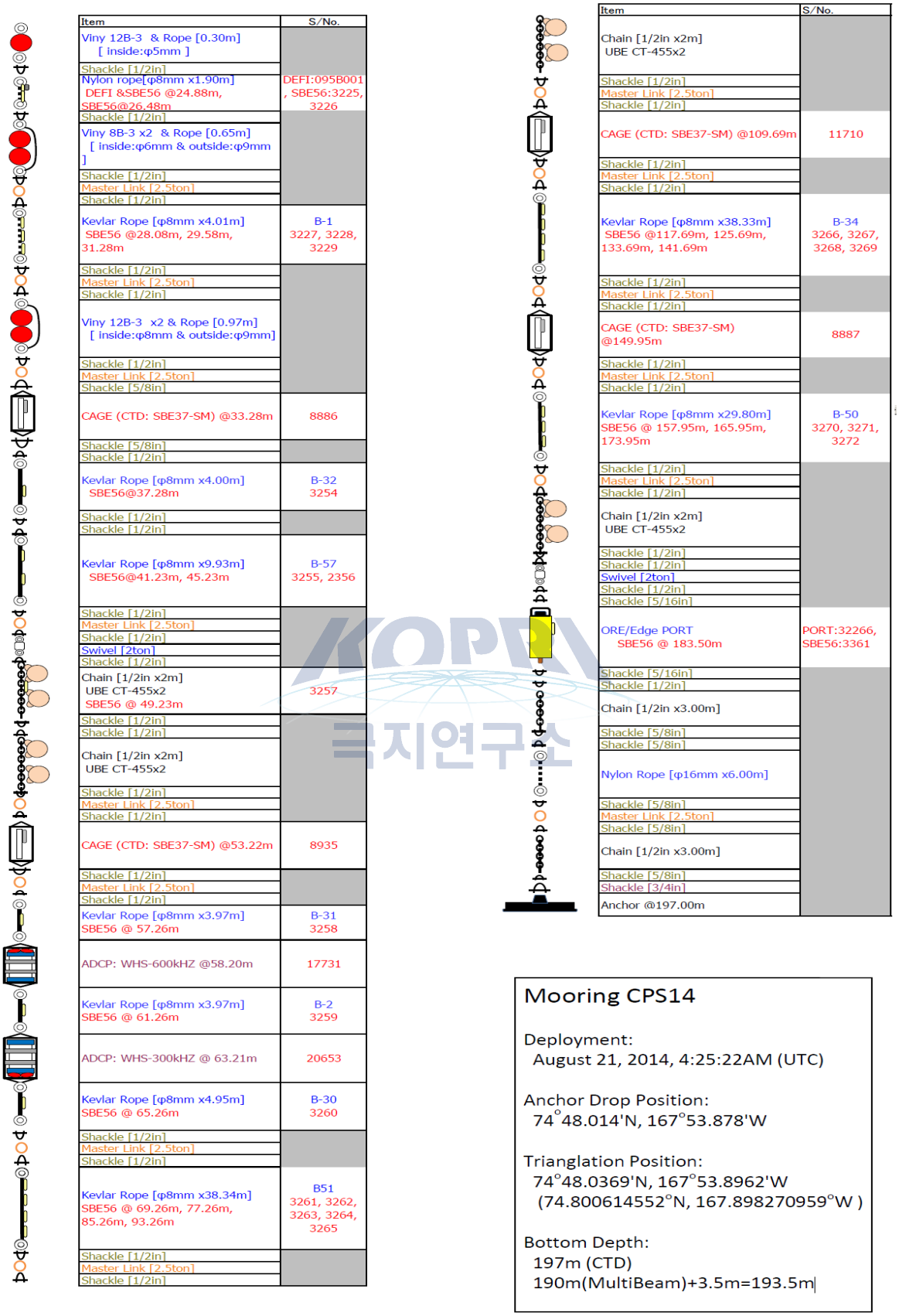

Item	S/No.
Viny 12B-3 & Rope [0.30m] [inside:φ5mm]	
Shackle [1/2in]	
Nylon rope[φ8mm x1.90m] DEFI &SBE56 @24.88m, SBE56@26.48m	DEFI:095B001, SBE56:3225, 3226
Shackle [1/2in]	
Viny 8B-3 x2 & Rope [0.65m] [inside:φ6mm & outside:φ9mm]	
Shackle [1/2in]	
Master Link [2.5ton]	
Shackle [1/2in]	
Kevlar Rope [φ8mm x4.01m] SBE56 @28.08m, 29.58m, 31.28m	B-1 3227, 3228, 3229
Shackle [1/2in]	
Master Link [2.5ton]	
Shackle [1/2in]	
Viny 12B-3 x2 & Rope [0.97m] [inside:φ8mm & outside:φ9mm]	
Shackle [1/2in]	
Master Link [2.5ton]	
Shackle [5/8in]	
CAGE (CTD: SBE37-SM) @33.28m	8886
Shackle [5/8in]	
Shackle [1/2in]	
Kevlar Rope [φ8mm x4.00m] SBE56@37.28m	B-32 3254
Shackle [1/2in]	
Shackle [1/2in]	
Kevlar Rope [φ8mm x9.93m] SBE56@41.23m, 45.23m	B-57 3255, 2356
Shackle [1/2in]	
Master Link [2.5ton]	
Shackle [1/2in]	
Swivel [2ton]	
Shackle [1/2in]	
Chain [1/2in x2m] UBE CT-455x2 SBE56 @ 49.23m	3257
Shackle [1/2in]	
Shackle [1/2in]	
Chain [1/2in x2m] UBE CT-455x2	
Shackle [1/2in]	
Master Link [2.5ton]	
Shackle [1/2in]	
CAGE (CTD: SBE37-SM) @53.22m	8935
Shackle [1/2in]	
Master Link [2.5ton]	
Shackle [1/2in]	
Kevlar Rope [φ8mm x3.97m] SBE56 @ 57.26m	B-31 3258
ADCP: WHS-600kHZ @58.20m	17731
Kevlar Rope [φ8mm x3.97m] SBE56 @ 61.26m	B-2 3259
ADCP: WHS-300kHZ @ 63.21m	20653
Kevlar Rope [φ8mm x4.95m] SBE56 @ 65.26m	B-30 3260
Shackle [1/2in]	
Master Link [2.5ton]	
Shackle [1/2in]	
Kevlar Rope [φ8mm x38.34m] SBE56 @ 69.26m, 77.26m, 85.26m, 93.26m	B51 3261, 3262, 3263, 3264, 3265
Shackle [1/2in]	
Master Link [2.5ton]	
Shackle [1/2in]	

Item	S/No.
Chain [1/2in x2m] UBE CT-455x2	
Shackle [1/2in]	
Master Link [2.5ton]	
Shackle [1/2in]	
CAGE (CTD: SBE37-SM) @109.69m	11710
Shackle [1/2in]	
Master Link [2.5ton]	
Shackle [1/2in]	
Kevlar Rope [φ8mm x38.33m] SBE56 @117.69m, 125.69m, 133.69m, 141.69m	B-34 3266, 3267, 3268, 3269
Shackle [1/2in]	
Master Link [2.5ton]	
Shackle [1/2in]	
CAGE (CTD: SBE37-SM) @149.95m	8887
Shackle [1/2in]	
Master Link [2.5ton]	
Shackle [1/2in]	
Kevlar Rope [φ8mm x29.80m] SBE56 @ 157.95m, 165.95m, 173.95m	B-50 3270, 3271, 3272
Shackle [1/2in]	
Master Link [2.5ton]	
Shackle [1/2in]	
Chain [1/2in x2m] UBE CT-455x2	
Shackle [1/2in]	
Shackle [1/2in]	
Swivel [2ton]	
Shackle [1/2in]	
Shackle [5/16in]	
ORE/Edge PORT SBE56 @ 183.50m	PORT:32266, SBE56:3361
Shackle [5/16in]	
Shackle [1/2in]	
Chain [1/2in x3.00m]	
Shackle [5/8in]	
Shackle [5/8in]	
Nylon Rope [φ16mm x6.00m]	
Shackle [5/8in]	
Master Link [2.5ton]	
Shackle [5/8in]	
Chain [1/2in x3.00m]	
Shackle [5/8in]	
Shackle [3/4in]	
Anchor @197.00m	

Mooring CPS14

Deployment:
August 21, 2014, 4:25:22AM (UTC)

Anchor Drop Position:
74°48.014'N, 167°53.878'W

Trianglation Position:
74°48.0369'N, 167°53.8962'W
(74.800614552°N, 167.898270959°W)

Bottom Depth:
197m (CTD)
190m(MultiBeam)+3.5m=193.5m

Fig. 2.3. Diagram of mooring CPS14.

(a)

(b)

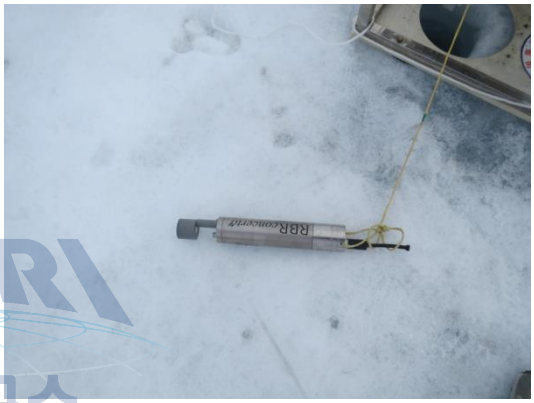

(c)

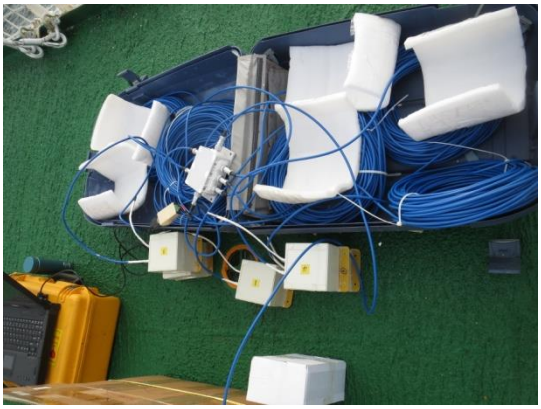

(d)

(e)

Fig. 2.4. Instruments used by OUC for sea ice camp: (a) Lowered ADCP, (b) winch, (c) RBR-CTD, (d) laser sensors, and (e) drifting buoy.

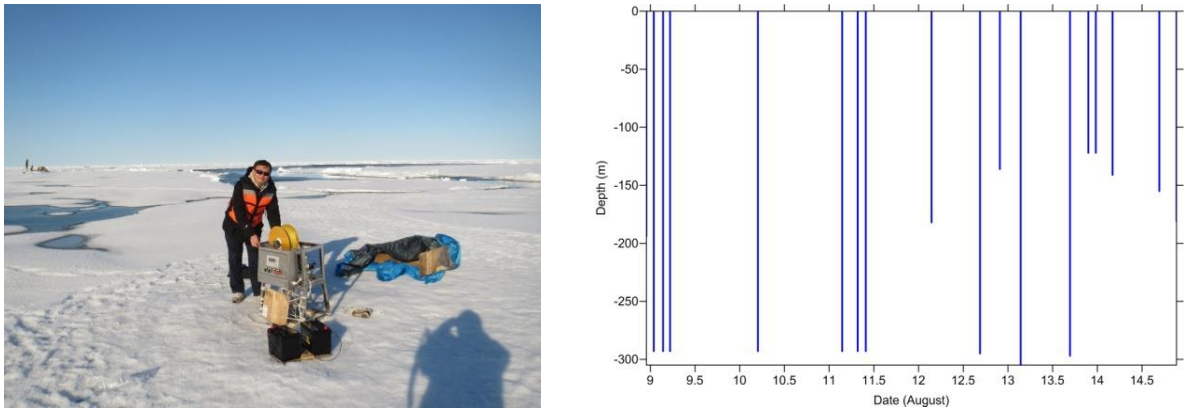

Fig. 2.5. OUC CTD deployment (left) and depth of each profile (right).

Fig. 2.6. TUMSAT CTD profiling measurements on the sea ice floe (upper) and TUMSAT melt pond survey using SBE56 and SBE37 (lower).

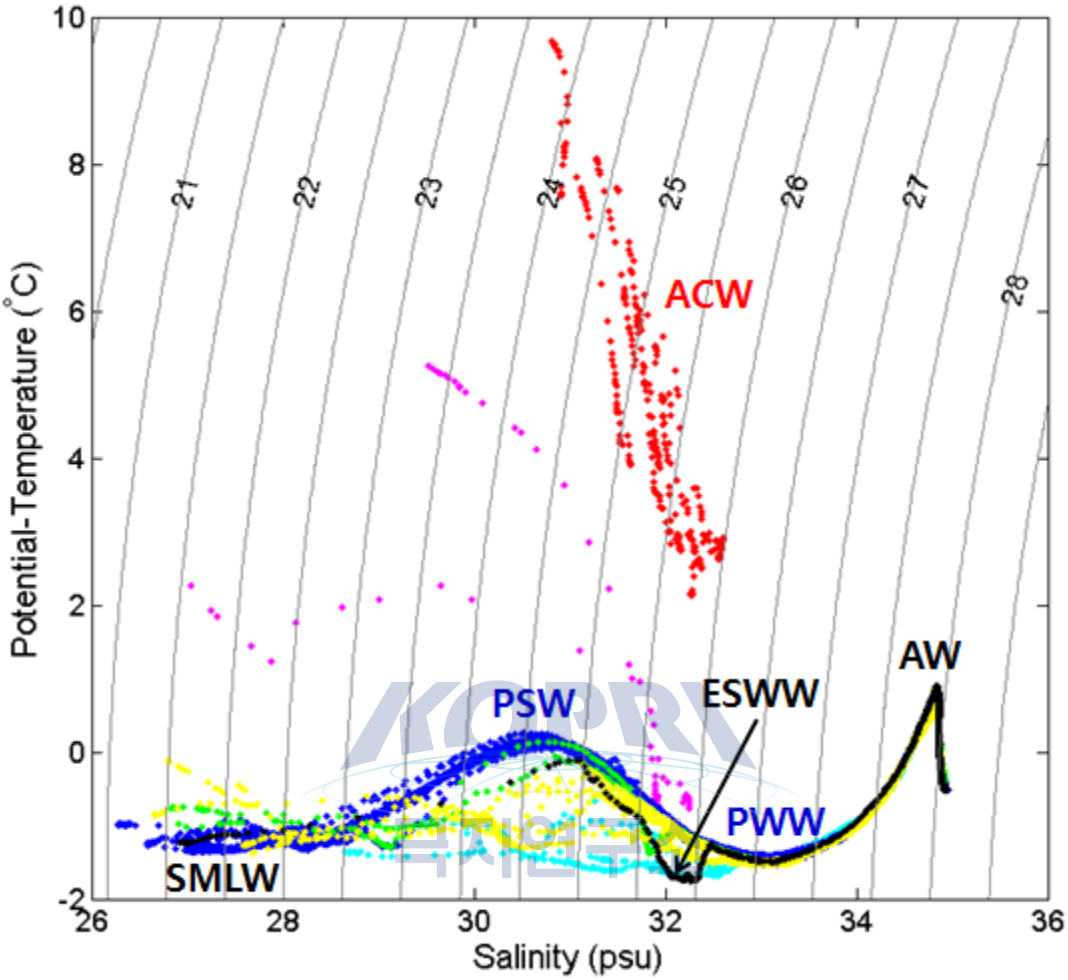

Fig. 2.7. Potential temperature (θ)–salinity (S) diagram from ship-based CTD stations. SMLW: surface mixed layer water; PSW: Pacific summer water; PWW: Pacific winter water; AW: Atlantic water; ACW: Alaskan coastal water; and ESWW: East Siberian Sea winter shelf water. Red (St. 1 to St. 9); pink (St. 10 to St. 11); cyan (St. 12 to St. 14); blue (St. 15 to St. 22); green (St. 23 to St. 24); yellow (St. 25 to St. 28, and St. 30); and black (St. 29).

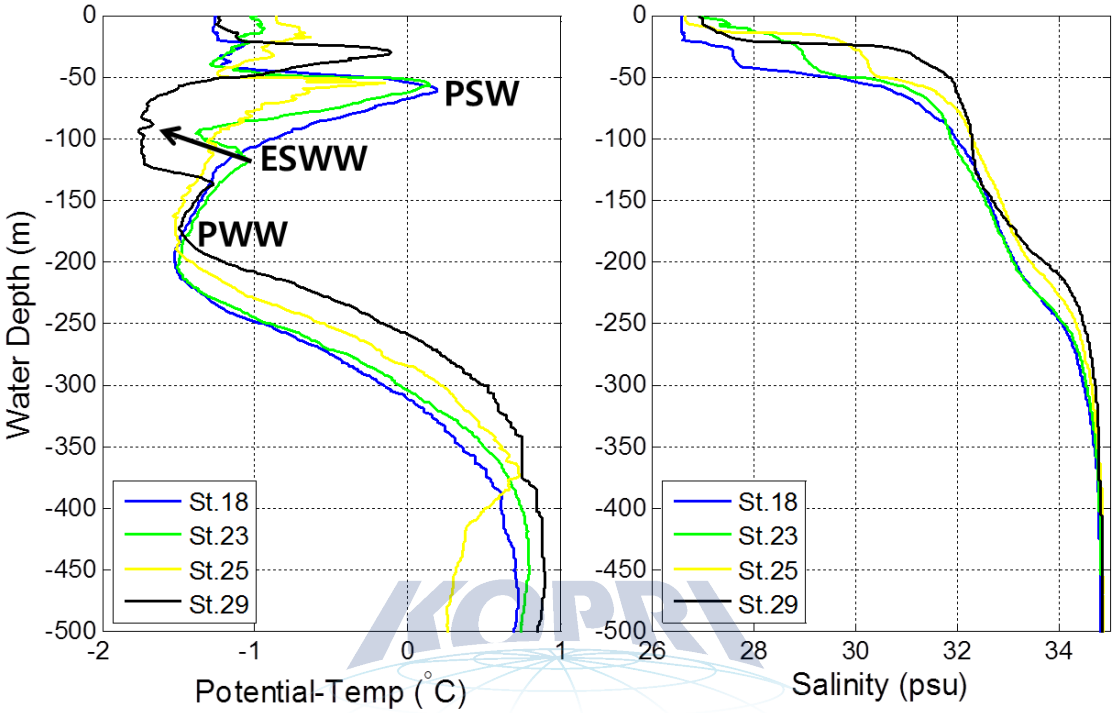

.Fig. 2.8. Vertical structures of potential temperature (left) and salinity (right) at different CTD stations.

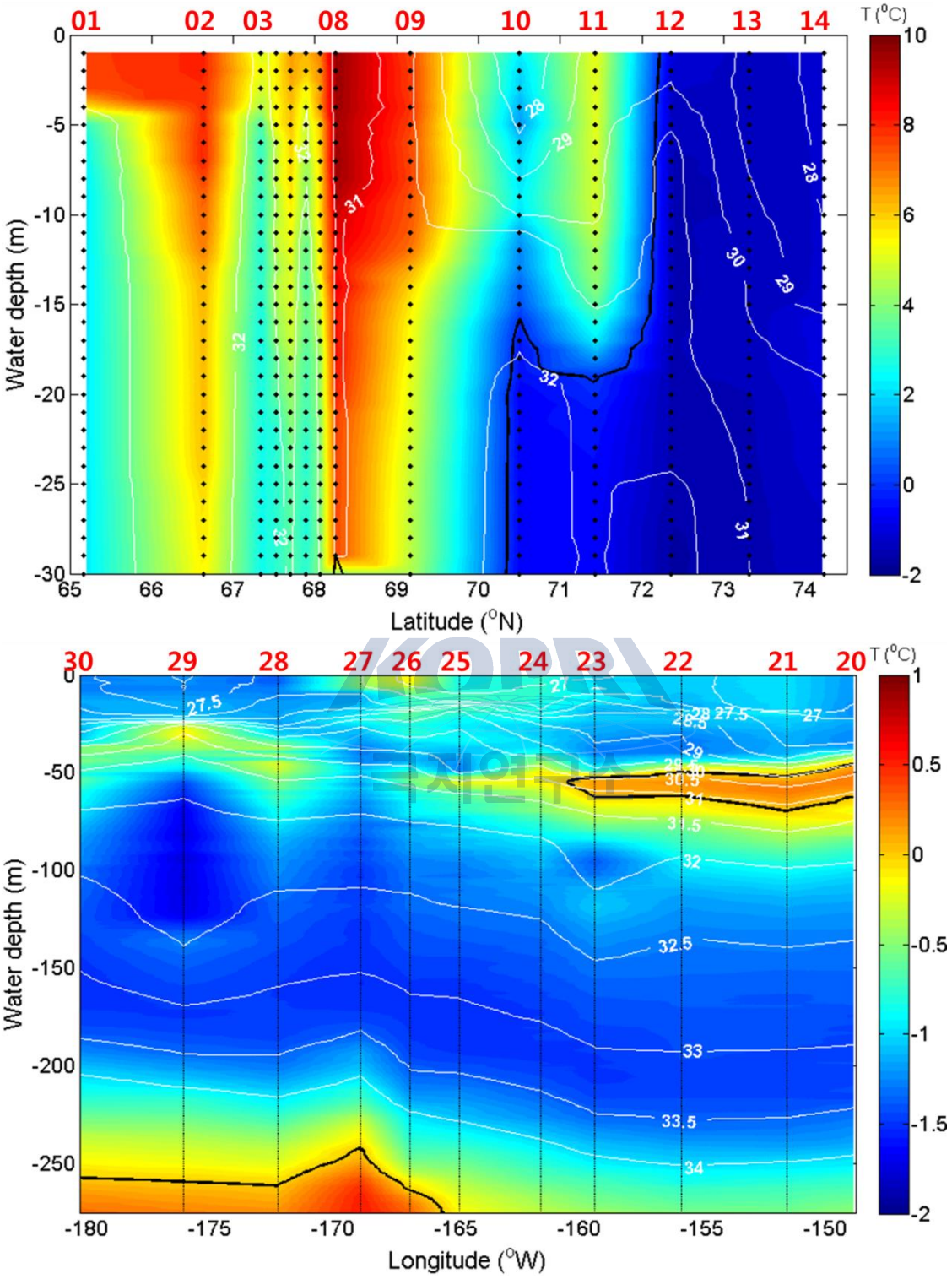

.Fig. 2.9. Vertical structures of potential temperature (colored) and salinity (white contours) at the transect lines from St. 1 to St. 14 (upper) and St. 20 to St. 30 (lower).

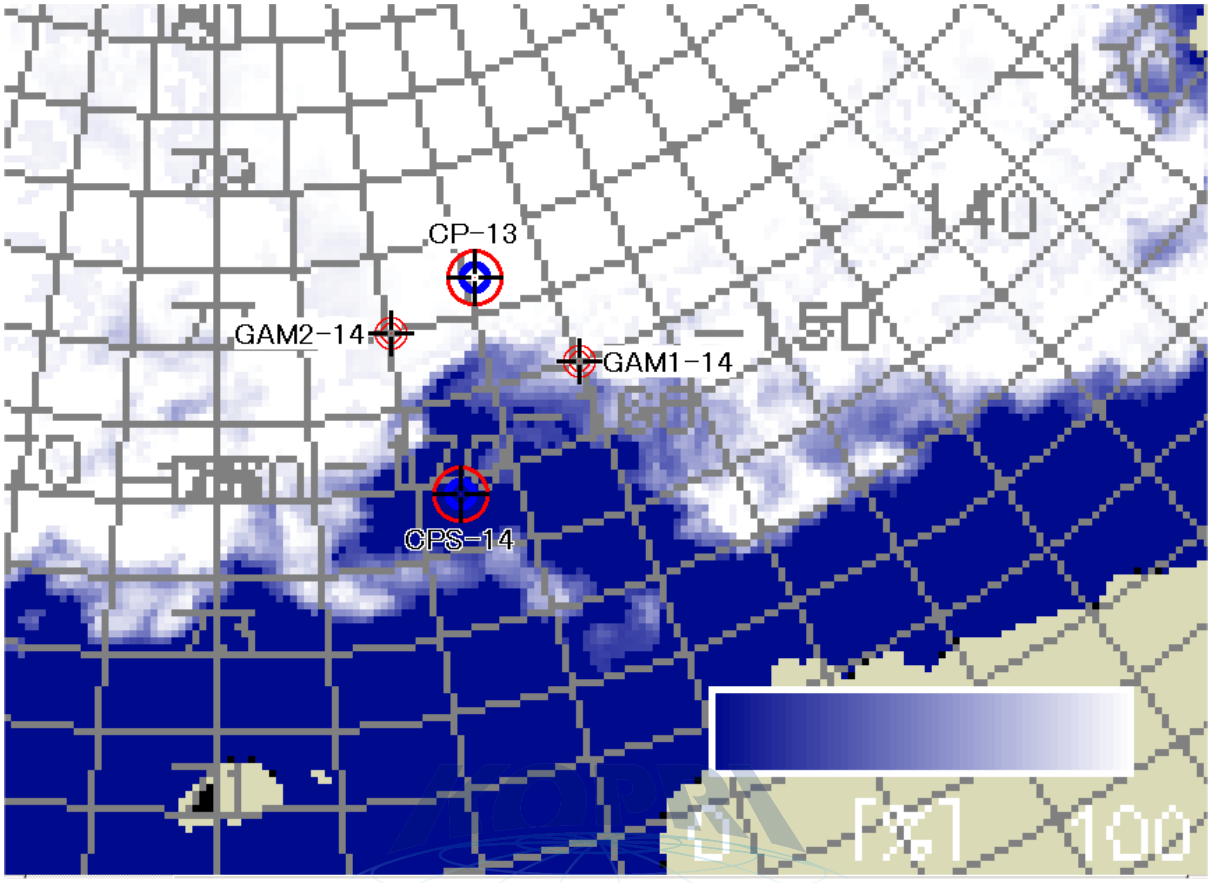

Fig. 2.10. AMSR-2 sea ice concentration on Aug. 15, 2014. Symbols are the locations of moorings by TUMSAT.

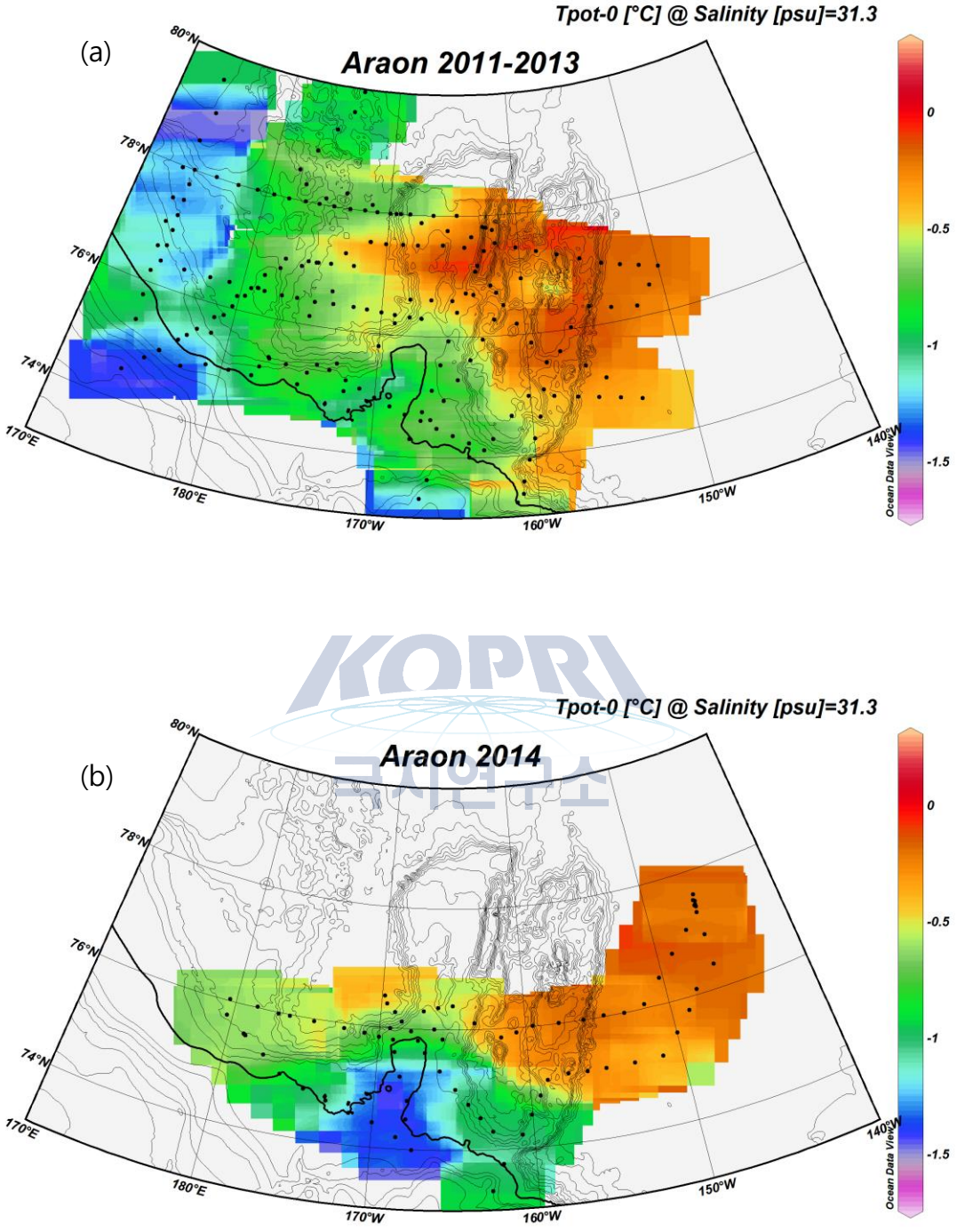

Fig. 2.11. Spatial distribution of potential temperature on S=31.3 near the temperature maximum of PSW in 2011-2013 and 2014.

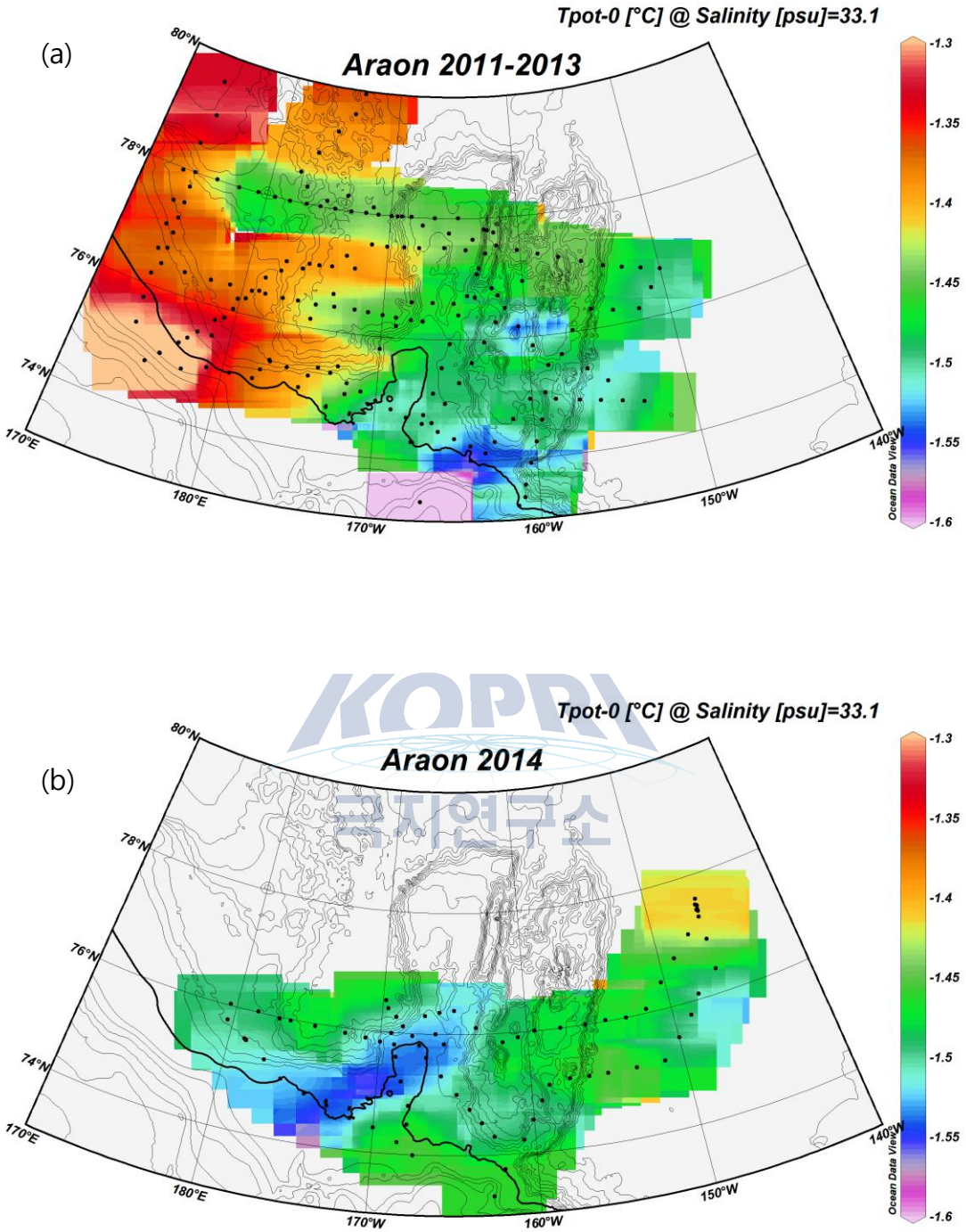

Fig. 2.12. Spatial distribution of potential temperature on S=33.1 near the temperature minimum of PWW in 2011-2013 and 2014. The cold color indicates the newly delivered PWW.

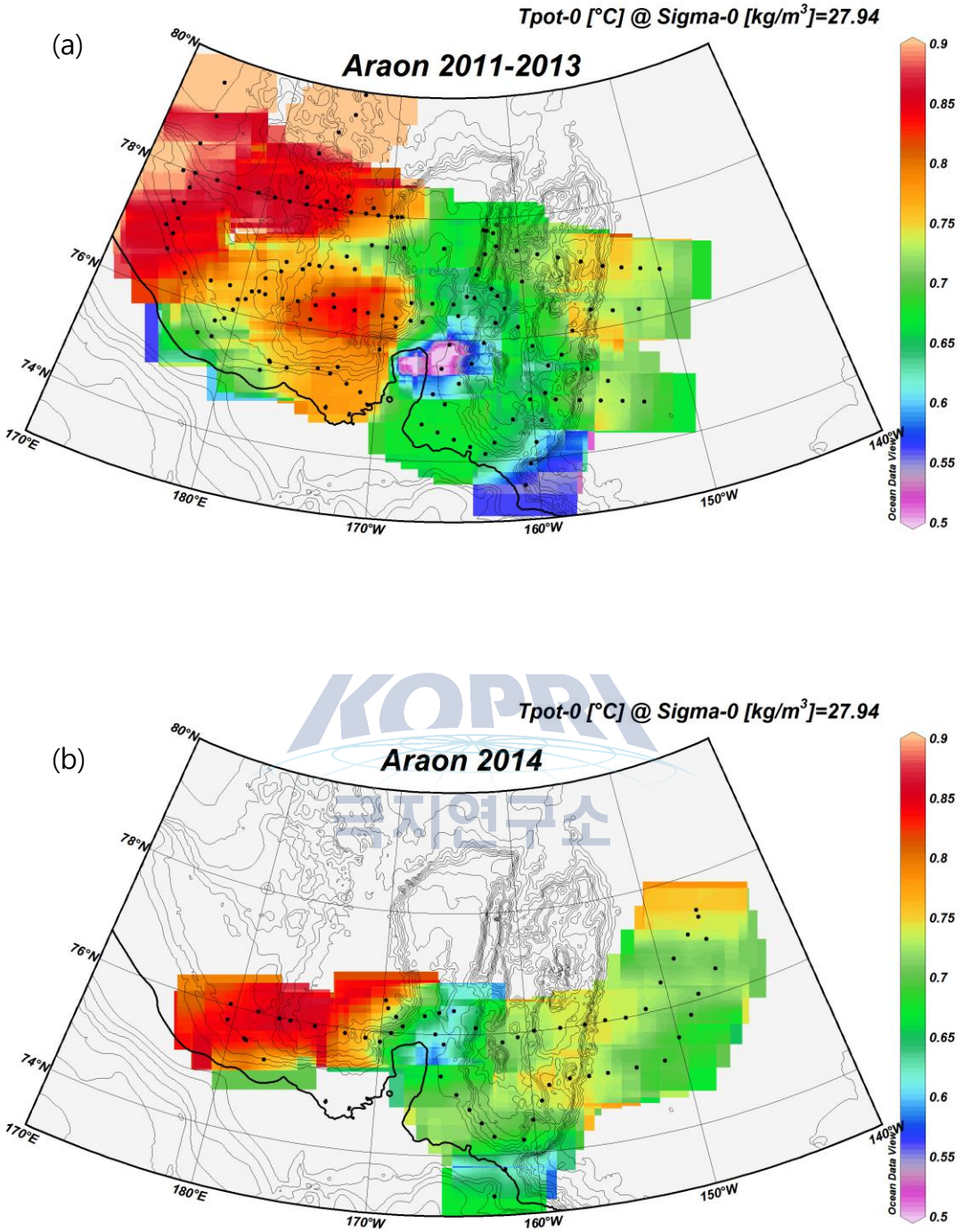

Fig. 2.13. Spatial distribution of potential temperature on σ_ϑ=27.94 near the temperature minimum of FSBAW in 2011-2013 and 2014.

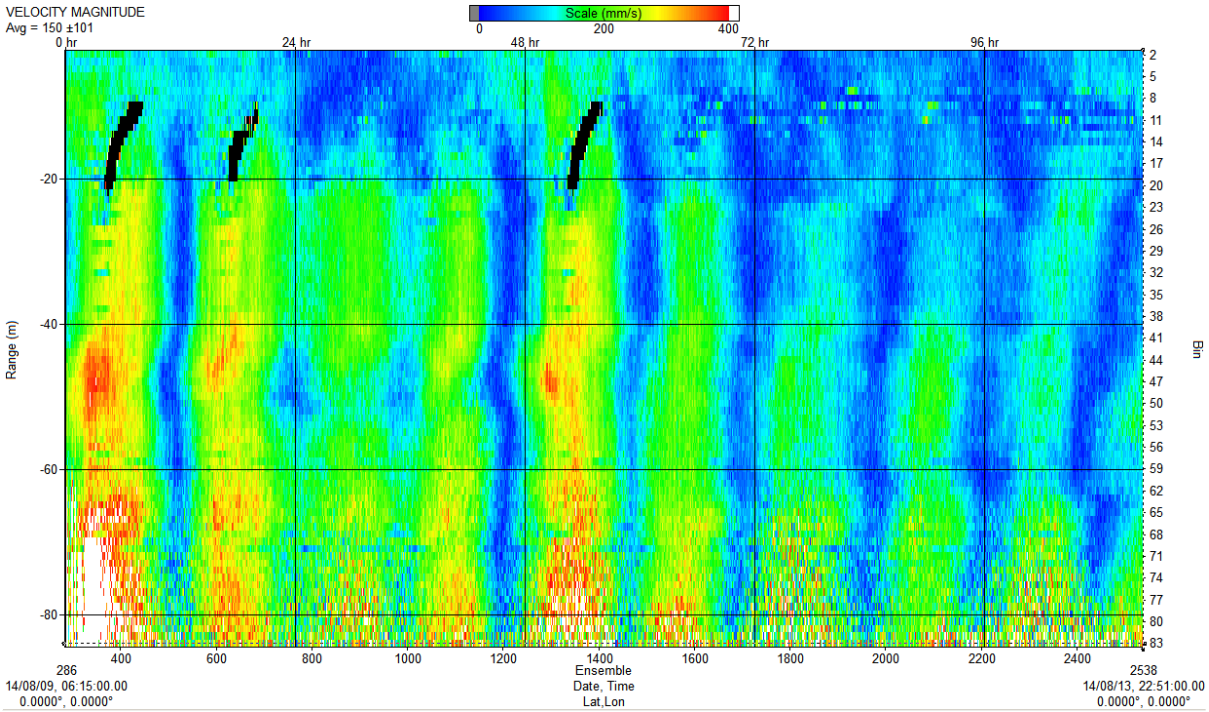

Fig. 2.14. Velocity magnitude relative to sea ice (WHS300KHz nearby Araon)

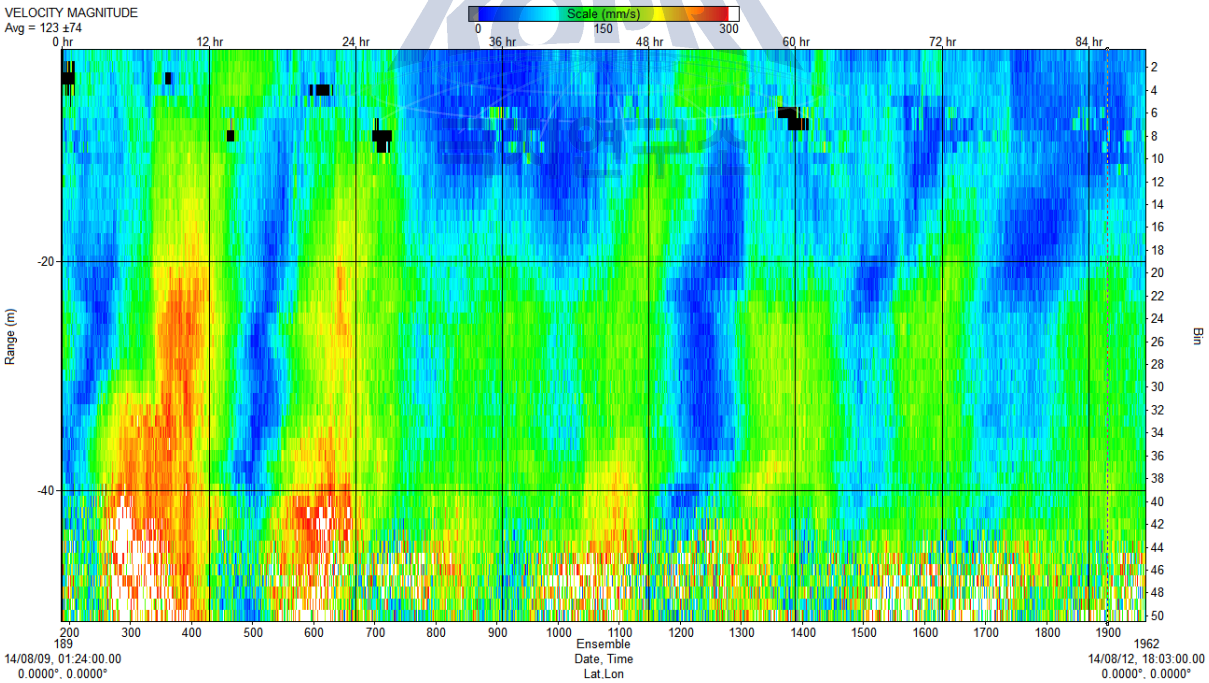

Fig. 2.15. Velocity magnitude relative to sea ice (WHS600KHz 50km away from Araon)

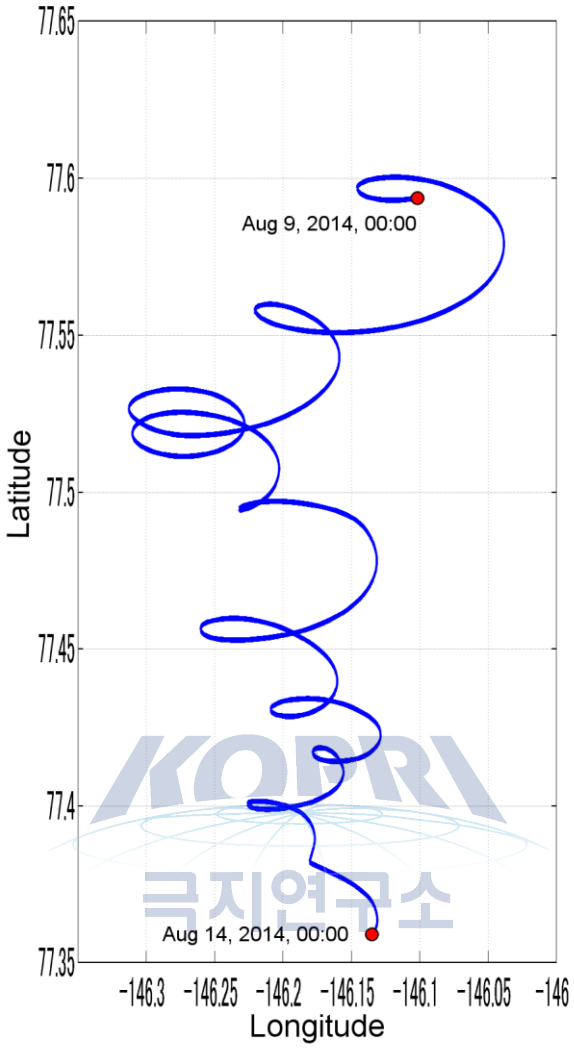

Fig. 2.16. GPS positions at Araon during the first ice camp during Aug. 9, 00:00 AM to Aug. 14, 00:00 AM.

Appendix I. Daily Log Sheets

Scientific Cruise Daily Log

Ship: R/V Araon Cruise: ARA05 Leg: B Prepared by C. Y. Kang (KOPRI) chanyoung85@kopri.re.kr

STN No.	Gear	Cast No.	Date (UTC)	Cast start (UTC)	Bottom or at depth (UTC)	Cast end (UTC)	Latitude	Longitude	Water depth (m)	Cast depth (m)	Cable payout (m)	No. of spl. depth Core length	Wind speed knot	Wind direction (°)	Ship speed knot	Heading (°)	Remarks	Device Driver
Arctic																		
CTD: CTD; XCT: XCTD; PHY: Phytoplankton Net; BON: Bongo Net; RIN: Ring Net; SEC: secchi; HPR: HPRO; OPT: Optics; ICE: Sea ice; MIC: Micro Layer; BUO: Buoy; UVR: UV Radiometer																		
1	SEC	1	08-01-2014	09:05		09:10	65° 10.398N	168° 41.441W		7							Secchi disk	S. H. Lee
1	CTD	1	08-01-2014	09:40		09:53			49	40		24	4.1	200.3	0.07	213.5	First deep casting	T. W. Kim
1	PHY	1	08-01-2014	10:12		10:20				40							Vertical towing - mesh size 20 um	H. M. Joo
1	BON	1	08-01-2014	10:25		10:40				40							Vertical towing - mesh size 330 um ,500 um	D. B. Lee
2	CTD	1	08-01-2014	17:55		18:11	66° 37.794N	168° 41.251W	40	33		24	4.3	167.3	0.01	176.0	First deep casting	T. W. Kim
2	SEC	1	08-01-2014	18:15		18:19				12							Secchi disk	S. H. Lee
2	HPR	1	08-01-2014	18:20		18:38				43							HPRO II (Hyper - Spectroradiometer)	C. U. Hyun
2	CTD	2	08-01-2014	19:05		19:22	66° 41.244N	168° 41.244W	44	35		24	3.9	179.0	0.07	195.4	Second shallow casting	K. H. Cho
2	PHY	1	08-01-2014	19:31		19:38				35							Vertical towing - mesh size 20 um	H. M. Joo
2	BON	1	08-01-2014	19:43		19:56				30							Vertical towing - mesh size 330 um ,500 um	D. B. Lee
3	CTD	1	08-01-2014	23:50		00:13	67° 20.008N	168° 50.001W	49	40		24	2.4	152.2	0.14	324.0	First deep casting	K. H. Cho
3	SEC	1	08-02-2014	00:13		00:25				8							Secchi disk	S. H. Lee
3	BON	1	08-02-2014	00:25		00:36				30							Vertical towing - mesh size 330 um ,500 um	D. B. Lee
3	PHY	1	08-02-2014	00:36		00:43				30							Vertical towing - mesh size 20 um	H. M. Joo
3	CTD	2	08-02-2014	00:58		01:20	67° 19.999N	168° 49.991W	49	40		24	3.2	193.1	0.07	190.2	Second shallow casting	T. W. Kim
3	HPR	1	08-02-2014	01:30		01:33				31							HPRO II (Hyper - Spectroradiometer)	C. U. Hyun
4	CTD	1	08-02-2014	02:55		03:15	67° 31.016N	168° 26.003W	47	40		24	3.0	211.0	0.55	219.9	First deep casting	K. H. Cho
5	CTD	1	08-02-2014	04:44		05:04	67° 42.009N	168° 02.008W	49	40		24	1.4	241.1	0.03	238.0	First deep casting	T. W. Kim
5	SEC	1	08-02-2014	05:05		05:07				14							Secchi disk	S. H. Lee
5	CTD	2	08-02-2014	06:48		06:07	67° 42.001N	168° 02.001W	49	40		24	2.4	257.0	0.10	261.9	Second shallow casting	K. H. Cho
6	CTD	1	08-02-2014	07:35		07:55	67° 52.989N	167° 38.031W	59	53		24	1.2	276.0	0.07	221.1	First deep casting	T. W. Kim
6	PHY	1	08-02-2014	08:04		08:16				50							Vertical towing - mesh size 20 um	H. M. Joo
6	BON	1	08-02-2014	08:19		08:34				50							Vertical towing - mesh size 330 um ,500 um	D. B. Lee
7	CTD	1	08-02-2014	10:08		10:30	68° 04.003N	167° 14.002W	51	42		24	2.6	289.1	0.04	2.3	First deep casting	T. W. Kim
8	CTD	1	08-02-2014	12:20		12:38	68° 14.993N	166° 50.131W	35	28		24	2.4	313.5	0.93	66.6	First deep casting	K. H. Cho
8	SEC	1	08-02-2014	12:40		12:45				8							Secchi disk	S. H. Lee
8	BON	1	08-02-2014	12:46		12:56				30							Vertical towing - mesh size 330 um ,500 um	D. B. Lee
8	PHY	1	08-02-2014	12:56		13:10				2							Vertical towing - mesh size 20 um	H. M. Joo
8	CTD	2	08-02-2014	13:16		13:26	68° 14.997N	166° 49.988W	35	22		24	2.6	340.2	0.01	201.6	Second shallow casting	K. H. Cho
8	HPR	1	08-02-2014	13:30		13:35				10							HPRO II (Hyper - Spectroradiometer)	C. U. Hyun
9	CTD	1	08-02-2014	19:16		19:34	69° 10.002N	168° 39.981W	51	40		24	3.7	60.9	0.07	89.7	First deep casting	T. W. Kim
9	SEC	1	08-02-2014	19:35		19:38				14							Secchi disk	S. H. Lee
9	PHY	1	08-02-2014	20:08		20:16				40							Vertical towing - mesh size 20 um	H. M. Joo
9	BON	1	08-02-2014	20:18		20:33				30							Vertical towing - mesh size 330 um ,500 um	D. B. Lee
9	CTD	2	08-02-2014	20:45		21:02	69° 09.971N	168° 40.018W	51	41		24	4.1	68.6	0.02	191.8	Second shallow casting	T. W. Kim
9	HPR	1	08-02-2014	21:15		21:19				34							HPRO II (Hyper - Spectroradiometer)	C. U. Hyun
9	ICE	1	08-02-2014	21:30		21:51											Deck arrangement	P. Hwang
10	CTD	1	08-03-2014	04:43		05:05	70° 29.995N	168° 40.011W	40	32		24	4.0	120.7	0.04	121.8	First deep casting	K. H. Cho
10	SEC	1	08-03-2014	05:07		05:09				15							Secchi disk	S. H. Lee
10	CTD	2	08-03-2014	05:45		05:56	70° 29.995N	168° 40.012W	40	32		24	3.0	150.4	0.06	126.9	Second shallow casting	K. H. Cho
10	HPR	1	08-03-2014	06:00		06:04				22							HPRO II (Hyper - Spectroradiometer)	C. U. Hyun
11	CTD	1	08-03-2014	11:40		11:55	71° 25.800N	166° 40.600W	45	37		24	1.7	74.3	0.12	46.7	First deep casting	K. H. Cho
11	SEC	1	08-03-2014	11:55		11:58				16							Secchi disk	S. H. Lee
11	BON	1	08-03-2014	12:00		12:10				30							Vertical towing - mesh size 330 um ,500 um	D. B. Lee
11	PHY	1	08-03-2014	12:10		12:20				30							Vertical towing - mesh size 20 um	H. M. Joo
11	RIN	1	08-03-2014	12:20		12:30				30							Vertical towing - mesh size 200 um	D. B. Lee
11	CTD	2	08-03-2014	12:35		12:50	71° 25.801N	166° 40.598W	45	37		24	1.9	72.5	0.04	44.3	Second shallow casting	K. H. Cho
12	CTD	1	08-03-2014	21:09		21:32	72° 21.600N	164° 41.208W	47	40		24	3.7	51.8	0.50	320.4	First deep casting	K. H. Cho
12	SEC	1	08-03-2014	21:34		21:37				19							Secchi disk	S. H. Lee

Scientific Cruise Daily Log

Ship: R/V Araon Cruise: ARA05 Leg: B Prepared by C. Y. Kang (KOPRI) chanyoung85@kopri.re.kr

STN No.	Gear	Cast No.	Date (UTC)	Cast start (UTC)	Bottom or at depth (UTC)	Cast end (UTC)	Latitude	Longitude	Water depth (m)	Cast depth (m)	Cable payout (m)	No. of spl. depth Core length	Wind speed knot	Wind direction (°)	Ship speed knot	Heading (°)	Remarks	Device Driver
Arctic																		
CTD: CTD; XCT: XCTD; PHY: Phytoplankton Net; BON: Bongo Net; RIN: Ring Net; SEC: secchi; HPR: HPRO; OPT: Optics; ICE: Sea ice; MIC: Micro Layer; BUO: Buoy; UVR: UV Radiometer																		
12	PHY	1	08-03-2014	21:45		21:54				40							Vertical towing - mesh size 20 um	H. M. Joo
12	CTD	2	08-03-2014	22:08		22:25	72° 21.597N	164° 41.213W	47	40		24	4.6	66.5	0.03	281.1	Second shallow casting	K. H. Cho
12	HPR	1	08-03-2014	22:31		22:34				28							HPRO II (Hyper - Spectroradiometer)	C. U. Hyun
13	CTD	1	08-04-2014	12:06		12:40	73° 18.726N	162° 38.592W	104	95		24	2.3	102.7	0.03	6.8	First deep casting	T. W. Kim
13	SEC	1	08-04-2014	12:40		12:45				28							Secchi disk	S. H. Lee
13	BON	1	08-04-2014	12:55		13:00				90							Vertical towing - mesh size 330 um ,500 um	D. B. Lee
13	PHY	1	08-04-2014	13:13		13:23				90							Vertical towing - mesh size 20 um	H. M. Joo
13	RIN	1	08-04-2014	13:23		13:33				90							Vertical towing - mesh size 200 um	D. B. Lee
13	CTD	2	08-04-2014	13:40		14:00	73° 18.585N	162° 38.404W	100	76		24	2.5	152.2	1.05	23.2	Second shallow casting	T. W. Kim
X1	XCT	1	08-04-2014	17:55		18:02	73° 45.282N	161° 56.844W	276	276							XCTD(Conductivity,Temperature,Depth)	Koji Shimada
14	CTD	1	08-04-2014	22:35		23:22	74° 13.166N	160.42.427W	554	545		24	2.2	195.9	0.06	276.2	First deep casting	T. W. Kim
14	SEC	1	08-04-2014	23:22		23:27				32							Secchi disk	S. H. Lee
14	HPR	1	08-04-2014	23:32		23:56				63							HPRO II (Hyper - Spectroradiometer)	C. U. Hyun
14	CTD	2	08-05-2014	00:00		00:27	74° 13.262N	160.42.074W	554	100		24	3.5	205.2	0.06	330.8	Second shallow casting	T. W. Kim
14	CTD	3	08-05-2014	01:59		02:20	74° 13.332N	160.41.973W	554	100		24	3.4	185.1	0.09	293.5	Third Shallow casting	T. W. Kim
X2	XCT	1	08-05-2014	05:22		05:26	74° 32.208N	160° 02.916W	632	632							XCTD(Conductivity,Temperature,Depth)	Koji Shimada
X3	XCT	1	08-05-2014	07:52		07:59	74° 50.508N	159° 24.108W	1874	1086							XCTD(Conductivity,Temperature,Depth)	Koji Shimada
15	BUO	1	08-05-2014	11:39			75° 05.400N	158° 51.100W									Deployed SWIFT15	Craig Lee
15	BUO	1	08-05-2014	11:45			75° 05.400N	158° 51.100W									Deployed Seaglider177	Craig Lee
15	BUO	1	08-05-2014	12:03		12:40	75° 05.400N	158° 51.100W	840	5							ADCP 600kHz Test	J. Y. Chol
15	SEC	1	08-05-2014	12:05		12:10				36							Secchi disk	S. H. Lee
15	CTD	1	08-05-2014	12:45		13:50	75° 05.408N	158° 51.139W	840	830		24	7.0	215.9	0.04	242.0	First deep casting	K. H. Cho
15	BON	1	08-05-2014	14:09		14:23				100							Vertical towing - mesh size 330 um ,500 um	D. B. Lee
15	PHY	1	08-05-2014	14:23		14:40				100							Vertical towing - mesh size 20 um	H. M. Joo
15	RIN	1	08-05-2014	14:40		15:00				300							Vertical towing - mesh size 200 um	D. B. Lee
15	OPT	1	08-05-2014	15:20		16:04				103							Optical Property measurement	Eurico D'sa
15	CTD	2	08-05-2014	16:24		17:22	75° 05.852N	158° 49.464W	845	837		24	8.0	223.1	0.04	246.0	Second shallow casting	K. H. Cho
15	CTD	3	08-05-2014	18:14		19:04	75° 06.195N	158° 53.922W	854	300		24	8.2	230.0	0.03	281.6	Third Shallow casting	K. H. Cho
X4	XCT	1	08-05-2014	21:41		21:47	75° 09.354N	157° 29.310W	1443	1086							XCTD(Conductivity,Temperature,Depth)	Koji Shimada
X5	XCT	1	08-06-2014	00:21		00:27	75° 08.928N	156° 14.022W	3877	1086							XCTD(Conductivity,Temperature,Depth)	Koji Shimada
16	CTD	1	08-06-2014	03:57		07:03	75° 09.063N	154° 59.984W	3843	3830		24	7.8	275.2	0.03	285.4	First deep casting	T. W. Kim
16	PHY	1	08-06-2014	07:13		07:27				100							Vertical towing - mesh size 20 um	H. M. Joo
16	CTD	2	08-06-2014	08:12		08:34	75° 09.478N	154° 59.352W	3843	100		24	5.3	298.4	0.04	358.2	Second shallow casting	T. W. Kim
16	OPT	1	08-06-2014	08:45		09:28				125							Optical Property measurement	Eurico D'sa
X6	XCT	1	08-06-2014	13:48		13:54	75° 09.390N	153° 06.036W	3840	1086							XCTD(Conductivity,Temperature,Depth)	Koji Shimada
17	CTD	1	08-06-2014	18:01		20:44	75° 09.965N	151° 13.726W	3835	3825		24	6.0	8.4	0.07	62.9	First deep casting	K. H. Cho
17	PHY	1	08-06-2014	21:03		21:13				100							Phytoplankton process	H. M. Joo
17	BON	1	08-06-2014	21:15		21:45				200							Vertical towing - mesh size 330 um ,500 um	D. B. Lee
17	RIN	1	08-06-2014	21:47		22:10				300							Vertical towing - mesh size 200 um	D. B. Lee
17	SEC	1	08-06-2014	22:19		22:23				32							Secchi disk	S. H. Lee
17	HPR	1	08-06-2014	22:23		22:32				80							HPRO II (Hyper - Spectroradiometer)	C. U. Hyun
17	OPT	1	08-06-2014	22:52		23:35				104							Optical Property measurement	Eurico D'sa
17	CTD	2	08-07-2014	00:10		00:30	75° 09.369N	151° 16.451W	3835	87		24	7.2	68.2	0.13	182.4	Second shallow casting	K. H. Cho
17	CTD	3	08-07-2014	01:05		01:35	75° 09.319N	151° 17.411W	3835	100		24	7.6	68.6	0.26	156.2	Third Shallow casting	K. H. Cho
X7	XCT	1	08-07-2014	05:41		05:47	75° 28.800N	149° 57.400W	3830	1086							XCTD(Conductivity,Temperature,Depth)	Koji Shimada
18	CTD	1	08-07-2014	10:10			75° 47.381N	148° 47.688W									CTD Delayed due to Sensor problem	T. W. Kim
18	CTD	2	08-07-2014	10:55		11:57	75° 47.381N	148° 47.688W	3822	1000		24	4.1	46.0	0.05	91.4	First deep casting	T. W. Kim
18	ICE	1	08-07-2014	12:55		13:20											Helicopter(NO.302) Ice Camp searching for survey	S. H. Kang
18	ICE	2	08-07-2014	14:10		16:12											Helicopter(NO.302) Ice Camp searching for survey	S. H. Kang

Scientific Cruise Daily Log

Ship: R/V Araon Cruise: ARA05 Leg: B Prepared by C. Y. Kang (KOPRI) chanyoung85@kopri.re.kr

STN No.	Gear	Cast No.	Date	Cast start	Bottom or at depth	Cast end	Latitude	Longitude	Water depth	Cast depth	Cable payout	No. of spl. depth / Core length	Wind speed	Wind direction	Ship speed	Heading	Remarks	Device Driver
			(UTC)	(UTC)	(UTC)	(UTC)			(m)	(m)	(m)		knot	(°)	knot	(°)		
Arctic																		
CTD: CTD; XCT: XCTD; PHY: Phytoplankton Net; BON: Bongo Net; RIN: Ring Net; SEC: secchi; HPR: HPRO; OPT: Optics; ICE: Sea ice; MIC: Micro Layer; BUO: Buoy; UVR: UV Radiometer																		
X8	XCT	1	08-07-2014	17:40		17:46	76° 05.334N	147° 56.238W	3815	1086							XCTD(Conductivity,Temperature,Depth)	Koji Shimada
	ICE	1	08-07-2014	22:51		01:25	76° 24.000N	146°11.000W									Helicopter(NO.302) Ice Camp searching for survey	S. H. Kang
	ICE	2	08-07-2014	23:18		01:33											Helicopter(NO.301) Ice Camp searching for survey	S. H. Kang
X9	XCT	1	08-08-2014	02:03		02:09	76° 24.420N	146° 15.552W	3802	1086							XCTD(Conductivity,Temperature,Depth)	Koji Shimada
X10	XCT	1	08-08-2014	06:14		06:20	76° 55.080N	146° 13.908W	3801	1086							XCTD(Conductivity,Temperature,Depth)	Koji Shimada
X11	XCT	1	08-08-2014	10:26		10:26	77° 25.410N	146° 15.270W	3807	1086							XCTD(Conductivity,Temperature,Depth)	Koji Shimada
19	ICE	1	08-08-2014	12:30		13:40	77° 36.580N	146° 05.060W									Helicopter recon for the ice camp location	P. Hwang/M. Doble
19	ICE	2	08-08-2014	14:00		14:00	77° 36.580N	146° 05.060W									Araon parked beside the ice camp floe	
19	ICE	3	08-08-2014	16:00		19:00	77° 36.580N	146° 05.060W									Anchoring Araon on the ice camp floe	P. Hwang & H. S. La
19	ICE	4	08-08-2014	20:00		23:30	Ice camp site										6'X12' Hut Assembled and transported to observation site 200 m off Araon port beam	J. Stockell & S. Gallaher
19	ICE	5	08-08-2014	20:45			76° 16.900N	145° 56.260W									WB230 deployment	M. Doble
19	ICE	6	08-08-2014	22:30		23:30	Ice camp site										AWS deployment at the ice camp site	P. Hwang
19	ICE	7	08-09-2014	01:00		03:09	Ice camp site										6m Flux Frame Deployed from Ice Hut	J. Stockell & S. Gallaher
19	ICE	8	08-09-2014	01:12			77° 55.070N	147° 36.700W									WB232 deployment	M. Doble
19	CTD	1	08-09-2014	04:56		05:15	77° 36.002N	146° 07.786W	3805	200		6	6.5	316.2	0.27	34.8	Ice Camp CTD Operation (Cast 1)	K. H. Cho
19	CTD	2	08-09-2014	19:00		19:20	77° 33.552N	146° 11.903W	3805	200		24	6.4	351.9	0.24	37.4	Ice Camp CTD Operation (Cast 2)	K. H. Cho
19	ICE	9	08-09-2014	19:35			77° 33.580N	146° 12.490W									WB231 deployment	M. Doble
19	CTD	3	08-09-2014	20:56		21:25	77° 32.984N	146° 09.839W	3805	200		3	6.1	344.1	6.50	37.5	Ice Camp CTD Operation (Cast 3)	K. H. Cho
19	ICE	10	08-09-2014	22:00		22:40	77° 28.870N	145° 49.650W									IMB23 deployment at 10 km southeast from the ice camp	P. Hwang & J. H. Kim
19	ICE	11	08-09-2014	22:40		23:20	77° 30.320N	146° 32.510W									IMB23 deployment at 10 km southeast from the ice camp	P. Hwang & J. H. Kim
19	CTD	4	08-09-2014	22:52		23:22	77° 32.034N	146° 10.050W	3805	200		6	5.5	344.0	0.51	37.4	Ice Camp CTD Operation (Cast 4)	T. W. Kim
19	ICE	12	08-10-2014	00:30		01:20	77° 13.720N	144° 47.390W									IMB21 deployment at 50 km southeast from the ice camp	P. Hwang & Craig Lee
19	CTD	5	08-10-2014	00:56		01:16	77° 31.265N	146° 13.136W	3805	200			5.5	340.1	0.47	36.7	Ice Camp CTD Operation (Cast 5)	T. W. Kim
19	ICE	13	08-10-2014	01:46			77° 36.050N	145° 39.230W									WB233 deployment	M. Doble
19	CTD	6	08-10-2014	02:55		03:20	77° 31.728N	146° 16.844W	3805	200			5.3	347.0	0.36	36.4	Ice Camp CTD Operation (Cast 6)	T. W. Kim
19	CTD	7	08-10-2014	05:00		05:24	77° 31.506N	146° 18.703W	3805	200		3	4.6	18.8	0.30	36.8	Ice Camp CTD Operation (Cast 7)	K. H. Cho
19	CTD	8	08-10-2014	06:57		07:23	77° 31.903N	146° 17.814W	3805	200		3	3.7	355.2	0.28	37.3	Ice Camp CTD Operation (Cast 8)	K. H. Cho
19	CTD	9	08-10-2014	08:55		09:27	77° 31.871N	146° 15.074W	3805	200		3	4.8	348.5	0.30	37.2	Ice Camp CTD Operation (Cast 9)	K. H. Cho
19	CTD	10	08-10-2014	10:53		11:13	77° 31.302N	146° 13.691W	3805	200			4.4	347.5	0.32	36.3	Ice Camp CTD Operation (Cast 10)	K. H. Cho
19	CTD	11	08-10-2014	13:00		13:18	77° 30.769N	146° 15.043W	3805	200			3.5	351.3	0.30	35.7	Ice Camp CTD Operation (Cast 11)	K. H. Cho
19	CTD	12	08-10-2014	14:55		15:18	77° 30.761N	146° 17.571W	3805	200			2.9	337.9	0.26	35.9	Ice Camp CTD Operation (Cast 12)	K. H. Cho
19	CTD	13	08-10-2014	16:58		17:21	77° 31.187N	146° 18.590W	3805	200		3	2.6	326.6	0.26	36.1	Ice Camp CTD Operation (Cast 13)	K. H. Cho
19	ICE	14	08-10-2014	17:00		18:00	Ice camp site										SIMB deployment at the ice camp site	P. Hwang & J. H. Kim
19	CTD	14	08-10-2014	18:57		19:21	77° 31.522N	146° 16.828W	3805	200		3	1.9	298.5	0.26	36.6	Ice Camp CTD Operation (Cast 14)	T. W. Kim
19	ICE	15	08-10-2014	19:33			77° 51.310N	144° 44.500W									WB236 deployment	M. Doble
19	CTD	15	08-10-2014	21:00		21:17	77° 31.266N	146° 13.692W	3805	200			3.8	320.0	0.43	36.6	Ice Camp CTD Operation (Cast 15)	T. W. Kim
19	CTD	16	08-10-2014	22:55		23:24	77° 30.542N	146° 12.194W	3805	200		4	1.8	288.0	0.30	35.0	Ice Camp CTD Operation (Cast 16)	T. W. Kim
19	ICE	16	08-11-2014	00:30		00:50	77° 30.160N	146° 52.260W									IMB24 deployment at 10 km northeast from the ice camp (S Lee's 1st melt pond survey)	P. Hwang & S. H. Lee
19	ICE	17	08-11-2014	00:37			77° 37.890N	146° 10.800W									WB235 deployment	M. Doble
19	ICE	18	08-11-2014	00:50		01:40	77° 30.190N	145° 52.310W									IMB25 deployment at 10 km northwest from the ice camp (S Lee's 2nd melt pond survey)	P. Hwang & S. H. Lee
19	CTD	17	08-11-2014	00:55		01:18	77° 29.867N	146° 12.847W	3805	200			2.2	278.6	0.27	35.5	Ice Camp CTD Operation (Cast 17)	K. H. Cho
19	CTD	18	08-11-2014	02:55		03:20	77° 29.667N	146° 13.894W	3805	200		4	3.7	280.0	0.05	36.3	Ice Camp CTD Operation (Cast 18)	T. W. Kim
19	CTD	19	08-11-2014	04:58		05:26	77° 29.792N	146° 13.246W	3805	200			6.8	293.7	0.20	36.7	Ice Camp CTD Operation (Cast 19)	K. H. Cho
19	CTD	20	08-11-2014	06:56		07:34	77° 29.762N	146° 10.817W	3805	500		7	5.1	305.6	0.31	37.2	Ice Camp CTD Operation (Cast 20)	K. H. Cho
19	CTD	21	08-11-2014	08:55		09:17	77° 29.211N	146° 08.261W	3805	200			8.0	334.9	0.53	34.6	Ice Camp CTD Operation (Cast 21)	K. H. Cho
19	CTD	22	08-11-2014	10:53		11:15	77° 28.160N	146° 08.260W	3805	200			6.9	342.1	0.05	35.6	Ice Camp CTD Operation (Cast 22)	K. H. Cho
19	CTD	23	08-11-2014	12:55		13:15	77° 27.372N	146° 11.026W	3805	200			6.3	342.7	0.47	33.0	Ice Camp CTD Operation (Cast 23)	T. W. Kim
19	CTD	24	08-11-2014	14:55		15:20	77° 27.181N	146° 14.403W	3805	200		4	6.7	342.0	0.31	32.8	Ice Camp CTD Operation (Cast 24)	T. W. Kim
19	CTD	25	08-11-2014	16:59		17:30	77° 27.454N	146° 15.552W	3805	500			5.1	340.6	0.19	342.0	Ice Camp CTD Operation (Cast 25)	T. W. Kim

Scientific Cruise Daily Log

Ship: R/V Araon Cruise: ARA05 Leg: B Prepared by C. Y. Kang (KOPRI) chanyoung85@kopri.re.kr

STN No.	Gear	Cast No.	Date (UTC)	Cast start (UTC)	Bottom or at depth (UTC)	Cast end (UTC)	Latitude	Longitude	Water depth (m)	Cast depth (m)	Cable payout (m)	No. of spl. depth / Core length	Wind speed knot	Wind direction (°)	Ship speed knot	Heading (°)	Remarks	Device Driver
Arctic																		
CTD: CTD; XCT: XCTD; PHY: Phytoplankton Net; BON: Bongo Net; RIN: Ring Net; SEC: secchi; HPR: HPRO; OPT: Optics; ICE: Sea ice; MIC: Micro Layer; BUO: Buoy; UVR: UV Radiometer																		
19	ICE	19	08-11-2014	17:20		17:40	77° 26.550N	146° 12.780W									SIESTA deployment at 1 km southeast from the ice camp (S Lee's 3rd melt pond survey)	P. Hwang & S. H. Lee
19	ICE	20	08-11-2014	17:40		18:00	77° 26.930N	146° 14.480W									SIESTA deployment at 1 km southwest from the ice camp (S Lee's 4th melt pond survey)	P. Hwang & S. H. Lee
19	ICE	21	08-11-2014	18:00		18:40	77° 26.940N	146° 20.100W									S Lee's 5th melt pond survey	P. Hwang & S. H. Lee
19	CTD	26	08-11-2014	18:57		19:25	77° 27.577N	146° 13.691W	3805	500			4.9	327.7	0.29	35.1	Ice Camp CTD Operation (Cast 26)	T. W. Kim
19	ICE	22	08-11-2014	19:00		00:00	Ice camp site										AOFB deployment approximately 225 m off the Araon port quarter	
19	CTD	27	08-11-2014	20:55		21:24	77° 27.174N	146° 11.021W	3805	200							Ice Camp CTD Operation (Cast 27)	K. H. Cho
19	ICE	23	08-11-2014	22:00		00:00	Ice camp site										SATICE deployment	P. Hwang & Craig Lee
19	CTD	28	08-11-2014	22:56		23:23	77° 26.452N	146° 09.633W	3805	200		5	3.9	310.0	0.37	34.0	Ice Camp CTD Operation (Cast 28)	T. W. Kim
19	ICE	24	08-11-2014	23:15			77° 27.740N	146° 10.080W									WB237 deployment	M. Doble
19	ICE	25	08-12-2014	00:48			77° 25.740N	146° 12.220W									WB238 deployment	M. Doble
19	CTD	29	08-12-2014	00:55		01:35	77° 26.452N	146° 09.633W	3805	200			4.1	311.9	0.25	34.0	Ice Camp CTD Operation (Cast 29)	K. H. Cho
19	CTD	30	08-12-2014	03:00		03:20	77° 25.741N	146° 12.205W	3805	200		4	3.8	308.0	0.15	34.1	Ice Camp CTD Operation (Cast 30)	T. W. Kim
19	ICE	26	08-12-2014	04:10			77° 26.590N	146° 15.700W									WB234 deployment	M. Doble
19	CTD	31	08-12-2014	04:55		05:24	77° 25.938N	146° 12.341W	3805	200		4	4.0	317.2	0.19	33.8	Ice Camp CTD Operation (Cast 31)	T. W. Kim
19	CTD	32	08-12-2014	06:58		07:22	77° 26.048N	146° 10.618W	3805	500			4.2	314.7	0.25	33.5	Ice Camp CTD Operation (Cast 32)	T. W. Kim
19	CTD	33	08-12-2014	08:56		09:17	77° 25.778N	146° 08.483W	3805	200			4.5	314.5	0.28	33.2	Ice Camp CTD Operation (Cast 33)	T. W. Kim
19	CTD	34	08-12-2014	10:55		11:17	77° 25.322N	146° 07.723W	3805	200			4.0	314.1	0.20	32.9	Ice Camp CTD Operation (Cast 34)	K. H. Cho
19	CTD	35	08-12-2014	12:55		13:30	77° 24.957N	146° 08.453W	3805	500		5	3.7	341.5	0.21	32.7	Ice Camp CTD Operation (Cast 35)	K. H. Cho
19	CTD	36	08-12-2014	14:55		15:25	77° 24.877N	146° 09.991W	3805	200		5	4.0	351.2	0.46	32.0	Ice Camp CTD Operation (Cast 36)	K. H. Cho
19	CTD	37	08-12-2014	16:58		17:29	77° 25.012N	146° 10.692W	3805	200		5	3.6	351.8	0.10	32.0	Ice Camp CTD Operation (Cast 37)	K. H. Cho
19	ICE	27	08-12-2014	17:00		17:30	Ice camp site										Re-adjust the heading of AWS wind sensor (Junction box to due south)	P. Hwang
19	ICE	28	08-12-2014	17:00		17:40	77° 11.200N	147° 48.800W									SIESTA deployment at 50 km southwest from the ice camp	P. Hwang
19	CTD	38	08-12-2014	18:56		19:46	77° 25.105N	146° 10.214W	3805	500		24	3.4	4.3	0.09	32.0	Ice Camp CTD Operation (Cast 38)	K. H. Cho
19	CTD	39	08-12-2014	20:55		21:20	77° 24.848N	146° 09.501W	3805	200			3.0	347.0	0.16	31.8	Ice Camp CTD Operation (Cast 39)	T. W. Kim
19	ICE	29	08-12-2014	22:00		22:30	Ice camp site										UpTempO (238150) deployment	P. Hwang
19	ICE	30	08-12-2014	22:33			77° 22.670N	146° 09.800W									WB239 deployment	M. Doble
19	CTD	40	08-12-2014	22:55		23:16	77° 24.406N	146° 09.554W	3805	200			4.8	359.0	0.25	31.0	Ice Camp CTD Operation (Cast 40)	T. W. Kim
19	CTD	41	08-13-2014	00:55		01:15	77° 24.041N	146° 11.068W	3805	200			3.4	348.0	0.24	31.7	Ice Camp CTD Operation (Cast 41)	T. W. Kim
19	CTD	42	08-13-2014	02:55		03:25	77° 23.944N	146° 12.867W	3805	200		5	3.8	346.0	0.13	31.7	Ice Camp CTD Operation (Cast 42)	T. W. Kim
19	CTD	43	08-13-2014	04:57		05:28	77° 24.044N	146° 13.557W	3805	200		5	4.2	345.4	0.05	32.0	Ice Camp CTD Operation (Cast 43)	T. W. Kim
19	CTD	44	08-13-2014	07:01		07:29	77° 24.087N	146° 12.922W	3805	200		4	3.6	316.9	0.13	31.7	Ice Camp CTD Operation (Cast 44)	T. W. Kim
19	CTD	45	08-13-2014	08:55		09:18	77° 23.978N	146° 11.728W	3805	200			4.3	327.1	0.17	31.3	Ice Camp CTD Operation (Cast 45)	T. W. Kim
19	CTD	46	08-13-2014	10:55		11:27	77° 23.621N	146° 10.787W	3805	200			3.6	316.5	0.18	31.4	Ice Camp CTD Operation (Cast 46)	K. H. Cho
19	CTD	47	08-13-2014	12:55		13:20	77° 23.256N	146° 10.643W	3805	200			1.4	287.3	0.17	31.4	Ice Camp CTD Operation (Cast 47)	K. H. Cho
19	MIC	1	08-13-2014	13:20		15:30				5							Sea Surface Micro Layer Sampler	Y. Y. Yang
19	CTD	48	08-13-2014	14:55		15:20	77° 22.969N	146° 10.822W	3805	200			2.5	282.2	0.10	31.3	Ice Camp CTD Operation (Cast 48)	K. H. Cho
19	CTD	49	08-13-2014	17:00		17:30	77° 22.828N	146° 10.401W	3805	200		24	4.2	285.0	0.14	31.0	Ice Camp CTD Operation (Cast 49)	K. H. Cho
19	ICE	31	08-13-2014	17:30		21:00	Ice camp site										Last Flux Frame Profile - Ice Hut Disassembled Slung to Ship	J. Stockell & S. Gallaher
19	SEC	1	08-13-2014	18;10		18:14				36							Secchi disk	S. H. Lee
19	PHY	1	08-13-2014	18:27		18:38				100							Vertical towing - mesh size 20 um	H. M. Joo
19	BON	1	08-13-2014	18:41		18:54				200							Vertical towing - mesh size 330 um ,500 um	D. B. Lee
19	RIN	1	08-13-2014	19:13		19:31				300							Vertical towing - mesh size 200 um	D. B. Lee
19	CTD	50	08-13-2014	20:00		20:29	77° 22.411N	146° 08.653W	3805	200		24	5.2	315.7	0.24	30.8	Ice Camp CTD Operation (Cast 50)	T. W. Kim
19	CTD	51	08-14-2014	08:05		10:58	77° 18.102N	146° 16.801W	3800	3790		24	5.9	353.6	0.12	41.7	Ice Camp Deep Casting	T. W. Kim
X12	XCT	1	08-14-2014	16:14		16:21	77° 04.464N	147° 24.948W	3824	1086							XCTD(Conductivity,Temperature,Depth)	Koji Shimada
20	CTD	1	08-14-2014	23:30		00:30	76° 45.719N	148° 54.397W	3820	1000		24	3.1	311.9	0.26	244.2	First deep casting	K. H. Cho
20	ICE	1	08-15-2014	00:30		01:00	77° 11.200N	147° 48.800W									UptempO (238160) deployment	P. Hwang & S. H. Lee
X13	XCT	1	08-15-2014	08:54		09:00	76° 26.004N	150° 16.212W	3838	1086							XCTD(Conductivity,Temperature,Depth)	Koji Shimada
21	CTD	1	08-15-2014	13:30		16:06	76° 04.173N	151° 41.961W	3834	3820		24	4.4	62.4	0.13	236.8	First deep casting	

Scientific Cruise Daily Log

Ship: R/V Araon | Cruise: ARA05 | Leg: B | Prepared by C. Y. Kang (KOPRI) chanyoung85@kopri.re.kr

STN No.	Gear	Cast No.	Date	Cast start	Bottom or at depth	Cast end	Latitude	Longitude	Water depth	Cast depth	Cable payout	No. of spl. depth / Core length	Wind speed	Wind direction	Ship speed	Heading	Remarks	Device Driver
			(UTC)	(UTC)	(UTC)	(UTC)			(m)	(m)	(m)		knot	(°)	knot	(°)		
Arctic																		
CTD: CTD; XCT: XCTD; PHY: Phytoplankton Net; BON: Bongo Net; RIN: Ring Net; SEC: secchi; HPR: HPRO; OPT: Optics; ICE: Sea ice; MIC: Micro Layer; BUO: Buoy; UVR: UV Radiometer																		
X14	XCT	1	08-15-2014	19:06		19:13	75° 59.622N	153° 09.150W	3842	1086							XCTD(Conductivity,Temperature,Depth)	Koji Shimada
X15	XCT	1	08-15-2014	21:25		21:31	76° 01.008N	154° 34.656W	3851	1086							XCTD(Conductivity,Temperature,Depth)	Koji Shimada
22	CTD	1	08-16-2014	00:26		01:35	76° 00.037N	156° 00.280W	1260	1250		24	4.7	87.8	0.12	302.0	First deep casting	K. H. Cho
22	PHY	1	08-16-2014	02:02		02:15				100							Vertical towing - mesh size 20 um	H. M. Joo
22	BON	1	08-16-2014	02:18		02:32				200							Vertical towing - mesh size 330 um ,500 um	D. B. Lee
22	RIN	1	08-16-2014	02:36		03:00				300							Vertical towing - mesh size 200 um	D. B. Lee
22	CTD	2	08-16-2014	03:05		03:28	76° 00.074N	155° 59.827W	1260	100		24	2.3	100.6	0.04	252.4	Second shallow casting	T. W. Kim
22	OPT	1	08-16-2014	03:35		04:28				145							Optical Property measurement	Eurico D'sa
22	HPR	1	08-16-2014	4:34		4:40				52							HPRO II (Hyper - Spectroradiometer)	C. U. Hyun
X16	XCT	1	08-16-2014	08:23		08:27	76° 00.066N	157° 42.276W	580	580							XCTD(Conductivity,Temperature,Depth)	Koji Shimada
23	CTD	1	08-16-2014	12:24		13:35	76° 00.024N	159° 30.016W	1510	1490		24	6.3	102.8	0.01	359.7	First deep casting	T. W. Kim
23	HPR	1	08-16-2014	13:40		13:50				54							HPRO II (Hyper - Spectroradiometer)	C. U. Hyun
23	CTD	2	08-16-2014	14:33		14:54	76° 00.032N	159° 30.324W	1510	100		24	5.7	78.1	0.08	152.4	Second shallow casting	K. H. Cho
X17	XCT	1	08-16-2014	17:12		17:19	75° 55.014N	160° 38.466W	2061	1086							XCTD(Conductivity,Temperature,Depth)	Koji Shimada
24	CTD	1	08-16-2014	19:23		21:02	75° 51.001N	161° 42.139W	2110	2090		24	7.9	86.6	0.53	261.0	First deep casting	K. H. Cho
24	SEC	1	08-16-2014	21:11		21:14				46							Secchi disk	S. H. Lee
24	PHY	1	08-16-2014	21:20		21:31				100							Vertical towing - mesh size 20 um	H. M. Joo
24	BON	1	08-16-2014	21:33		21:50				200							Vertical towing - mesh size 330 um ,500 um	D. B. Lee
24	RIN	1	08-16-2014	21:51		22:13				300							Vertical towing - mesh size 200 um	D. B. Lee
24	CTD	2	08-16-2014	22:21		22:39	75° 50.894N	161° 42.031W	2110	116		24	8.1	87.3	0.05	132.1	Second shallow casting	K. H. Cho
24	HPR	1	08-16-2014	22:43		22:53				67							HPRO II (Hyper - Spectroradiometer)	C. U. Hyun
24	OPT	1	08-16-2014	23:00		23:45				125							Optical Property measurement	Eurico D'sa
24	CTD	3	08-16-2014	23:59		00:21	75° 50.871N	161° 43.124W	2110	100		24	8.2	89.7	0.30	112.6	Third shallow casting	K. H. Cho
X18	XCT	1	08-17-2014	04:22		04:27	76° 06.090N	163° 39.640W	1171	1086							XCTD(Conductivity,Temperature,Depth)	Koji Shimada
25	CTD	1	08-17-2014	07:13		07:53	76° 23.179N	164° 59.866W	519	505		24	7.9	103.2	0.21	88.4	First deep casting	T. W. Kim
25	PHY	1	08-17-2014	07:57		08:18				200							Vertical towing - mesh size 20 um	H. M. Joo
25	CTD	2	08-17-2014	08:32		08:52	76° 23.147N	164° 59.931W	519	102		24	7.8	89.3	0.35	143.6	Second shallow casting	T. W. Kim
25	HPR	1	08-17-2014	09:00		09:04				41							HPRO II (Hyper - Spectroradiometer)	C. U. Hyun
X19	XCT	1	08-17-2014	11:15		11:21	76° 00.228N	166° 00.598W	992	992							XCTD(Conductivity,Temperature,Depth)	Koji Shimada
26	CTD	1	08-17-2014	12:47		13:24	76° 17.918N	167° 00.021W	392	375		24	9.1	86.4	0.08	251.5	First deep casting	K. H. Cho
26	BON	1	08-17-2014	13:35		13:45				200							Vertical towing - mesh size 330 um ,500 um	D. B. Lee
26	PHY	1	08-17-2014	13:45		14:00				100							Vertical towing - mesh size 20 um	H. M. Joo
26	RIN	1	08-17-2014	14:00		14:10				300							Vertical towing - mesh size 200 um	D. B. Lee
26	SEC	1	08-17-2014	14:10		14:15				30							Secchi disk	S. H. Lee
26	CTD	2	08-17-2014	14:27		14:46	76° 18.617N	167° 01.145W	392	81		24	9.5	89.4	0.06	231.6	Second shallow casting	K. H. Cho
26	HPR	1	08-17-2014	14:50		15:05				58							HPRO II (Hyper - Spectroradiometer)	C. U. Hyun
26	OPT	1	08-17-2014	15:10		15:55				116							Optical Property measurement	Eurico D'sa
X20	XCT	1	08-17-2014	18:14		18:15	76° 00.270N	166° 15.804W	331	331							XCTD(Conductivity,Temperature,Depth)	Koji Shimada
	BUO	1	08-17-2014	20:10		20:33	75° 50.000N	165° 38.700W									SWIFT15 recovered	Craig Lee
X21	XCT	1	08-17-2014	20:41		20:44	75° 50.088N	165° 40.770W	492	492							XCTD(Conductivity,Temperature,Depth)	Koji Shimada
X22	XCT	1	08-17-2014	22:55		22:57	75° 48.294N	167° 20.058W	237	237							XCTD(Conductivity,Temperature,Depth)	Koji Shimada
27	CTD	1	08-18-2014	01:02		01:15	75° 48.000N	169° 00.000W									CTD pump operation error	T. W. Kim
27	HPR	1	08-18-2014	01:15		01:30				53							HPRO II (Hyper - Spectroradiometer)	C. U. Hyun
27	OPT	1	08-18-2014	01:30		02:22				145							Optical Property measurement	Eurico D'sa
27	CTD	2	08-18-2014	02:29		02:58	75° 48.059N	169° 00.772W	290	275		24	9.4	93.3	0.03	127.5	First deep casting	T. W. Kim
27	SEC	1	08-18-2014	03:00		03:05				27							Secchi disk	S. H. Lee
27	BON	1	08-18-2014	03:10		03:25				200							Vertical towing - mesh size 330 um ,500 um	D. B. Lee
27	PHY	1	08-18-2014	03:25		03:38				100							Vertical towing - mesh size 20 um	H. M. Joo

Scientific Cruise Daily Log

Ship: R/V Araon Cruise: ARA05 Leg: B Prepared by C. Y. Kang (KOPRI) chanyoung85@kopri.re.kr

STN No.	Gear	Cast No.	Date (UTC)	Cast start (UTC)	Bottom or at depth (UTC)	Cast end (UTC)	Latitude	Longitude	Water depth (m)	Cast depth (m)	Cable payout (m)	No. of spl. depth Core length	Wind speed knot	Wind direction (°)	Ship speed knot	Heading (°)	Remarks	Device Driver
Arctic																		
CTD: CTD; XCT: XCTD; PHY: Phytoplankton Net; BON: Bongo Net; RIN: Ring Net; SEC: secchi; HPR: HPRO; OPT: Optics; ICE: Sea ice; MIC: Micro Layer; BUO: Buoy; UVR: UV Radiometer																		
27	RIN	1	08-18-2014	03:38		03:46				300							Vertical towing - mesh size 200 um	D. B. Lee
27	CTD	3	08-18-2014	03:48		04:14	75° 48.061N	169° 00.771W	290	100		24	7.1	91.8	0.05	124.0	Second shallow casting	T. W. Kim
X23	XCT	1	08-18-2014	05:35		05:39	75° 49.926N	170° 00.054W	677	677							XCTD(Conductivity,Temperature,Depth)	Koji Shimada
X24	XCT	1	08-18-2014	06:54		07:00	75° 52.620N	171° 00.096W	1640	1086							XCTD(Conductivity,Temperature,Depth)	Koji Shimada
28	CTD	1	08-18-2014	09:32		11:21	75° 55.092N	172° 23.474W	1922	1900		24	6.5	84.1	0.05	301.9	First deep casting	T. W. Kim
28	PHY	1	08-18-2014	11:27		11:38				100							Vertical towing - mesh size 20 um	H. M. Joo
28	OPT	1	08-18-2014	11:55		12:33				103							Optical Property measurement	Eurico D'sa
28	CTD	2	08-18-2014	12:46		13:07	75° 54.997N	172° 24.474W	1922	100		24	4.5	87.2	0.03	262.3	Second shallow casting	T. W. Kim
28	SEC	1	08-18-2014	13:30		13:35				28							Secchi disk	S. H. Lee
28	CTD	3	08-18-2014	13:37		13:51	75° 54.842N	172° 24.552W	1922	76		24	5.1	97.6	0.05	241.7	Third shallow casting	K. H. Cho
X25	XCT	1	08-18-2014	18:41		18:46	75° 57.480N	174° 29.952W	2145	1086							XCTD(Conductivity,Temperature,Depth)	Koji Shimada
29	CTD	1	08-18-2014	22:57		00:33	75° 58.709N	176° 11.986W	1960	1945		24	2.0	264.6	0.49	61.1	First deep casting	K. H. Cho
29	BON	1	08-19-2014	00:40		00:57				200							Vertical towing - mesh size 330 um ,500 um	D. B. Lee
29	PHY	1	08-19-2014	00:58		01:13				100							Vertical towing - mesh size 20 um	H. M. Joo
29	RIN	1	08-19-2014	01:15		01:23				300							Vertical towing - mesh size 200 um	D. B. Lee
29	CTD	2	08-19-2014	02:00		02:21	75° 59.438N	176° 11.649W	1960	100		24	3.8	257.3	0.40	87.2	Second shallow casting	T. W. Kim
29	HPR	1	08-19-2014	02:30		02:36				59							HPRO II (Hyper - Spectroradiometer)	C. U. Hyun
29	OPT	1	08-19-2014	02:40		03:25				134							Optical Property measurement	Eurico D'sa
X26	XCT	1	08-19-2014	05:02		05:08	75° 58.704N	176° 59.854W	1208	1086							XCTD(Conductivity,Temperature,Depth)	Koji Shimada
X27	XCT	1	08-19-2014	08:17		08:23	76° 00.876N	178° 29.208W	1040	1040							XCTD(Conductivity,Temperature,Depth)	Koji Shimada
30	CTD	1	08-19-2014	11:58		12:59	76° 01.648N	179° 34.133E	1167	1150		24	4.4	262.1	0.03	122.0	First deep casting	T. W. Kim
30	BON	1	08-19-2014	13:03		13:17				200							Vertical towing - mesh size 330 um ,500 um	D. B. Lee
30	PHY	1	08-19-2014	13:17		13:29				100							Vertical towing - mesh size 20 um	H. M. Joo
30	RIN	1	08-19-2014	13:29		13:38				300							Vertical towing - mesh size 200 um	D. B. Lee
30	CTD	2	08-19-2014	13:40		14:02	76° 01.605N	179° 33.856E	1167	100		24	5.5	260.7	0.06	108.3	Second shallow casting	K. H. Cho
30	HPR	1	08-19-2014	14:05		14:15				57							HPRO II (Hyper - Spectroradiometer)	C. U. Hyun
30	OPT	1	08-19-2014	14:25		15:10				120							Optical Property measurement	Eurico D'sa
30	SEC	1	08-19-2014	15:35		15:38				36							Secchi disk	S. H. Lee
30	CTD	3	08-19-2014	15:41		16:02	76° 01.687N	179° 33.856E	1167	98		24	5.2	238.3	0.03	277.5	Third shallow casting	K. H. Cho
			08-19-2014	17:50			75° 52.100N	178° 56.400E									Deviated course to barrow in order to send a patient to hospital	
X28	XCT	1	08-19-2014	19:10		19:16	75° 45.672N	179° 36.939E	1040	1040							XCTD(Conductivity,Temperature,Depth)	Koji Shimada
X29	XCT	1	08-19-2014	21:46		21:52	75° 30.204N	178° 50.364W	997	997							XCTD(Conductivity,Temperature,Depth)	Koji Shimada
X30	XCT	1	08-20-2014	00:40		00:45	75° 15.564N	177° 25.128W	760	760							XCTD(Conductivity,Temperature,Depth)	Koji Shimada
X31	XCT	1	08-20-2014	03:30		03:35	74° 59.970N	176° 09.750W	246	246							XCTD(Conductivity,Temperature,Depth)	Koji Shimada
X32	XCT	1	08-20-2014	06:24		06:26	74° 49.764N	174° 31.410W	246	246							XCTD(Conductivity,Temperature,Depth)	Koji Shimada
X33	XCT	1	08-20-2014	08:34		08:36	74° 41.070N	173° 00.042W	279	279							XCTD(Conductivity,Temperature,Depth)	Koji Shimada
X34	XCT	1	08-20-2014	10:35		10:37	74° 31.860N	171° 30.144W	234	234							XCTD(Conductivity,Temperature,Depth)	Koji Shimada
X35	XCT	1	08-20-2014	12:40		12:42	74° 24.570N	169° 59.994W	188	188							XCTD(Conductivity,Temperature,Depth)	Koji Shimada
X36	XCT	1	08-20-2014	15:10		15:12	74° 11.514N	168° 29.994W	185	185							XCTD(Conductivity,Temperature,Depth)	Koji Shimada
X37	XCT	1	08-20-2014	17:24		17:26	73° 59.346N	167° 29.064W	206	206							XCTD(Conductivity,Temperature,Depth)	Koji Shimada
X38	XCT	1	08-21-2014	00:10		00:12	74° 30.000N	167° 59.442W	277	277							XCTD(Conductivity,Temperature,Depth)	Koji Shimada
31	CTD	1	08-21-2014	03:00		03:40	74° 48.037N	167° 53.889W	193	180		24	2.2	292.5	0.08	233.0	First deep casting	T. W. Kim
31	MOO	1	08-21-2014	03:55		04:25	74° 47.980N	167° 53.830W									Deployed Mooring	Koji Shimada
31	MOO	2	08-21-2014	04:25		05:15											400m Radius Triangle survey	Koji Shimada
31	OPT	1	08-21-2014	05:20		06:05				126							Optical Property measurement	Eurico D'sa
X39	XCT	1	08-21-2014	08:27		08:28	75° 11.328N	168° 25.806W	170	170							XCTD(Conductivity,Temperature,Depth)	Koji Shimada
X40	XCT	1	08-21-2014	10:25		10:27	75° 35.910N	168° 52.464W	210	210							XCTD(Conductivity,Temperature,Depth)	Koji Shimada
X41	XCT	1	08-21-2014	12:21		12:25	75° 59.652N	169° 16.602W	800	800							XCTD(Conductivity,Temperature,Depth)	Koji Shimada

Scientific Cruise Daily Log

Ship: R/V Araon Cruise: ARA05 Leg: B Prepared by C. Y. Kang (KOPRI) chanyoung85@kopri.re.kr

STN No.	Gear	Cast No.	Date (UTC)	Cast start (UTC)	Bottom or at depth (UTC)	Cast end (UTC)	Latitude	Longitude	Water depth (m)	Cast depth (m)	Cable payout (m)	No. of spl. depth / Core length	Wind speed knot	Wind direction (°)	Ship speed knot	Heading (°)	Remarks	Device Driver
									Arctic									
CTD: CTD; XCT: XCTD; PHY: Phytoplankton Net; BON: Bongo Net; RIN: Ring Net; SEC: secchi; HPR: HPRO; OPT: Optics; ICE: Sea ice; MIC: Micro Layer; BUO: Buoy; UVR: UV Radiometer																		
X42	XCT	1	08-21-2014	14:29		14:35	76° 23.634N	169° 36.498W	2206	1086							XCTD(Conductivity,Temperature,Depth)	Koji Shimada
32	ICE	1	08-21-2014	15:30			76° 30.602N	169° 43.800W									Sea Ice Camp (Melting pond, Ice Core)	E. J. Yang & S. H. Lee
32	MIC	1	08-21-2014	23:30		03:05	76° 30.602N	169° 43.800W									Sea Surface Micro Layer Sampler	Y. Y. Yang
32	ICE	1	08-23-2014			00:35	76° 31.200N	169° 48.000W									Completed 2nd Sea Ice Camp	E. J. Yang & S. H. Lee
32	HPR	1	08-23-2014	01:23		01:32				54							HPRO II (Hyper - Spectroradiometer)	C. U. Hyun
32	OPT	1	08-23-2014	01:40		02:55				145							Optical Property measurement	Eunice D'sa
32	SEC	1	08-23-2014	03:05		03:08				28							Secchi disk	S. H. Lee
32	CTD	1	08-23-2014	03:08		05:08	76° 31.369N	169° 48.0854W	2231	2190		24	3.3	182.0	0.05	332.0	First deep casting	K. H. Cho
32	CTD	2	08-23-2014	05:49		06:16	76° 31.200N	169° 48.000W	2231	100		24	6.2	172.0	0.50	331.0	Second shallow casting	T. W. Kim
X43	XCT	1	08-23-2014	08:26		08:32	76° 15.652N	169° 36.498W	1961	1086							XCTD(Conductivity,Temperature,Depth)	Koji Shimada
X44	XCT	1	08-23-2014	09:29		09:35	76° 06.518N	168° 30.054W	1196	1086							XCTD(Conductivity,Temperature,Depth)	Koji Shimada
X45	XCT	1	08-23-2014	10:42		10:44	75° 57.480N	167° 50.130W	270	270							XCTD(Conductivity,Temperature,Depth)	Koji Shimada
X46	XCT	1	08-23-2014	13:04		13:06	75° 36.368N	166° 50.028W	250	250							XCTD(Conductivity,Temperature,Depth)	Koji Shimada
X47	XCT	1	08-23-2014	15:12		15:14	75° 18.288N	165° 50.034W	529	529							XCTD(Conductivity,Temperature,Depth)	Koji Shimada
X48	XCT	1	08-23-2014	17:08		17:12	75° 00.192N	164° 50.004W	546	546							XCTD(Conductivity,Temperature,Depth)	Koji Shimada
X49	XCT	1	08-23-2014	18:46		18:52	74° 45.120N	164° 00.000W	978	978							XCTD(Conductivity,Temperature,Depth)	Koji Shimada
X50	XCT	1	08-23-2014	20:14		20:20	74° 31.578N	163° 15.042W	1109	1086							XCTD(Conductivity,Temperature,Depth)	Koji Shimada
X51	XCT	1	08-23-2014	21:42		21:48	74° 17.976N	162° 29.916W	1220	1086							XCTD(Conductivity,Temperature,Depth)	Koji Shimada

Appendix II. XCTD stations

(1) Instrument

XCTD (eXpendable Conductivity, Temperature & Depth profiler), Tsurumi-Seiki Co.
XCTD digital converter model MK-150, Tsurumi-Seiki Co.
XBT/XCTD hand launcher, Tsurumi-Seiki Co.

(2) Data

According to the manufacturer's nominal specifications, the range and accuracy of parameters measured by the XCTD (eXpendable Conductivity, Temperature and Depth profiler) are as follows:

Parameter	Range	Accuracy
Conductivity	0 ~ 60 [mS/cm]	+/- 0.03 [mS/cm]
Temperature	-2 ~ 35 [deg-C]	+/- 0.02 [deg-C]
Depth	0 ~ 1100 [m]	5 [m] or 2 [%] (either of them is major)

However, the actual data contain bias in salinity (conductivity) dependent on serial number of XCTD probes. From X01 to X04 minus bias relative to CTD data was observed. From X05 to X12, the bias value was quite small. After X13, large plus bias about 0.1 psu was observed. After the cruise, calibration of XCTD data is planned, using CTD data calibrated by bottle salinity data.

(2) Observation log

Table 2.4. XCTD observation log

Station	Lat. Deg.	Lat. Min.		Lon. Deg.	Lon. Min.		Bottom Depth	month/day/year (UTC)	hhmmss (UTC)	FileName without extention
XCTD01	73	45.280	N	161	56.841	W	276m	8/4/2014	175630	XCTD-000120140804
XCTD02	74	32.206	N	160	2.917	W	632m	8/5/2014	052320	XCTD-000220140805
XCTD03	74	50.510	N	159	24.106	W	1874m	8/5/2014	075306	XCTD-000320140805
XCTD04	75	9.356	N	157	29.312	W	1443m	8/5/2014	214149	XCTD-000420140805
XCTD05	75	8.927	N	156	14.019	W	3877m	8/6/2014	002140	XCTD-000520140805
XCTD06	75	9.388	N	153	6.038	W	3840m	8/6/2014	134842	XCTD-000620140806
XCTD07	75	28.783	N	149	57.477	W	3830m	8/7/2014	054153	XCTD-000720140807

XCTD08	76	5.333	N	147	56.237	W	3815m	8/7/2014	173959	XCTD-000820140807
XCTD09	76	24.420	N	146	15.551	W	3802m	8/8/2014	020403	XCTD-000920140808
XCTD10	76	55.081	N	146	13.910	W	3801m	8/8/2014	061449	XCTD-001020140808
XCTD11	77	25.407	N	146	15.273	W	3807m	8/8/2014	102113	XCTD-001120140808
XCTD12	77	4.463	N	147	24.949	W	3824m	8/14/2014	161522	XCTD-001220140814
XCTD13	76	26.003	N	150	16.214	W	3838m	8/15/2014	085434	XCTD-001320140815
XCTD14	75	59.621	N	153	9.153	W	3842m	8/15/2014	190724	XCTD-001420140815
XCTD15	76	1.005	N	154	34.653	W	3851m	8/15/2014	212623	XCTD-001520140815
XCTD16	76	0.063	N	157	42.274	W	580m	8/16/2014	082336	XCTD-001620140816
XCTD17	75	55.015	N	160	38.464	W	2081m	8/16/2014	171325	XCTD-001720140816
XCTD18	76	6.091	N	163	29.637	W	1171m	8/17/2014	042232	XCTD-001820140817
XCTD19	76	21.229	N	166	0.589	W	992m	8/17/2014	111554	XCTD-001920140817
XCTD20	76	0.270	N	166	15.806	W	331m	8/17/2014	181448	XCTD-002020140817
XCTD21	75	50.089	N	165	40.772	W	492m	8/17/2014	204214	XCTD-002120140817
XCTD22	75	48.291	N	167	20.055	W	237m	8/17/2014	225625	XCTD-002220140817
XCTD23	75	49.929	N	170	0.056	W	677m	8/18/2014	053625	XCTD-002320140818
XCTD24	75	52.623	N	171	0.095	W	1660m	8/18/2014	065511	XCTD-002420140818
XCTD25	75	57.480	N	174	29.952	W	2145m	8/18/2014	184114	XCTD-002520140818
XCTD26	75	58.706	N	176	58.854	W	1208m	8/19/2014	050227	XCTD-002620140819
XCTD27	76	0.878	N	178	29.208	W	1040m	8/19/2014	081758	XCTD-002720140819
XCTD28	75	45.672	N	179	36.936	E	1040m	8/19/2014	191050	XCTD-002820140819
XCTD29	75	30.203	N	178	50.364	W	997m	8/19/2014	214652	XCTD-003120140819
XCTD30	75	15.563	N	177	25.131	W	760m	8/20/2014	004037	XCTD-003220140820
XCTD31	74	59.972	N	176	9.752	W	246m	8/20/2014	033228	XCTD-003320140820
XCTD32	74	49.763	N	174	31.408	W	246m	8/20/2014	062427	XCTD-003420140820
XCTD33	74	41.070	N	173	0.040	W	279m	8/20/2014	083524	XCTD-003520140820

XCTD34	74	31.862	N	171	30.142	W	234m	8/20/2014	103605	XCTD-003620140820
XCTD35	74	24.669	N	169	59.995	W	188m	8/20/2014	124023	XCTD-003720140820
XCTD36	74	11.516	N	168	29.993	W	185m	8/20/2014	151056	XCTD-003820140820
XCTD37	73	59.345	N	167	29.063	W	206m	8/20/2014	172411	XCTD-003920140820
XCTD38	74	30.002	N	167	55.443	W	277m	8/21/2014	000955	XCTD-004020140821
XCTD39	75	11.931	N	168	25.806	W	170m	8/21/2014	082753	XCTD-004120140821
XCTD40	75	35.909	N	168	52.465	W	210m	8/21/2014	102615	XCTD-004220140821
XCTD41	75	59.653	N	169	16.605	W	800m	8/21/2014	122215	XCTD-004320140821
XCTD42	76	23.633	N	169	36.496	W	2206m	8/21/2014	142926	XCTD-004420140821
XCTD43	76	15.553	N	169	0.058	W	1981m	8/23/2014	082736	XCTD-004520140823
XCTD44	76	6.514	N	168	30.051	W	1196m	8/23/2014	093011	XCTD-004620140823
XCTD45	75	57.482	N	167	50.130	W	270m	8/23/2014	104252	XCTD-004720140823
XCTD46	75	36.364	N	166	50.029	W	250m	8/23/2014	130244	XCTD-004820140823
XCTD47	75	18.289	N	165	50.036	W	529m	8/23/2014	151124	XCTD-004920140823
XCTD48	75	0.189	N	164	50.003	W	546m	8/23/2014	170948	XCTD-005020140823
XCTD49	74	45.119	N	164	0.000	W	978m	8/23/2014	184750	XCTD-005120140823
XCTD50	74	31.575	N	163	15.043	W	1109m	8/23/2014	201506	XCTD-005220140823
XCTD51	74	17.978	N	162	29.916	W	1220m	8/23/2014	214219	XCTD-005420140823

Chapter 3 .Chemical Oceanography

3.1. Air-sea CO_2 exchange and water column carbonate system

Dong-Woo Kim[1] and Tae Siek Rhee[2]

[1] *Korea Maritime &Ocean University (kimduocean@naver.com)*

[2]*Korea Polar Research Institute, Incheon, Korea (Rhee@kopri.re.kr)*

3.1.1. Objectives

The Arctic climate changed rapidly in the various aspects (ACIA, 2005). In particular, the regional warming rate of the Arctic is atop together with the Antarctic Peninsula. Steep reduction of summer sea-ice extent in the Arctic Ocean becomes a symbol of global climate change as it demonstrates the sensitive response of the Arctic to the regional warming which in turn returns as a positive feedback. Sea-ice retreat of the Arctic Ocean results in change in the Arctic ecosystem in the ocean as the sunlit penetrates the water column and air-sea gas exchange will be active as the sea-ice thaws away. Shoaling the seasonal mixed layer due to radiative warming of the surface water together will provide habitat to thrive phytoplankton, ending up with enhancement of primary production. This will alter the ecosystem and carbon cycle in the water column of the Arctic Ocean. We aim to investigate the impact of the retreating sea-ice onto the Arctic carbon cycle, in particular air-sea exchange and the change in the carbonate system in the water column along this project.

3.1.2. Work at sea

1) Air-sea CO_2 flux

CO_2 flux across the sea surface is usually determined by the concentration difference between the dissolved CO_2 in the surface mixed layer and the atmospheric CO_2 overlying the surface with a parameterized gas transfer velocity *k*. Dissolved CO_2, so called pCO_2, was determined using an aqueous and gaseous phase equilibration technique with an small Weiss-type equilibrator. The air above the surface was withdrawn from the intake cup

mounted at the foremast at 29 m above sea-level. The CO_2 in the air and the equilibrator headspace was analyzed with Li-cor 7000 in which 4.5 um wavelength of photon is selectively absorbed by CO_2. The analyzing system was calibrated every 6 hours using a series of calibration gases and one zero air. pCO_2 in the seawater was acquired every minute in a computer and atmospheric CO_2 every 6 hours. The raw data will then be corrected for the effect of temperature difference between the in-situ and the equilibrator after coming back to the institute, and gas transfer velocity k will also be determined using parameterization with wind speed which has been logged in DADIS onboard Araon.

2) Carbonate system of the water column

Carbonate system in the water column compose of ionic form of carbonate (CO_3^{2-}), bicarbonate (HCO_3^-), hydrogen ion (hydronium) and neutral form of carbonic acid and dissolved CO_2. These carbonate species exist in equilibrium in seawater depending on alkalinity of the seawater. These species, however, cannot be analyzed directly using analytical instruments except CO_2 and hydronium. Thus, To determine the carbonate system in the water column, we measure total dissolved inorganic carbon (DIC) and total alkalinity (TA) by which one can derive ionic and neutral form of carbonate system. DIC and TA are defined as follows:

$DIC = [HCO_3^-] + [CO_3^{2-}] + [CO_2] + [H_2CO_3]$

$TA = [HCO_3^-] + 2[CO_3^{2-}] + \Sigma[anions] - \Sigma[cations]$

DIC and TA will be analyzed in the laboratory after collecting seawater samples aboard at the hydrographic stations. To prevent the seawater samples from being altered due to biological activities in the seawater, 100 uL of $HgCl_2$ solution (50%) were injected upon collecting the samples from the Niskin seawater collected attached in CTD/Rosette. The sample bottles were flushed 3 times before starting collection in 250 mL bottle. Making small headspace, injecting $HgCl_2$ solution, and tightening the lid with black electric tape, the samples were stored in a dark place before analysis.

We also collect seawater samples for analysis of pH onboard. The procedure of collection is the same as that for DIC and TA.

To analyze dissolved CO_2 in the water column, a specially designed bottle was employed

to avoid contact with ambient air onboard. The bottle composes of one stopcock and septum lid on both sides. Seawater flows through these two ends and the body of the bottle which was upright overflowing a certain time period to flush the bottle and to get rid of any bubbles inside. Upon collecting the seawater, 50 mL of CO_2 free N_2 gas was injected into the jar to equilibrate it with the water in. The equilibrated headspace air will then be analyzed onboard or in the laboratory. 40 uL of $HgCl_2$ was injected to avoid contamination from biological activities.

3) pCO_2 variation under the sea-ice

In order to investigate the impact of sea-ice on carbonate system of the seawater under sea-ice, pCO_2 mooring system was deployed during the sea-ice camp event starting from August 9 to August 13. The system consists in in-situ pCO_2 analyzer (CO_2 Pro, Pro-oceanus), dissolved oxygen sensor (Optode Aanderra), fluorescence sensor (Cyclops 7, Turner design), PAR sensor (Li-cor), and temperature and salinity sensors (Microcat, seabird) (Fig. 3.1).

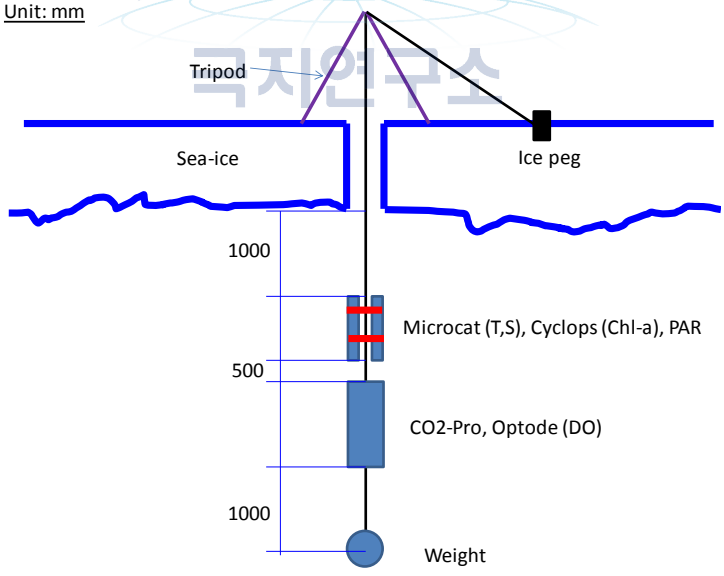

Fig. 3.1. pCO_2 mooring system deployed in the sea-ice camp

3.1.3. Results

Over 2800 measurements of pCO_2 in the surface seawater and 90 measurements of atmospheric CO_2 were performed during the expedition. These data need to be corrected for the instrumental drift and change in the seawater temperature during the transport in the ship. Spatial distributions of pCO_2 and of atmospheric CO_2 will be gained after the expedition.

Over 200 seawater samples were collected at 25 hydrographic stations for analyses of DIC, TA, and pH. These samples are stored in a dark room and will be analyzed in the laboratory. The sampling information is listed in Table 3.1.

The results from the pCO_2 mooring system for 4 days were stored in a storage device through the data logging system. These data will be further analyzed after coming back to the laboratory.

Table 3.1. Hydrographic information of station, sampling time, items, and sampling depth

Station	01	02	03	04	05	06	07
Cast	1	1	1	1	1	1	1
Sampling time	2014-08-01 09:40	14-08-01 17:58	14-08-01 23:50	14-08-02 02:54	14-08-02 04:44	14-08-02 07:37	14-08-02 10:06
Items	pCO_2 DIC/TA pH	pCO_2 DIC/TA pH	pCO_2 DIC/TA pH	pCO_2 DIC/TA pH	pCO_2 DIC/TA pH	pCO_2 DIC/TA pH	pCO_2 DIC/TA pH
Depth (m)	0	0	0	0	0	0	0
	6	10	8	10	10	14	10
	10	20	20	22	20	25	20
	20	30	30	30	30	30	30
	40		40	40	40	53	42

Table 3.1. Hydrographic information of station, sampling time, items, and sampling depth (continue)

Station	08	09	10	11	12	13	14
Cast	1	1	1	1	1	1	1
Sampling time	2014-08-02 12:19	14-08-02 19:18	14-08-03 04:44	14-08-03 11:40	14-08-03 21:09	14-08-04 12:15	14-08-04 22:36
Items	pCO_2 DIC/TA pH	pCO_2 DIC/TA pH	pCO_2 DIC/TA pH	pCO_2 DIC/TA pH	pCO_2 DIC/TA pH	pCO_2 DIC/TA pH	pCO_2 DIC/TA pH
Depth (m)	0	0	0	0	0	0	140
	10	12	10	10	10	20	200
	20	25	18	20	20	38	250
	28	40	30	35	28	60	360
					39	95	450
							545

Station	14	15	15	16	17	18	19
Cast	3	1	2	1	1	1	51
Sampling time	2014-08-05 -	14-08-05 12:50	14-08-05 16:25	14-08-03 04:00	14-08-06 17:53	14-08-07 10:57	14-08-14 08:05
Items	pCO_2 DIC/TA pH	pCO_2 DIC/TA pH	pCO_2 DIC/TA pH	pCO_2 DIC/TA pH	pCO_2 DIC/TA pH	pCO_2 DIC/TA pH	pCO_2 DIC/TA pH
Depth (m)	0	150	0	0	0	0	0
	15	200	20	20	20	40	20
	40	250	40	40	60	70	58
	50	450	60	70	70	100	75
	70	650	80	100	100	200	100
	100	830	100	200	200	300	200
				300	300	450	300
				500	500	700	450
				1000	1000	1000	800
				1600	1400		1200
				2000	2000		2000
				3830	3000		2500
					3825		3000
							3790

Table 3.1. Hydrographic information of station, sampling time, items, and sampling depth (continue)

Station	22	23	24	25
Cast	1	1	1	1
Sampling time	2014-08-16 00:35	14-08-16 12:28	14-08-16 19:25	14-08-17 07:20
Items	DIC/TA pH	DIC/TA pH	DIC/TA pH	DIC/TA pH
Depth (m)	0	0	0	0
	30	40	20	20
	60	60	57	40
	80	80	80	58
	100	100	100	70
	150	120	200	100
	200	150	300	200
	300	200	450	300
	450	300	600	400
	600	450	1000	505
	800	700	1400	
	1000	1000	1800	
	1250	1200	2090	
		1495		

3.2. Nutrients and organic carbon measurements

Jinyoung Jung[1], Sun-Yong Ha[1] and Jun Oh Min[1]

[1]*Korea Polar Research Institute, Incheon 406-840, Korea (jinyoungjung@kopri.re.kr; sundragon@kopri.re.kr; jomin@kopri.re.kr)*

3.2.1. Introduction

The oceanic cycles of life's essential elements—carbon (C), nitrogen (N) and phosphorus (P)—are closely coupled through the metabolic requirements of phytoplankton, whose average proportions of these elements, C/N/P = 106:16:1, are known as the Redfield ratios. The similarity between the average N/P ratio of plankton biomass and spatial variations of dissolved nitrate (NO_3^-) and phosphate (PO_4^{3-}) has long been taken to imply that a relatively constant number of N atoms per atom of P are assimilated by phytoplankton throughout the surface ocean and released by the respiration of organic matter at depth. The Redfield N/P ratio is therefore viewed as a critical threshold between the N-limitation and P-limitation of marine photosynthesis and the carbon it sequesters (Weber and Deutsch, 2010). The operation of the biological carbon pump in the sea is inextricably linked to the biogeochemical cycling of other nutrient elements. Limitation by macronutrients, such as N or micronutrients, such as iron (Fe), diminishes phytoplankton growth and ultimately the export of organic carbon to the deep sea. Carbon export is also governed by the relative use of new and recycled nutrients by the phytoplankton, which sets an upper limit on the fraction of primary production that can be exported to depth (Brzezinski et al., 2003). To improve our understanding of roles of nutrients in biological processes such as variations of N/P ratio in water column and N and P uptake ratio by different phytoplankton species, we investigated spatial and temporal variations of nutrients (PO_4^{3-}, NO_3^-+NO_2^-, NH_4^+, and SiO_2) in seawater collected over the Chukchi Sea. The results for nutrients would be valuable for filling the data gap, and useful to understand biogeochemical cycles of C, N, and P as well as carbon sequestration by biological carbon pump in the Chukchi Sea.

It is generally known that the Arctic Ocean may significantly affect and be affected by global climate changes. In addition the Arctic Ocean has been shown to have large seasonal

changes in sea-ice coverage and thickness, irradiance regime, fresh water input. Due to the impact of these, the Arctic Ocean has dynamic ecosystem and extremely regional contrasts in biological production and biogenic matter concentration in water column. The Chukchi Sea Shelf, one of the major shelf seas in the Arctic Ocean, particulate production rate is 208 mmol C m^{-2} d^{-1} because inflow of nutrient-rich North pacific water through Bering Strait (Cota et al., 1996; Wheeler., 1996) whereas dissolved organic carbon exhibited only minor seasonal variations. Concentration of DOC did not show a significant seasonal change in surface waters of the Canada Basin (Davis and Bener, 2005) but particulate organic carbon concentration were strongly correlated with chlorophyll-a, indicating a plankton source of freshly produced organic matter. The central Arctic Ocean is the notably low productive area but dissolved organic carbon concentration in surface waters are among the highest in the world ocean (Anderson et al., 1998; Bussman and Kattner, 2000). On the other hand, the wide shelves of the Arctic Ocean receive large riverine input, suggesting that terrigenous organic carbon is one of major source of organic matter together with autochthonous production. However the distribution pattern and role of DOC and POC in response to the regional extreme environmental condition in the Arctic Ocean is rarely defined. The objective of this study is to understand the controls on distribution and variability of organic carbon in both the dissolved and particulate form.

Interactions between oceanic microbes and dissolved organic matter (DOM) are expected to influence the global carbon cycle (Kujawinski 2011). A small fraction of the largely uncharacterized oceanic DOM pool is compound important of dissolved free amino acids (DFAA) (Sarmento et al., 2013). The aim of the present study is to characterize the DFAA pool composition in the Arctic ocean.

3.2.2. Materials and methods

Seawater sampling for nutrients was carried out at 30 stations over the Chukchi Sea using a CTD/rosette sampler holding 24-10 L Niskin bottles (OceanTest Equipment Inc., FL, USA) during Korea research ice breaker R/V Araon cruise (ARA05B, July 31, 2014–August 25, 2014) (Fig. 3.2). Samples for nutrients were collected from the Niskin rosette into 50 ml conical tubes and immediately stored in a refrigerator at 2°C prior to chemical analyses. All

nutrients samples were analyzed within 3 days. Concentrations of nutrients were measured using standard colorimetric methods adapted for use on a 4-channel continuous Auto-Analyzer (QuAAtro, Seal Analytical). The channel configurations and reagents were prepared according to the 'QuAAtro Applications'. Standard curves were run with each batch of samples using freshly prepared standards that spanned the range of concentrations in the samples. The r^2 values of all the standard curves were greater than or equal to 0.99. In addition, reference materials for nutrients in seawater (RMNS) provided by 'KANSO Technos' (Lot. No. 'BV') were used along with standards at every batch of run in order to ensure accurate and inter-comparable measurements.

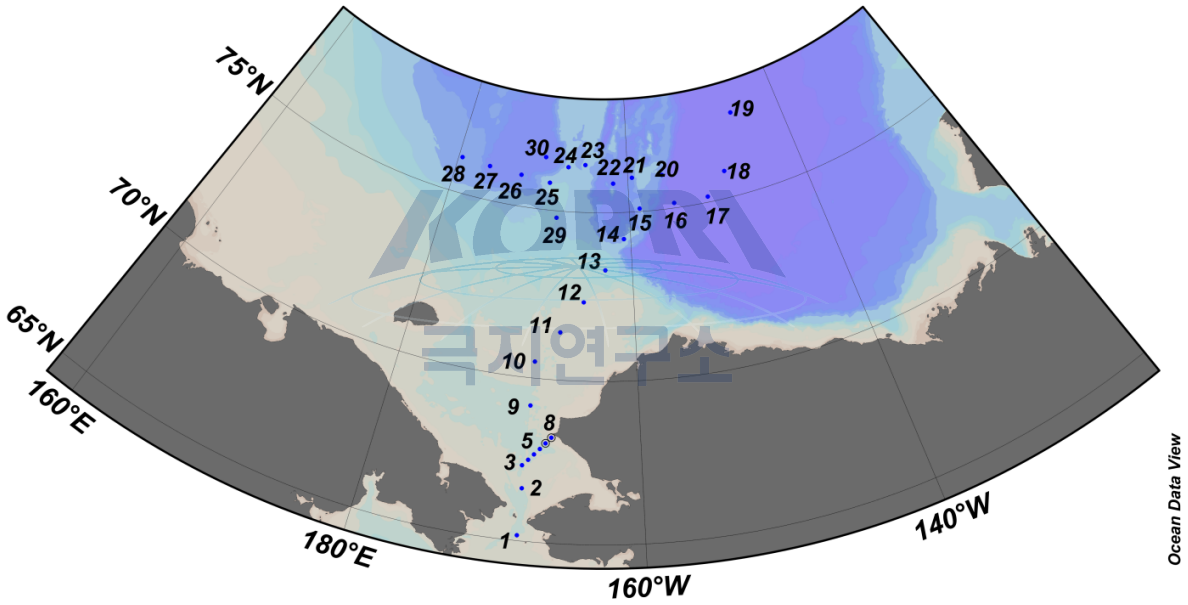

Fig. 3.2. Map of study area. Blue dots show the CTD stations during the expedition. The numbers indicate the station numbers.

Water column samples for analysis of dissolved organic carbon (DOC) and particulate organic carbon (POC) were drained from the Niskin bottles into amber polyethylene bottle. DOC samples were collected with pre-combusted (6 hrs. at 450C) GF/F filters using a nitrogen gas purging system under low (<1.0 atm) pressure (Fig. 3.3). After 20 ml of DOC samples were collected into a pre-combusted amber glass vial, 0.1 ml of $MgSO_4$ was added

to samples to remove inorganic carbon. POC samples were collected with same procedure as DOC sample by filtration of known seawater volume. Both DOC and POC samples were stored frozen at –20°C until analysis in the home laboratory. DOC samples will be analyzed with high-temperature oxidation (HTCO) method (Sugimura & Suzuki, 1988) using a Shimadzu TOC-V system. To maintain quality control of sample analysis, 3–4 point calibration curve of seawater DOC reference standards will be made. POC samples will be determined with a CHN analyzer according to JGOFS protocol (JGOFS, 1996).

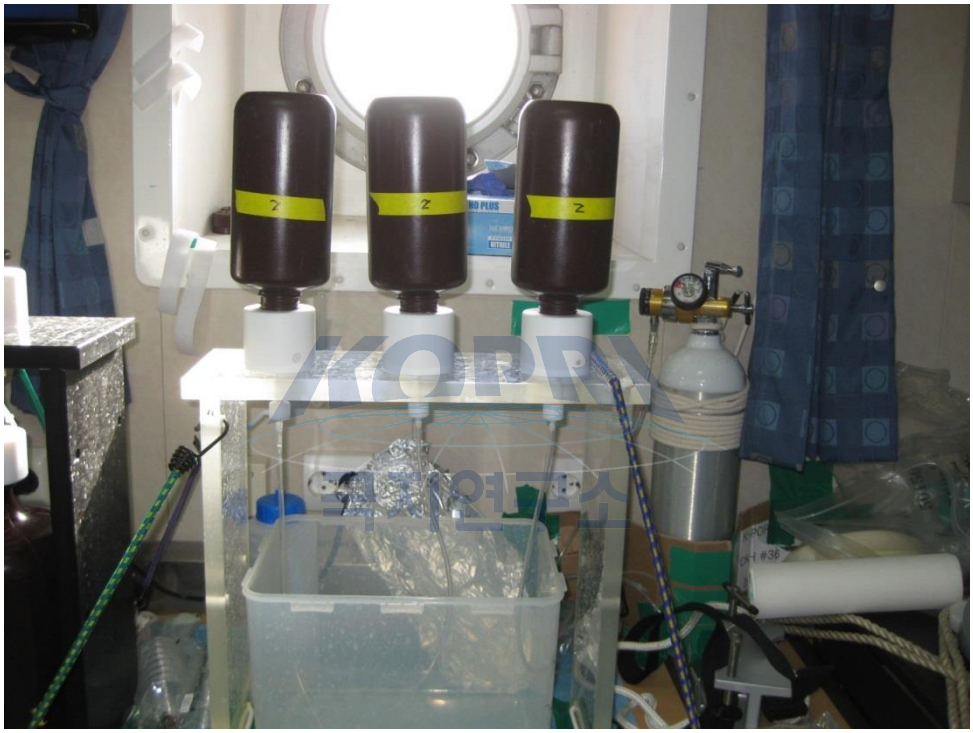

Fig. 3.3. Nitrogen gas purging system for collecting DOC and POC

DFAA samples were collected with GF/F filters using a filtering system. After 5 ml of DFAA samples were collected into a pre-combusted (400°C, 6hr) amber glass vial, 0.5ml of 100% methanol was added to samples. After sampling, these were then at store –80°C. Quantification by HPLC was achieved by precolumn derivatization with OPA and detected using Agilent 1260 HPLC.

References

Anderson, L, G., Olsson, K., Chierici, M., 1998. A carbon budget for the Arctic Ocean. Global Biogeochemical Cycles, 12(3): 455-465.

Bussman, I., Kattner, G., 2000. Distribution of dissolved organic carbon in the central Arctic Ocean: the influence of physical and biological properties. J. of Marine System, 27:209-219

Brzezinski, M.A., Dickson, M.-L., Nelsonc, D.M., Sambrotto, R., 2003. Ratios of Si, C and N uptake by microplankton in the Southern Ocean. Deep-Sea Research II, 50, 619–633.

Cota, G, F., Pomeroy, L. R., Harison. W. G., Jones, E. P., Peters, F., Sheldon Jr., W. M. Weingartner, T. R., 1996. Nutrients, primary production and microbial heterotrophy in the southeastern Chukchi Sea; arctic summer nutrient depletion and heterotriphy. Mar. Ecol. Pro. Ser., 135:247-258.

Davis J and R. Benner, 2005. Seasonal trends in the abundance, composition and bioavailability of particulate and dissolved organic matter in the Chukchi/Beaufort Seas and western Canada Basin. Deep-Sea Res., 52:3396-3410.

Sarmento, H., Romera-Castillo, C., Lindh, M., Pinhassi, J., Sala, M. M., Celia Marrase, J. M., Taylor, G. T., 2013. Phytoplankton species-specific release of dissolved free amino acids and their selective consumption by bacteria. Limnol. Oceanogr. 58(3) 1123-1135, doi:10.54319/lo.2013.58.3.1123.

Kujawinski, E. B., 2011. The impact of microbial metabolism on marine dissolved organic matter. Annu. Rev. Mar. Sci. 3: 567-599, doi:10.1146/annurev-marine-120308-081003.

Weber, T.S., Deutsch, C., 2010. Ocean nutrient ratios governed by plankton biogeography. Nature, 467, 550-554.

Wheeler, P. A., Gosselin, M., Sherr, E., Thibault, D., Kirchman, D. L., Benner, R., Whitledge, T. E., 1996. Active cycling of organic carbon in the central Arctic Ocean. Nature 380:697-699.

3.3. Dimethylsulfide(DMS)

Se Hyun Jang and Young Ho Ko

Pohang University of Science and Technology, Pohang, 790-784, Korea

(sehyun@postech.ac.kr, sldla@postech.ac.kr)

3.3.1. Introduction

Dimethylsulfide (DMS) is a biogenic gas produced by various biological processes in the surface ocean. DMS is climatically important compound because of its role as a climate feedback. When it is oxidized, the products can increase the albedo of the Earth's surface directly (as sulfate aerosols) and indirectly (as cloud condensation nuclei) (Charlson et al., 1987). If the albedo increases, the environment for the biomass generating DMS is also changing such as temperature and UV radiation. Therefore, the production of the DMS is reduced because of the environmental condition changes. As a result of this, the albedo of the earth can be changed the opposite direction compared to the previous condition. We call it 'Negative feedback of DMS on the climate'.

DMS is produced by the enzymatic breakdown of dimethylsulfoniopropionate (DMSP) derived from marine phytoplankton. In phytoplankton cells that produce DMSP, most of the cellular organic sulfur is in this form; the DMSP is subsequently transformed into gaseous DMS through complex food web processes. To gain an understanding of the sulfur cycle in the ocean–atmospheric system, it is critical to know the concentrations of various organic sulfur pools among the diverse marine phytoplankton species and their dynamics under differing oceanic conditions.

3.3.2. Materials and methods

1) DMS and DMSP

For DMS analysis, Samples were collected at selected stations (Table 3.2). DMS and dissolved DMSP were sampled based on the 'Small-volume gravity filtration' procedure (Kiene and slezak, 2006). Each water sample (about 50mL) was filtered onto a 47mm GF/F

filter by gravity pressure. 20mL of the filtered water was collected for the DMS analysis. And other 20mL of the filtered water sample was collected for dissolved DMSP analysis with addition of 100uL of the 50% H_2SO_4 to preserve DMSP for the later analysis. For total DMSP analysis, 20mL of the not-filtered water sample was collected with addition of the 50% H_2SO_4. DMS was measured through the Purging and trapping & desorption system (connected with GC Agilent Technologies 7890A). DMS sample is purged with pure nitrogen gas for the adsorption of the DMS onto the trap (packing material; TENAX TA). For the DMSP analysis, we add NaOH solution to oxidize the DMSP to DMS, and then the DMSP sample is also analyzed as the DMS sample.

To compare the distribution of DMS with that of pCO_2, samples are also collected for the measurement of total alkalinity (A_T) and Dissolved Inorganic carbon (C_T). A_T of all seawater samples were determined using potentiometric acid titration during the cruise. For A_T measurements, the seawater samples were titrated with HCl (~0.2 M) to approximately pH of 3.0; during the titration the volume of acid added was recorded at an average of 17 pH values. Values of A_T were then computed from the resulting titration data using a non-linear least squares approach (e.g. Dickson et al., 2007). C_T will be measured in POSTECH by coulometric titration using VINDTA system (Marianda, Kiel, Germany). pH and pCO_2 will be calculated from a pair of A_T and C_T using a seawater thermodynamic model that includes the carbonic acid dissociation constants of Mehrbach et al. (1973), refitted in different functional forms by Dickson and Millero (1987), and other ancillary thermodynamic constants summarized in Millero (1995).

Fig. 3.4. DMS measurement system & GC

2) Particulate Organic Sulfur (POS)

Depending on the cell density, 10–50 mL of each sample was filtered onto a precombusted 25 mm GF/F filter under low vacuum (<100 mmHg), using a hand pump. The filter was then rapidly rinsed five times with isotonic 3.2% ammonium formate to remove sea-salt sulfate. The filter was folded and placed into a glass vial containing 90% acetone. POS will be measured based on the method developed for minimizing sulfur loss (Park et al., 2014) at POSTECH. The organic sulfur content in the extract is quantified using a NSX-2100 V (Mitsubishi Chemical Analytech Co., Ltd.) trace sulfur analyzer. The sulfur detector in this analyzer enables stable measurement of sulfur at ppb levels. Approximately 90 µL of extract was injected into a reaction tube maintained at 1000 °C, using argon as the carrier gas. In this process, sulfur compounds in the sample are degraded by pyrolysis and oxidized by O_2, resulting in the formation of SO_2. The SO_2 is carried into the sulfur detector and exposed to ultraviolet radiation (190–230 nm) inside the fluorescence chamber.

Table 3.2. Sampling location and sampling depth at each station for DMS analysis

Station	Lat.	Long.	Sampling depth(m)
ARA05B_#01	65°10.42'	168°41.50'	0, 40, 60
ARA05B_#03	67°19.99'	168°49.99'	0, 8, 40
ARA05B_#05	67°42.00'	168°02.00'	0, 39
ARA05B_#09	69°09.97'	168°40.01'	0, 25
ARA05B_#11	71°25.80'	166°40.59'	0, 20, 35
ARA05B_#13	73°18.73'	162°38.59'	0, 38, 95
ARA05B_#15	75°05.85'	158°49.46'	0, 60, 100
ARA05B_#17	75°09.31'	151°17.42'	0, 40, 74
ARA05B_#19	77°22.82'	146°10.37'	0, 57, 100
ARA05B_#25	76°23.13'	164°59.49'	0, 58, 70
ARA05B_#27	75°48.05'	169°00.77'	0, 48, 70
ARA05B_#28	75°54.99'	172°24.15'	0, 46, 70
ARA05B_#29	75°58.42'	176°11.64'	0, 40, 50
ARA05B_#30	76°01.60'	179°33.84'	0, 44, 70

Reference

Charlson, R.J., J.E. Lovelock, M.O. Andreae, and S.G. Warren. (1987) Oceanic phytoplankton atmospheric sulphur, cloud albedo and cilimate, Nature, 326, 6550661.

Ronald P. Kiene and Doris Slezak. (2006) Low dissolved DMSP concentrations in seawater revealed by small-volume gravity filtration and dialysis sampling, Limnol. Oceanogr.: Methods 4, 2006, 80–95

Ki-Tae Park, Kitack Lee, Kyoungsoon Shin, Hae Jin Jeong, and Kwang Young Kim. Improved Method for Minimizing Sulfur Loss in Analysis of Particulate Organic Sulfur. Anal. Chem. 2014, 86, 1352−1356

Dickson A. G., Sabine C. L. and Christian J. R. (2007) Guide to best practice for ocean CO_2 measurements, PIECES Special Publication.

Dickson A. G. and Millero F. J. (1987) A comparison of the equilibrium constants for the dissociation of carbonic acid in seawater media. *Deep-Sea Res. Part I* **34**, 1733−1743.

Merhbach C., Culberson C. H., Hawley J. E. and Pytkowicz R. M. (1973) Measurement of the apparent dissociation constants of carbonic acid in seawater at atmospheric pressure. *Limnol. Oceanogr.* **18**, 897−907.

Millero F. J. (1995) Thermodynamics of the Carbon-Dioxide System in the Oceans. *Geochim. Cosmochim. Acta* **59**, 661−677.

Chapter 4. Plankton Ecology

4.1. Bacteria

Jung-Ho Hyun and Bomina Kim

Department of Marine Sciences and Convergent Technology, Hanyang University 55 Hanyang Daehak-ro, Ansan, Gyeonggi-do 426-791, Korea (hyunjh@hanyang.ac.kr; bomina0315@hanyang.ac.kr)

4.1.1. Introduction

Respiration represents the transfer of carbon from organic pool to inorganic pool, and reflects the rate of organic matter supply that is available to the biota within the system (Jahnke and Craven, 1995). Long-term shifts in respiration have a potential to provide the best warning system for global change (del Giorgio and Williams, 2005). Therefore, it is particularly important to measure the respiration in polar ocean to better understand any shifts in biogeochemical carbon cycles.

4.1.2. Materials and methods

During this cruise, we measured the microbial respiration rates in the water column of the Chukchi Sea and Beaufort Sea and at the melting ponds with different salinity level. In the water column, water samples were collected using a Sea-bird Electronics CTD system equipped with specific sensors such as photosynthetically active radiation (PAR) sensor, fluorometer, transmissometer and dissolved oxygen meter. In the melting pond, water samples were collected from 20 cm depth of the surface of the pond using silicon tubing connected to peristaltic pump.

Water samples for bacterial abundance were fixed with glutaraldehyde (final concentration, 1%) and kept in the freezer for cell enumeration in the lab. Respiraton rates were measured onboard from the decrease of dissolved oxygen concentration during incubation using a spectrophotometeric-Winkler method (Labasque et al. 2004). Briefly,

water samples were transferred into six or eight 300-ml BOD bottles (Wheaton Co.) that were washed and rinsed with acid (10% HCl) and distilled water, respectively. The BOD bottles were wrapped with aluminum foil, and then were incubated for 48 – 72 hours in the dark in incubator through which in situ seawater continuously flowed. At the end of incubation, BOD bottles were immediately fixed by adding 2 ml of manganese chloride and 2 ml of alkaline iodide reagents. After being vigorously shaken for about 1 min, the BOD bottles were stored in the dark. When most of the flocculation had settled, the bottles were reopened and 2 ml of sulfuric acid solution was added. The mixture was then gently stirred with a magnetic stirrer until all the precipitate had dissolved. Absorbance was measured onboard within 3 min using a Shimadzu UV-1700 spectrophotometer. The spectrophotometric Winkler method has a precision of 0.1% for the onboard measurement. Respiration rates were calculated from the linear regression of time-course measurement of dissolved oxygen concentration with time.

4.1.3. Preliminary results

A water samples for measuring microbial community respiration and bacterial abundance were collected from the 10 and 21 sampling stations, respectively, in the water column of the Beaufort Sea and Chukchi Sea (Table 4.1). Additional samples to measure microbial community respiration and to enumerate bacterial cell number were collected at the 11 and 20 melting ponds, respectively (Table 4.2).

An example of respiration measured at the melting pond with different salinity range is presented in Fig. 4.1. Average (± 1 SD) respiration rates at the melting ponds with salinity < 1 psu was 2.27 (± 1.95) mmol m^{-3} d^{-1}, whereas those measured at the melting ponds with salinity range of 20 – 25 psu and > 25 psu appeared 10.14 (± 6.76) mmol m^{-3} d^{-1} and 15.37 (±5.89) mmol m^{-3} d^{-1}, respectively. The respiration at the melting ponds with salinity < 1 psu was significantly different with that in the melting ponds with salinities 20 – 25 psu ($P = 0.043$) and salinity > 25 psu ($P = 0.004$). The results indicated that habitat changes by melting ponds have a great influence on the microbial metabolic activities and biogeochemical C cycles.

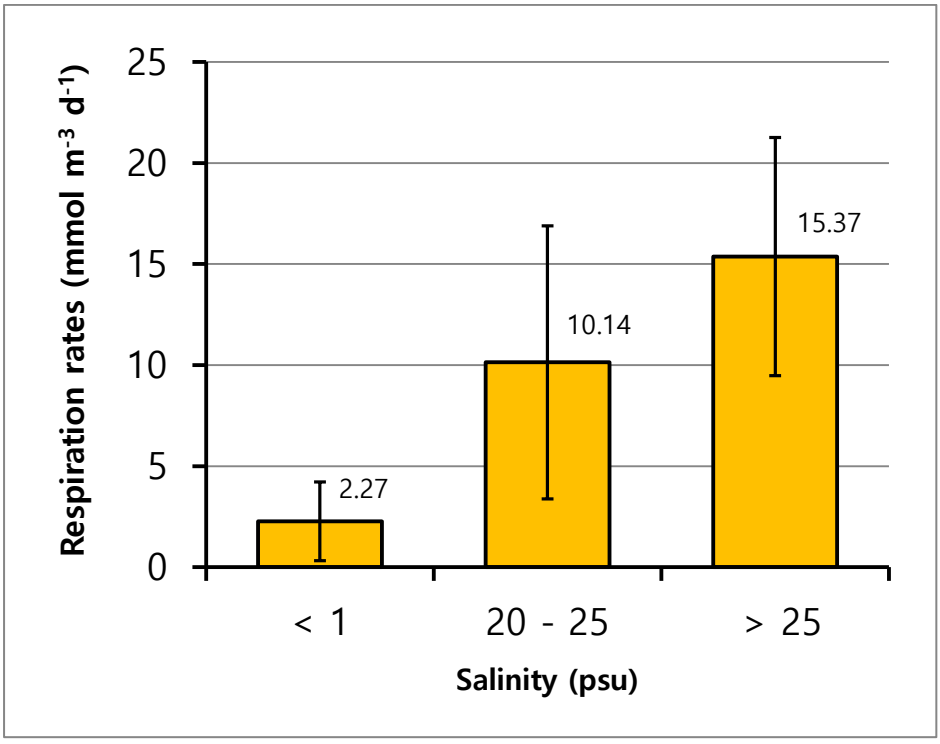

Fig. 4.1. A respiration rates measured in the melting ponds with different salinity range

Table 4.1. Sampling station, location, and items for estimating bacterial abundance (BA) and microbial community respiration (CR) in the water column of the Beaufort Sea and Chukchi Sea

St.	Latitude/ Longitude	Depth (m)	Sampling depth (m)	Item	Remark
1	65° 10.3986N 168° 41.4413W	49	0	BA	
			6	BA	
			10	BA	
			20	BA	
			40	BA	
2	66° 37.7942N 168° 41.2562W	40	0	BA	
			10	BA	
			20	BA, CR	
			30	BA	
3	67° 19.9996N 168° 49.9931W	49	0	BA	
			8	BA, CR	
			20	BA	
			30	BA	
			40	BA	
9	69° 09.9868N 168° 39.9516W	51	0	BA, CR	
			12	BA	
			20	CR	
			25	BA	
			40	BA	
10	70° 29.9915N 168° 40.0115W	45	0	BA	
			10	BA	
			18	BA	
			32	BA	
11	71° 25.5044N 166° 41.2047W	45	0	BA, CR	
			10	BA	
			20	BA, CR	
			35	BA	
12	72° 21.6002N 164° 41.2089W	47	0	BA, CR	
			10	BA	Resource
			20	BA	
			28	BA	
			39	BA	
13	73° 18.7260N 162° 38.5907W	104	0	BA	
			20	BA	
			38	BA	
			60	BA	
			95	BA	

Table 4.1. Sampling station, location, and items for estimating bacterial abundance (BA) and microbial community respiration (CR) (Continued) in the water column of the Beaufort Sea and Chukchi Sea (Continued)

St.	Latitude/ Longitude	Depth (m)	Sampling depth (m)	Item	Remark
14	74^{O} 13.1862N 160^{O} 42.4263W	550	0	BA	
			15	BA	
			40	BA	
			50	BA	
			70	BA	
			100	BA	
15	75^{O} 05.8659N 158^{O} 49.4661W	842	0	BA	
			20	BA	
			40	BA	
			60	BA	
			80	BA	
			100	BA	
16	75^{O} 09.4706N 154^{O} 59.3517W	3843	0	BA	
			20	BA	
			40	BA	
			70	BA	
			80	BA	
			100	BA	
17	75^{O} 09.3692N 151^{O} 16.4557W	3835	0	BA, CR	
			20	BA	
			40	BA	
			55	BA	
			66	CR	
			74	BA	
			100	BA	
19	77^{O} 22.3892N 146^{O} 08.5894W	3805	0	BA	
			25	BA	
			40	BA	
			57	BA, CR	
			75	BA	
			100	BA	
24	75^{O} 50.8940N 161^{O} 42.0300W	2110	0	BA	
			20	BA	
			25	CR	
			40	BA	
			55	BA	
			70	BA	
			100	BA	

Table 4.1. Sampling station, location, and items for estimating bacterial abundance (BA) and microbial community respiration (CR) (Continued) in the water column of the Beaufort Sea and Chukchi Sea (Continued)

St.	Latitude/ Longitude	Depth (m)	Sampling depth (m)	Item	Remark
25	76^{O} 23.1390N 154^{O} 59.4938W	519	0	BA	
			20	BA	
			40	BA	
			58	BA, CR	
			70	BA	
			100	BA	
26	76^{O} 18.5184N 167^{O} 01.1498W	392	0	BA	
			15	BA	
			30	BA	
			50	BA	
			70	BA	
			100	BA	
27	75^{O} 48.0591N 169^{O} 00.7743W	290	0	BA	
			15	BA	
			30	BA	
			48	BA	
			70	BA	
			100	BA	
28	75^{O} 55.0886N 172^{O} 23.4360W	1922	0	BA	
			20	BA, CR	
			35	BA	
			46	BA, CR	
			70	BA	
			100	BA	
29	75^{O} 58.7097N 176^{O} 11.9863W	1960	0	BA	
			20	BA	Resource
			40	BA	
			50	BA	
			70	BA	
			100	BA	
30	76^{O} 01.6036N 179^{O} 33.8391E	1167	0	BA	
			20	BA	
			44	BA	
			55	BA	
			70	BA	
			100	BA	

Table 4.2. Sampling station, location, and items for estimating bacterial abundance (BA) and microbial community respiration (CR) in melting pond (Continued)

Station	Salinity (psu)	Item	Remark
MP1	0.2	BA, CR	
MP3	0.5	BA, CR	
MP4	0.4	BA, CR	
MP5	24.8	BA, CR	
MP6	22.7	BA	
MP7	26.3	BA	Resource
MP8	23.2	BA	
MP9	26	BA, CR	
MP11	26.8	BA, CR	
MP12	26.7	BA	
MP13	0.9	BA, CR	Resource
MP14	25.7	BA	
MP15	22.2	BA, CR	
MP16	1.5	BA	
MP17	22.2	BA, CR	
MP18	21.4	BA	
MP19	19.9	BA, CR	Resource
MP20	15.2	BA	
MP21	17.6	BA	
MP22	0	BA, CR	

References

del Giorgio, P. A. and Williams, P. J. le B., 2005. The global significance of respiration in aquatic ecosystems: from single cells to the biosphere. In: P.A. del Giorgio and P. J. le B. Williams (eds) respiration in aquatic ecosystems. Oxford University Press, New York, pp. 267-303.

Jahnke, R. A. and Craven, D. B., 1995. Quantifying the role of heterotrophic bacteria in the carbon cycle: a need for respiration rate measurements. Limnology and Oceanography. 40: 436-441.

Labasque, T., Chaumery, C., Aminot, A., and Kergoat, G., 2004. Spectrophotometric Winkler determination of dissolved oxygen:re-examination of critical factors and reliability, Marine Chemistry, 88, 53-60.

4.2. Phytoplankton

Recent species compositions of phytoplankton and chlorophyll a concentration in the Western Arctic Ocean

Hyoung Min Joo

Korea Polar Research Institute, Incheon 406-840, Korea (hmjoo77@kopri.re.kr)

4.2.1 Introduction

High-latitude marine ecosystems are particularly sensitive to climate change. In part, this is because small temperature changes can have large effects on the extent and thickness of sea ice (Holland et al., 2006), and sea ice has a major influence on the mineral nutrient status of Arctic waters. Arctic sea ice has become thinner and less extensive in Canadian waters (Comiso et al., 2008). Rising air temperature will reduce the area of multi-year ice cover, and the extent of the seasonal ice zone will reach farther north into the Arctic Ocean during late summer (Serreze et al., 2007). Upper water column stratification will strengthen with increasing solar heating and freshwater inputs from melting sea ice and glaciers, excess net precipitation, and increased river discharge (Peterson et al., 2002). These processes will expose phytoplankton to elevated surface irradiance levels, although light availability at depth may decrease through increases in suspended sediments and colored dissolved organic matter inputs from river runoffs. Strong stratification will reduce recycling of mineral nutrients from deep waters. Conversely, with reduced sea ice cover, increasing wind strengths during storms may deepen the surface mixed layer (Carmack and Wassmann, 2006). This in turn may enhance the nutrient supply, but also decrease the light available for phytoplankton (Smetacek and Nicol, 2005; Behrenfeld et al., 2006; Wassmann et al., 2006). Tremblay et al. (2009) suggests that coming changes in the vertical water column structure in the Arctic will have more effects on the larger size phytoplankton fraction than on the smaller size fraction. Interannual environmental variability can be considerable in the western Arctic and adds background noise that confuses long-term trends in the effects of rapidly declining Arctic perennial ice cover over the last two decades (Wassmann et al., 2006). Nevertheless, Wang et al. (2005) reported that phytoplankton biomass increases

much earlier in the Beaufort Sea when ice cover decreases early in the year. They also demonstrated that annual chlorophyll fluctuations peak with delays of up to two months in cold years with extensive ice cover.

The main objective of this research was to investigate in phytoplankton communities to surface and subsurface nutrient availabilities and the chlorophyll a maximum depth in the Chukchi and East Siberian Sea during summer 2014.

4.2.2. Materials and methods

The data were collected in the Chukchi and eastern Siberian Sea from August 1 to 21 in 2014 (Table 4.3). A total of 26 stations were visited. Water samples were collected at 4-6 depths (Surface, 10m, 20m, 30m, 50m, 100m, and subsurface chlorophyll a maximum depth) with a rosette sampler equipped with 20 L Niskin-type bottles, an in situ fluorometer, and a high-precision Sea-Bird plus CTD probe. The subsurface chlorophyll maximum layer depths were estimated by CTD profiles.

To analysis phytoplankton community composition, water samples were obtained with a CTD/rosette unit in 20 L PVC Niskin bottles during the 'up' casts. Aliquots of 125 mL were preserved with glutaraldehyde (final concentration 1%). Sample volumes of 50 to 100 mL were filtered through Gelman GN-6 Metricel filters (0.45 µm pore size, 25 mm diameter). The filters were mounted on microscopic slides in a water-soluble embedding medium (HPMA, 2-hydroxypropyl methacrylate) on board. The HPMA slides were used for identification and estimation of cell concentration and biovolume. The HPMA-mounting technique has some advantages over the classical Utermöhl sedimentation method. Samples were also collected via phytoplankton net tows (20 µm mesh) and preserved with glutaraldehyde (final concentration 2%); these samples were used only for identification of small species in the phytoplankton assemblage. Since the results from this can be biased towards larger specimens, these data were not used for statistical analysis, but only for morphological and systematic analysis. Based on the HPMA slide method, the total 300 slides were made for identifying species compositions of phytoplankton later at the laboratory in KOPRI.

The chl a concentration was estimated by Fluorometer. Particulates were collected

on 25 mm glass fiber filters (GF/F) and the filters were then left in the dark for 12 h in 90% acetone at 4°C for pigment extraction.

References

Behrenfeld, M.J., O'Malley, R.T., Siegel, D.A., McClain, C.R., Sarmiento, J.L., Feldman, G.C., Milligan, A.J., Falkowski, P.G., Letelier, R.M., Boss, E. S., 2006. Climate-driven trends in contemporary ocean productivity. Nature 444, 752-755.

Carmack, E., Wassmann, P., 2006. Food webs and physicalbiological coupling on pan-Arctic shelves: unifying concepts and comprehensive perspectives. Progress in Oceanography 71, 446-477.

Comiso, J.C., Parkinson, C.L., Gersten, R., Stock, L., 2008. Accelerated decline in the Arctic sea ice cover. Geophysical Research Letters 35, L01703, doi:10.1029/2007GL031972.

Holland, M.M., Bitz, C.M., Hunke, E.C., Lipscomb, W.H., Schramm, J.L., 2006: Influence of the Sea Ice Thickness Distribution on Polar Climate in CCSM3. J. Climate 19, 2398–2414.

Peterson, B.J., Holmes, R.M., McClelland, J.W., Vörösmarty, C.J., Lammers, R.B., Ratkova, T.N., Wassmann, P., 2002. Seasonal variation and spatial distribution of phyto- and protozooplankton in the central Barents Sea. Journal of Marine Systems 38, 47-75.

Serreze, M.C., Holland, M.M., Stroeve, J., 2007. Perspectives on the Arctic's shrinking sea-ice cover. Science 315, 1533-1536.

Smetacek, V., Nicol, S., 2005. Polar ocean ecosystems in a changing world. Nature 437, 362-368.

Tremblay, G., Belzile., C., Gosselin., M., Poulin., M., Roy, S., Tremblay, J.É., 2009. Late summer phytoplankton distribution along a 3500 km transect in Canadian Arctic waters: strong numerical dominance by picoeukaryotes. Aquatic Microbial Ecology 54, 55-70.

Wang, J., Cota, G.F., Comiso, J.C., 2005. Phytoplankton in the Beaufort and Chukchi Seas: Distribution, dynamics, and environmental forcing. Deep Sea Research Part II 52, 3355-3368.

Wassmann, P., Reigstad, M., Haug, T., Rudels, B., Carroll, M.L., Hop, H., Gabrielsen, G.W., Falk-Petersen, S., Denisenko, S.G., Arashkevich, E., Slagstad, D., Pavlova, O., 2006. Food webs and carbon flux in the Barents Sea. Progress in Oceanography 71, 232-287.

Table.4.3. Sampling locations of phytoplankton species compositions during the ARA05B 2014 cruise.

No.	St. name	Sampling Date	Sampling time	Latitude	Longitude	Bottom Depth [m]	Remark
1	ARA05B01	2014-08-01	9:41	65°10.43'N	168°41.50'W	46	
2	ARA05B02	2014-08-01	17:50	66°37.79'N	168°41.25'W	43	
3	ARA05B03	2014-08-02	0:00	67°19.99'N	168°49.99'W	49	DBO line
4	ARA05B04	2014-08-02	3:05	67°30.99'N	168°26.00'W	48	
5	ARA05B05	2014-08-02	4:50	67°42.00'N	168°02.00'W	49	
6	ARA05B06	2014-08-02	7:45	67°52.99'N	167°38.03'W	59	
7	ARA05B08	2014-08-02	12:25	68°14.88'N	166°50.36'W	35	
8	ARA05B09	2014-08-02	19:20	69°09.97'N	168°40.02'W	51	
9	ARA05B11	2014-08-03	11:45	71°25.50'N	166°41.20'W	45	
10	ARA05B12	2014-08-03	21:15	72°21.60'N	164°41.21'W	47	
11	ARA05B13	2014-08-04	12:25	73°18.73'N	162°38.60'W	104	
12	ARA05B14	2014-08-04	2:05	74°13.19'N	160°42.43'W	560	
13	ARA05B15	2014-08-05	16:40	75°05.87'N	158°49.47'W	830	
14	ARA05B16	2014-08-06	8:20	75°09.23'N	154°59.45'W	3843	
15	ARA05B17	2014-08-07	1:25	75°09.37'N	151°16.45'W	3835	
16	ARA05B19	2014-08-12	17:00	77°22.82'N	146°10.36'W	3800	Ice Station I
17	ARA05B22	2014-08-16	3:10	76°00.08'N	155°59.83'W	1250	
18	ARA05B23	2014-08-16	14:40	76°00.03'N	159°30.32'W	1510	
19	ARA05B24	2014-08-16	0:10	75°50.86'N	161°43.06'W	2110	
20	ARA05B25	2014-08-17	8:30	76°23.12'N	164°59.47'W	519	
21	ARA05B26	2014-08-17	13:00	76°17.92'N	167°00.02'W	392	
22	ARA05B27	2014-08-18	4:00	75°48.06'N	169°00.77'W	280	
23	ARA05B28	2014-08-18	13:00	75°54.99'N	172°24.16'W	1922	
24	ARA05B29	2014-08-18	2:10	75°58.42'N	176°11.64'W	1960	
25	ARA05B30	2014-08-19	13:50	76°01.61'N	179°33.85'E	1167	
26	ARA05B32	2014-08-21	6:00	76°31.40'N	169°47.35'W	2210	Ice Station II

Fig. 4.2 Sampling by 20um messhed Phytoplankton Net

Fig. 4.3 HPMA Slides for Quantity analysis of phytoplankton communities.

4.3. ~~Primay producitonPrimary production~~ and macromolecular composition

Sang Heon Lee, Ho Jung Song, Jae Hyoung Lee, and Gwan Woo Kim

Department of Oceanography, Pusan National University, Korea (sanglee@pusan.ac.kr)

4.3.1. Carbon and nitrogen productions of phytoplankton and contribution of bacteria to the nitrogen uptake rate in the Northern Chukchi Sea

Over the past several decades, higher temperatures have decreased the extent and thickness of perennial sea ice as well as increased the number of melting pond in the Arctic Ocean (Perovich et al., 2009). The removal of permanent sea ice cover and increasing number of melting pond altered several important processes, such as the depth of mixing, stratification, light penetration, nutrient supply, temperature-related processes, and possibly photochemical reactions (Tremblay et al., 2008; Codispoti et al., 2009; Lee et al., 2010). These recent changes in climate and ice conditions could change the patterns and the total amount of carbon production of phytoplankton and consequently the production at higher trophic levels (Tynan and DeMaster, 1997). However, whether these climate change conditions enhance or reduce the overall production in the Arctic Ocean is controversial. However, whether these climate change conditions enhance or reduce the overall production in the Arctic Ocean is controversial. Arrigo et al. (2008) reported increases in annual net primary production (NPP) by phytoplankton based on a satellite ocean color data were particularly large on the continental shelves of the Chukchi Sea, whereas Lee et al. (2007) reported that the primary production rates from *in situ* measurement up to three times lower than those previously reported in the shelf of the Chukchi Sea. In this cruise, our main objectives are to determine main controlling factors for primary and new productions of phytoplankton and to find the effects of current environmental changes on the overall production in the Chukchi Sea. Therefore, the main objectives are to determine main controlling factors for phytoplankton production and to find the effects of current environmental changes, especially decrease in sea ice extent and thickness, on the overall production in the Arctic Ocean.

4.3.1.1. Methods and Materials

To estimate carbon and nitrogen uptake of phytoplankton at different locations, productivity experiments were executed by incubating phytoplankton in the incubators on the deck for 4-5 hours (Fig. 4.4) after stable isotopes (^{13}C, $^{15}NO_3$, and $^{15}NH_4$) as tracers were inoculated into each bottle. Total 10 and 46 productivity experiments were completed at water column and sea ice (melting pond : 39, sea ice core : 4, under sea ice : 3) station during this cruise, respectively. At every CTD station, the productivity waters were collected by CTD rosette water samplers at 6 different light depths (100, 50, 30, 12, 5, and 1%). In addition, the contribution of heterotrophic bacteria to the nitrogen (nitrate and ammonia) uptake rate of phytoplankton was estimated using the prokaryotic and eukaryotic metabolic inhibitors SM and CHI, respectively (Fouiland et al. 2008).

Fig. 4.4. In situ incubation on deck for 4-5 hours.

After the incubation, all productivity sample waters were filtered on GF/F (ø = 25 mm or 47 mm) filters for laboratory isotope analysis at University of Alaska Fairbanks after this cruise.

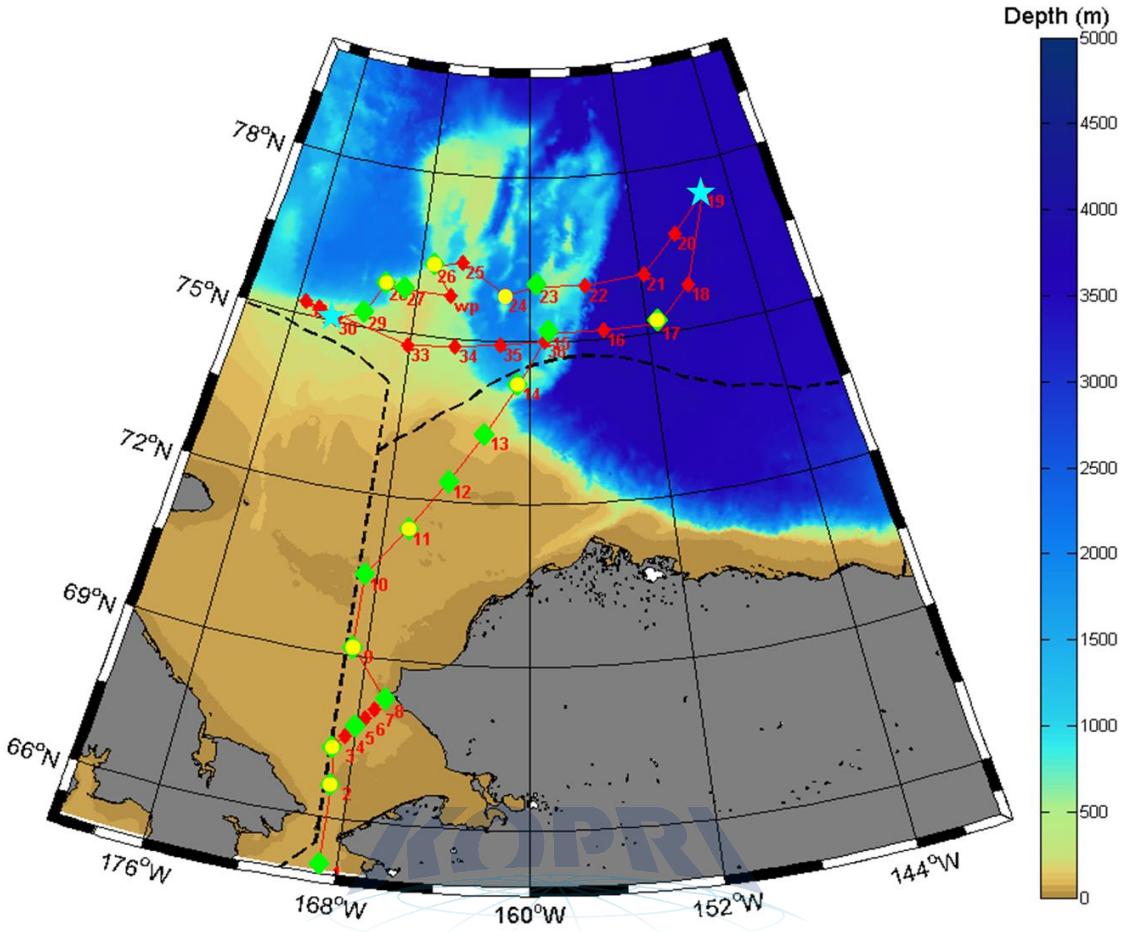

Fig. 4.5. Stations for primary (yellow circle) and macromolecular (green square) productivity, and sea ice (blue star) during the 2014 Arctic cruise.

For the background data for the productivity stations, water samples were collected for alkalinity, macro nutrient concentrations (Nitrate, Nitrite, Silicate, Ammonium, and Phosphate), and total and size-fractionated (only for 100, 30, and 1% of light depth) chlorophyll-a concentrations.

4.3.2. Analysis of macromolecular compositions of phytoplankton and proximate analysis of zooplankton in the Chukchi Sea

The biochemical composition and biosynthetic patterns of phytoplankton can provide important clues for their physiological status (Morris 1981; Smith et al. 1997; Lee et al. 2009) and also for the cycling and trophic transfer of photosynthetically fixed carbon in

the marine food web (Laws 1991, Parrish et al. 1995). Consequently, these photosynthetically synthesized biochemical composition (proteins, lipids, polysaccharides, and low-molecular-weight metabolites (LMWM) could influence the nutritional status of higher trophic levels (Scott, 1980; Lindqvist and Lignell, 1997). Therefore, current physiological status of phytoplankton as a food quality as well as primary production as a food quantity are needed for better understanding of the impact of ongoing changes in climate and sea-ice conditions on the Arctic marine ecosystems. The primary objective in this study is to find differences in the macromolecular compositions of primary producers under ambient environmental conditions in the Chukchi Sea. The second objective is to evaluate nutritional status of zooplankton community based on their proximate compositions related to food source such as phytoplankton macromolecular compositions.

4.3.2.1. Methods and Materials

Samples for macromolecular compositional analysis of phytoplankton were obtained at selected 26 stations in the Chukchi Sea (Fig. 4.5 and Table 4.4). Mesozooplankton samples for compositional analysis were collected within the upper 200 m with a Bongo net (mesh apertures 330 and 500 μm) at selected 11 stations (Fig. 4.5 and Table 4.4).

1) Macromolecular compositional analysis of phytoplankton

Water samples for macromolecular composition of phytoplankton obtained from 3 light depths (100, 30, and 1%). One-liter of each seawater sample went through a pre-combusted 47mm GF/F filter (Whatman, 0.7 μm pore) and was then immediately stored at -80 °C until analysis. Quantitative analysis of protein followed the method of Lowry et al. (1951) was conducted. Absorbance was measured at 750 nm using a spectrophotometer (Labomed, Germany). The concentration of protein was calculated by calibration curves with the protein standard solution (2 mg mL^{-1}, SIGMA). Carbohydrate analyses were performed following extraction with the phenol-sulfuric method from Dubois et al. (1956). The concentration of carbohydrate was determined by measuring the absorbance of samples at 490 nm with the glucose standard solution (1 mg mL^{-1}, SIGMA). Lipid was extracted from POM with chloroform and methanol (1:2, v/v) according to Bligh and Dyer (1959) and Marsh

and Weinstein (1966). Absorbance for lipids was measured at 360 nm. Tripalmitin solutions were used as standard for lipid concentration.

2) Proximate analysis of mesozooplankton

Lipid, water, ash, and protein contents were determined from bulk mesozooplankton samples using proximate analysis following procedures outlined in Foy (1996). The samples combined with an amount of water equivalent to 49 percent of the sample weight and then homogenized using a T 10 basic ultra-turax homogenizer (IKA, China) for about 5 minutes. Finally, the homogenized sample was distributed for each analysis. Lipid was extracted using a mixture of chloroform: methanol: water (2:1:1 by volume) according to the modified method of Bligh and Dyer (1959). Water content was determined by drying of homogenate aliquots, which were placed in a 65℃ oven during approximately 24 h. Ash content was determined by combusting of homogenate aliquots in a muffle furnace at 600℃ for four hours until constant weight was attained. Protein content was determined by finely grinding a subsample of dried homogenate from the water content analysis. The dried samples (about 0.5 mg aliquot) were analyzed with a CHN elemental analyzer (Eurovector 3000 Series, Milan, Italy) coupled with a continuous-flow isotope ratio mass spectrometer (IsoPrime, GV Instruments, Manchester, UK) in the POSTEC Ocean Science and Technology Institute. Protein was then estimate by multiplying percent nitrogen by a factor of 6.25, on the basis of a 16% nitrogen content in protein (Winberg 1971; Dowgiallo 1975).

Table 4.4. Sampling locations and depths at each station for primary and new production and macromolecular composition of phytoplankton during the 2014 Arctic cruise.

Station	Primary production	Macro composition	Zooplankton composition
1	x	o	o
2	o	o	o
3	o	o	o
4	x	x	x
5	x	o	x
6	x	x	x
7	x	x	x
8	x	o	o
9	o	o	o
10	x	o	x
11	o	o	o
12	x	o	x
13	x	o	x
14	o	o	o
15	x	o	x
16	x	o	x
17	o	o	o
18	x	o	x
19	o	o	o
20	x	o	x
21	x	o	x
22	x	o	x
23	x	o	x
24	o	o	o
25	x	o	x
26	o	o	o
27	x	o	x
28	o	o	o
29	x	o	x
30	o	o	o

References

Arrigo, K.R., van Dijken, G., Pabi, S., 2008. Impact of a shrinking Arctic ice cover on marine primary production. Geophys. Res. Lett. 35, L19603. doi:10.1029/2008GL035028.

Bligh, E.G., Dyer, W.J., 1959. A rapid method of total lipid extraction and purification, Canadian. J. Biochem. Physiol. 37, 911-917.

Codispoti LA, Flagg CN, Swift JH (2009) Hydrographic conditions during the 2004 SBI process experiments. Deep-Sea Research II 56:1144-1163.

Dowgiallo, A., 1975 Chemical composition of an animal's body and its food. In: Grodzinski, W., Klekowski, R.Z., Duncan, A. (Eds.), Methods for Ecological Bioenergetics. IBP Handbook No. 24. Blackwell, London, pp. 160-199.

Dubois, M., Gilles, K.A., Hamilton, J.K., Rebers, P.A., Smith, F., 1956. Colorimetric method for determination of sugars and related substances. Anal. Chem. 28, 350-356.

Foy, R.J., 1996. Seasonal proximate composition and food source comparisons of Dolly Varden char in the Kugururok River, Alaska. Ph.D. Thesis, University of Alaska Fairbanks.

Lee, S.H., Whitledge, T.E., Kang, S.H., 2007. Recent carbon and nitrogen uptake rates of phytoplankton in Bering Strait and the Chukchi Sea. Cont. Shelf Res. 27, 2231-2249.

Lee, S.H., Kim, H.J., Whitledge, T.E., 2009. High incorporation of carbon into proteins by the phytoplankton of the Bering Strait and Chukchi Sea. Cont. Shelf Res. 29, 1689-1696.

Lee SH, Stockwell D, Whitledge TE (2010). Uptake rates of dissolved inorganic carbon and nitrogen by under-ice phytoplankton in the Canada Basin in summer 2005. Polar Biology.33:1027-1036

Lindqvist, K., Lignell, R., 1997. Intracellular partitioning of $^{14}CO_2$ in phytoplankton during a growth season in the northern Baltic. Mar. Ecol. Prog. Ser. 152, 41-50.

Lowry, O.H., Rosebrough, N.J., Farr, A.L., Randall, R.J., 1951. Protein measurement with the folin phenol reagent. J. Biol. Chem. 193, 265-275.

Marsh, J.B., Weinstein, W.J., 1966. Simple charring method for determination of lipids. J. Lipid Res. 7, 574-576.

Morris, M.J., Hopkins, T.L., 1983. Biochemical composition of crustacean zooplankton from the eastern Gulf of Mexico. J. Exp. Mar. Biol. Ecol. 69, 1–19.

Parrish, C.C., McKenizie, C.H., MacDonald, B.A., Hatfield, E.A., 1995. Seasonal studies of

seston lipids in relation to microplankton species composition and scallop growth in South Broad Cove, Newfoundland. Mar. Ecol. Prog. Ser. 129, 151-164.

Perovich DK, Richter-Menge JA (2009) Loss of sea ice in the Arctic. Annual Review of Marine Science 1:417-441

Scott, C.L., Kwasniewski, S., Falk-Petersen, S., Sargent, J.R., 2000. Lipids and life strategies of *Calanus finmarchicus, Calanus glacialis* and *Calanus hyperboreus* in late autumn, Kongsfjorden, Svalbard. Polar Biol. 23, 510–516.

Smith, R.E.H., Gosselin, M., Kattner, G., Legendre, L., Pesant, S., 1997a. Biosynthesis of macromolecular and lipid classes by phytoplankton in the Northeast Water Polynya. Mar. Ecol. Prog. Ser. 147, 231–242.

Tremblay, J.-É., Simpson, K., Martin, J., Miller, L., Gratton, Y., Barber, D., Price, N.M., 2008. Vertical stability and the annual dynamics of nutrients and chlorophyll fluorescence in the coastal, southeast Beaufort Sea. Journal of Geophysical Research 114, C07S90, doi:10.1029/2007JCoo4547, 2008.

Tynan, C.T., DeMaster, D.P., 1997. Observations and predictions of Arctic climatic change: potential effects on marine mammals. Arctic 50, 308-322.

Winberg, G.G., 1971b. Methods for the estimation of production of aquatic animals. (Translated by Duncan, A.) Academic Press, London.

4.4. Protozoan Ecology

Eun Jin Yang and Jin Ah Oh

Korea Polar Research Institute, Incheon 406-840, Korea (ejyang@kopri.re.kr and jaoh@kopri.re.kr)

4.4.1. Introduction

Heterotrophic protozoa are key components of pelagic food webs. They are important grazers of phytoplankton and act as a food source for consumers at higher trophic levels. These micro-grazers are highly abundant, ubiquitous in the world's oceans, grow rapidly and have unique feeding mechanisms that allow ingestion of wide spectrum of food particle sizes. This combination of attributes makes micrograzers essential elements in the functioning of pelagic ecosystems (Calbet and Landry, 2004; Calbet and Saiz, 2005; Saiz and Calbet, 2011). The importance of heterotrophic protists in pelagic ecosystems has become increasingly evident in the past two decades, and trophic interaction between heterotrophic protists and phytoplankton has been reported in various marine. However, there is no information on the relative importance of heterotrophic protists in the pelagic ecosystem of the Western Arctic Sea. The Arctic Ocean is currently undergoing rapid environmental change resulting from natural and anthropogenic drivers, which include accelerated warming (Steele et al., 2008; Zhang et al., 2010), decreased extent of sea ice cover (e.g., Comiso et al., 2008) and other physical changes. These changes will have a major impact on ecosystem functioning and biogeochemical cycling in the Arctic Ocean (e.g., Sakshaug and Slagstad, 1992; Walsh et al., 2004). Because of ongoing changes in the Arctic, there is an urgent imperative for better characterization and understanding of food web structures that are key elements of the arctic pelagic ecosystem. In this study area, we investigated the meso-scale variations and structure of heterotrophic protist communities and grazing rates on phytoplankton in the various environmental conditions such as open ocean, sea ice zone and melting ponds. During this cruise, we investigated protozoa abundance, biomass and grazing rate in total 20 stations (Table 4.5).

4.4.2. Materials and methods

1) Abundance and community structure of heterotrohic protists

We measured abundance and community structure of heterotrophic protists in the water column of the Chukchi Sea and Beaufort Sea and at the melting ponds with different salinity level. In the water column, water samples were collected using a Sea-bird Electronics CTD system equipped with specific sensors such as photosynthetically active radiation (PAR) sensor, fluorometer, transmissometer and dissolved oxygen meter. In the melting pond, water samples were collected from 20 cm depth of the surface of the pond using silicon tubing connected to peristaltic pump.

For ciliates and sarcodina, 500 ml water from the vertical profiles was preserved with 1% acid Lugol's iodine solution these samples were then stored in darkness. For heterotrophic nanoflagellates and heterotrophic dinoflagellates smaller than 20 µm, 500 ml of water was preserved with glutaraldehyde (0.5% final concentration) and stored at 4° C.

2) Grazing experiments

Grazing rates of heterotrophic protists were determined by the dilution method (Landry and Hassett 1982). Water for grazing experiments was collected from 3 depth (surface, SCM, 1% light depth) of each station, and gently filtered through a 200-µm mesh. At each station, 30L seawater were collected in a Niskin bottle and transferred to a polycarbonate carboy. Part of this water was filtered through the 0.22-µm filtration system. Dilution series were set up in ten 1.3 L PC bottles. Ten bottles were used to establish a nutrient-enriched dilution series consisting of replicate bottles with 11, 28, 50, 75, and 100% natural seawater. The bottles were incubated on deck for 24 – 48 h at ambient sea surface temperatures and screened to the ambient light level with neutral density screening. Subsamples were collected from replicate bottles at 0 and 24-48h to determine chlorophyll-a concentrations.

Table 4.5. Sampling locations of heterotrophic protists community structure and grazing rates at water column during the ARA05B 2014 cruise.

St.	Latitude/ Longitude	Depth (m)	Sampling depth (m)	Community	Grazing
1	65° 10.3986N 168° 41.4413W	49	60	o	o
2	66° 37.7942N 168° 41.2562W	40	30	o	o
3	67° 19.9996N 168° 49.9931W	49	40	o	
9	69° 09.9868N 168° 39.9516W	51	40	o	o
10	70° 29.9915N 168° 40.0115W	45	32	o	
11	71° 25.5044N 166° 41.2047W	45	40	o	o
12	72° 21.6002N 164° 41.2089W	47	40	o	
13	73° 18.7260N 162° 38.5907W	104	90	o	
14	74° 13.1862N 160° 42.4263W	550	100	o	o
15	75° 05.8659N 158° 49.4661W	842	100	o	
16	75° 09.4706N 154° 59.3517W	3843	100	o	o
17	75° 09.3692N 151° 16.4557W	3835	100	o	
19	77° 22.3892N 146° 08.5894W	3805	100	o	o
24	75° 50.8940N 161° 42.0300W	2110	100	o	
25	76° 23.1390N 154° 59.4938W	519	100	o	o
26	76° 18.5184N 167° 01.1498W	392	100	o	
27	75° 48.0591N 169° 00.7743W	290	100	o	o
28	75° 55.0886N 172° 23.4360W	1922	100	o	
29	75° 58.7097N 176° 11.9863W	1960	100	o	o
30	76° 01.6036N 179° 33.8391E	1167	100	o	

Table 4.6. Sampling station of heterotrophic protists community structure and grazing rates at melt ponds during the ARA05B 2014 cruise.

Station	Salinity (psu)	Community	Grazing
MP1	0.2	o	o
MP3	0.5	o	o
MP4	0.4	o	
MP5	24.8	o	o
MP6	22.7	o	
MP7	26.3	o	o
MP8	23.2	o	
MP9	26	o	o
MP11	26.8	o	
MP12	26.7	o	
MP13	0.9	o	o
MP14	25.7	o	
MP15	22.2	o	o
MP16	1.5	o	
MP17	22.2	o	
MP18	21.4	o	o
MP19	19.9	o	o
MP20	15.2	o	
MP21	17.6	o	
MP22	0	o	o

References

Calbet, A., Landry, M.R., 2004. Phytoplankton growth, microzooplankton grazing, and carbon cycling in marine systems. Limnol. Oceanogr. 40, 51-57.

Calbet, A., Saiz, E., 2005. The ciliate–copepod link in marine ecosystems. Aquat. Microb. Ecol. 38, 157-167.

Comiso, J.C., Parkinson, C.L., Gersten, R., Stock, L., 2008. Accelerated decline in the Arctic sea ice cover. Geophys. Res. Lett. 35, L01703. doi: 10.1029/2007GL031972

Landry, M.R., Hassett, R.P., 1982. Estimating the grazing impact of marine micro-zooplankton. Mar. Bio. 67, 283-288.

Saiz, E., Calbet, A., 2011. Copepod feeding in the ocean: scaling patterns, composition of their diet and the bias of estimates due to microzooplankton grazing during incubation. Hydrobiologia. 666, 181-196.

Sakshaug, E., Slagstad, D., 1992. Sea ice and wind: Effects on primary productivity in the Barents Sea. Atmos. Ocean, 30, 579-591.

Steele, M., Ermold, W., Zhang, J., 2008. Arctic Ocean surface warming trends over the past 100 years. Geophys. Res. Lett., 35, L02614, doi:10.1029/2007GL031651.

Walsh, J. J., Dieterle, D.A., Maslowski, W., Whitledge, T.E., 2004. Decadal shifts in biophysical forcing of Arctic marine food webs: Numerical consequences. J. Geophys. Res., 109, C05031, doi:10.1029/ 2003JC001945.

Zhang, J., Spitz, Y. H., Steele, M., Ashjian, C, Campbell, R., Berline, R., Matrai, P., 2010. Modeling the impact of declining sea ice on the Arctic marine planktonic ecosystem, J. Geophys. Res., 115, C10015, doi:10.1029/2009JC005387

4.5. Zooplankton Ecology

Mesozooplankton distribution patterns and metabolism of major copepods

Doo Byoul Lee

Korea Polar Research Institute, Incheon 406-840, Korea (copepod@kopri.re.kr)

4.5.1. Introduction

Copepods and euphausiids constitute >70% of the total metazooplankton biomass in Arctic waters, where they play a major role in energy flow and biogeochemical cycles. Some of the ingested organic carbon of zooplankton is used for metabolic activities, so quantifying this carbon is of prime importance to better understand energy transfer and elemental cycling via zooplankton in Arctic ecosystems.

Oxygen consumption rates reflect the metabolic demand of copepods. Most of the previous metabolic studies have employed the Winkler titration method, polarographic oxygen electrodes (Clark, 1956), or measurement of the electron transfer system (ETS) (Packard, 1971). Recently, oxygen microsensor technology has been used for measuring a range of metabolic activities such as pericellular oxygen consumption for human cells, respiration of the rotifer, hydromedusae, benthic foraminifera, and midges (Diptera; Chironomidae), oxygen consumption rates of copepod eggs and copepods fecal pellets (Petterson et al., 2005; Jensen et al., 2006; Marshalonis and Pinckney, 2007; Nielsen et al., 2007; Brodersen et al., 2008; Shek and Liu, 2010; Geslin et al., 2011). An oxygen microsensor can be placed inside each experimental bottle to monitor the decline in oxygen concentrations during the course of experiments.

The Chukchi Sea is one of the major gateways into the Arctic where large quantities of Pacific heat, nutrients, phytoplankton and mesozooplankton enter the region through the shallow Bering Strait in a complicated mixture of water masses. Mesozooplankton abundance and biomass generally have been considered to be low in the Arctic Ocean. Nevertheless, mesozooplankton is numerically important element and plays a major role in the food webs. Mesozooplankton grazing, especially copepods, is a key factor controlling composition and dynamics of phytoplankton communities. In the Arctic Ocean, *Calanus* spp.

are regarded as biological indicators of Arctic (*Calanus glacialis* and *C. hyperboreus*) and Atlantic (*C. finmarchicus*) water masses, respectively. They are the most important biomass species and the prime herbivores in these waters. Over the past several decades, atmospheric warming has increased the Arctic Ocean temperature and resulted in decreased extent and thickness of se ice. The removal of seasonal and permanent sea ice can greatly influence a number of important ecological processes such as photochemical reactions, stratification-related nutrient supply, phytoplankton bloom patterns and mesozooplankton distribution. For predicting climate change impacts in the ecosystems by rapid sea ice melting, it is important to understand the dynamics of the mesozooplankton community.

The primary objectives were, 1) to understand the interactions between the environmental factors (i.e. seawater temperature, salinity and chlorophyll *a* concentration) and the mesozooplankton community 2) to examine oxygen consumption rate of the major copepods with different life cycle strategies using an oxygen microsensor.

4.5.2. Material and methods

Mesozooplankton samples were collected with a Bongo net (60 cm diameter, 330 and 500 µm mesh size). The net was towed vertically within the upper 200 m of the water column. Samples from 330 µm mesh were immediately fixed and preserved with buffered formaldehyde (pH 8, final concentration ca. 5%) for quantitative analyses. From the 500 µm mesh size samples, Undamaged healthy adult females of each copepod species were immediately sorted and transferred into 2.6-litre polycarbonate bottles where they were put to rest for about 3 h in 200-µm prescreened natural seawater at in situ temperatures. These live specimens for experimentation were then placed in 300-ml polycarbonate bottles filled with 0.45-µm filtered seawater at in situ temperatures and starved for 12 h. Each individual was placed in a 4 ml BOD-style glass micro respiration chamber filled with 0.45-µm filtered seawater at the natural seawater condition in a dark room.

Respiration rate was monitored with a Micro respiration system (Unisense A/S, Denmark), which allows continuous recording of dissolved oxygen (DO) concentration with a time interval between consecutive measurements of 10 s. Measurements of DO concentration were made using Clark-type oxygen microelectrodes (Revsbech, 1989) with a

500-μm diameter tip connected to a picoammeter. Microelectrodes were calibrated using a two-point procedure with 0% (bubbling with nitrogen) and 100% (bubbling with air) saturation DO concentrations as endpoints. The respiration chambers rested in a submerged rack in a temperature-controlled water bath. Both control and experimental chambers were equipped with glass-coated mini magnetic stirrers rotating at 500 rpm to prevent oxygen gradient development. Animals were protected from interference with the stirrers by acid-proof stainless steel mesh dividers (200-μm) resting on glass cylinders. Individual stirrer heads were located in the rack directly underneath the chambers and did not emit heat. Moreover, magnet rotation did not alter the animals' swimming or position in the chamber. Animals were allowed to settle down for 10 min following transfer into the chambers until the oxygen reading stabilized, after which the oxygen consumption rate was taken as the linear slope of the DO concentration plotted against time for the next several hours. The short incubation times minimized the problem of oxygen depletion at the end of the incubation. All experiments were run under identical conditions to exclude the effect of incubation temperature.

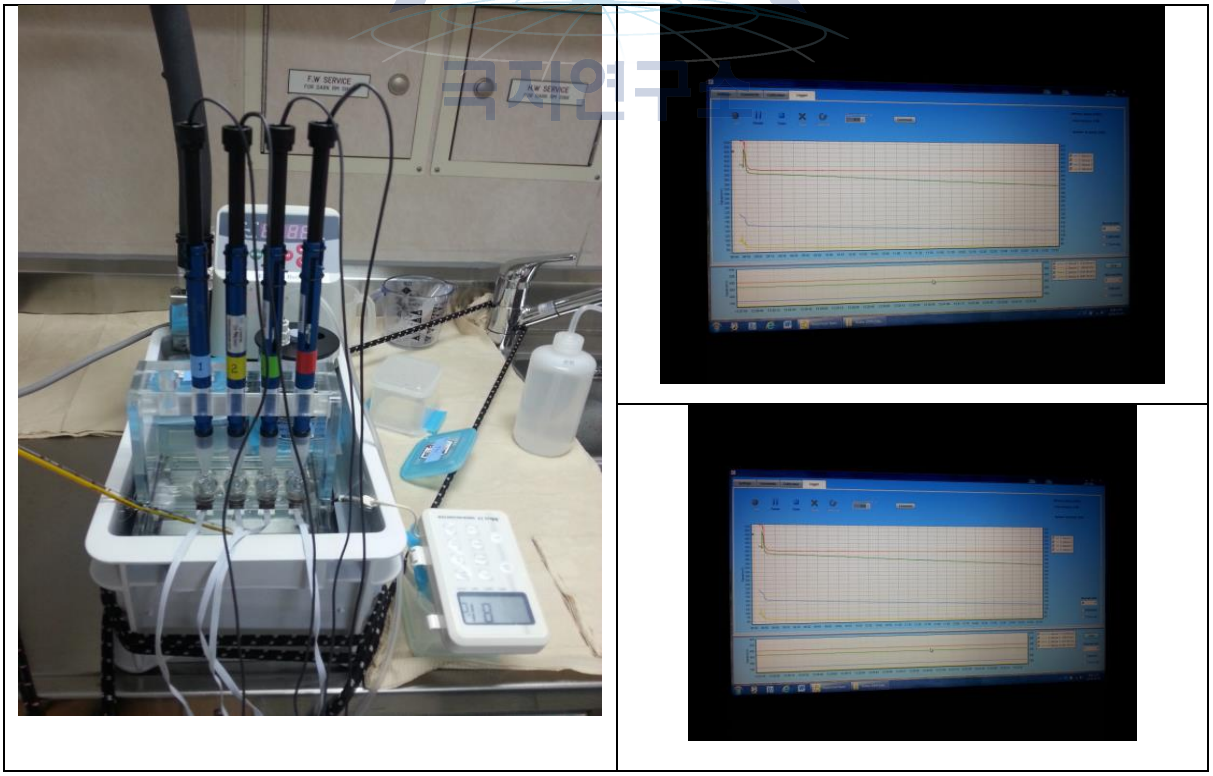

Fig. 4.6. Experimental setup for measurement of dissolved oxygen concentration using oxygen microsensor.

References

Brodersen, K. P., Pedersen, O., Walker, I. R., and Jensen, M. T., 2008. Respiration of midges (Diptera; Chironomidae) in British Columbian lakes: oxy-regulation, temperature and their role as palaeo-indicators. Freshwater Biology, 53, 593–602.

Clark, L. C., 1956. Monitor and control of blood and tissue oxygen tensions. Transactions-American Society for Artificial Internal Organs, 2, 41–48.

Geslin, E., Risgaard-Petersen, N., Lombard, F., Metzger, E., Langlet, D., and Jorissen, F., 2011. Oxygen respiration rates of benthic foraminifera as measured with oxygen microsensors. Journal of Experimental Marine Biology and Ecology, 396, 108–114.

Jensen, T. C., Anderson, T. R., Daufresne, M., and Hessen, D. O., 2006. Does excess carbon affect respiration of the rotifer Brachionus calyciflorus Pallas? Freshwater Biology, 51, 2320–2333.

Marshalonis, D. and Pinckney, J. L., 2007. Respiration rates of dominant hydromedusae in the North Inlet tidal estuary during winter and summer. Journal of Plankton Research, 29, 1031–1040.

Nielsen, P., Larsen, L. H., Ramløv, H., and Hansen, B. W., 2007. Respiration rates of subitaneous eggs from a marine calanoid copepod: monitored by nanorespirometry. Journal of Comparative Physiology B, 177, 287–296.

Packard, T. T., 1971. The measurement of respiratory electron transport activity in marine phytoplankton. Journal of Marine Research, 29, 235–244.

Chapter 5. Biodiversity Study

Yoon Yong Yang and Min Young Bang

Korea Polar Research Institute, Incheon 406-840, Korea (tazmenia@kopri.re.kr; alsdud0623@kopri.re.kr)

5.1. Introduction

Microbes (e.g. bacteria and viruses) are ubiquitous in marine ecosystems extending from the sea surface microlayer to the deep abyss. These organisms are at the bottom of the marine food web and play vital roles in global biogeochemical cycles. Heterotrophic bacteria are known to remineralize nutrients that support microbial production and transform dissolved organic carbon (DOC) into bacterial biomass supporting bacterial grazers (Azam 1998). Viruses are the most abundant entities in marine environments and significantly influence the production of DOC and the recycling of nutrients *via* viral lysis of host organisms (Fuhrman 1999).

Bacterial community structure is susceptible to physical environmental conditions (e.g. temperature and salinity). Simultaneously, bacterial community structure can be regulated by bottom-up and top-down mechanisms; the former includes the variables of chlorophyll *a*, nutrients and organic matters, whereas the latter includes viral lysis and grazing by protists. Advances in massively parallel sequencing technologies (e.g. pyrosequencing; Margulies et al. 2005) for the 16S rRNA gene, a molecular marker for phylogenetic analyses, have allowed us to gain deeper insight into bacterial communities and their relationships with physiochemical and/or biological variables.

In the Bering Sea, Chukchi Sea, Beaufort Sea & East Siberian Sea, these water masses can be distinguished by its unique properties of temperature and salinity (Ha et al. 2011), suggesting that spatial distribution of microbes and bacterial community structure might be reflected by these different ecological regimes. The objectives of the present study are to investigate the distribution of bacteria and viruses, and to examine bacterial community structure in the 4 kind of Seas.

5.2. Materials and methods

Seawater sampling for microbiological study was made at 20 stations during the icebreaker R/V Araon expedition (ARA05B; Aug 1 to Aug 20 in 2014; 65.1-77.2^{o}N, 179^{o}E-146^{o}W) in the Bering/Chukchi/Beaufort/East Siberian Seas. Samples were collected from 3-6 depths (surface to 3830 m) with 10 l Niskin bottles mounted on a CTD rosette.

For measurements of viral (VA) and bacterial abundance (BA), seawater samples (2 ml) were fixed with 0.02 µm filtered formalin (final conc. of 2%), and were stored at -80^{o}C.

To isolations of bacterial strains, seawater samples(1ml) were added with 0.2um autoclaved Glycerol(final conc. of 2%), and were stored at -80^{o}C

Seawaters (4 L) for bacterial community analysis were pre-filtered through 3.0 µm pore-sized Nuclepore filters (Whatman) and collected onto 0.2 µm pore-sized Nuclepore filters (Whatman). Filters were immediately transferred to cryovial tubes containing 1 ml RNAlater (Ambion) to avoid decomposition of nucleic acids, and stored at -80^{o}C. In a land-based laboratory, extraction of nucleic acids and pyrosequencing of the 16S RNA gene will be made as previously described by Bowman et al. (2012).

Seawaters (4 L) for viruses community were added 0.01% FeCl3 solution(0.483g FeCl3 up to 10ml diluted water) in the 0.2 µm filtered seawater and obtained from 0.8 µm pore-sized Nuclepore filters (Whatman). Filters were moved to 50ml conical tubes, and stored at -80^{o}C

5.3. Expected result

Preliminary results of bacterial community structure were not available on aboard since further analyses need to be made in a land-based laboratory. However, it is expected that bacterial community structure in the study area may show spatial variability in horizontal and vertical distributions based on the preliminary observations of hydrographic properties and spatial heterogeneity in microbial abundances.

5.4. Summary and conclusions

Bacteria and viruses are at the bottom of the marine food web and play important roles in biogeochemical cycles of organic matters and nutrients. To understand the characteristics of microbial ecology in Arctic subzero waters, distributions of bacteria and

viruses were investigated along with bacterial community structure in the Bering/Chukchi/ Beaufort/East Siberian Seas during summer 2014.

References

Azam, F. (1998) Microbial control of oceanic carbon flux: the plot thickens, Science 280, 694-696

Fuhrman, J. A. (1999) Marine viruses and their biogeochemical and ecological effects, Nature, 399, 541-548

Margulies, M., Egholm, M., Altman, W. E., Attiya, S., Bader, J. S., Bemben, L. A., Berka, J. et al. (2005) Genome sequencing in microfabricated high-density picolitre reactors. Nature, 437, 376-380

Ha, H. K., Shimada, K., Kim, T. W., Lee, H. J., Yoshizawa, E., and Kawashima, S. (2011) Chapter 1. Hydrographic survey, KOPRI Cruise Report

Hwang, C. Y., and Cho, B. C. (2008) Effects of storage on the estimates of virus-mediated bacterial mortality based on observation of preserved seawater samples with TEM. Aquatic Microbial Ecology, 52, 263-271

Bowman, J. S., Rasmussen, S., Blom, N., Deming, J. W., Rysgaard, S., and Sicheritz-Ponten, T. (2012) Microbial community structure of Arctic multiyear sea ice and surface seawater by 454 sequencing of the 16S RNA gene, The ISME Journal, 6, 11-20

Chapter 6. Ocean Optics

6.1. Ocean Optics

Chang-Uk Hyun and Hong Lyun Park

[1]*Korea Polar Research Institute, Incheon 406-840, Korea (cuhyun@kopri.re.kr, parkhonglyun@kopri.re.kr)*

6.1.1. Introduction

Optical properties are important factors reflecting the physical processes related to the solar energy absorption and distribution in ocean and sea ice. The data of optical properties can be used to analyze the influence from biomasses, including phytoplankton and algae within the light field. Also, the light absorption and scattering influence the heat transportation and dispersion in the ocean. On the other hand, the optical data, together with the analysis for the inherent optical property of particles in the water, can be used for calibration and validation of visible remote sensing data.

In this cruise, we tried to get bio-optical relationships to improve ocean color data quality by observing inherent optical properties (IOPs) of water such as absorptions by phytoplankton, suspended sediment (SS), and colored dissolved organic matters (CDOM), and apparent optical properties (AOPs) of water such as downward irradiances (E_d) and upwelling radiance (L_u) over a spectrum range of 350 ~ 800 nm wavelength.

Our major goal in this study was to collect bio-optical data in conjunction with measurements of CDOM, phytoplankton and detrital absorption in support of NASA's efforts to develop robust empirical and semi-analytic algorithms for ocean color products in high latitude regions. This effort is a part of longer strategic objective of understanding the impacts of changing climate on biological oceanographic processes in the Arctic Ocean using ocean color satellite data.

For this purpose, we prepared the instruments for apparent optical properties, inherent properties, and reflectivity to implement the cruise. Our observations include the optical profiles in water and in situ measurement on sea ice. In this chapter, we will introduce our

instrumentations and observations, and the potential results.

We focused our observations and researches on the areas of the Bering, Chukchi, Beaufort and east Siberian seas, which were less explored before. The optical properties of the ocean and sea ice in these areas are linked with the water structure that might be related to the Arctic surface water, Pacific water, shelf water, and the rivers' waters. The optical properties might describe the details of the waters from variety of spectral data.

The optical observations were performed at about 30 stations as shown in Fig. 6.1. The specification of the observations at stations is listed in Table 6.1.

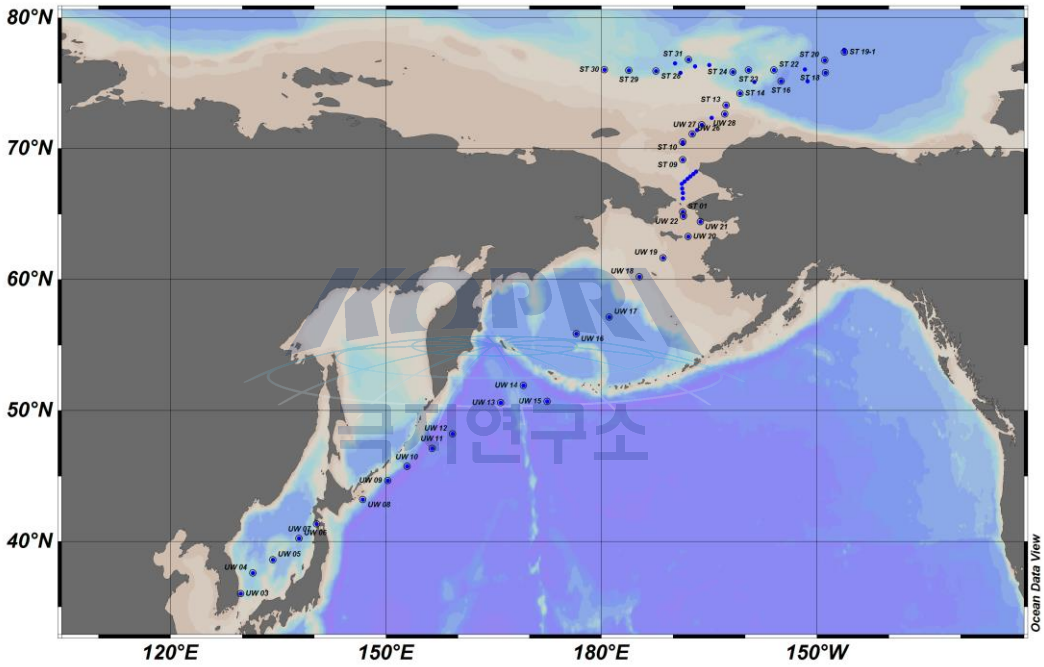

Fig. 6.2 A station map for optical observation (ST: station, UW: underway water sampling point)

Table 6.1 Specifications of optical observation stations

Station	Time* (UTC)	Latitude (degree)	Longitude (degree)	HPRO	Underway water sampling	CTD	BOP
Underway 03	07-19 10:30	36°01.28’	129°46.37’		✓		
Underway 04	07-19 23:20	37°35.99’	131°28.84’		✓		
Underway 05	07-20 10:30	38°37.05’	134°14.52’		✓		
Underway 06	07-21 01:05	40°14.69’	137°53.56’		✓		
Underway 07	07-21 10:30	41°20.67’	140°20.47’		✓		
Underway 08	07-22 10:50	43°12.66’	146°46.88’		✓		
Underway 09	07-23 00:30	44°39.01'	150°15.36’		✓		
Underway 10	07-23 11:30	45°43.81’	152°55.46’		✓		
Underway 11	07-23 23:30	47°06.80’	156°24.92’		✓		
Underway 12	07-24 10:45	48°12.68’	159°17.18’		✓		
Underway 13	07-25 10:40	50°35.41’	165°58.35’		✓		
Underway 14	07-25 22:10	51°54.57’	169°06.87’		✓		
Underway 15	07-26 10:25	50°41.41’	172°26.52’		✓		
Underway 16	07-27 03:00	55°52.69’	176°28.73’		✓		
Underway 17	07-27 11:30	57°09.08’	-178°55.56’		✓		
Underway 18	07-28 10:30	60°13.55’	-174°44.80’		✓		
Underway 19	07-28 22:30	61°39.70’	-171°25.82’		✓		
Underway 20	07-29 10:30	63°16.83’	-167°55.84’		✓		
Underway 21	07-31 22:30	64°25.16’	-166°15.04’		✓		
Underway 22	08-01 04:30	64°51.05’	-168°34.14’		✓		
Station 01	08-01 09:38	65°10.40’	-168°41.44’			✓	
Underway 23	08-01 16:30	66°13.26’	-168°41.14’		✓		
Station 02	08-01 17:56	66°37.79’	-168°41.25’	✓		✓	
Underway 24	08-01 22:30	66°57.95’	-168°45.54’		✓		
Station 03	08-01 23:53	67°20.01’	-168°50.01’	✓		✓	
Station 04	08-02 02:54	67°31.00’	-168°26.00’			✓	
Station 05	08-02 04:44	67°42.01’	-168°02.01’			✓	
Station 06	08-02 07:36	67°52.99’	-167°38.03’			✓	
Station 07	08-02 10:07	68°04.00’	-167°14.00’			✓	
Station 08	08-02 12:20	68°14.99’	-166°50.13’	✓		✓	
Station 09	08-02 19:17	69°10.00’	-168°39.98’	✓		✓	
Underway 25	08-03 04:45	70°21.73’	-168°39.92’		✓		
Station 10	08-03 04:44	70°30.00’	-168°40.01’	✓		✓	

Station	Time* (UTC)	Latitude (degree)	Longitude (degree)	HPRO	Underway water sampling	CTD	BOP
Underway 26	08-03 10:30	71°07.16’	-167°21.17’		✓		
Station 11	08-03 11:40	71°25.80’	-166°40.60’			✓	
Underway 27	08-03 16:30	71°49.13’	-166°03.52’		✓		
Station 12	08-03 21:09	72°21.60’	-164°41.21’	✓		✓	
Underway 28	08-04 04:30	72°38.40’	-162°49.57’		✓		
Station 13	08-04 12:16	73°18.73’	-162°38.59’			✓	
Station 14	08-05 01:59	74°13.33’	-160°41.97’	✓		✓	
Station 15	08-05 16:25	75°05.85’	-158°44.46’			✓	✓
Station 16	08-06 08:13	75°09.48’	-154°59.33’			✓	✓
Station 17	08-07 01:00	75°09.32’	-151°17.41’	✓		✓	✓
Station 18	08-07 10:57	75°47.38’	-148°47.69’				
Station 19	08-09 19:01	77°33.55’	-146°11.90’			✓	
Station 19-1	08-13 16:58	77°22.53’	-146°10.40’			✓	
Station 20	08-14 23:32	76°45.67’	-148°54.31’			✓	✓
Station 21	08-15 13:26	76°04.17’	-151°41.96’			✓	✓
Station 22	08-16 03:04	76°00.07’	-155°59.83’	✓		✓	✓
Station 23	08-16 14:33	76°00.03’	-159°30.34’	✓		✓	
Station 24	08-16 23:54	75°50.86’	-161°43.06’	✓		✓	✓
Station 25	08-17 08:32	76°23.12’	-164°59.47’	✓		✓	
Station 26	08-17 12:47	76°17.92’	-167°00.02’	✓		✓	✓
Station 27	08-18 01:10	75°48.00’	-169°00.01’	✓		✓	✓
Station 28	08-18 12:46	75°55.23’	-172°23.58’			✓	✓
Station 29	08-19 02:00	75°58.42’	-176°11.64’	✓		✓	✓
Station 30	08-19 13:40	76°01.60’	-179°33.84’	✓		✓	✓
Station 31	08-20 03:10	76°48.04	-167°53.89			✓	✓
Station 32	08-23 06:00	76°31.40	-169°47.35	✓		✓	✓

* The time of each station indicates the starting time of CTD operation.

6.1.2. Materials and methods

6.1.2.1. Ocean optical observation: IOPs

We sampled about 120 waters at about 30 stations (with 3 ~ 5 depths of surface, subsurface chlorophyll peak, and bottom within euphotic depth) and intermediate sites between stations in underway route. To measure inherent optical properties (IOPs) of water, seawater volumes of 1,000 ~ 1,800 ml were filtered on 25 mm glass-fiber filters (Whatman GF/F). For absorption by CDOM, seawater volumes of 50 ml were filtered onto disposable syringe filter unit of Advantec (cellulose acetate, 0.45 μm).

Optical densities of total particulate matters were measured directly on the wet filters by methods of Truper and Yentch (1967) with a double-beam recording spectrophotometer (Cary100, Agilent Technologies) in a spectral range 350 ~ 800 nm (spectrum resolution was 1 nm). The filter was placed in front of diffusing windows adjacent to an end-on photomultiplier of large surface area. For a reference blank and baseline variations, an unused wetted filter was taken as were automatically corrected. After the measurement of optical density of total pigments, the spectral absorption by nonalgal material was measured separately with method of Kishino et al. (1985). The filter was placed in absolute methyl-alcohol in order to extract pigments.

Table 6.2 Observation information: IOPs

Station	Depth of underway water sampling	Depth of CTD water sampling	Water depth
Underway 03	0 m		-
Underway 04	0 m		-
Underway 05	0 m		-
Underway 06	0 m		-
Underway 07	0 m		-
Underway 08	0 m		-
Underway 09	0 m		-
Underway 10	0 m		-
Underway 11	0 m		-
Underway 12	0 m		-
Underway 13	0 m		-
Underway 14	0 m		-
Underway 15	0 m		-
Underway 16	0 m		-
Underway 17	0 m		-
Underway 18	0 m		-
Underway 19	0 m		-
Underway 20	0 m		-
Underway 21	0 m		-
Underway 22	0 m		-
Station 01		0, 6, 10, 20, 40 m	49 m
Underway 23	0 m		-
Station 02		0, 10, 20, 30 m	44 m
Underway 24	0 m		-
Station 03		0, 8, 20, 30 m	49 m
Station 04		0, 10, 22, 30 m	47 m
Station 05		0, 10, 20, 30 m	49 m
Station 06		0, 14, 25, 30 m	59 m
Station 07		0, 10, 20, 30 m	51 m
Station 08		0, 10, 20 m	35 m
Station 09		0, 12, 25 m	51 m
Underway 25	0 m		-
Station 10		0, 10, 18 m	40 m

Station	Depth of underway water sampling	Depth of CTD water sampling	Water depth
Underway 26	0 m		-
Station 11		0, 10, 20, 35 m	45 m
Underway 27	0 m		-
Station 12		0, 10, 20 28, 39 m	47 m
Underway 28	0 m		-
Station 13		0, 20, 38, 60 m	104 m
Station 14		0, 15, 40, 50 m	557 m
Station 15		0, 20, 40, 60 m	845 m
Station 16		0, 20, 40, 70 m	3,843 m
Station 17		0, 20, 40, 55 m	3,835 m
Station 18	-	-	3,822 m
Station 19		0, 40, 55, 70 m	3,805 m
Station 19-1		0, 25, 40, 57, 75 m	3,805 m
Station 20		0, 20, 40, 60, 70 m	3,820 m
Station 21		0, 20, 40, 70, 80 m	3,828 m
Station 22		0, 20, 40, 60 m	1,260 m
Station 23		0, 20, 40, 65, 80 m	1,510 m
Station 24		0, 20, 40 , 55, 70 m	2,110 m
Station 25		0, 20, 40, 58, 70 m	519 m
Station 26		0, 50, 70 m	392 m
Station 27		0, 48, 70 m	280 m
Station 28		0, 46, 70 m	1,922 m
Station 29		0, 40, 50 m	1,960 m
Station 30		0, 45, 55 m	1,167 m
Station 31		0, 40, 55, 64 m	193 m

6.1.2.2. Ocean optical observation: AOPs

For the measuring of apparent optical properties (AOPs) of water, we deployed hyper-spectroradiometer of Satlantic Inc. (HPRO II, Figure.6.2.), which is free-fall type (0.5 m fall per second) with a spectral range of 350 ~ 800 nm of downward irradiance (E_d) and upwelling radiance (L_u). For the reference as ambient irradiance variation, downward irradiance (E_s) was measured on deck, where was not a shaded place of Araon. This data will be able to be used for calibrations and validations of currently operating ocean color remote sensing data.

Fig. 6.2 Deploy of hyper-spectroradiometer (HPRO II)

Table 6.3 Observation information: HPRO

Station	Time (UTC)	Depth of HPRO profiling	Water depth
Station 02	08-01 18:32	43 m	44 m
Station 03	08-02 01:27	31 m	49 m
Station 08	08-02 13:33	10 m	35 m
Station 09	08-02 21:14	34 m	51 m
Station 10	08-03 06:02	22 m	40 m
Station 12	08-03 22:10	28 m	47 m
Station 14	08-04 23:50	63 m	557 m
Station 17	08-06 22:23	80 m	3,835 m
Station 22	08-16 04:34	52 m	1,260 m
Station 23	08-16 13:46	54 m	1,510 m
Station 24	08-16 22:44	67 m	2,110 m
Station 25	08-17 09:00	41 m	519 m

Station	Time (UTC)	Depth of HPRO profiling	Water depth
Station 26	08-17 14:52	58 m	392 m
Station 27	08-18 01:20	53 m	280 m
Station 29	08-19 02:29	59 m	1,960 m
Station 30	08-19 14:18	57 m	1,167 m
Station 32	08-23 06:00	66 m	2,210 m

6.1.2.3. Melt ponds observation: spectral reflectance

In the study area, spectral measurements were conducted for selected 22 melt ponds (Fig. 6.3 and Fig. 6.4). A potable spectrometer, JAZ spectrometer of Ocean Optics Inc., was used to measure spectral reflectance of melt pond constituents, e.g., ice, snow and water, with an optical fiber of 25° field of view (FOV). The spectral reflectance reflects sea ice albedo and decaying characteristics of the sea ice. The spectra were measured within the range of 340 ~ 1,030 nm wavelength with 2,048 channels of about 0.3 nm resolution, and 10 spectra were averaged to minimize inherent noise. A white reference panel was used to calibrate the reflectance before the measurements of melt ponds reflectances.

Fig. 6.3 The selected melt ponds in the study area

Fig. 6.4. An example of spectral observation of melt ponds

After detailed in-situ investigation, structural and material constituents of the melt ponds were carefully classified as Table 6.4. Spectral characteristics of materials were considered for the classification and the spectral measurements were conducted with based on the results of the classifications for each pond.

Table 6.4 Classification of melt pond constituents in a view of spectral characteristics

Type	Description	Class
Snow	Coarse grain snow	S-1
	Melting snow	S-2
	Thin snow on ice	S-3
Water	Deep water	W-1
	Shallow water on flat bottom	W-2
	Shallow water on irregular shaped ice	W-3
Ice	Clear thin ice	I-1
	Thin ice with bubbles	I-2
	Uneven thick ice with bubbles	I-3
	Floating ice on pond (wet surface, thin water layer)	I-4

6.1.3. Preliminary results (or expected results)

6.1.3.1. Ocean Optical observation: IOPs

The results from the IOPs will be able to show the bio-optical characteristics in water at each station and at each depth of the water sample (Fig. 6.5).

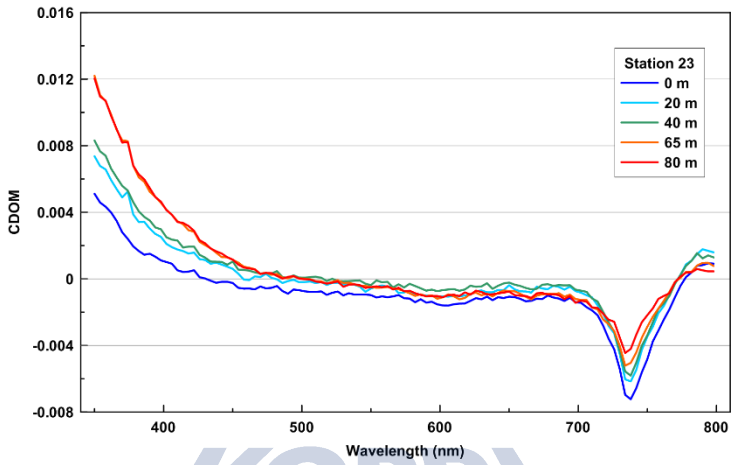

Fig. 6.5. An example of colored dissolved organic matter at the station 23

6.1.3.2. Ocean Optical observation: AOPs

The results from the AOPs, i.e. data from HPRO, will be able to reflect the continuous bio-optical characteristics of water surface and the bio-optical profiles at the operated station (Fig. 6.6).

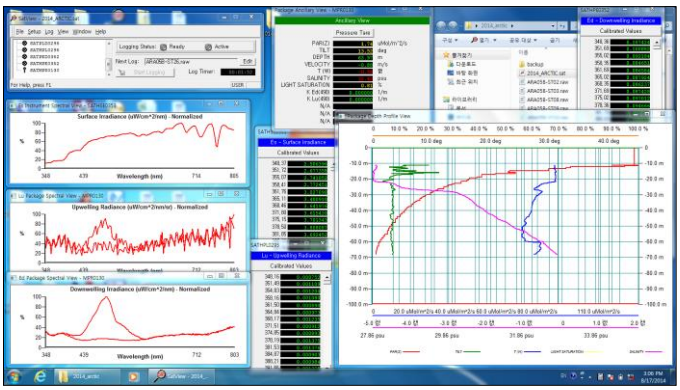

Fig. 6.6. An example of HPRO II data signal recorded at the station 26

6.1.3.3. Melt ponds optical observation: spectral reflectance

The melt ponds show rapid changes such as appearance and development. The results from the melt ponds optical observations will be able to be used to rapid differentiating the melt ponds from sea ice using satellite data (Fig. 6.7).

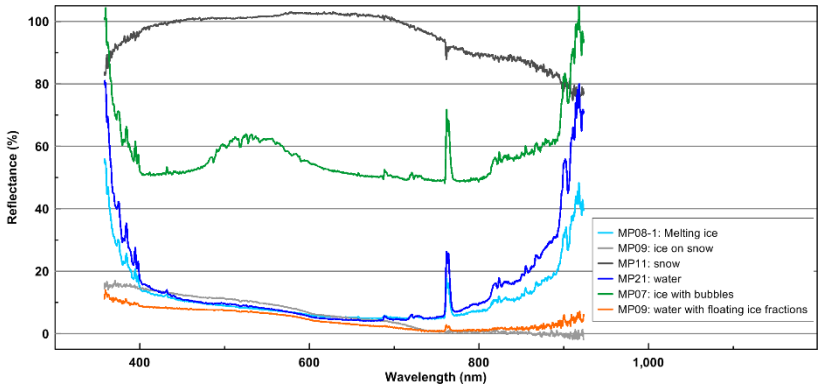

Fig. 6.7. Examples of spectral reflectances from melt pond observations

6.1.4. Summary and conclusions

During this Arctic cruise, the spectral characteristics of sea ice and the data for calibration/validation of satellite remote sensing ocean color data were collected. The IOPs reflected the bio-optical characteristics in water at the selected depths. The results from the AOPs such as data from HPRO showed continuous bio-optical characteristics of water surface and the bio-optical profiles at the operated stations. The optical observations of the melt ponds will be applied to rapid differentiating the melt ponds from sea ice using various satellite data. We are going to use these filed data for further detailed examination and correction of satellite data.

We would like to thank the Chief Scientist, Dr. Kang, and the other scientists, Dr. Eun Jin Yang, Dr. Tae Wan Kim, and Dr. Kyoung-Ho Cho for their great supports to our works. And we want to express our great appreciation to the Captain and crew of Araon for their devoted works for the deployment of the instruments.

References

Kishino, M., N. Okami, M. Takahashi, and S. Ichimura, 1986. Light utilization efficiency and quantum yield of phytoplankton in a thermally stratified sea. Limnol. Oceangr., 31, 557-566.

Truper, H. G. and C.S. Yentsch, 1967. Use of glass fiber filters for the rapid preparation of in vivo absorption spectra of photosynthetic bacteria. J. Bact.94, 1255-1256.

6.2. Bio-Optics

Eurico D'Sa[1] and Hyun-cheol Kim[2]

[1]Department of Oceanography and Coastal Sciences

Louisiana State University, Baton Rouge, LA 70803, USA (ejdsa@lsu.edu)

[2]Korea Polar Research Institute, Incheon 406-840, Korea (kimhc@kopri.re.kr)

6.2.1. Introduction

Changing climate conditions in the Arctic during the last two decades have been impacting its biogeochemical properties. Climate model projections indicate that these changes will continue thus potentially affecting the ecological conditions such as sea-ice ecosystems, biology, and higher trophic levels (Zhang et al. 2010). Field bio-optical and satellite ocean color data provides an important approach to monitor the changing biogeochemical conditions in the Arctic. The main objective of this joint study between researchers at KOPRI and Louisiana State University is to acquire a suite of in-situ bio-optical data that could be used to characterize the optical properties of dissolved and particulate matter and to assess satellite ocean color products for the Arctic Ocean.

6.2.2. Material and Methods

During the ARAON (ARA05B) Arctic research cruise data/samples were acquired using two methods: 1) the Bio-Optical Package (Optics) (Table 6.1), and 2) laboratory based analysis of water samples obtained from discrete depths in the water column during CTD casts. In addition, during the MIZ sea ice-camp, samples were also acquired from melting ponds, an ice core, and under ice water column in collaboration with Dr. Eunjin Yang. Underway UV light measurements were also made using a BIC radiometer.

6.2.2.1. Bio-optical profiling

A bio-optical package (Fig. 6.8) was used to acquire core optical measurements such as spectral absorption and scattering properties of the water column at the study sites. The

stations sampled with the Optical Profiler are shown in Table 6.1. The bio-optical profiling package comprised of the following instruments: i) **CTD**, ii) **ECO-Triplet** (WETLABS chlorophyll, CDOM (colored dissolved organic matter) fluorometer and phyco-erythrin sensors), iii) **ac-s** (WETLABS hyperspectral absorption-attenuation meter), iv) **Hyper OCI** (Satlantic hyperspectral downwelling irradiance sensor) , v) **Hyper OCR** (Satlantic hyperspectral upwelling radiance sensor, vi) **VSF-3** (WETLABS three-angle, three wavelength volume scattering function meter) and a **Fast Repetition Rate Fluorometer** (FRRF, JAPAN, for estimating quantum efficiencies (variable fluorescence) of ambient phytoplankton populations and rates of photosynthesis (Goes at al. 2014). The data from the FRRF (not shown) can be used to model the water column primary production. At some stations the LISST-100X profiler was also attached to the bio-optical profiler.

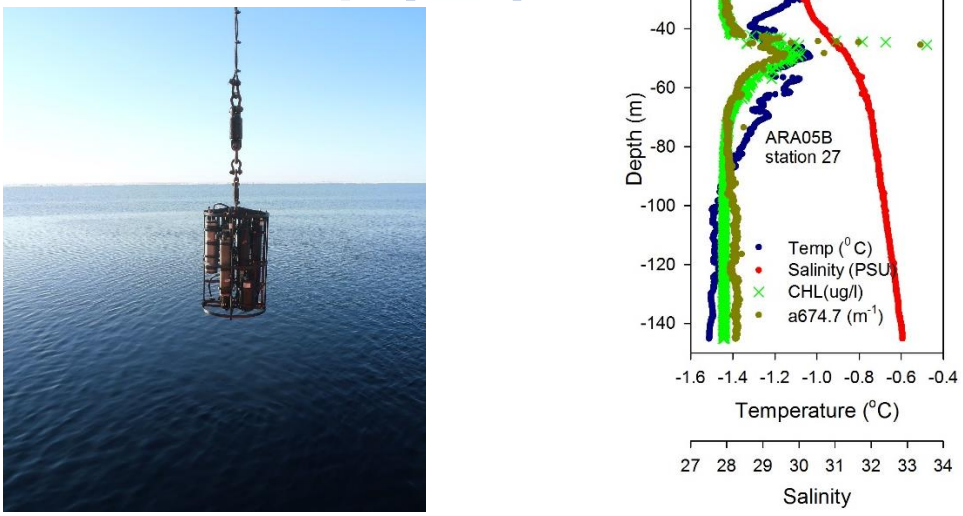

Fig. 6.8. Left - Deployment of the bio-optical profiler at a station during the ARA05B cruise. Right - An example profile at station 27 showing temperature, salinity, chlorophyll-a, and uncorrected absorption coefficient at 674 nm.

6.2.2.2 Discrete measurements

At each CTD station, water samples were collected from the Niskin bottles and the samples filtered for latter processing in the laboratory at LSU for CDOM absorption/fluorescence measurements. As different researchers use different types of filters for processing for CDOM absorption, measurements made during this cruise using two types of filters will be compared and studied for performance of the filters and the spectrophotometers from KOPRI and LSU.

Water samples collected from the Niskin bottles were also examined for particle size distribution and volume concentration on a Laser In Situ Scattering and Transmissometer (LISST-100X) instrument. In addition to depths shown in Table 6.2 obtained from shallow water CTD casts, water samples were also obtained at some stations from deep water CTD casts and will be processed for CDOM absorption and particle size distribution. Water samples collected at three depths at some of these same stations were also fixed with Lugol solution and will be examined in the laboratory for particle characteristics using a Flowcam Analyzer.

6.2.3. Expected results

Data collected during this cruise will be used to assess and validate satellite ocean color data for the Arctic Ocean. In addition, the various optical measurements of particulate and dissolved matter will help in better understanding of the dissolved and particulate matter characteristics in the western Arctic Ocean in the summer under extensive sea-ice conditions. Preliminary results from the bio-optical profiler are shown for a profile at station 27 (Fig. 6.8). In this example, the temperature, salinity, chlorophyll and particulate absorption at 674 nm (uncorrected) is shown. An example of particle size distribution measured by the LISST-100X is shown in Fig.6.9. In this example, the mean size of particles at the sampling location was about 40 μm with a low volume concentration of about 0.48 μl/l. CDOM and particle size distribution measurements obtained at the MIZ will be useful to study the influence of sea ice on the water column particle and dissolved properties.

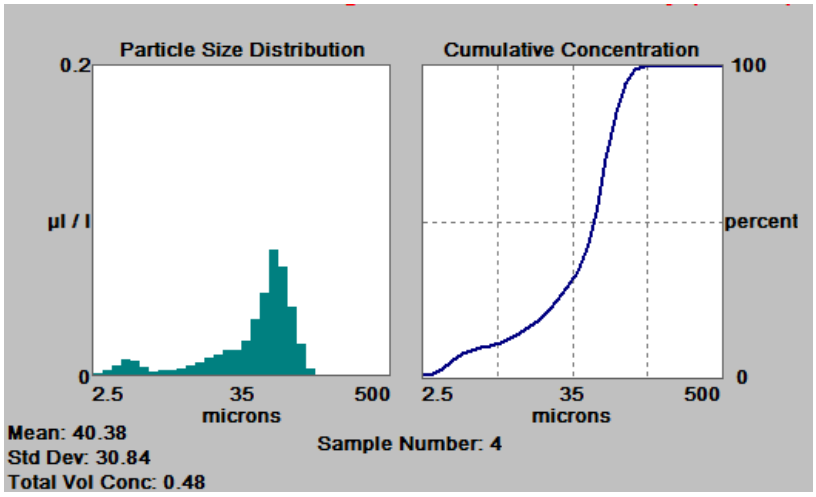

Fig. 6.9. An example showing the particle size distribution and cumulative concentrations obtained from a water sample collected during the ARA05B research cruise.

6.4. Summary and Conclusions

Preliminary results indicate that particle distribution in the water column appeared to be different at stations sampled before and after the MIZ ice-camp suggesting different influences in these waters. Bio-optical studies in conjunction with biological, chemical, and physical measurements will help to elucidate the influences on CDOM and particle characteristics in the study area. This study will also help compare CDOM measurements and ocean color algorithms developed for the eastern Bering Sea (Naik et al. 2013; D'Sa et al. 2014) with the western Arctic Ocean.

E. D'Sa would like to thank the Chief Scientist, Dr. Kang for the opportunity to participate in this cruise and Drs. Hyun-cheol Kim, Eun Jin Yang, Chang-Uk Hyun and Mr. Hong Lyun Park for help with the logistics and the field sampling during the cruise. We would also like to thank Drs. Tae Wan Kim, Kyoung-Ho Cho, Chang-Uk Hyun and the Captain and crew of the Araon for their support during the deployment of the optical profiling system.

References

D'Sa, E. J., J. I. Goes, H. Gomes, and C. Mouw. 2014. Absorption and fluorescence properties of chromophoric dissolved organic matter of the eastern Bering Sea in the summer with special reference to the influence of a Cold Pool. *Biogeosciences*, 11:3225-3244, doi:10.5194/bg-11-3225-2014.

Goes, J. I., H. R. Gomes, E. M. Haugen, K. T. McKee, E. J. D'Sa, A. M. Chekalyuk, D. K. Stoecker, P. J. Stabeno, S. Saitoh, and R. N. Sambrotto. 2014. Fluorescence, pigment and microscopic characterization of Bering Sea phytoplankton community structure and photosynthetic competency in the presence of a cold pool during summer. *Deep-Sea Research II* (online)

Naik, P., E. J. D'Sa, J. I. Goes, H. R. Gomes, and C. Mouw. 2013. Light absorption properties of southeastern Bering Sea waters: analysis, parameterization and implications for remote sensing. *Remote Sensing of Environment*, 134:120-134.

Zhang, J., Y. H. Spitz, M. Steele, C. Ashjian, R. Campbell, L. Berline, and P. Matrai. 2010. Modeling the impact of declining sea ice on the Arctic marine planktonic ecosystem. *Journal of Geophysical Research*, 115, C10015:1-24.

Chapter 7. Seaglider and SWIFT

7.1. Northwind Ridge Seaglider and SWIFT Float Deployments

Kyoung-Ho Cho[1], Hyoung Sul La[1], Eun Jin Yang[1], Mary Jane Perry[2], Jim Thomson[3] and Craig Lee[3]

[1]*Korea Polar Research Institute, Incheon 406-840, Korea (kcho@kopri.re.kr)*

[2]*Darling Marine Center, University of Maine, Walpole ME USA (perrymj@maine.edu)*

[3]*Applied Physics Laboratory, University of Washington, Seattle WA USA (craig@apl.washingotn.edu)*

7.1.1. Objectives

Seaglider sections and a SWIFT float drift will be used to investigate the impact of subsurface eddies and turbulence in driving the formation and evolution of the subsurface chlorophyll maximum (SCM) over the flank of the Northwind Ridge.

7.1.2. Introduction

Subsurface chlorophyll maximum areas are ubiquitous in the global oceans (Cullen, 1982) and can be represented by biomass maxima and hot spots of primary productivity attributing SCM maintenance to local growth (Anderson, 1969; Perry et al., 2008).

Low nutrient levels in the upper water column produce low near-surface phytoplankton biomass and optically clear waters, allowing deep light penetration and subsurface phytoplankton growth (Shulenberger and Reid, 1981).

In the western Arctic Ocean, waters are highly stratified and a large number of subsurface eddies populate the Canada Basin (Manley and Hunkins, 1985; Plueddemann and Krishfield, 2009). These eddies may produce subsurface chlorophyll maxima and thus have an influence on the Arctic ecosystem.

The Northwind Ridge is the region where water masses of the Pacific and Arctic Ocean undergo unique mixing patterns leading to change in the Arctic ecosystem (Grebmeier and Harvey, 2005).

Glider observations provide a unique view of the three-dimensional structure of the eddy (Martin et al. 2009; Todd et al., 2009). Measurement using autonomous gliders provides a continuous view of the phytoplankton bloom's evolution (Fennel et al., 2011; Alkire et al. 2012).

Two eddies were observed on the Northwind Ridge from IBRV Araon in July 2010, one of which exhibited elevated chlorophyll-a concentration. Because these observations constitute only a single snapshot, many questions remain, including whether these eddies are seasonal or year-round, how they evolve over their lifetimes and how they might modulate formation and evolution of subsurface chlorophyll maxima.

Long-endurance glider and floats may provide the temporal persistence and spatial distribution required to characterize eddies over the Northwind Ridge and their impact on the formation and evolution of subsurface chlorophyll maxima. The 2014 Araon cruise provides an opportunity to begin exploring this approach.

7.1.3. Instruments

1) Seaglider

Seagliders (Fig. 7.1 left) are small, reusable autonomous underwater vehicles designed to glide from the ocean surface to as deep as 1000 m and back while collecting profiles of temperature, salinity, dissolved oxygen concentration and optical properties. Given a typical 1:3 glide slope, the sawtooth dive/climb pattern is completed in about 8 hours and repeated roughly every 6 km. Gliders steer through the water by controlling attitude (pitch and roll) and can thus navigate between waypoints at typical speeds of 20 km/day to execute survey patterns. Seagliders are commanded remotely and report their measurements via Iridium satellite telephone at the conclusion of each dive. Seagliders also archive all data to onboard storage for delayed mode transmission or post-recovery interrogation. They use GPS navigation at the sea surface to dead reckon toward commanded targets, employing a continuous set correction to stem strong mean flows. Although Seagliders can navigate from a network of long-range (hundreds of kilometers) acoustic sources when working in ice-covered waters, no acoustics were deployed for this brief mission, and the glider navigates by dead reckoning while under ice. Seagliders use a combination of an on-board ice

climatology, near-surface temperature and an altimeter for ice-avoidance. Navigation and knowledge of vehicle buoyancy and pitch angle allows estimation of depth-averaged current and suitably energetic vertical velocity fluctuations. Seaglider's sensor suite includes Seabird Electronics temperature and conductivity sensors, Aanderra optode dissolved oxygen sensor and WET Labs BB2F (combination chlorophyll fluorometer, dual wavelength optical backscatter) and a multi-spectral downwelling irradiance sensor.

Hull	Anodized aluminum
Power	14 VDC, Alkaline or Lithium D cell packs
Weight	30 kg in air
Dimensions	1.25 m draft, 1.0 m mast, 0.35 m diameter
Shipping crate	1.65 m length, 0.5 m width, 0.5 m depth
Endurance	20 days (Alkaline), 60 days (Lithium)
Tracking (RF)	Garmin Astro DC40 collars (10 km range)
Tracking (Iridium)	Geoforce GT1 (global)
Telemetry	Iridium SBD
Processor	Sutron Xpert
Profiler	2 MHz Nortek Aquadopp HR
Met	Airmar PB200
IMU	Microstrain 3DM-GX3-35
CT	Aanderaa 4319
Camera	serial uCAM
Light	Yellow 1s flasher

Fig. 7.1. (left) Seaglider and (right) SWIFT.

2) Surface Wave Instrument Float with Tracking (SWIFT)

SWIFT floats (Fig. 7.1, right), designed and fabricated at the Applied Physics Laboratory, University of Washington, measure turbulence at the ocean surface in a wave-following reference frame. The turbulence measurements use up-looking pulse-coherent Doppler profilers. Secondary measurements include directional wave spectra, surface winds, salinity, water temperature, air temperature, and surface images. SWIFT15, used for this mission, also carried a Wetlabs BB2F (chlorophyll fluorometer and optical backscatter). The latest version (v3.1) includes onboard processing, Iridium SBD data telemetry, and month-long endurance. An alternative version uses a down-looking Doppler profiler for estimates of mixing up to 20 m depth. Drift deployments can last from a few hours up to one month. Drift speeds are approximately 5% of the surface winds, in the absence of currents. SWIFTs are tracked in real-time using a Garmin Astro radio collar (continuous updates with 10 km range) and an Iridium positioning beacon (updates once per hour with global coverage).

7.1.4. Planned Sampling Strategy

One Seaglider (SG177) and one SWIFT (SWIFT15) will be deployed along the eastern flank of the Northwind Ridge, between 74°~75°N and 155°~160°W, near the 2010 CTD section shown in Fig. 7.2. Deployments are planned early in the cruise (approximately 4 days after departing Nome). The glider will repeatedly occupy a section oriented across the ridge, while the SWIFT will drift with the prevailing winds and surface currents. Plans call for glider recovery at the end of the cruise, during the transit to Barrow. Depending on location, the SWIFT will either be recovered or, if too far away from Araon's transit track, left to sample through the freeze-up. This should provide roughly three weeks of sampling. Alternatively, the glider could be directed to transit west, to be recovered with the four MIZ gliders in late September by R/V Norseman. Timing and uncertainties associated with the long transit would force the glider to depart the Northwind Ridge earlier than the planned recovery date from Araon, making Norseman recovery a backup option. Collocated CTD casts from the Araon during glider and float deployment and recovery will provide data for calibrating oxygen and optical sensors carried aboard Seaglider and SWIFT.

7.1.5. Operations

Araon arrived at the Northwind Ridge early morning on 5 August to find ~60% ice coverage, punctuated with some large open water patches. We anticipated rapid melting over the coming weeks, and thus elected to deploy both glider and SWIFT into one of the larger regions of open water. SG177 and SWIFT15 were deployed at 75° 05.4' N, 158° 51.1' W. SWIFT15 was deployed first, at 03:39 L (11:39 Z), followed by SG177 at 03:45 L (11:45 Z). Araon maintained visual contact with SG177 until the glider's first dive, and located the glider during the next surface interval and conducted a calibration cast. Following this, the ship proceeded north.

SWIFT15 drifted northwest, experiencing one wave event on 16 August. This event also coincided with the failure of the SWIFT's Aquadopp velocity profiler.

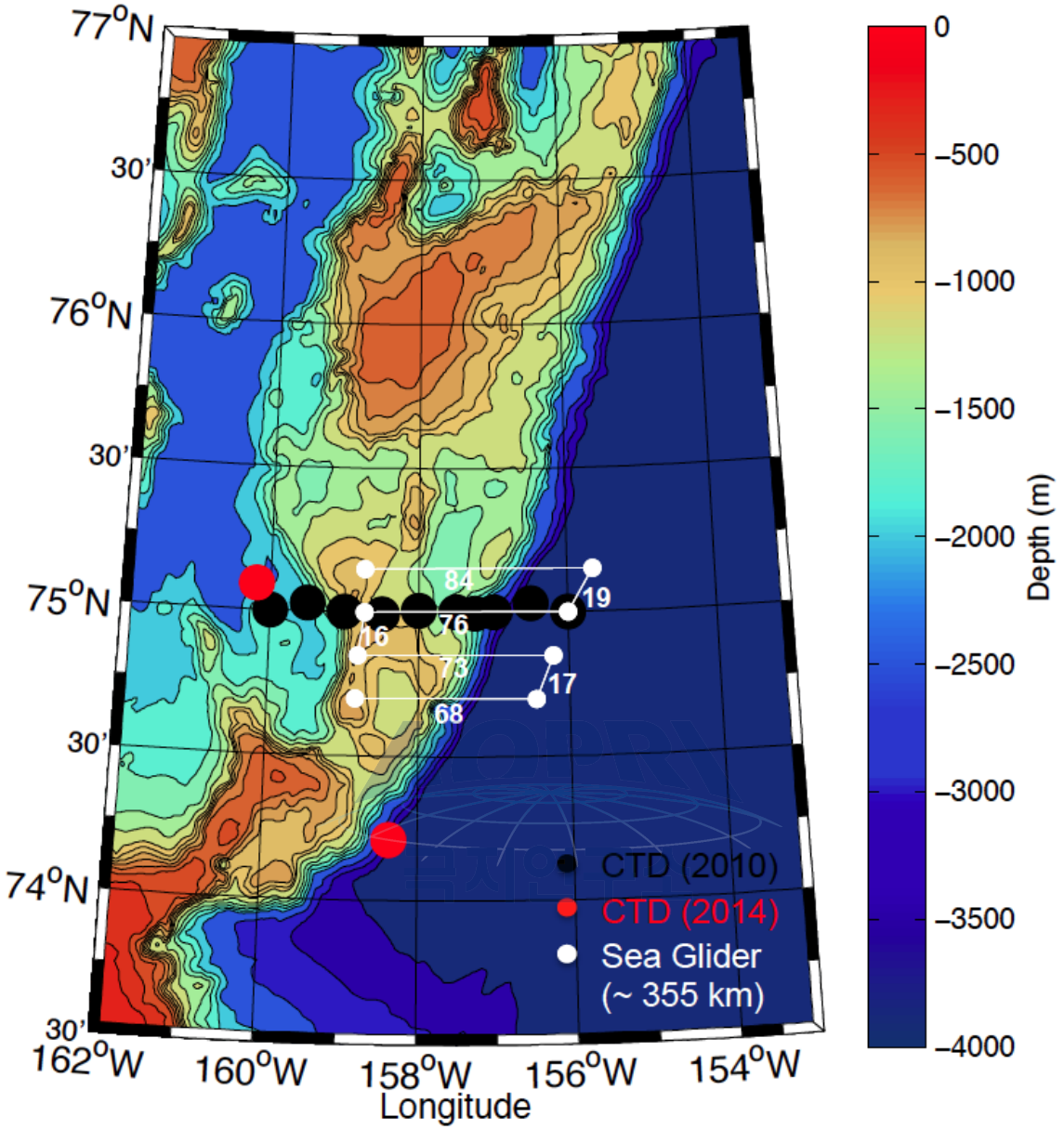

Fig.7.2. Tentative Seaglider sampling track (white), with 2010 (black) and planned 2014 (red) hydrographic stations. The 2014 Seaglider was assigned to repeatedly sample the zonal section along 75°N, corresponding to the line occupied in 2010.

SG177 ceased communicating on 6 August, after Araon departed the deployment site. The glider had been commanded to transit west along the sampling line. On 11 August, SG177 contacted mission control, reporting position at 74° 40' N, 160° 15' W, but no other data. The glider was held at the surface for diagnostics, but was eventually commanded to

continue diving. Although we were unable to identify the failure mode (and thus unable to implement a fix), it was deemed that the risks of an extended drift in >50% ice concentration were greater than those of continued operation. The glider was redirected to swim south, in hope of facilitating eventual recovery. Unfortunately, no further communications were received from SG177 after this event.

SWIFT15 was recovered at 20:33 Z (12:33 L) 17 August, at 75° 50.0’ N, 165° 38.7’ W. The SWIFT was in a small area of open water, canted at an angle and resting against a floe (Fig. 7.3). Araon nudged the surrounding floes aside to recover the float. On recovery, we note that the bottom (Aquadop) section has broken off at the standoffs (Fig. 7.4). One cable has parted (connectors show significant corrosion, especially on the SWIFT end), while the other is the only thing holding the two parts together.

Fig. 7.3. SWIFT15 prior to recovery. The SWIFT retained the distinctive cant when drifting free of the ice, likely produced the Aquadopp assembly, which was broken off and suspended by a single interconnect cable.

Fig. 7.4. SWIFT15 post recovery. The top and bottom halves have been separated by some severe impact, and are held together by only a thin interconnect cable. From the telemetered data and from the initial surface angle, it is certain that this damage was inflicted during the drift.

References

Alkire, M.B., E. D'Asaro. C.M. Lee, M.J. Perry, A. Gray, I. Cetinic, N. Briggs, E. Kallin, Jan Kaiser and A. Gonzalez-Posada (2012). Estimates of net community production and export using high-resolution, Lagrangian measurements of O2, NO3−, and POC through the evolution of a spring diatom bloom in the North Atlantic. *Deep Sea Research Part 1: Oceanographic Research Papers*, doi: 10.1016/j.dsr.2012.01.012.

Anderson, G. C. 1969. Subsurface chlorophyll maximum in the northeast Pacific Ocean. Limnol. Oceanogr. 14: 386–391.

Cullen, J. J. 1982. The deep chlorophyll maximum: Comparing vertical profiles of chlorophyll a. Can. J. Fish. Aquat. Sci. 39: 791–803.

Fennel, K., I. Cetinić, E. D'Asaro, C. Lee, and M. J. Perry (2011), Autonomous data describe North Atlantic spring bloom, *Eos Trans. AGU*, *92*(50), 465, doi:10.1029/2011EO500002.

Grebmeier, J. M., and H. R. Harvey (2005), The western Arctric Shelf-Basin Interactions (SBI) project: An overview, Deep Sea Res. Part II, 52, 3109– 3115, doi:10.1016/j.dsr2.2005.10.004.

Manley, T. O., and K. Hunkins (1985), Mesoscale eddies of the Arctic Ocean, J. Geophys. Res., 90, 4911 – 4930.

Martin , J. P., C. M. Lee, C. C. Eriksen, C. Ladd, and N. B. Kachel (2009), Glider observations of kinematics in a Gulf of Alaska eddy, *Journal of Geophysical Research*, *114*, C12021, doi:10.1029/2008JC005231.

Perry, M. J., B. S. Sackmann, C. C. Eriksen, and C. M. Lee. 2008. Seaglider observations of subsurface chlorophyll maxima off the Washington coast. *Limnology and Oceanography* **53(**5, part 2): 2169-2179.

Shulenberger, E., and J. L. Reid. 1981. The Pacific shallow oxygen maximum, deep chlorophyll maximum, and primary productivity, reconsidered. Deep-Sea Res. 28: 901–919.

7.2. Seaglider Optical Proxies

Mary Jane Perry[1] and Craig M Lee[2]

[1]*Darling Marine Center, University of Maine, Walpole ME USA (perrymj@maine.edu)*

[2]*Applied Physics Laboratory, University of Washington, Seattle WA USA (craig@apl.washingotn.edu)*

7.2.1. Introduction

The Arctic has experienced a dramatic decline in sea ice thickness, aerial extent, and age distribution (cf. references cited in Lee et al., 2012). Changing patterns in sea ice have significant implications for the planktonic food web and flow of carbon and nutrients in the Arctic, one of which is timing, vertical distribution and magnitude of phytoplankton blooms. Thinner ice and greater abundance of melt ponds allow for greater penetration of visible light through the ice, allowing planktonic photosynthetic organisms to flourish. Although light penetration is not a great as in ice-free open waters, penetration through thinner first year ice and associated melt water ponds is greater than through thicker, multi-year ice. Earlier and greater penetration of light through the thinner ice may change both the timing and vertical distribution of phytoplankton blooms. Relatively few comprehensive observations of phytoplankton in the water column under the ice exist, due to the logistical constraints of sampling under full ice cover and melting ice (cf. Arrigo et al., 2012). Autonomous underwater gliders, using acoustic navigation sources, provide a means to overcome these obstacles to sample phytoplankton under the ice. Application of carefully constructed biogeochemical proxies to measurements from calibrated optical sensors for chlorophyll fluorescence and optical backscatter allow determination of the spatial distributions of phytoplankton and particulate organic carbon.

In late July 2014, as part of the MIZ program, four Seagliders were deployed from a small research vessel operating out of Prudhoe Bay, Alaska, to follow the retreat of the marginal ice zone. The MIZ gliders navigated under ice from moored acoustic sound sources embedded in the MIZ autonomous observing array deployed earlier in spring. A fifth glider was deployed from the *Araon* on August 4. The sensor suite carried by the Seagliders include temperature, temperature microstructure, salinity, oxygen, chlorophyll fluorescence,

optical backscatter, and multi-spectral downwelling irradiance. Although the *IBRV Araon* did not directly encounter the four MIZ gliders, the use of cross calibrated optical sensors on the *Araon*'s CTD allow for the construction of optical proxies.

7.2.2. Materials and Methods

The protocol for calibrating glider sensors and building libraries of optical proxies are based on those developed during the 2008 North Atlantic bloom program, with modification for local conditions and logistics. The specific protocols for each sensor – backscatter and chlorophyll fluorescence – are described in sensor specific calibration reports available at the Biological and Chemical Oceanography Data Management Office website <http://osprey.bcodmo.org/dataset.cfm?id=13820&flag=view>. The samples collected from the *Araon* CTD profiles will be instrumental for constructing optical proxies.

All optical sensors were calibrated together at the factory before the experiment and will be recalibrated at the factory at the conclusion of the experiment. *In situ* calibration entails cross calibrating glider sensors against a reference sensor, i.e., that on the ship's CTD. The ideal protocol entails putting an individual glider into a shallow pre-calibration dive sequence, bringing the ship to the projected surfacing site, and navigating to within 100 m of the surfaced glider. A ship CTD profile is made simultaneously with a glider dive or as close as possible to the glider's last surfacing. Sensor data from the ship's CTD downcast is interpolated in density coordinate space to align with the glider profile. This was done for the four MIZ gliders; for the *Araon* glider, the ship profile was taken about 30 min at the last surfacing of the glider.

The optical proxy library is constructed by collecting water samples at a variety of depths and times, and regressing the optical vs. the biogeochemical measurement. Data were collected from over 40 CTD casts. The CTD is held at depth for 60 s before closing the Niskin bottle on the upcast; the average of the last 30 s of the CTD record is used for the regression of optical vs. biogeochemical measurement. Water samples for particulate organic carbon were collected from a Niskin bottle directly into a 1.1 L RBS-35 pre-washed polycarbonate bottle; a protective sampling bell was used to minimize airborne contaminants (Cetinic et al., 2012). Water was filtered through 25-mm Whatman GF/F

filters, precombusted at 400 degrees C for 4 hr, using a vented in-line filtration system at 200 mm Hg vacuum. Filters are frozen in precombusted aluminum foil sleeves until analysis (this autumn) on a Perkin Elmer 2400 CHN analyzer. Water samples for chlorophyll analysis were collected in 1.1 L bottles, filtered through Whatman GF/F filters, extracted in 90% acetone at -20 degree C for approximately 24 hr before fluorometric analysis in a Turner Designs Trilogy fluorometer using the non-acidification filter set (Welschmeyer, 1994). Additional chlorophyll samples collected by Dr. Yang will be included in the analysis.

Retrieval of the MIZ gliders is anticipated for late September. The phytoplankton and particulate organic carbon distribution data will be analyzed in collaboration with Dr. Yang.

7.2.3. Preliminary and Anticipated Results

Examples of the types of relationship between optical backscatter vs. particulate organic carbon and chlorophyll fluorescence vs. chlorophyll concentration are shown in Figs. 7.5 and 7.6 for samples collected during the subpolar North Atlantic spring bloom. Similar regressions are anticipated, although the slope of the regressions may be different (i.e., ifferent regional algorithms).

The four MIZ gliders are anticipated to yield a two-month data set of distributions of phytoplankton and carbon through from open water through the marginal ice zone to full ice cover.

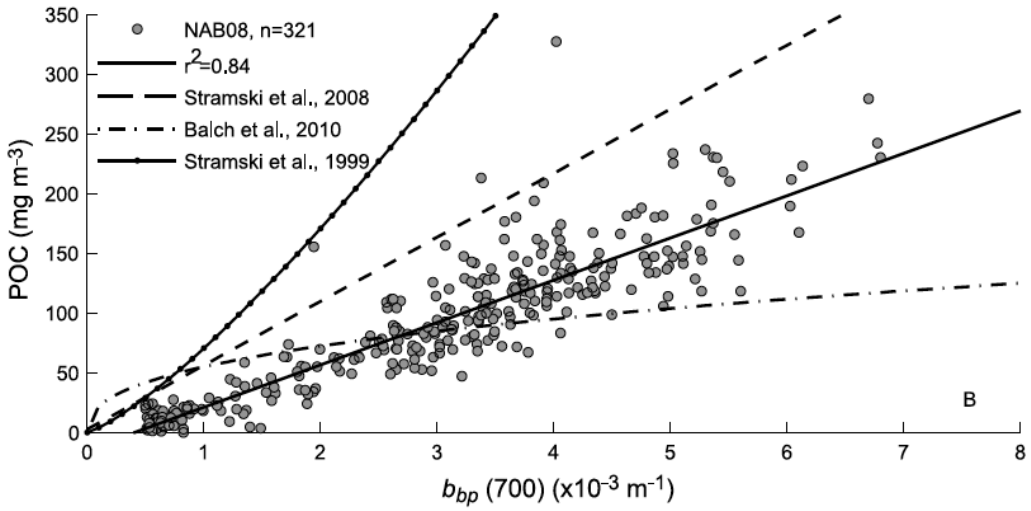

Fig. 7.5. Example of anticipated proxy relationship between particulate organic carbon and optical backscatter, from subpolar North Atlantic (solid line; Cetinic et al., 2012).

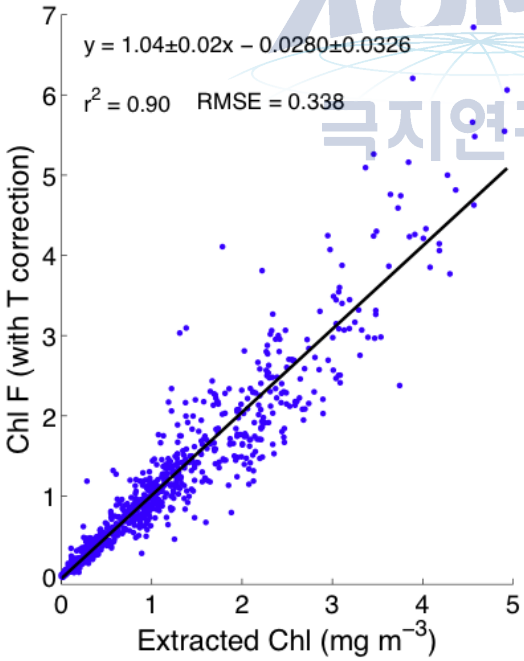

Fig. 7.6. Example of anticipated proxy relationship between extracted chlorophyll concentration and chlorophyll fluorescence, from subpolar North Atlantic (N. Briggs, unpublished).

7.2.4. Summary and Conclusions

The spatial and temporal patterns of distributions will be analyzed in concert with other available glider data – temperature, salinity, irradiance, and oxygen. These data are expected to provide a new comprehensive view of phytoplankton and organic carbon in the ice covered ocean.

We thank Dr. Sung-Ho Kang and Dr. Eun Jin Yang for their generosity and help in all phases of the project; we Dr. Tae Wan Kim, Dr. Kypung-Ho Cho, and Dr. Chan Yeong Gang for all their help in collecting CDT data.

References

Briggs, N. (University of Maine doctoral dissertation draft; dissertation completion anticipated November 2014). Using temporal variability in optical measurements to quantify phytoplankton production, particle size, and aggregation during the North Atlantic spring bloom from autonomous platforms.

Cetinić, I., M. J. Perry, N. Briggs, E. Kallin, E. A. D'Asaro, C. M. Lee. 2012. Particulate organic carbon and inherent optical properties during the 2008 North Atlantic Bloom Experiment. *Journal of Geophysical Research* 117, C06028, 18 pp. doi:10.1029/2011JC00777.

Lee, C.M., S. Cole, M. Doble, L. Freitag, P. Hwang, S. Jayne, M. Jeffries, R. Krishfield, T. Maksym, W. Maslowski, B. Owens, P. Posey, L. Rainville, B. Shaw, T. Stanton, J. Thomson, M.-L. Timmermans, J. Toole, P. Wadhams, J. Wilkinson, and Z. Zhang, 2012. Marginal Ice Zone (MIZ) Program: Science and Experiment Plan, Technical Report APL-UW 1201. Applied Physics Laboratory, University of Washington, Seattle, September 2012, 48 pages.

Welschmeyer, N.A. 1994. Fluorometric analysis of chlorophyll *a* in the presence of chlorophyll *b*and pheopigments. Limnology and Oceanography 39: 1985-1992.

Chapter 8. Ocean circulation

Ocean Circulation in the Chukchi Sea, Beaufort Sea, Northwind Ridge, Chukchi Plateau and East Siberian Sea

Byoung Woong An

Finnish Meteorological Institute (byoung.woong.an@fmi.fi)

Abstract

K-PORT /MIZ 2014 expedition was executed. CTD casts and XCTD were used to collect water columnproperties. The current measurements were also conducted by using the shipboard ADCP and moored ADCP in the Beaufort Sea and the Chukchi Sea for a duration of 25 days with IBRV Araon.Data from this cruise were analysed in order to identify the variation of the physical properties and its dynamic and thermodynamic processes, especially low frequency components of Arctic water mass variation which is essential for understanding the global climate change and sea ice extent. This report describes the basic information about raw data, processing scheme, and graphical results of the analysis.Out of (number) total CTD and (number) XCTD profiles were determined the Pacific Summer Water (PSW) and confirmed surface and subsurface mixing. Pacific Winter Water (PWW) was appeared around the branch of the East Siberian Sea and the Beaufort Sea. Within the Beaufort Gyre, upper halocline with minimum temperature between (value) and (value) deg C and salinity maximum between (value) and (value) psu, centered around (value) m depth were dominant.Lower halocline with (similar as the previous sentence) were dominant over the Bering Strait and the Chukchi Sea. Over the Beaufort Gyre (Northwind Ridge), upper and lower halocline were appeared, but were relatively smaller, shallower and less intense at (places).

Key words: buoyancy forcing, insolation, surface heating, heat transport, basal and lateral melting, wind and wave attenuation, eddy stress, ocean current, internal wave radiation, ice-ocean shear, ice divergence and convergence, mixed layer entrainment, deepening mixed layer, circulation and consumption of intermediate water (warmer and fresher) and thermocline water, diabatic flow, momentum balance

8.1. Introduction

The Arctic sea ice is affected mainly by atmospheric forcing and by Pacific water inflow beneath the sea ice andit responds sensitively during the transient period for melting and freezing period. In addition, Arctic sea ice has a fundamental role in the global climate and the Earth system. Therefore systematic understanding of the Arctic Ocean circulation and its interaction with sea ice are essential for predicting the near future climate in the Arctic.

The Arctic Ocean is a Mediterranean Sea and its thermohaline circulation is affected by inflow waters through straits, i.e. the Bering Strait is connected to the Pacific Ocean (cold fresh) and the Fram Strait to the Atlantic Ocean (warm salty).This area is also concerned acidification and freshwater ecosystem under warming climate conditions. Flow pathways vary significantly with topography and wind. The Bering Sea Water which consists nutrient rich Gulf of Anadyr Water ($32.8 < S < 33.2$) and nutrient low Bering Shelf Water ($32.5 < S < 32.8$), flows into the Arctic Ocean through the Bering Strait via Barrow Canyon, Central Channel and Herald Canyon. This water is divided and so some flows follow the shelf break and some flows move into Canada Basin. Alaskan Coastal Current (S ~32, Coachman et al., 1975) is presented summer to late autumn and loses water to central Chukchi Sea. One less dense water from Alaska Coastal Water (ACW) flows down to the Barrow Canyon and the other from Bering Strait Summer Water (BSSW) flows down to the Herald Canyon (Steele et al., 2004). Salinity of the upper temperature maximum determines which water mass is present, and thus tracing the circulation. Bering Strait Winter Water (BSWW) enters west of the Chukchi Cap (Coachman et al., 1975) and a less dense fraction enters east of the Chukchi Cap (McLaughlin et al., 2004). Fresh and cold Siberian Coastal Current appeared during some summer months may reach Bering Straits, or may exit into the central Chukchi. BSSW temperature is above freezing point and salinity is around 32.5 psu. The maximum temperature is around 75 m in the Canada basin. BSWW temperature is freezing point and salinity is 33.1 psu. The maximum temperature is at 150-200 m (Coachman and Barnes, 1961).

Pacific water penetrates deeper than nutrient maximum ($S > 33.1$) of the upper halocline due to excessive brine release in polynyas on the Chukchi shelf leading to $S > 34$ (Weingartner et al., 1998), $S > 36$ (Aagaard et al., 1985), high enough to sink into lower

halocline.

Temperature minimum is associated with an oxygen minimum and a nutrient maximum. Remineralisation of organic matter from the shelf bottom, convection of brine-enriched water to the shelf bottom, leaves the shelf, sinking into deep Canada basin forming the upper halocline. This halocline water is originated from Anadyr water. The lower halocline water is formed by brine-enriched, more saline and nutrient poor water.

Northwind ridge sea ice reduction can be explained by increase of PSW temperature and can be checked by the coherence between Arctic sea ice concentration margin and Pacific Summer Water distribution. Eastern Arctic is influenced by AO and highly correlated, but western Arctic isn't (Shimada et al., 2006).Melting and the northward retreat of the drift ice act as a buoyancy source and create a low salinity surface flow. The haline influence can be a counterpart of the thermal influence. In this way the hydrological cycle works to undo the density advantage provided by cold winter temperatures. At steady state, the excess fresh water must be mixed away just as fast as it is supplied by precipitation and runoff.

8.2. In situ observations

The main purpose of this cruise was to investigate the structure and processes in the water column and subsurface (sediment) around the North Bering Sea, Chukchi Sea, the North of East Siberian Sea and Beaufort Sea in rapid transition, and to understand the sea ice dynamics and sea ice ecosystem.

The primary observations in the Beaufort Sea and the Chukchi Sea research cruise in summer 2014 areshipboard CTD and XCTDfor the targeted specific processes and mooring observations are supplemented for long time series measurement. Theobjectives proposed by FMI are focused on:

1. internal mixing processes below strongly stratified upper 100-150m where dominated by advection
2. input of halocline water from the shelves
3. spreading and circulation of Atlantic water
4. changes in characteristics between different basins
5. heat and freshwater fluxes in the upper layer

6. heat and freshwater storages in different water masses (Atlantic and Pacific Waters) using ITP (influence of diffusion coefficients and Ekman transport)
7. find a minimum temperature (-1.6 C, freezing Canadian Basin, -1.5~-1.0 C in summer) in the upper layer (30~50m) and lower limit of minimum temperature depth
8. ocean interior (geostrophy), Sverdrup transport
9. warm (cold) eddy
10. source and sink of intermediate, deep, bottom water

Fig 1 (Chapter 2) shows the schematic view of the field observation and cruise track and sampling stations. The cruise track was mainly depending on the sea ice condition and also on the basis of the scientific interests of participated parties during the cruise.

.

The sampling at open water (Bering Strait, DBO line, Bering Sea, Beaufort Sea): wind, wave, surface fluxes and ocean profiles were measured. On the ice edge, a wave buoy and a glider were deployed. The goal of this mission was to quantify the evolution of a sea state in the presence of a variable fetch and the subsequent effect on the heat and momentum in the upper layer.

At the sea ice camp, current and water column profiles were measured to understand the transfer of heat and momentum between air, sea and ice, and to compare these processes with the wave driven processes that occur in open water.

One of the scientific interest is to catch eddies generated by barotropic and baroclinic interaction in the Arctic Ocean. To do this, identifying velocity shear between sea-ice and surface layer, and also determining branches of PWW and PSW interacted by bathymetry and Beaufort Gyre and Eastern Siberian Coastal Current.

Arctic Ocean has a typical water structure and it can be identified by the source of the water temperature and salinity, i.e. presence of melt ice water in surface layer, Pacific Summer Water (PSW) near 60 m depth, and Atlantic water up to (value) m depth and Bottom water.

CTD installed in Araon was used for profiling and identifying the vertical variation of temperature and salinity. In the spring time when the sea ice starts to melt, temperature in

the boundary layer (thermocline) can be lower. The stratification is thought to be closely associated with the release of brine as salt at the sea ice surface, left from the previous winters freeze-up, are exposed to light the following spring.

Characteristics of the Water column changes are affected by changes in currents, salinity, temperature and sea surface height. Warm layer and cold layer and its layer thickness vary with the season and year.

Northwind ridge and Chukchi plateau are the center of the arctic sea change (sea ice and biological aspect) and summer months sea ice extent anomalies are higher around Northwind ridge. Where there is sea ice, there are upper and lower haloclines. Pacific summer water and sea ice melt water are shown in upper halocline, and winter water is shown in lower halocline. Buoyancy driven pacific water flows eastward (Canadian sea), but wind driven flows westward during the summer. Atlantic water (300~500 m) never interacts with sea ice melt water and Pacific water, and flows beneath the Arctic water, so cannot penetrate and not interact with the Pacific water. Summer and winter pacific inflow are different in strength, and interaction with Beaufort Gyre is also different (depends on the strength of the Beaufort Gyre).Water masses move as a form of wavelike structure.

Generally ocean circulation follows the bathymetry, but sea ice does not follow the topography. Eddy is generated cape of Barrow and followed the bathymetry (moving along the Northwind ridge and Chukchi plateau). There is no eddy found at east side of Chukchi plateau (Eastern Siberian side).

8.3. Summary and Discussions

The Arctic Ocean strongly influences regional and global climate, and vice versa.The K-PORT/MIZ2014 program in the Arctic Ocean was executed process studies and the variability and sensitivity of Arctic Ocean dynamics interacted between atmosphere, ocean and sea ice. We have made remarkable progress in understanding the Arctic Ocean during the K-PORT program initiated since 2011.

CTD profiles and ADCP current data will show the spatial variation in water column and will indicate the interaction between ice-ocean dynamics and thermodynamics. This data also will show the place and magnitudes of mixing, mechanisms of water mass formation,

and modes of variability.

If a melt water layer is formed, it will reduce the heat transfer, increase the ice drifting very rapidly and keep the melt water layer thin, and therefore forcing contact with warm water continuously.

If a cold (warm) halocline is absent, warm Pacific Summer Water will be entrained into the winter mixed layer and also will be influenced the ice formation rate and heat flux to the atmosphere.

If sinking cold, saline water isformeda watermass in the density range of the halocline, itwill be transformed to the deeper water layer of the Arctic Ocean Basin.

Acknowledgement

I express my gratitude toK-PORT program manager Dr. Sung-ho Kang for hissupport in the Arctic Oceanresearch and all the scientists and the crew members who have participated in this expedition.Ialso appreciate Prof. Koji Shimada for his insightful comments during this cruise.

References

Aagaard K, Swift JH, Carmack EC (1985), Thermohaline circulation in the Arctic Mediterranean Seas. J Geophys Res 90:4833-4846

Coachman LK, Aagaard K, Tripp R (1975), Bering Strait: the regional physical oceanography. University of Washington Press, Seattle, 172 pp

Coachman LK, Barnes CA (1961), The contribution of Bering Sea water to the Arctic Ocean. Arctic 14:147-161

McLaughlin FA, Carmack EC, Macdonald RW, Melling H, Swift JH, Wheeler PA, Sherr BF, Sherr EB (2004), The joint roles of Pacific and Atlantic-origin waters in the Canada Basin, 1997-1998. Deep Sea Res I 51:107-128

Shimada, K., T. Kamoshida, M. Itoh, S. Nishino, E. Carmack, F. A. McLaughlin, S. Zimmermann, and A. Proshutinsky (2006), Pacific Ocean inflow: Influence on catastrophic reduction of sea ice cover in the Arctic Ocean, Geophys. Res. Lett., 33, L08605, doi:10.1029/2005GL025624.

Steele M, Morison JH, Ermold W, Rigor I, Ortmeyer M (2004), Circulation of summer Pacific water in the Arctic Ocean. J Geophys Res 109:C02027. doi: 10.1029/2003JC002009

Weingartner TJ, Cavalieri DJ, Aagaard K, Sasaki Y (1998), Circulation, dense water formation and outflow on the northeast Chukchi Sea shelf. J Geophys Res 103:7647–7662

Abbreviations/Glossary

IMB ice mass balance buoy

ITPIce Tethered Profiler (ITP is an autonomous package of sensors fixed to an ice floe. It provides continuous observations of the water below the ice as the floe drifts around in the Beaufort Gyre)

K-PORT Korea-Polar Ocean Rapid Transition

LIDAR light detection and ranging

MIZ marginal ice zone

UpTempO

SWIFT surface wave instrument float with tracking

XCTD expandable CTD

Chapter 9. Particle flux under sea ice

Hyoung Sul La[1],Eun Jin Yang[1], Jin Yeol Choi[2]and Jun Oh Min[1]

[1]*Korea Polar Research Institute, Incheon 406-840, South Korea (hsla@kopri.re.kr; ejyang@kopri.re.kr; jomin@kopri.re.kr)*

[2]*Inha University, Incheon 402-751, South Korea (cjy13@inha.edu)*

9.1. Introduction

The recent dramatic decreasing trend of sea ice coverage results in an increase of inorganic and organic particles to the Arctic Ocean, which is important to understand the air-ice-sea fluxes, carbon cycle flux and effect of ecosystems. The particulate material and ice algae within sea ice could significantly contribute to increase the suspended particle material by the high melting and sea ice breakup during Arctic summer time. As the lithogenic particle is carried within sea ice and often drifted from the Beaufort Sea, many studies have been investigated the variability of sea ice coverage and thickness (Steele et al., 2010; Woodgate et al., 2010). However a few studies have been conducted the temporal variability in suspended materials under Arctic sea ice.

In order to address the particle flux under sea ice, we carried out a field experiment using sediment trap during about four days and holographic and acoustic sensors were operated to measure the particle size distribution and water column properties around sediment trap. We also analyzed the particulate organic carbon (POC) to evaluate the biogenic portion among the particulate material. This research could contribute to understand the Arctic particle dynamics in the rapidly-melting summer sea ice, and quantify the concentration and flux of suspended materials and the subsequent effect to marine ecosystem.

9.2. Material and methods

The experiment was performed in the Canada Basin in Arctic Ocean from 14:34 UTC on August 10 to 04:48 UTC on August 13, 2014. The experiment position was covered by high sea ice concentration (>75%) with 0.8 – 4 m ice thickness (Fig. 9.1).

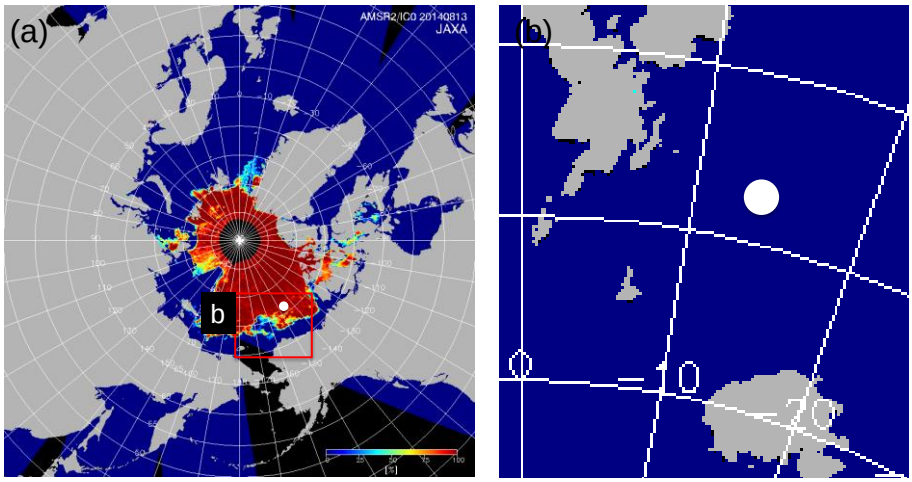

Fig. 9.1. Map of study area (white dot) in the Canadian Basin, Arctic Ocean. Color represents sea ice concentration by AMSR2 on August 13, 2014.

Icebreaker R/V *Araon* anchored at the marginal ice floe and the experimental site (initial position: 77° 36.741'N, 146° 6.072'W) was on a drifting multi-year ice floe (Fig. 2a). Mooring package (three sediment traps with AQUAscatt 1000R/S, LISST-Holo and ADCP) was located near melting pond about 200 m away from *Araon* (Fig. 9.2b).

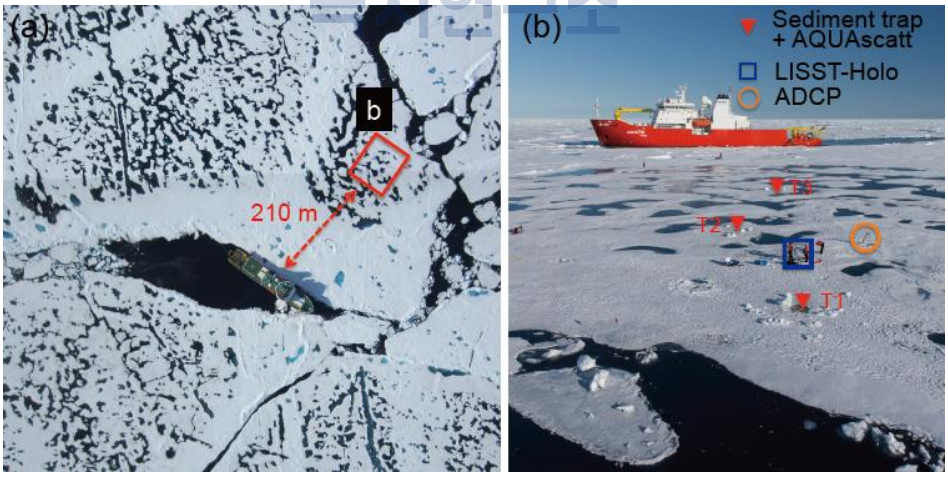

Fig. 9.2. (a) The sea ice condition in the vicinity of the experiment site and (b) mooring location of sediment trap with AQUAscatt 1000R/S, LISST-Holo, and ADCP near melting pond. Photographs were taken from helicopter (courtesy of P. Hwang and C. Lee).

Using 24'' and 36'', the ice floe was drilled to make five holes for submersible digital

holographic camera (Sequoia, LISST-Holo) and a 600-kHz acoustic Doppler current profiler (ADCP) (RDI, WorkHorse Sentinel), three sediment traps (T1, T2 and T3), MicroCats (Seabird, SBE-37), and a suspended sediment profiler (AQUAscat 1000R/S) (Fig. 9.3 and 9.4). For seawater sampling, a 10L Niskin bottle was used from 5−6 depths.

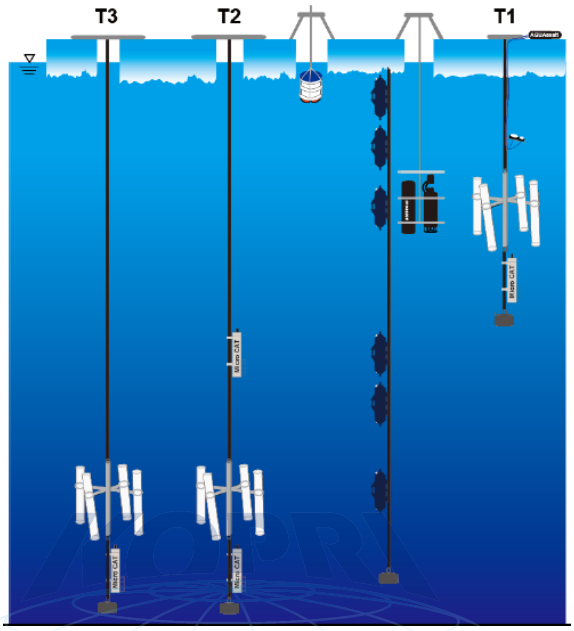

Fig. 9.3. Schematic design of setup for the sea ice experiment.

9.2.1 Sediment trap with AQUAscatt 1000R/S

Three sediment traps were moored in the same sea ice floe to collect the suspended particle materials by sea ice melting during Arctic summer. A sediment trap has four cylinders (the length of 50 cm and mouth area of 7 cm^2). One sediment trap was positioned at 15 m depth from sea surface and the other two traps were moored at 60 m depth, which was similar depth of subsurface chlorophyll maximum (SCM). The time series of suspended sediment distribution was measured with a suspended sediment profiler (AQUAscatt 1000R/S), which was moored in an upward-looking configuration at a depth of 9 m in the T1 (Fig. 3). AQUAscatt 1000R/S has 4 transducers with different frequencies (0.3, 0.5, 1, and 5 MHz), which was oriented with a slant angle of 10° off the vertical axis to escape from the noise of vertical mooring rope. It measured 255 bins with 4-cm bin length. The sampling interval was set to 8 pings per ensemble every 1 sec. ensonifying the water column from 9 m

to sea surface.

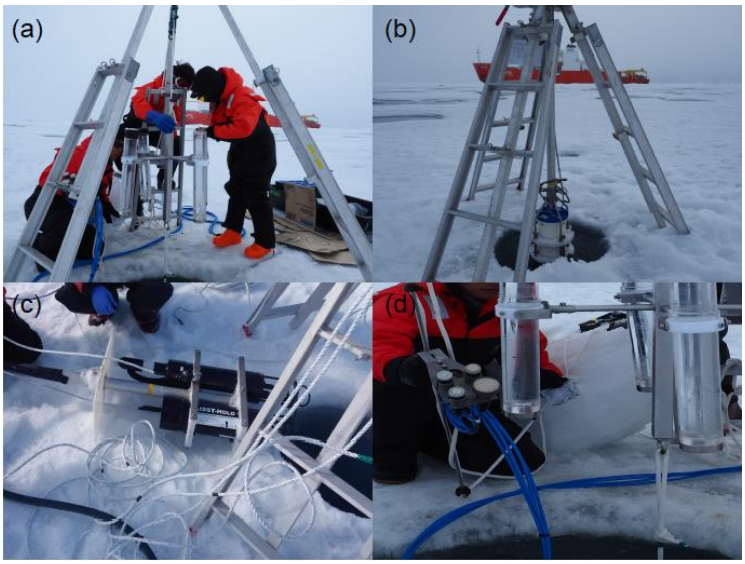

Fig. 9.4. Holographic and acoustic sensors: (a) Sediment trap, (b) ADCP,(c) LISST-Holo and (d) AQUAscatt 1000R/S.

9.2.2 LISST-Holo

LISST-Holo was mounted at the end of rope attached to another tripod. In a configuration that readily enabled deployment and recovery through the ice hole, LISST-Holo was lowered to a depth of 15 m, so that its sampling volume was colocated in the sediment trap and 28th ADCP bin. LISST-Holo was operated at 5-min burst mode storing the digital holographic images of SPM at a sampling rate of 0.2 Hz. In each burst, a total of 98 images were recorded during a 90-s running interval, and then the system was switched to a 210-s sleeping interval. The sampling volume was 1.86 cm^3 with an optical path length of 100 mm, and the wavelength of the solid-state diode laser was 658 nm (Sequoia, 2011).

9.2.3 ADCP

The downward-looking ADCP was mounted at the end of a stainless-steel pipe attached to a tripod. The transducer was positioned at a depth of 1.5 m from the sea surface and blanking distance was 0.5 m, so the depth range ensonified was 1.7–51 m. The size and number of bins were 0.5 m and 62 bins, respectively. The ADCP was continuously operated

to record current velocity and acoustic backscatter intensities at a sampling rate of 1 Hz.

9.2.4 Water samples

Water column samples were collected by 10-liter Niskin bottle at six depths (2, 4, 8, 15, 25 and 40) for the ground-truth estimate of suspended particle concentration and particle size distribution and five depths (2, 8, 15, 25 and 60 m) for total chlorophyll and particulate organic carbon (POC) every 12-h during four days.

For the estimation of total suspended particle concentration, collected water samples were vacuum pumped through pre-dried, pre-weighted 47-mm Whatman GF/F filters (0.7- m pore size) in on-board laboratory.

POC samples were collected with precombusted (6 hrs. at 450°C) GF/F filters using a nitrogen gas purging system under low pressure (Fig. 9.2). The samples were stored frozen at −20 until analysis in the home laboratory. POC samples will be determined with a CHN analyzer according to JGOFS protocol (JGOFS, 1996).

Table 1.Sampling time and location for total suspended particle concentration, Chl *a*, and POC

Cast	Date (UTC)	Start Time (UTC)	Latitude (N)	Longitude (W)	Description
1	2014/08/11	04:10	77° 31.269	146° 13.692	* Total suspended particle concentration: 2,4,8,15,25, and 40-m depth. * Chl *a* and POC: 2, 8, 15, 25, and 60-m depth
2	2014/08/11	17:20	77° 31.519	146° 59.62	
3	2014/08/12	03:50	77° 26.766	146° 12.375	
4	2014/08/12	17:40	77° 24.93	146° 9.636	
5	2014/08/13	03:50	77° 23.943	146° 12.874	
6	2014/08/13	17:40	77° 22.884	146° 10.679	

9.3. Preliminary results

Three sediment traps were recovered on August 13 after moored for about 4 days (Fig. 9.5a). We found a few sediment particles with some biological materials such as Arctic copepod (Fig. 9.5b) in the sediment trap moored at 15 m, while there was no biogenic

materials in the sediment trap at 60-m depth.

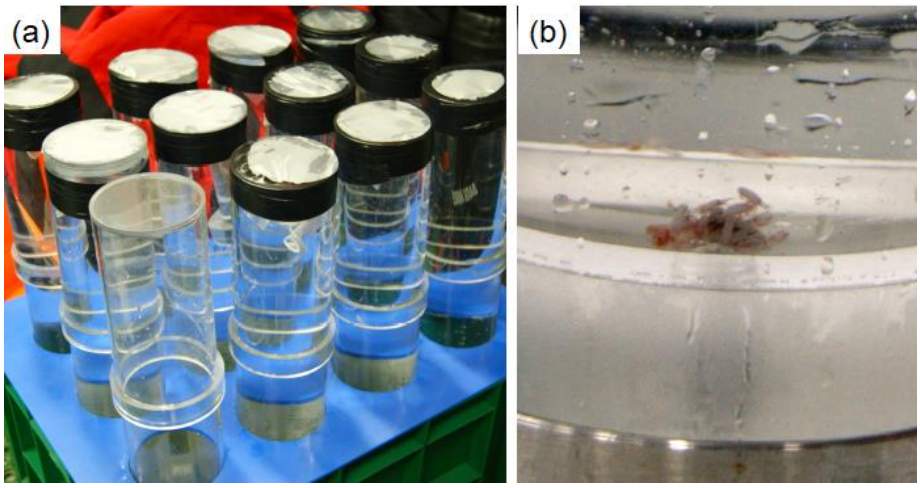

Fig. 9.5. (a) Collected samples from sediment trap and (b) Biogenic materials in the sediment trap.

Ice floe motion was calculated using GPS data of *Araon* (Fig. 9.6). As *Araon* was anchored on the sea ice we assumed that *Araon* could not affect on this ice motion. Blue dots represent all the GPS data collected and black arrows show the drift velocities of ice floe.

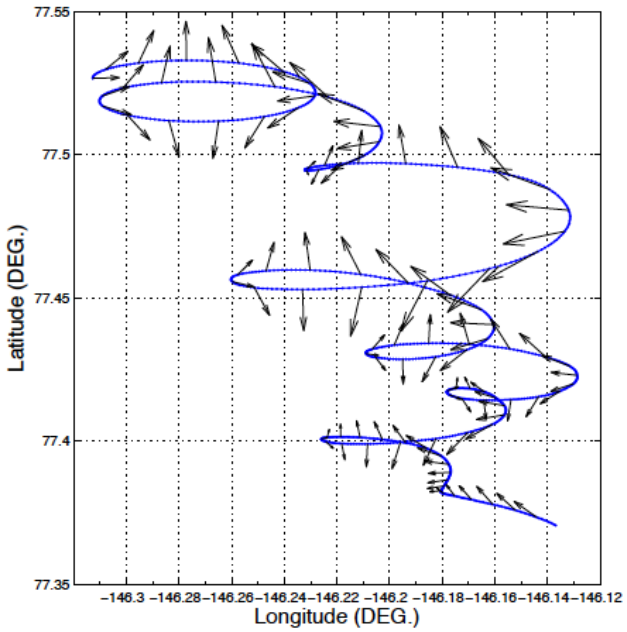

Fig. 9.6.Trajectory of sea ice floe and flow vectors derived from the trajectory

Drift velocities were simply estimated for the time series by dividing the distance of two consecutive GPS points by the time span (Fig. 9.7). The flow fields could be consistent over the area occupied by *Araon*. These data were used to correct for the relative motion of ice where the ADCP was moored.

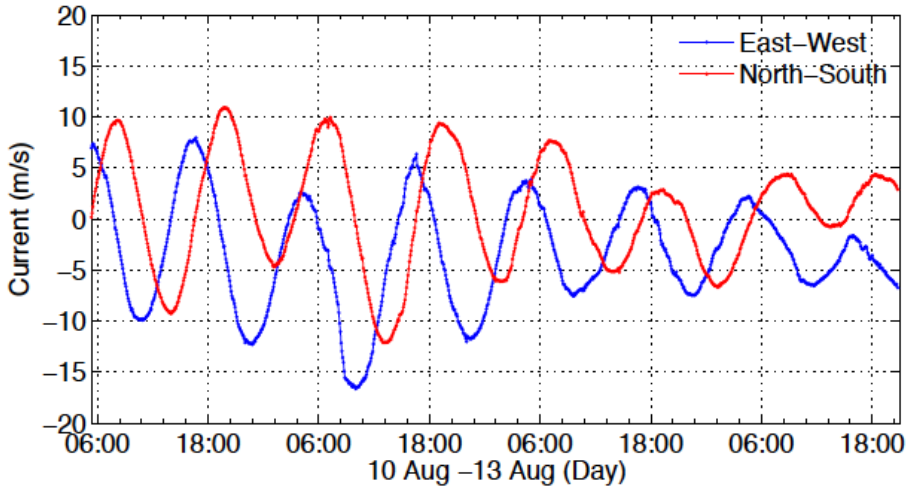

Fig. 9.7. Time series of ice floe velocities derived from *Araon* GPS data

ADCP data were collected every 1 min. during about 3.5 days, and the data were post-processed by using WinADCP that is provided by Teledyne RD Instruments (Fig. 9.8). The current (U and V) were corrected with drift velocities of sea ice motion and all the data was low pass filtered with 1-h window. The data show clear temporal variability of ~12 hour cycle, which might be due to the inertial motion. When the current pattern is compared with the ice floe motion in Fig. 9.6, the U and V showed similar pattern with the pattern of ice floe. Acoustic gain control (AGC) represents the relative acoustic intensity variation, which could be backscattered by suspended particle materials within water column. It shows that the most of suspended particles are mainly distributed near surface below 10 m and the relatively high backscattered signals were detected at around 20 m.

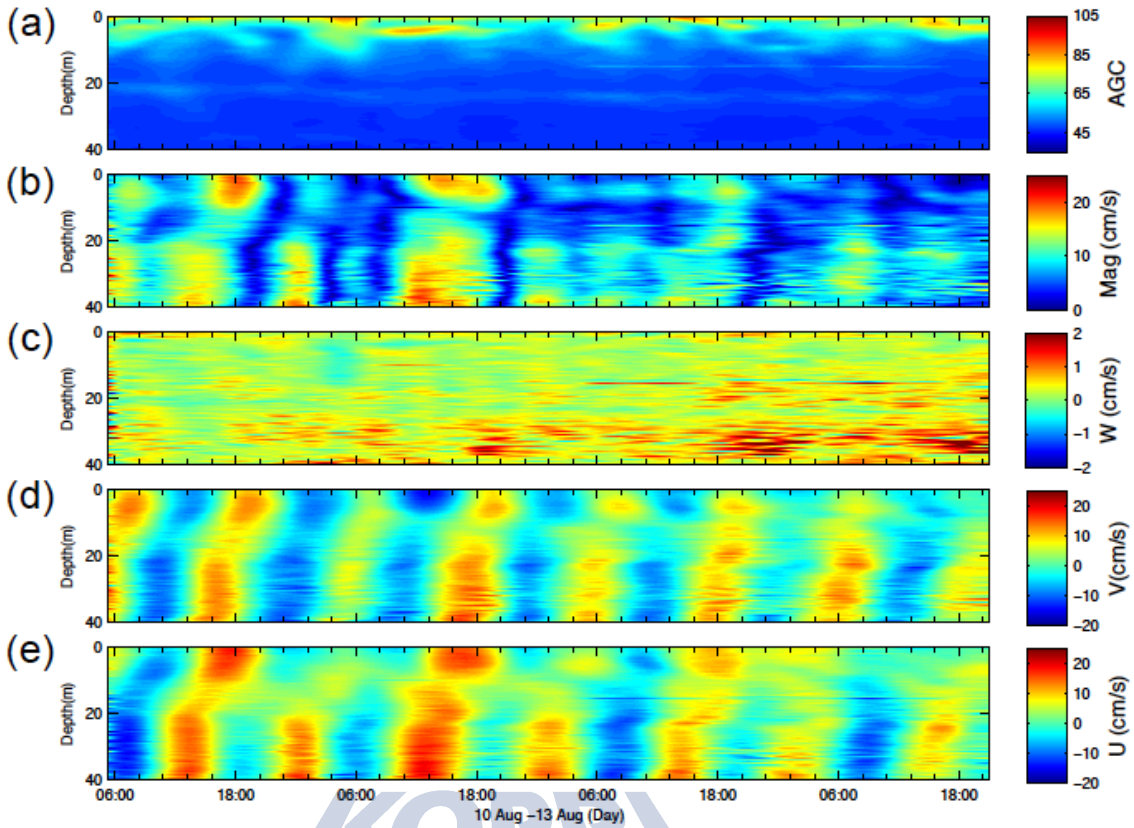

Fig. 9.8. Time-series of raw ADCP data from beneath the ice floe: (a) Vertical structure of acoustic gain control (AGC), which represents the relative acoustic intensity, (b) magnitude of current velocity, (c) vertical velocity of current, (d) horizontal velocity East-West current and (e) North-South current.

Fig. 9.9 shows the time series of ADCP velocities at the near-surface (5 m), 15 m, and 30 m below the surface. Blue and green lines represent the U (East-West) and V (North-South) current velocities, respectively. The black solid and dashed lines indicated the current velocities after 1-h low pass filter. This shows clear difference in the current pattern between surface and deeper layer while the current at 15 and 30 m look similar pattern.

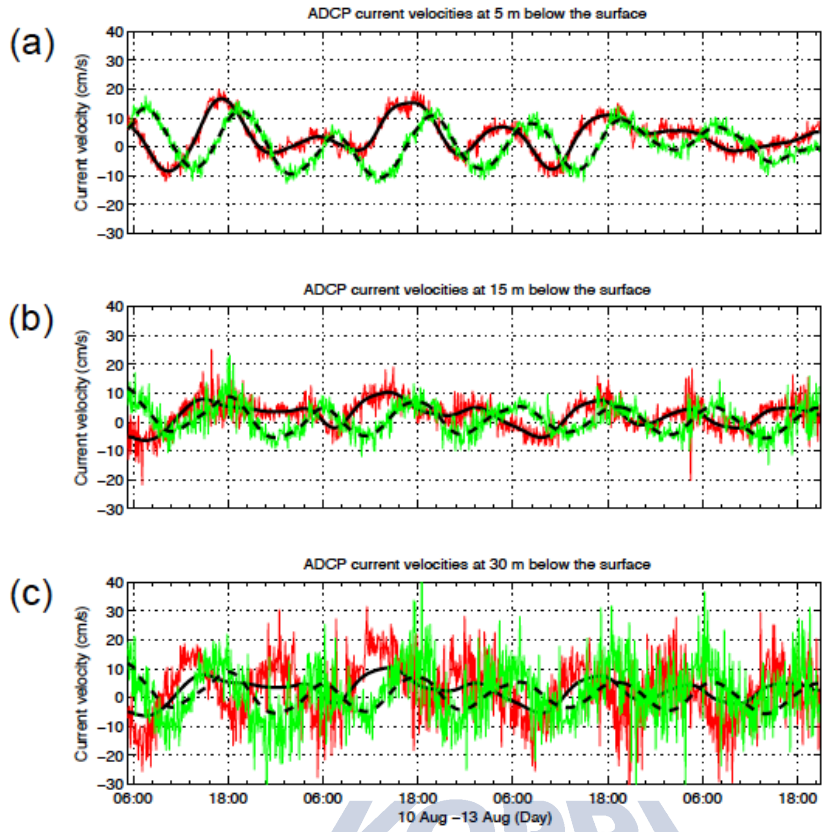

Fig. 9.9. Time series of raw ADCP current velocities at (a) 5 m, (b) 15 m, and (c) 30 m below water surface.

To detect the suspended particles falling from the bottom of sea ice, the high frequency acoustic transducers ranging from 0.3 to 5 MHz were deployed at about 8-m depth under sea ice. The data were recorded during about 3 days however, unfortunately, we could not observe the clear acoustic signals backscattered from suspended particle materials (Fig. 9.10). The strong acoustic signals were shown at around 8-m depth representing the sea ice bottom.

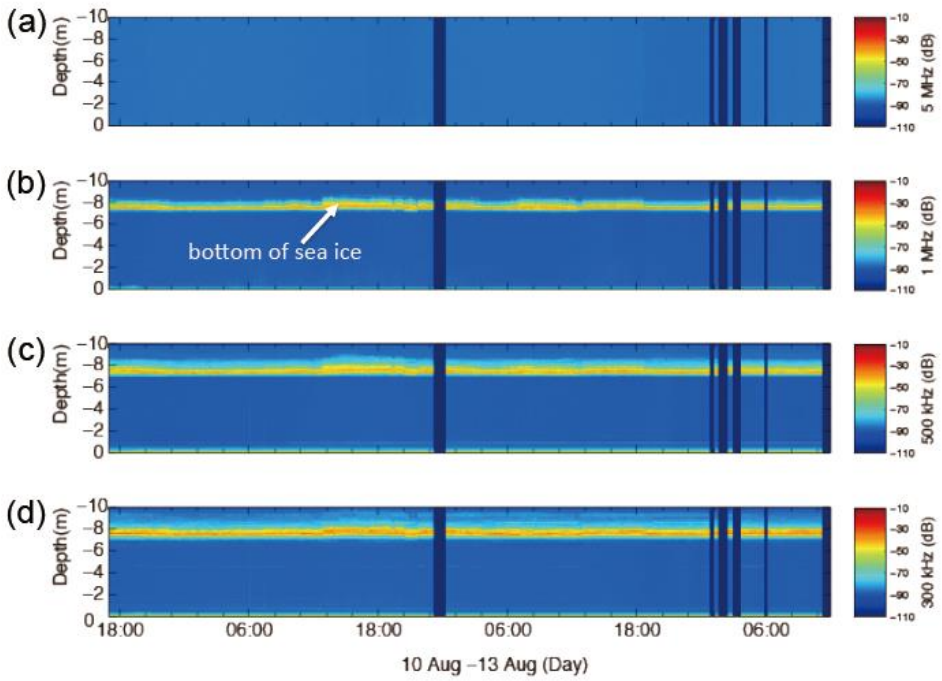

Fig. 9.10. Time series of acoustic intensity collected by AQUAscatt 1000R/S with four frequencies: (a) 5, (b) 1, (c) 0.5 and (d) 0.3 MHz.

References

Sequoia, 2011. LISST-Holo: Operating manual. Sequoia Scientific Inc., Bellevue, WA, 48pp.

Steele, M., Zhang, J., Ermold, W., 2010. Mechanisms of summertime upper Arctic Ocean warming and the effect on sea ice melt. Journal of Geophysical Research 115, C11004, 472 doi:10.1029/2009JC005849.

Woodgate, R.A., Weingartner, T.J., Lindsay, R., 2010. The 2007 Bering Strait oceanic Heat flux and anomalous Arctic sea-ice retreat. Geophysical Research Letters 37, L01602, 491 doi:10.1029/2009GL041621.

Chapter 10. Sea ice dynamics

Phil Hwang

Scottish Association for Marine Science, PA37 1QA (phil.hwang@sams.ac.uk)

Collaborators: Pedro Elosegui (ICM/CSIC), Jeremy Wilkinson (BAS), David Jones (BAS), Bruce Elder (ERDC-CRREL), and Mike Steele (PSC/APL)

10.1. Introduction

Our objectives for the ARA05B cruise for sea ice dynamics are two folded; 1) to construct multi-scale buoy arrays for small-scale sea ice deformation studies, and 2) to deploy long-term collaborative buoys in the Arctic. The buoy arrays include ONR MIZ assets (ITP80, AOFB, WB30-39, AWS05 and IMB21-25 see Chapter 8 for the details) and non MIZ assets (SATICE, SIESTA, SIMB, and UpTempO). Some of the buoys have their own primary objectives (e.g. ocean profiling for ITP and upper ocean temperature for UpTempO), but others have direct objective for sea ice dynamics study (i.e. forming GPS arrays for SIESTA). As most buoys are equipped with standard GPS receiver, here we attempted to coordinate the buoy deployment to construct the buoy arrays at various spatial scales (100 m to 50 km scales). In this way, we can investigate the sea ice deformation at various scales.

Sea ice deformation is very common in the Arctic sea ice (e.g., Kwok and Sulsky, 2010), e.g. significant portion of sea ice is estimated to deformed ice. Variable wind and currents cause sea ice to be deformed, forming leads, rafting, and ridging. As recent thinning of Arctic sea ice continue and even intensify, so do Arctic sea ice deformation (Rampal et al., 2009; Zhang et al., 2012). One of important nature of sea ice deformation is that sea ice deformation is highly localized and intermittent, and often described as multifractal scale-invariant (e.g., Marsan et al. 2004; Rampal et al., 2008). This means that small-scale deformation (both in space and time) is more violent than large-scale one, so such small-scale deformation significantly contributes actual fracturing of sea ice. Current estimate for amount of sea ice fracturing (lead forming, rafting and ridging) varies significantly as fracturing parameter (i.e. brittle transition) is also dependent on scale (e.g. Schulson, 2004).

Scale-dependence of sea ice deformation has been studied by using buoy array (Hutchings et al. 2011) or satellite-derived data (Marsan et al. 2004). Marsan et al (2004)

suggests that deformation can be described as multifractal, i.e. scale-independent, meaning small-scale deformation can be “predicted”. Meanwhile Hutchings et al (2011) argued that whitening of spectra increase as the deformation spatial scale decreases, suggesting small-scale deformation is de-coupled from large-scale ones (not “predictable”). In summary we do not have complete understanding on how much small-scale sea ice deformation occurs and be affected by external forcing at small to medium scales. The experiment has been planned to address these questions.

10.2. Buoy array configuration

10.2.1. Floe-scale buy configuration

In Hwang et al (2014) we observed floe-scale sea ice deformation events from multiple buoys deployed on the singe ice floe during the Araon 2012 cruise. We found that floe-scale deformations at hundreds of meters can be measured by using combination of standard GPS-equipped buoys receiver (about 5-m accuracy) and high-precision GPS buoy (SATICE) (centimeter accuracy). This time we planned the similar floe-scale buoy arrays as far as collaborative buoys meet their primary objectives. We planned to place the high-precision GPS buoy, SATICE (SI05), at the center of the buoy array, but the location of SI05 shifted to a side of the array as it offered thicker ice but away from rafted ice (see Fig. 10.1). AWS was placed 91 m from the SATICE SI05 on thick ice. CRREL SIMB was deployed 128 m from the SATICE SI05 on thinner ice to meet the ice thickness criteria for the deployment (see Section 10.3.3). UpTempO (2014-5) was deployed 141 m from SATICE SI05 where K. Shimada conducted continuous CTD casts during the ice camp. ITP 80 was deployed 203.5 m away from SATICE SI05 (the location of ITP was selected and deployed by Jeff). In the end five-buoy array was formed at about 100 m scale (Fig. 10.1 and 10.2).

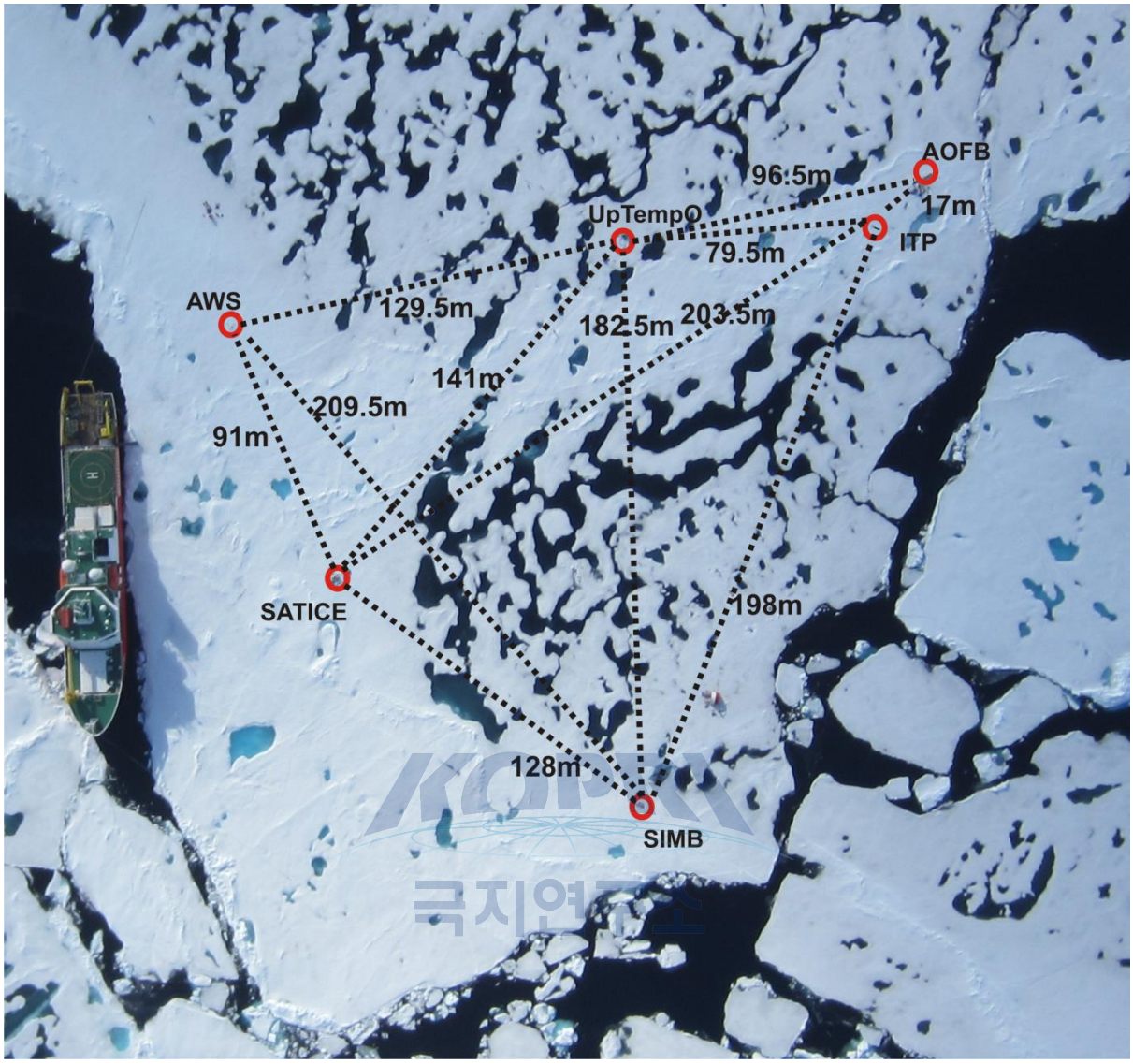

Fig. 10.1 Floe-scale (about 100 m) buoy array at the ice camp floe. The distance between buoy systems were measured by a laser range finder at the site. The background aerial photo is taken from Canon IXUS220 HS (Phil Hwang), helicopter survey was done by Martin Doble.

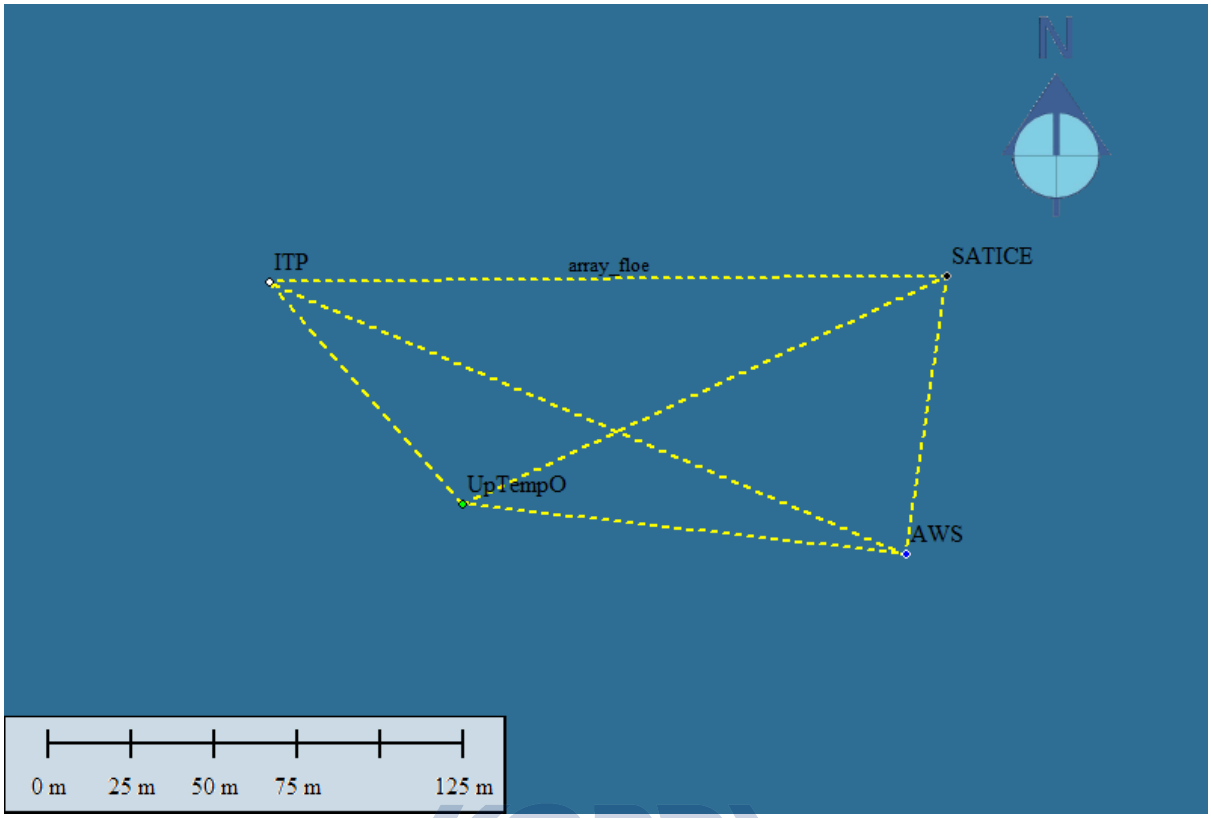

Fig. 10.2 Actual floe-scale buoy array on August 14 02:00 UTC. Location of SIMB 2014F was not shown in here.

10.2.2. Large scale buoy configuration

Floe-scale buoy array was extended to larger scale. Original plan was to form the buoy arrays at 1-2 km, 10 km, and 50 km scale (Fig. 10.3). The deployment of buoys were made as close as possible to the plan, but some of the buoys have no data at the time of writing this report. Figure 7.4 shows all the buoys which we had access to the data at the time of writing this report. Figure 7.5 - 7 show the actual buoy arrays at 2-km, 10-km and 50-km scales, respectively.

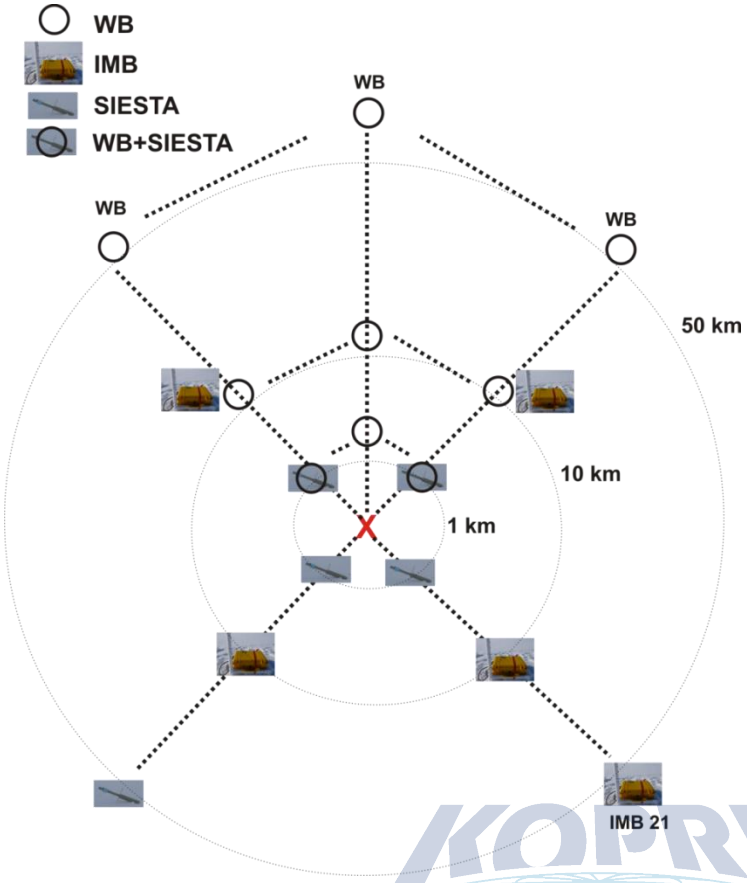

Fig. 10.3 A schematic diagram for planning the large scale buoy array configuration.

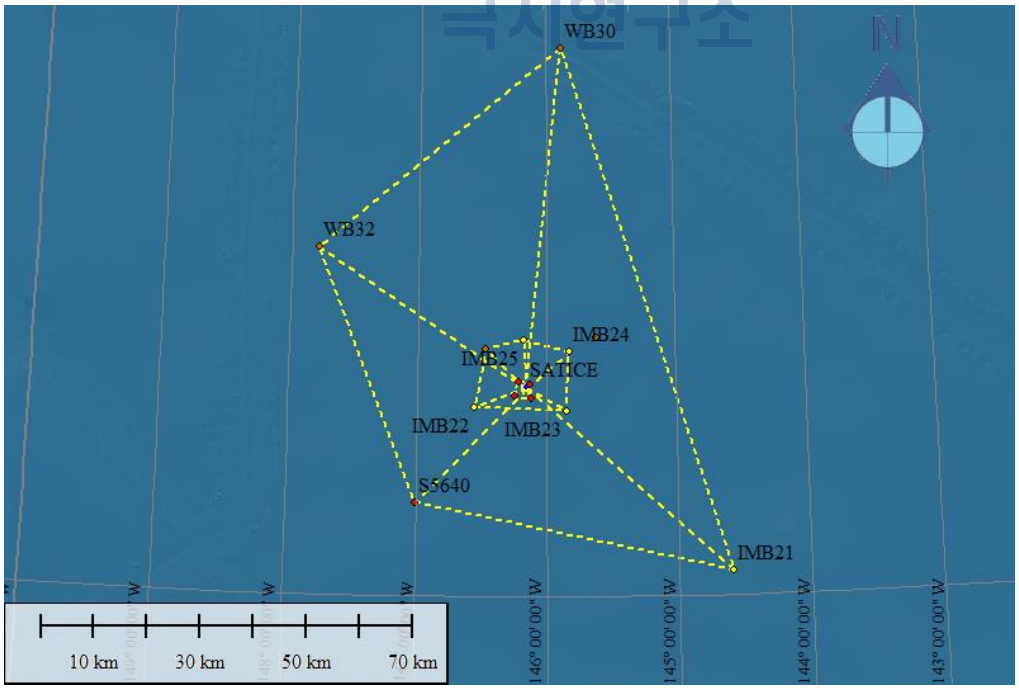

Fig. 10.4 Actual buoy array after the deployment on August 14 2014 02:00 UTC.

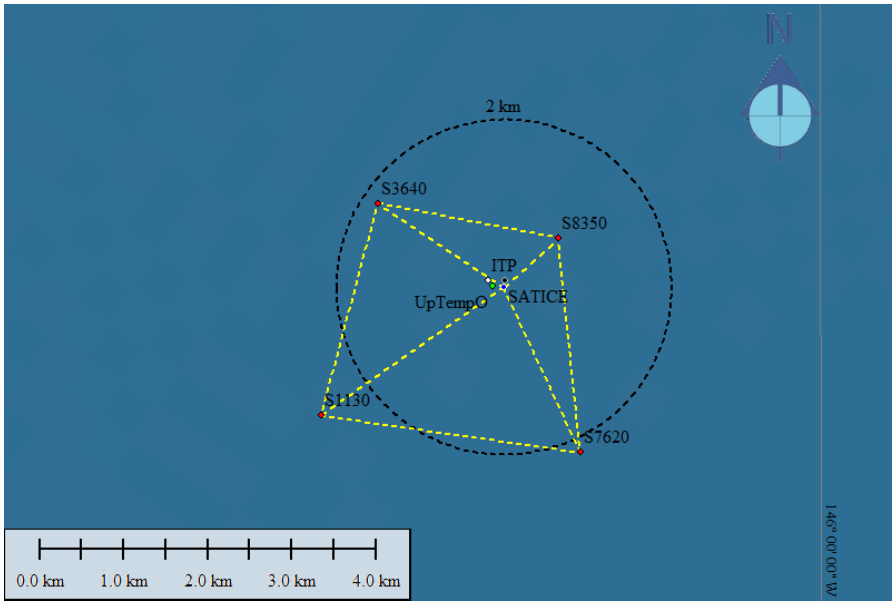

Fig. 10.5 Actual configuration of the buoy array at the 1-2 km spatial scale on August 14 02:00 UTC. SATICE is at the center of the array, and four SIESTA (S1130, 7620, 3640, 8350) buoys forming the array.

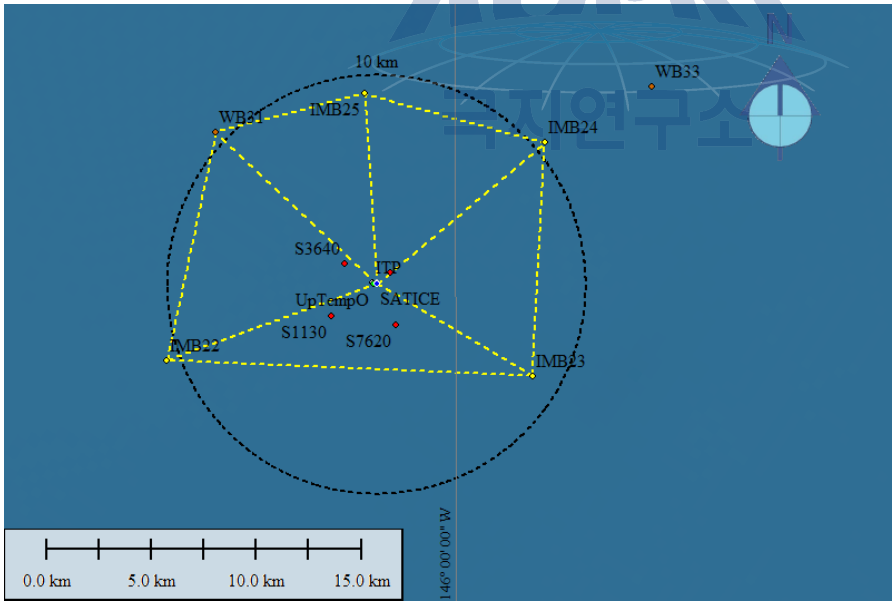

Fig. 10.6 Actual configuration of the buoy array at the 10 km spatial scale. SATICE is at the center of the array, and four IMBs (IMB 22, 23, 24, 25) and two WBs (WB31, 33) forming the array.

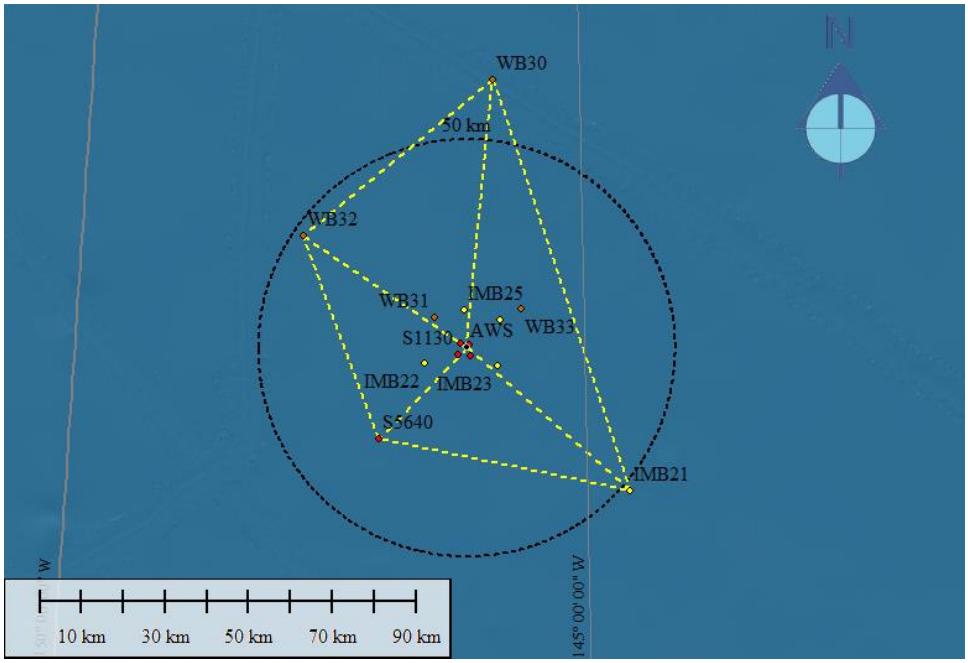

Fig. 10.7 Actual configuration of the buoy array at the 50 km spatial scale. SATICE is at the center of the array, and one IMB (IMB21), one SIESTA (S5640) and two WBs (WB30, 32) forming the array.

10.3. Buoy deployment

10.3.1. SATICE (SI05) deployment

The location of SI05 was selected in the thick ice near the ship's mooring. Ice close to the ship's mooring was rafted, so we placed SI05 inward away from the rafted ice but thick enough to maximize the survival of the buoy. The ice thickness at the site was 208 cm, freeboard 52 cm, and the distance from ice surface to the sounder was 156 cm. SI05 deployment began on August 10 19:00 LST. A 10-inch hole was made, and the connector lines from the bottom pipe were fed into anchor pipe and then the two pipes were connected to the insulation wood board (Fig. 10.8). The connected pipe and insulation wood board was inserted into the 10-inch hole. SI05 deployment resumed on August 11 14:00 LST (22:00 UTC) and completed its installation on 15:52 LST (23:52 UTC). The power was connected around 15:30 LST (23:52 UTC), and confirmed the tac-tac-tac sounds from the snow depth sensor. SATICE buoys were designed to measure cm-scale variation in three dimensional GPS location. The buoys are also equipped with an automatic weather station, snow depth sounder, under ice pressure sensor, mini CT (conductivity and temperature),

digital camera, and Iridium antenna (Figure 7.8).

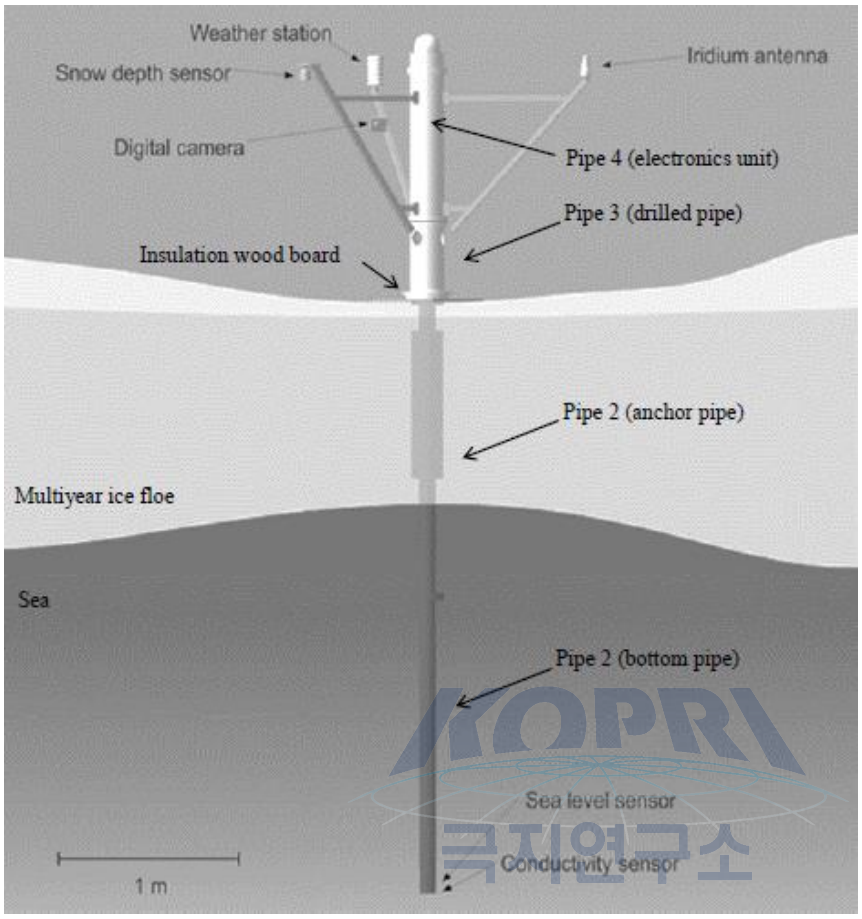

Fig.10.8 Schematic diagram of the SATICE system.

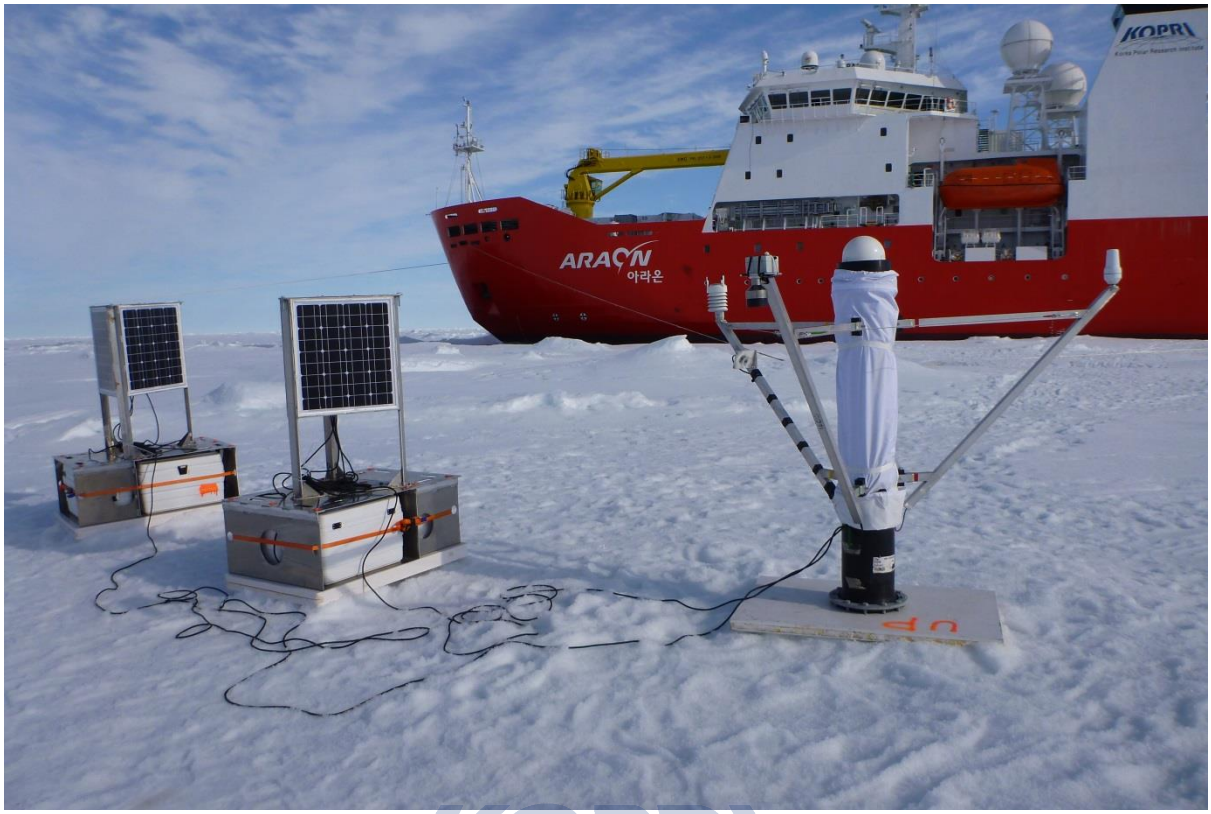

Fig. 10.9 Photo of SATICE (SI05) at the deployment.

10.3.2. SIESTA deployment

SIESTA (Sea Ice Sensor Thrown from Aircraft) is an air-droppable buoy. It measure GPS location, air temperature, humidity and pressure every hour, and transmitting the measured data every 12 hour. During ARA05B we deployed five SIESTA buoys; four of them within 1 km from the ice camp and one at about 50 km from the ice camp. During the test on the ship SIESTA 5640 failed to communicate. Later it was discovered that half of Lithium battery in serial connection with the buoy was malfunctioned. We re-arranged the battery only with good batteries, and the problem was resolved (thus, S5640 contain half of the batteries).

SIESTA 7620 and 1130 were deployed in the morning (09:35 LST and 09:49 LST) of August 11 2014 (Table 10.1). In the helicopter there were Phil Hwang, Sang Lee and his student. The deployment photos are shown in Figs 10.10-11. For SIESTA 7620, the ice thickness at the site was more than 5 m thick, and the buoy was placed on slightly elevated surface and away from ridges and melt ponds. For SIESTA 1130, the flat ice thickness was 2.5

m, and it was also placed slightly elevated ice surface. SIESTA 8350 and 3640 were deployed in the afternoon of August 13 by Martin Doble with Wave Buoys (WBs). No information and photos of these deployments was not available at the time of writing this report. SIESTA 5640 was deployed on August 13 by Phil Hwang, after the communication problem of the buoy had been resolved. It was planned to deploy about 50-km southwest from the ice camp, but no suitable ice floe was found. Thus the actual location of the buoy was about 30-km from the ice camp (see Fig. 10.7). Again the buoy was deployed on slightly elevated surface, away from ridges and melt ponds (Fig. 10.12).

Table 10.1 Summary of SIESTA buoy deployment.

ID	Date (UTC) y/m/d	Time (UTC)	Ice thick (cm)	freeboard (cm)	Snow depth (cm)	Note
7620	2014/08/11	17:35	>5	-	-	About 1 km SE from the ice camp site. Sang Lee's 3rd Melt Pond survey. 77° 2655' N/146° 12.78' W.
1130	2014/08/11	17:49	2.5	38	7-10	About 1 km SW from the ice camp site. Ice thickness. Nearby the melt pond ice thickness measured 219 cm. Sang Lee's 4th Melt Pond survey with me. 77° 26.93'N/146° 14.48'W.
8350	2014/08/13		-	-	-	About 1 km NE from the ice camp. Deployed with WB together (webcam pointing to SIESTA buoy).
3640	2014/08/13		-	-	-	About 1 km NW from the ice camp. Deployed with WB together (webcam pointing to SIESTA buoy).
5640	2014/08/13	17:23	-	-	-	About 50 km SW from the ice camp site. 77° 11.20' N/147W 1.80' W.

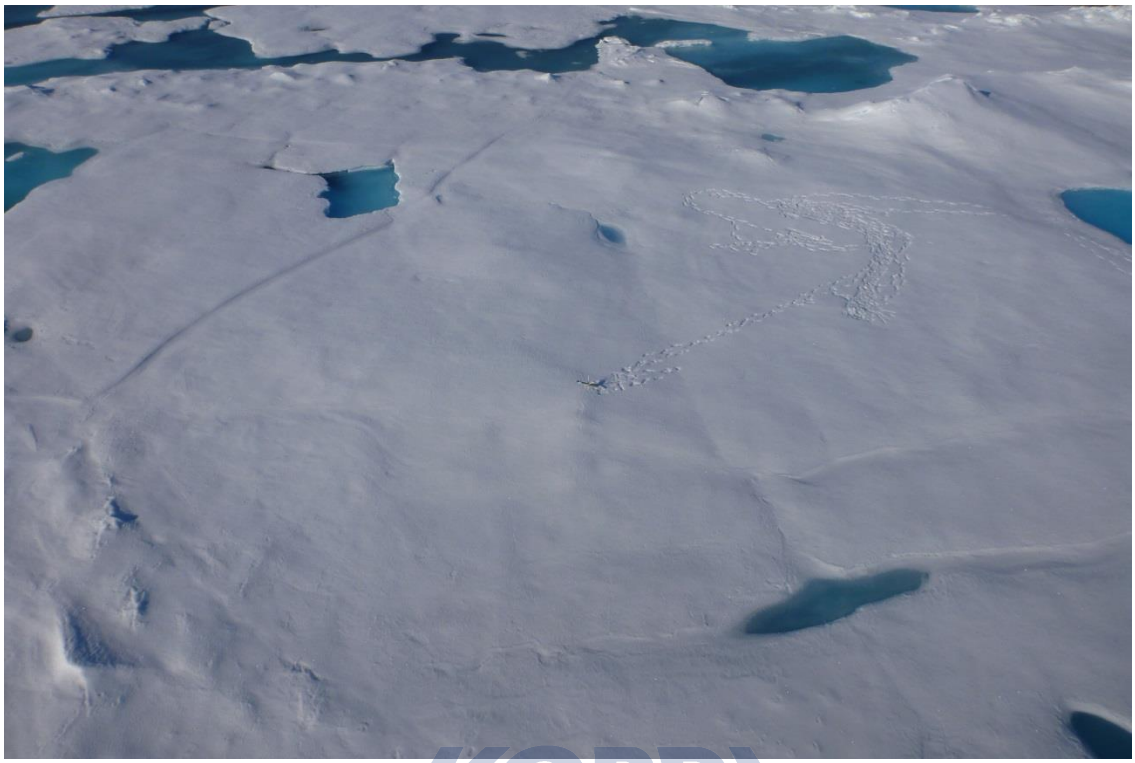

Fig. 10.10 Photo of SIESTA 7620 at the deployment.

Fig. 10.11 Photo of SIESTA 1130 at the deployment.

Fig. 10.12 Photo of SIESTA 5640 at the deployment.

10.3.3. CRREL SIMB (2014F) deployment

The deployment of SIMB 2014F started on August 10 2014 09:00 LST (17:00 UTC) and completed at 11:29 LST (19:29 UTC). The deployment was done by Phil Hwang (SAMS), B. W. An (FMI - Finnish Meteorological Institute), and J.H. Kim (KOPRI). When it turned on at 19:29 UTC, the time readings from SIMB 2014F was 20:29, yet actual UTC time was 19:29, so there was 1 hour offset for SIMB 2014F. At the deployment site, the ice thickness was 170 cm, freeboard 13 cm, and snow depth 5.0 cm. The distance from the top of temperature pipe to ice surface was 33 cm. The distance from surface snow sounder to the ice surface was 146 cm. SIMB 2014F was located about 50 m from the nearest edge of the ice floe, and at least 10 m away from the nearest melt ponds.

We revisited SIMB 2014F one or two days later and found that it was frozen to the ice (could not move it). Five autonomous observation platforms (ITP 80, AOFB, SATICE SI05, AWS 05, and UpTempO 2014-5) were deployed with SIMB 2014F on the same ice floe at the ice camp (see Fig. 10.1). ITP 80, AOFB and AWS 05 were deployed as part of ONR MIZ program. SATICE (SI05) was deployed as part of an EU project (see details in Section 3.1 in

this chapter). UpTempO (2014-5) was owned and provided by Mike Steel at the University of Washington.

CRREL SIMB is a floatable buoy to survive melt-out of the ice floe. SIMB is engineered and owned by US ERDC-CRREL. We have been collaborating with US ERDC-CRREL last two years to deploy their SIMB. It has air temperature and barometric pressure sensors, under ice sounder (distance to the ice bottom), snow sounder (distance to the snow surface), under ice pressure sensor, and temperature string. The new version added radiation sensors at the ice surface and at the ice bottom, measuring incoming solar radiation as well as light transmission through the ice.

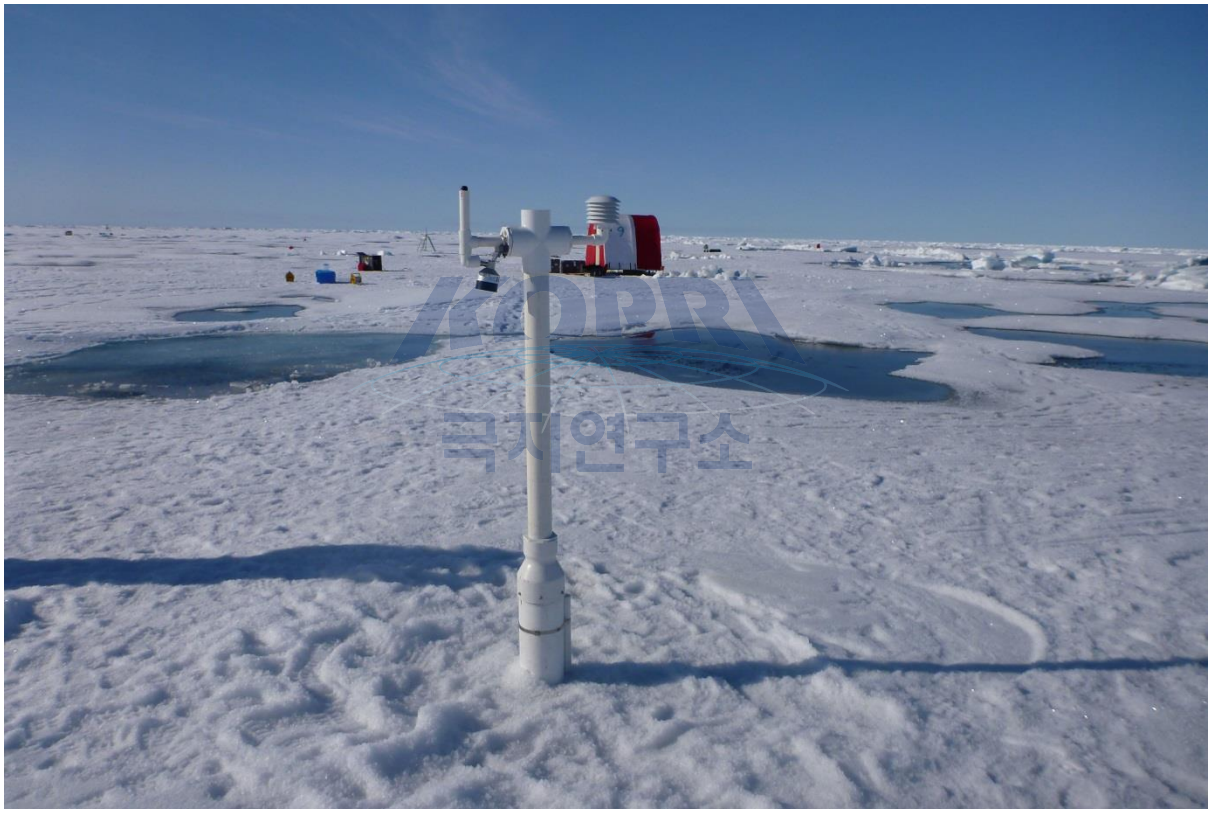

Fig. 10.13 Photo of CRREL SIMB 2014F at the deployment.

10.3.4. UpTempO (2014-5 & 2014-8) deployment

The first UpTempO (2014-5) was deployed on August 13 22:15 UTC. The deployment hole was made couple of days ago, but it was occupied with K. Shimada CTD/ADCP casts. At the last day of ice camp Shimada's CTD/ADCP was cleared up, and UpTempO (2014-5) was deployed through the same hole. The ice thickness was about 1.5 m thick at the site. The

distance from the ITP 80 was 79.5 m (see Fig. 10.1).

The second UpTempO (2014-8) was deployed at ST 20, the very next station after the ice camp (August 14 2014, 16:55 LST, D+1 00:55 UTC), (76° 45’ 46.82” N, 148° 54’ 24.32” W). The original plan was to deploy in the East Siberian Sea. However, Araon had the engine problem after the ice camp, so no possibility to go northern East Siberian Sea was shown at that time. Thus the decision was made to deploy the second UpTempO (2014-8) with ITP 82. The distance between UpTempO and ITP 82 was kept about 70 m apart. The ice thickness at the site was about 1.3 m.

Fig. 10.14 Photo of UpTempO (2014-5) at the deployment.

Fig. 10.15 Photo of UpTempO (2014-8) at the deployment.

References

Marsan. D., Stern, H., Lindsay, R., Weiss J., 2004, Scale Dependence and Localization of the Deformation of Arctic Sea Ice. Physical Review Letters 93 (17), doi:10.1103/PhysRevLett.93.178501.

Hutchings, J., Roberts, A., Geiger, C.A., Richter-Menge, J., 2011. Spatial and temporal characterization of sea-ice deformation. Annals of Glaciology 52 (57), 360-368.

Hutchings, J.K., Heil, P., Steer, A., Hibler III, W.D., 2012. Subsynoptic scale spatial variability of sea ice deformation in the western Weddell Sea during early summer, J. Geophys. Res., 117, C01002, doi:10.1029/2011JC006961.

Hwang, B., P. Elosegui, and J. Wilkinson, 2014. Small-scale deformation of an Arctic sea ice floe detected by GPS and satellite imagery, Deep Sea Research II, in revision.

Rampal, P., Weiss, J., Marsan, D., Lindsay, R., Stern, H., 2008. Scaling properties of sea ice deformation from buoy dispersion analysis. Journal Geophysical Research 113, C03002, doi:10.1029/2007JC004143.

Rampal, P., J. Weiss, J., Marsan, D., 2009. Positive trend in the mean speed and deformation rate of Arctic sea ice, 1979–2007. Journal of Geophysical Research 114, C05013, doi:10.1029/2008JC005066.

Schulson, E.M., 2004. Compressive shear faults within arctic sea ice: Fracture on scales large and small. Journal of Geophysical Research 109, C07016, doi:10.1029/2003JC002108.

Zhang, J., Lindsay, R., Schweiger, A., Rigor, I., 2012. Recent changes in the dynamic properties of declining Arctic sea ice: A model study. Geophysical Research Letters 39, L20503, doi:10.1029/2012GL053545.

Chapter 11. Ice Camp I : Marginal Ice Zone Program Activities

Martin Doble[1], Shawn Gallagher[2], Phil Hwang[3], Craig Lee[4], Mary Jane Perry[5], Jeff Pietro[6] and Jim Stockel[2]

[1]*Laboratoire d'Océanographie de Villefranche (doble@obs-vlfr.fr)*

[2]*Naval Postgraduate School (sggallah1@nps.edu; stockel@nps.edu)*

[3]*The Scottish Association for Marine Science (SAMS) (phil.hwang@sams.ac.uk)*

[4]*University of Washington (craig@apl.washington.edu)*

[5]*University of Maine (perrymj@maine.edu)*

[6]*Woods Hole Institute of Oceanography (WHOI), (jpietro@whoi.edu)*

11.1. Objectives

Marginal Ice Zone program objectives for the ARA05B primary ice camp included:

- Deploy an array of autonomous instruments for sampling the upper ocean, ocean, sea ice and atmospheric boundary layer in the consolidated ice to the north of the previously-deployed MIZ arrays. Ideally, sea ice at this location would survive the summer melt, allowing the array to sample through the coming year.
- Conduct high-resolution time series of upper ocean velocity, stratification and turbulence through the duration of the camp.
- Conduct aerial, high-resolution photographic surveys of the region surrounding the ice camp for floe size distribution analyses.
- Provide logistical and scientific support for other ice camp activities, including hole drilling, positioning of equipment and flight coordination.

11.2. Introduction

Because the sea ice cover moderates atmosphere–ocean fluxes and the ocean affects the ice cover through fracturing, divergence, and melting, the ice–ocean system is strongly coupled within the MIZ. Highly variable ice and ocean conditions are a source of large perturbations that can trigger feedbacks leading to rapid summertime retreats of the sea ice cover.

Key upper ocean processes that contribute to strong coupling within the MIZ ocean–ice system are:

- Propagation and attenuation of ocean surface waves
- Absorption and storage of incoming solar radiation and its subsequent lateral transport
- Vertical mixing within and at the base of the ocean mixed layer

Surface wave induced deformations are responsible for fracturing the ice cover and reducing the size of floes across the MIZ. Small broken-up ice floes are more mobile than large, compacted floes of the pack interior. Floes at the seaward edge of the MIZ are vulnerable to being swept out to the open ocean. Small floes within the MIZ readily respond to divergent oceanic or atmospheric forcing compared to the ice pack, decreasing ice concentration inside the MIZ during divergent forcing events.

Heat from solar radiation can manifest in many ways including: direct surface melting/ablation, bottom and/or lateral melting as a result of ocean redistribution of heat absorbed locally through leads and adjacent open water areas, and entrainment into the surface layer of subsurface ocean heat carried into or redistributed within the Arctic by ocean currents.

Lateral in homogeneities resulting from non-uniform heat absorption in the MIZ produce complicated vertical structure in the surface mixed layer. In heavily ice-covered conditions, ice melt derives from direct surface melting/ablation and entrainment of warmer waters from below, with local heating through existing leads being less important. Vertical entrainment depends on the intensity of turbulence about the base of the surface mixed layer, which in turn depends on the forcing of the mixed layer at its upper boundary. Towards the end of winter the surface buoyancy forcing of the ocean tends towards neutral while the extensive sea ice cover inhibits wind forcing of the upper ocean. As ice concentration decreases through spring and into summer, several positive feedbacks can accelerate ice melt. Increased areas of open water allow more heat to enter the ocean from above that is then available for basal and lateral ice melting. In addition, winds acting on a less concentrated, thus more mobile ice pack as well as acting directly on larger open water

regions, can generate near-inertial motions that enhance the shear and mixing about the mixed layer base and, by radiating vertically, support increased shear and turbulent mixing throughout the water column increasing vertical fluxes of heat below the mixed layer. Strong lateral temperature gradients, intense solar heating, and temperatures elevated well above the freezing point significantly complicate the vertical heat transport processes in the MIZ.

The ONR Marginal Ice Zone (MIZ) program focuses on the emergent, seasonal MIZ in the Beaufort Sea in an effort to:

1. Collect and analyze a benchmark dataset that resolves the key processes controlling MIZ evolution, with sufficient spatial and temporal scope to capture a broad, representative range of environmental conditions
2. Understand the processes that govern the evolution of the MIZ, identify key interactions and feedbacks in the ice–ocean–atmosphere system, and investigate how these might change with the predicted increased seasonality in arctic sea ice cover
3. Evaluate the ability of existing models to predict MIZ seasonal evolution, and improve parameterization of key processes with the goal of enhancing seasonal forecast capability

Specific science questions include:

1. What processes govern the temporal and spatial evolution of the MIZ in the Beaufort Sea?
2. How do the vertical structure of temperature and salinity, internal wave variability, turbulent mixing, and radiative warming vary as a function of ice cover, extending from open water, though the MIZ, and deep into the fully ice-covered ocean?
3. What are the respective roles of surface wave driven mechanical forcing, solar radiation driven thermodynamic forcing, and the delivery of heat through advection and diapycnal mixing (driven by direct wind forcing, internal waves and small-scale, wind stress curl driven vertical exchange) in governing MIZ evolution? How do these processes couple?
4. How do surface waves evolve within the MIZ as a function of fetch and season?

What is the input–dissipation balance of waves in a mixed fetch of open water and ice floes? How do surface waves attenuate/collimate across the MIZ?

5. What is the ice floe response to surface waves? What are the short-scale flexural variations across a floe?
6. How does the upper ocean response to wind forcing vary as a function of ice cover? How do wind stress and ice–ocean stress vary across the MIZ, and how do they relate to mixed layer currents and internal wave intensity? What influence do extreme events (i.e., storms) have on the evolution of the MIZ?
7. Do these processes, combined with the increasing areas of open water, act to amplify the seasonality of Arctic Ocean ice cover?
8. Can the historical evolution of Beaufort–Chukchi ice–ocean variability (ice thickness, floe size distribution, seasonality) be quantified and understood in the context of these processes?
9. What feedback mechanisms become important in the emerging Beaufort Sea MIZ?

Coincident and continuous measurements of the atmosphere, sea ice, and ocean are required to resolve the complex processes and feedbacks affecting the large-scale MIZ evolution and seasonal ice retreat. To achieve this, The MIZ program employs a suite of autonomous instruments capable of: (i) sampling from full ice cover, though the MIZ and into open water, (ii) following the MIZ as it retreats northward, and (iii) resolving processes that occur at short spatial and temporal scales.

Ice-mounted instruments were deployed using aircraft in March 2014, along a meridional line stretching from roughly 71° 50’ N to 75° 15’ N along 136° W. Drifting (floats) and mobile (Seagliders and Wavegliders) platforms were deployed in July 2014 in open water near the ice edge. Mobile platforms were commanded to follow the northward retreat of the MIZ, sampling under the ice, within the MIZ and in open water to the south. The instrument array deployed from the ARA05B ice camp were intended as the northernmost element of the network, positioned deep into the consolidated ice to maximize its chances of surviving the summer melt back.

11.3. Operations

The following sections summarize instrument deployments and sampling conducted as part of the MIZ program contribution to the ARA05B ice camp. Numerous assets were deployed in and near the primary camp (Fig. 11.1).

11.3.1. Ice camp selection

On 8 August 2014 Araon arrived at the nominal target site for the ice camp, 'ST19', situated in between MIZ clusters 3 and 4, and to be as far north as Araon's schedule would allow. The location of ST 19 was determined by the location of MIZ cluster 3 and 4. The initial target site was in uncompacted ice, riddled with through melt ponds. In an attempt to find consolidated ice, a helicopter reconnaissance set out at 05:00 L (13:00 UTC) to explore conditions to the north. P Hwang and M. Doble flew to 77° 22'N (as far as time would have permitted Araon to travel) without encountering more suitable ice. The reconnaissance team thus returned to search for a suitable ice floe in the vicinity of Araon's position (77° 36.15' N, 146° 05.04' W), ultimately selecting a floe about 500 m north of the ship's location. The floe had thick, rafted ice at the water's edge connected with thinner ice riddled with numerous melt ponds (Fig. 11.2). MIZ activities required 2-3 m ice thickness, while KOPRI scientists required less than 2 m thickness and a variety of melt ponds. Drilling revealed thickness ranging from 1.5 m (areas with many melt ponds) to 4 m or more (ice near ridges), meeting the requirements of both groups. The ship positioned along the open water, portside to the floe. At 08:00 L (16:00 UTC), the crew and a science team (P. Hwang and H.S. La) went out on the ice and prepared 10-inch holes for anchoring Araon. Ice at the anchor points was rafted (layered). Securing Araon to the floe thus required over three hours.

11.3.2. Automated Weather Station Deployment

AWS 05 was deployed on the first of ice camp (8 August 2014, 22:30 UTC) at the ice camp site (Fig. 11.3). AWS 05 was placed on thick ice (< 5 m) for longer survival of melting out. At the deployment the wooden base of the AWS tripod was secured with the rope connected to the weight through the 2-inch ice hole. AWS 05 is part of MIZ 5th cluster to be deployed on board Araon. It records hourly GPS location (FSTR2 C10521-01), wind (R.M.

Young model 05103-45), heading (Honeywell HM6352), temperature and humidity (Vaisala HMP155), barometric pressure (CS100 Setra), and solar radiation (Apogee pyranometer sp 110). The recorded data is transmitted by Iridium 9602 SBD modem. The sensor and sampling configuration are identical to other MIZ AWS systems that were deployed during MIZ spring deployment.

Sample data between 9 August 2014, 00:00 UTC and 18 August, 2014 15:00 UTC are shown in Fig. 11.4 for air temperature, barometric pressure, humidity and solar radiation. All data has shown reasonable values, including solar radiation. During the test mode on the ship solar radiation sensor was not properly recognized in the CR1000 program. Once the modified CR1000 program (identical to the one used in the MIZ spring campaign) uploaded to the data logger, the solar radiation values show reasonable daily fluctuations. Also note that CRREL SIMB 2014F (about 200 m from AWS 05) has the Apogee SP radiation sensor, so the solar radiation can be compared with the data from CRREL SIMB 2014F.

Calibration of wind data: Wind direction on the drifting ice floe is difficult to calibrate. R.M. Young wind sensor recommend to point the junction box of the sensor to due south at the deployment for the wind direction correction. Thus, on 12 August 2014, 17:23 UTC, the junction box of AWS was re-adjusted to point due south. Due south was determined by hand-held GPS unit by working in line to get the heading. In addition R/V *Araon* has independent set of measurements for wind, GPS, and the ship's heading every second (refer to *Araon* DADIS data). Fig. 11.5 and Table 11.1 show comparisons of wind direction between AWS 05 and Araon DADIS. The vertical arrow marks the time when the junction box of AWS 05 changed to point due south. Before the adjustment of the junction on 17 August, 17:23 UTC, AWS 05 wind direction was off-set by -41°. After the adjustment, AWS 05 wind direction was offset by 44°.

11.3.3. Ice Mass Balance Buoy Deployments

Five IMBs were deployed in array at 10 km and 50 km from the ice camp location. Four IMBs (22, 23, 24 and 25) were deployed at four corners of the buoy array, while one IMB (21) was deployed at 50 km southeast from the ice camp location (see Fig. 11.6). The objectives

of IMB deployment are two folded; being part of sea ice deformation array at different length scale and investigating differential melt/growth of sea ice within 10 km and 50 km spatial scale.

IMB measures GPS location (Fasttrax UP501 or similar), temperature profile (DS28EA00 thermometer chips with a 1 K heater resistor), and the recorded data is transmitted back via Iridium 9602 SBD modem. Each IMB has a 10-m long chain (upper 5-m for 240 sensors with 2-cm interval and bottom 5-m for 10 sensors with 50-cm interval). 'Hot-wire' mode is used to delineate the surrounded media (i.e., air, snow, ice and water) based on different thermal conductivity of the media. The tightly spaced thermistors allow us to measure the temperature profile at higher resolution, and allow us to study the detailed thermal characteristics within snow and ice (e.g., internal melting and heat transport).

Table 11.2 contains the deployment summary for the five IMBs. All five IMBs were deployed on the second-year ice floe with blue melt ponded ice, typically ridges at one side. For the deployment of IMB 21 we (P. Hwang and C. Lee) flew about 50 km southeast from the ice camp site. The deployment was completed on 9 August 2014, 16:59 L (10 August 2014, 00:59 UTC). This deployment was right after the deployment of IMB 22 and 23 on the same day. It was foggy during the deployment of the three buoys. The selected ice floe for IMB 21 was a second-year ice floe with the elongated ridges (and with blue melt ponds) (Fig.11.7). The ice thickness at the deployment site was 240 cm and freeboard 45 cm (Table 11.2). The IMB 21 was placed relative smooth but elevated ice surface.

The deployment of IMB 22 and 23 was done by one helicopter flight (P. Hwang and J.H. Kim). First we flew to 10-km southeast from the ice camp site and deployed IMB 23 on 9 August 2014, 14:27 L (22:27 UTC). The selected ice floe was similar to the one for IMB 21 (see Fig. 11.7). The ice thickness at the deployment site was 274 cm and freeboard 44 cm (Table 11.2). Right after this we flew to IMB 22 site (10-km southwest from the ice camp site). The deployment of IMB 22 was completed on 15:17 L (23:17 UTC). The ice thickness at the deployment site was 244 cm and freeboard 42 cm (Table 11.2).

IMB 24 and 25 were deployed next day (10 August local) at the 10 km northeast (IMB 24) and 10 km northwest (IMB 25) from the ice camp site. This time S. Lee (PNU) joined the helicopter flight for his melt pond biology survey work. The deployment of IMB 24

completed at 16:44 L (11 August 2014, 00:44 UTC), and IMB 25 at 17:40 L (11 August 2014, 01:40 UTC). The selected ice floe for IMB 24 was flat ice floe, and only small ridges existed at the side of the ice. The ice thickness at the deployment site was 191 cm and freeboard 18 cm, thinnest ice floe among the IMB deployment floes. During this deployment S. Lee (PNU) conducted his 1st melt pond biology survey. Right after this, we flew to the IMB 25 site. The selected ice floe was a typical second-year ice with large elongated ridge (Fig.11.7). The ice thickness at the deployment site was 297 cm and freeboard 37 cm.

11.3.4. Seismic Wave Buoy Deployments

Ten Seismic Wave Buoys (SWBs, Fig.11.8) were deployed - in nested arrays of 1, 10 and 50 km scale (Fig.11.9) - to measure both surface gravity wave attenuation at these various scales and to examine the feasibility of travel time tomography (Doble, 2010) and noise cross correlation (Marsan *et al*., 2012) to extract ice thickness information within the array.

Each buoy is made up of a core electronics package - controlled by a low-power single board Linux microprocessor (*ACME Systems Fox G20*) and several custom circuit boards - interfaced to an *Iridium* satellite modem, GPS position, barometer and webcam. Primary sensors are:

a) An Attitude and Heading Reference System (AHRS), which combines input from three-axis accelerometers, magnetometers and gyroscopes into Kalman filter optimised for marine applications. The *SBG Systems IG-500A* package computes heave, roll and tilt from these inputs, and these channels are logged at 1 Hz, together with the pre-Kalman raw x/y/z accelerations, also at 1 Hz.

b) A highly sensitive seismometer (*Nanometrics Trillium Compact*), which measures velocity in three axes. The output is digitised by a custom 24-bit low-noise ADC board, and logged at 1 Hz, as for the AHRS.

The system streams nine channels of 1 Hz timeseries data over the *Iridium* satellite link, together with hourly GPS fixes and surface air pressure readings, 6-hourly webcam images and various engineering data. Heading is logged at one-minute intervals.

Four 20W solar panels charging a 56Ah/12V lead-acid battery provide power during

the polar day (approximately end February to end September), and the buoy has 2300Ah/12V of alkaline batteries installed to carry it through the dark months. Total weight of the package is around 310 kg, and is housed in an 80x60x60 cm aluminium *Zarges K470* case. A 12 mm aluminium plate is mounted on the base of the box, to ensure good coupling between the seismometer and the ice. The figure below shows one such buoy, installed close to the Araon at the ice station.

The buoy deployments were co-ordinated with other GPS-reporting buoys, in order to build a multi-scale array for ice deformation studies. Other instruments making up the array include five BAS/SAMS ice mass balance buoys (IMBs), and four prototype air-droppable BAS SIESTA ice beacons. These were deployed by Dr. Phil Hwang (SAMS).

By preference, buoys were installed on thicker ice associated with large deformation features, since the seismic data require the instruments to survive into the next Winter. Details of the deployments are summarised in Table 11.1.

1.3.5. Autonomous Ocean Flux Buoy Deployment

The Naval Postgraduate School Autonomous Ocean Flux Buoy (AOFB) consisted of:

- Flux Package
  - Acoustic Current Meter (ACM – 4 Arm System)
  - Thermistor (Fast Response)
  - Conductivity Sensor (Inductive Coil System)
- CTD Profiler & Altimeter
- ADCP
- Thermistor String (30 cm separation)
- Atmospheric Sensor Tree
  - Bulk Met Sensor
  - Ultrasonic Anemometer
  - Shortwave Radiometer
  - GPS / Iridium Transceiver

The AOFB was successfully deployed on 11 August 2014, situated to collect long timeseries of turbulent fluxes in the ice-ocean boundary layer, spanning several seasonal evolutions in the MIZ and near MIZ environment.

11.3.6. Ice Tethered Profiler Deployment

The Ice-Tethered Profiler (ITP) is an easily deployed, automated instrument developed to measure changes in upper ocean temperature and salinity within the polar oceans in all seasons. The ITP (Fig.11.10) consists of three components: a surface instrument that sits on top of an ice-floe, a weighted plastic-jacketed wire-rope tether suspended from the surface instrument, and an underwater instrument that profiles up and down the wire tether. Deployment of ITP's can be conducted either from ice camps or icebreakers, utilizing a self-contained tripod/winch system that requires no power source. Shortly after deployment, the ITP profiles the water column at its programmed sampling interval. After it gathers each acquired temperature and salinity profile, the underwater unit transfers the data to the surface package using an inductive modem and it waits in a queue for the Iridium transceiver to send the data to a WHOI logger computer.

Two ITPs were deployed as part of ARA05B. ITP-V 80 was the fourth system deployed as part of the MIZ array in the Beaufort Sea. The MIZ ITP's have an integrated Modular Acoustic Velocity Sensor (MAVS)- an acoustic travel-time current sensor. In order to measure the profiler's attitude, in addition to a three-axis current sensor, a three-axis magnetometer, a three-axis accelerometer, and a three-axis angle rate gyro are recorded by the ITP-V. ITP-V 80 was deployed in 2.6 meters of ice with 25cm of freeboard on 13 August 2014 at 77° 24.30'N and 146° 10.25'W (Fig.11.11). The deployment was an ice-based deployment using the ITP winch, tripod, and a 24" hydraulic auger to accommodate the larger diameter ITP-V. As of 17 August 2014 it has transmitted 27 profiles back to Woods Hole Oceanographic Institution and the nearly real time data can be found at http://www.whoi.edu/itp.

An additional ITP system was deployed as part of the U.S National Science Foundation Arctic Observing Network. ITP 87 was deployed on 15 August 2014 at 77° 22.49'N and 146° 08.90'W (Fig.11.12 & 11.13). This was also an ice-based deployment using the ITP winch, tripod, and standard 10" hole auger. Both deployments were supported by Maritime Helicopters to transport the equipment to and from the ship. Although the ship was down to one thruster and did not want to go into heavy ice, the MIZ team was still able to find a fairly large ice floe with 1.65 meters of ice and 15 cm of freeboard. The nearly real-time data and results of this profiler can be found at http://www.whoi.edu/itp.

11.3.7. Naval Postgraduate School Flux and Under Ice Imaging Measurements

In situ measurements collected during the ice camp included direct measurements of upper ocean turbulent fluxes from instrumentation operated from a hut deployed on the ice and acoustic imaging of the underside of the ice.

In order to study ice-ocean boundary layer (IOBL) entrainment processes, sufficient wind stress is required to transfer momentum from the atmosphere to the base of the seasonal mixed layer. It seems reasonable to assume (pre-analysis) that the dynamic instabilities produced by ice motion toward the start of our observation period were in quasi-steady state given the well be established mixed layer down to ~22 meters and persistent 10-15 knot winds. Starting on day 2, winds decreased to 5-10 knots and decreased further to 5 knots in follow on days for the remainder of the Ice Camp resulting in a transition from a steady state IOBL to a de-acceleration of shear resulting in a transition of the seasonal mixed layer from ~22 meters to ~10 meters. Turbulent processes in support of this transition will be analyzed from the upper and lower flux packages and provided at a later time.

The Turbulence Flux Frame data targets short term boundary layer transitions not easily studied from static depth flux packages (AOFB). Sensors include:

- Upper (+ pressure sensor) and Lower Flux Packages
- ADCP
- Thermistor String
- SBE19 CTD (Moored mode 10 sec response)

Hut and flux package were deployed on 9 August 2014, and operated through 13 August, 2014. Hut deployment went very well with only minor difficulties positioning the hut from the ship to the site (helo drag). Communications issues with the 6 meter Flux Frame and supporting winch system restricted data collection to fixed depths (no profiling) during the first 2 days of operation, but were mostly mitigated by day 3 thanks to the intense troubleshooting efforts of Jim Stockel. The primary problem appeared to be the presence of EM noise from the various sources in the hut interfering with the Ethernet cable communications from the Flux Frame. Nevertheless, Flux Frame placement (with assistance of ship's CTD profile) straddling the upper halocline appeared to be effective and is likely

that Flux Frame sensors captured the transition of the mixed layer during the relaxing wind stress conditions and subsequent reductions in IOBL shear.

NPS also set out to test a new imaging system integrating an acoustic imager (BlueView Acoustic Imager), EO camera (Underwater Prosilica EO camera) and motor actuator using a matlab control and archiving program. As with any new program some bugs were discovered in the fielding of the system, but overall the integrated system performed quite well. The NPS team was able to image 6 different locations to include the Flux Frame, AOFB, ITP and three other hydro-holes between these sites - overall imaging goals were 100% obtained. Acoustic and EO images will provide data for characterizing under ice drag critical for boundary layer turbulence calculations.

11.3.8. Acoustic Backscatter Measurements

This task addresses the considerable challenge of monitoring and quantifying the ecologically-key mid-trophic levels (zooplankton) in the rapidly changing Arctic Ocean. We are only just beginning to appreciate the gap in our understanding and expectations of these ecosystems in the Arctic, as exemplified by recent findings (Arrigo *et al*., 2012) which measured under-ice phytoplankton biomass hugely in excess of expectations and higher than typical open-water concentrations.

While phytoplankton can be relatively easily measured using fluorimetry, estimating the zooplankton population is far more challenging. Traditional, labour-intensive methods such as net sampling have many problems with avoidance by the larger organisms. Traditional techniques are clearly not amenable to future application in autonomous systems, which must be the future of all oceanographic monitoring - especially in the Arctic.

Acoustic methods are "*the only means that can efficiently observe the large biomass of the mid-trophic levels at ecologically important temporal and spatial scales*" (Wiebe et al., 2002). Acoustic data are inherently ambiguous when measured in isolation, however. The amplitude of the back-scattered energy depends on the interacting effects of the number of animals, the species composition and their size distribution and orientation. Inverse modelling techniques are able to untangle these interacting factors, but only with sufficient independent knowledge of the animals present.

A key factor in gaining understanding of the acoustic signal is the use of multiple frequencies. Different species have varying responses across the acoustic spectrum and the ratios between backscatter at different frequencies can be used to identify the dominant organisms in a swarm. The instrument used for acoustic measurements is the Aquascat 1000R, manufactured by Aquatec Ltd. Rated to 1000m depth, it has four cabled transducers (we choose 500kHz, 1MHz, 2MHz and 4MHz) which allow the maximum flexibility in mounting the electronics/battery housing, for instance onto a CTD rosette.

Measurements will be used to optimise the complex instrument parameters for Arctic work, with three main aims:

a) Comprehensive pan-Arctic observations of the acoustic signatures of key species, in conjunction with a full suite of supporting measurements (optical, physical, nets). The aim is to build a library of acoustic backscatter characteristics, allowing us to move towards a uniquely acoustic characterisation of the functional groups present.
b) Incorporation of this knowledge into a prototype autonomous acoustic profiling system, as part of the IAOOS profiling drifters (project partners CNRS-LOCEAN, UPMC)
c) Incorporation of our measured zooplankton biomass in the Arctic ecosystem models

In the context of the current cruise, the LOV Aquascat instrument and four transducers were mounted on the NPS turbulence string, towards the bottom of that array (Fig. 11.14). The arrangement is shown in the figure overleaf. The aim was to acquire backscatter data for the plankton community in the ice camp region, with repeated profiles from the surface to 60 m, with prolonged data acquisition at the 'parking depth' of around 20 m. Supporting measurements by KOPRI and LSU groups on board (particle size distribution from LISST and sediment traps, species composition from nets) provide the necessary 'ground truth'.

In the event, the surface waters below the ice camp floe were extremely clear, and almost devoid of particles. We theorise that the advance state of ice melt meant that the water-column seeding of initial ice melt had long-since passed, and nutrients had been exhausted in the freshwater-stabilised surface water.

Unfortunately the Aquascat malfunctioned during the deployment, locking up (and

ceasing logging) approximately 22 hours after deployment (last file written at 1132Z on August 9th). One complete profile was obtained, together with several hours data at the chosen 'parking depth' of 23 m (Fig.11.15). 119 sets of 10 minute bursts were logged in total. Data was acquired at 16 Hz and averaged internally to 1 Hz. Transmit gain was set to +12 dB, to account for the expected sparse scattering environment.

Data from KOPRI investigators suggested that the water at the camp was exceptionally clear (actually purer than milliQ water at depth), and this is confirmed by results of the Aquascat inversion model - there were essentially no particles that Aquascat can detect.

The Aquascat was then mounted on the Araon's CTD rosette for stations shallower than the 1000 m rating of the device. This took place at "Station 31" and was in the water at 0305Z, 21/8, for a 190 m cast. The water column was very interesting from a particle viewpoint, with thin layers and spikes of high particle concentration. Aquascat was set to log for one hour, using the external trigger box. File 20140821-023433.aqa (one hour).

Shortly afterwards, Eurico d'Sa (LSU) did an additional cast with a full set of optical instruments on a frame, close to Koji Shimada's mooring site. Aquascat was mounted on this frame and logged concurrently for the cast down to 180m. File 20140821-052007.aqa (one hour)

Finally a cast was made at the 24-hour ice station, again using Eurico d'Sa's optical frame with the Aquascat, this time to 100 m only. File 20140823-014521.aqa (one hour).

11.3.9. Aerial Photography

A campaign of high-resolution aerial photography was carried out, using downward-looking digital cameras (*Olympus OM-D E-M5* with *Olympus PRO 12-40 mm f/2.8* lens and *Olympus TG-3*) installed on the nose of helicopter 301MH. The aim was to acquire the highest-possible resolution images, for comparison with co-incident overpasses of visible and SAR satellite images. The aim of this comparison is to allow the parameters of the satellite-derived images to be directly evaluated, i.e.:

1. Provide the best possible floe size distribution (FSD) where aerial images are available
2. Evaluate the skill of the optical and SAR satellite products to provide a

meaningful FSD

3. Determine the mix of environmental conditions (ice, water and wind) which allow a high confidence in the optical and SAR satellite-derived results.

Other derived parameters will also be compared, including melt pond fraction and spatial spectra of the melt pond distributions, deformed ice fraction and pressure ridge parameters.

The uncharacteristically-clear weather conditions during and after the ice camp allowed a total of nine sorties to be flown, consisting of long transects to- and from the most distant buoy deployment sites, as well as four mosaic surveys close to the ship. Mosaics with coverage 1x1, 2x2, and 3x3 nm were performed.

Cameras were set to 28 mm equivalent focal length (chosen as a compromise between coverage, resolution and optical distortion associate with wider focal lengths), flying at 2000 feet (610 m) altitude. Image dimensions on the ground were therefore 784 x 627 m, with a pixel size of 17 cm (sensor is 4608 x 3456 pixels). The camera was controlled by an intervalometer (*Hahnel Giga T-Pro 2*), taking an image every 8 seconds and giving 20% overlap between images to allow reliable mosaicking of the final result. The image strip (Fig. 11.16) shows an example mosaic of five images over the ship and ice camp.

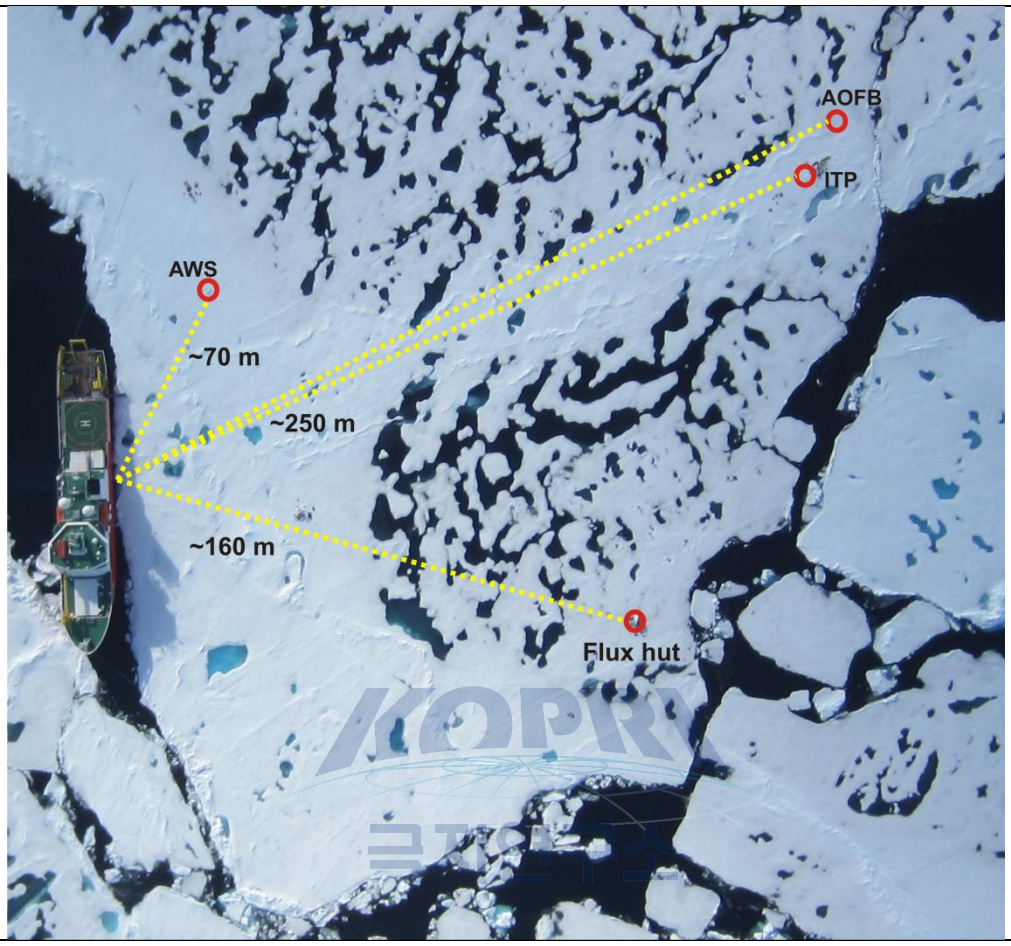

Fig. 12.1. Relative locations of MIZ assets deployed at the ARA05B ice camp.

Fig. 11.2. The ice floe selected for the ARA05B camp, at the time of floe selection, prior to mooring the Araon.

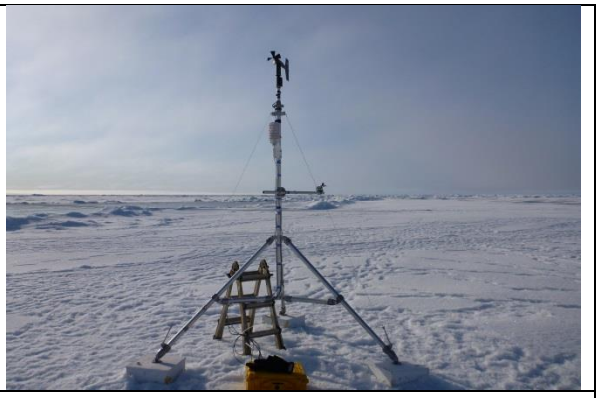

Fig. 11.3. Deployment of AWS05.

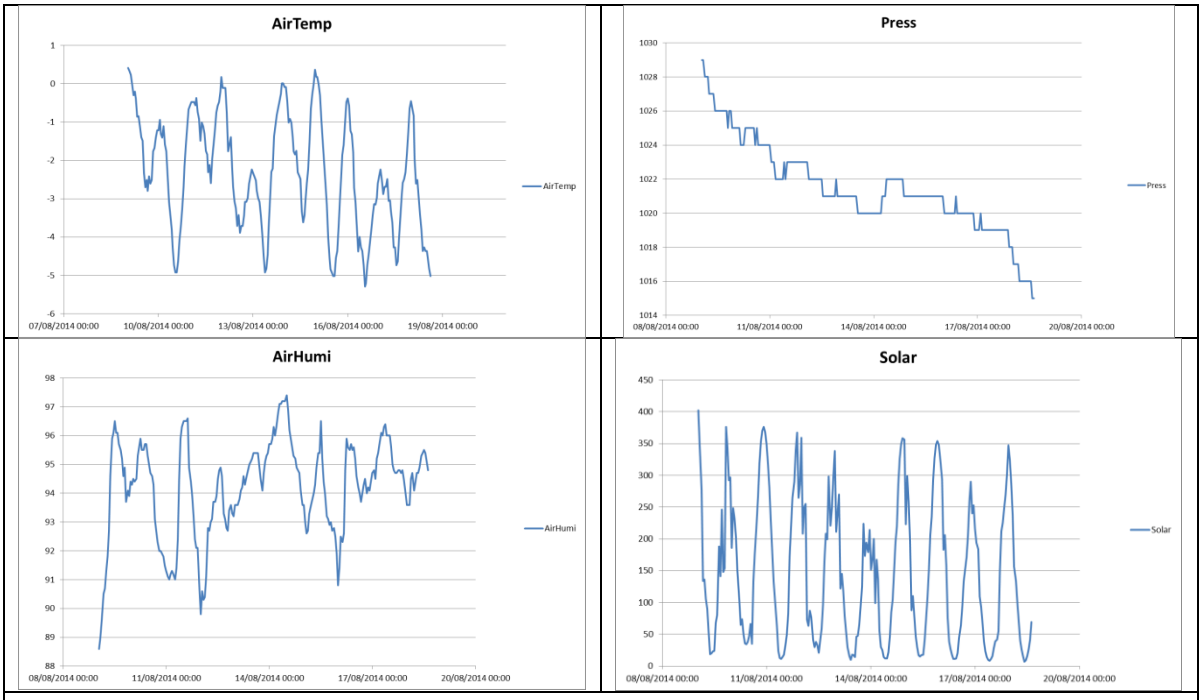

Fig. 11.4. Preliminary data from AWS05. (upper left) air temperature, (upper right) surface pressure, (lower left) Relative humidity, (lower right) shortwave radiation.

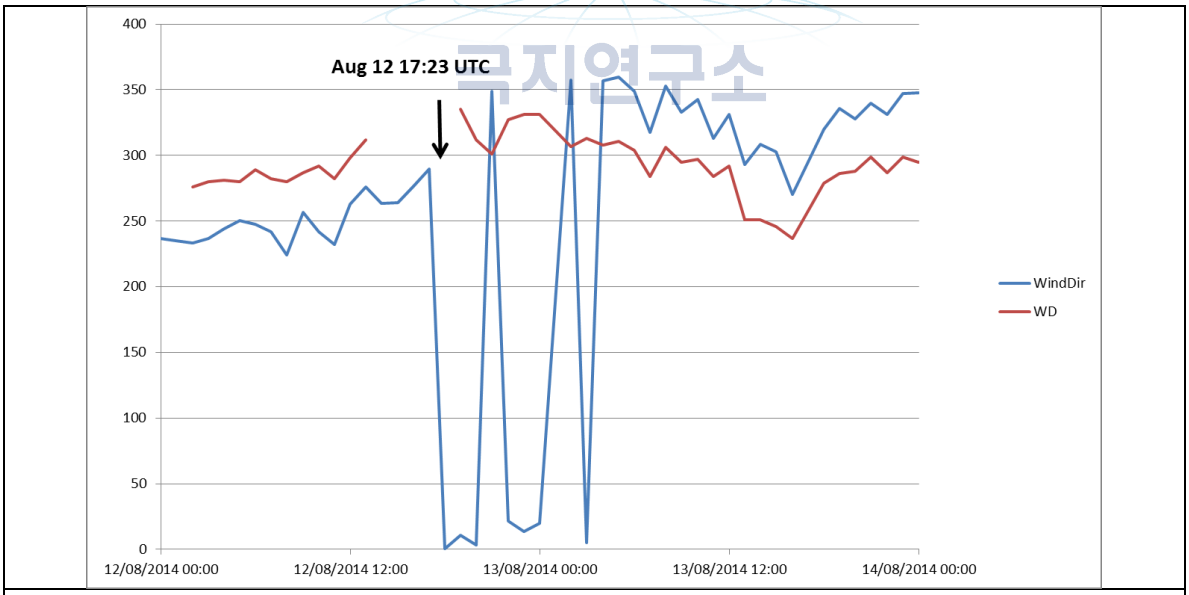

Fig.11.5. AWS05 wind direction (blue) and Araon DADIS wind direction (red).

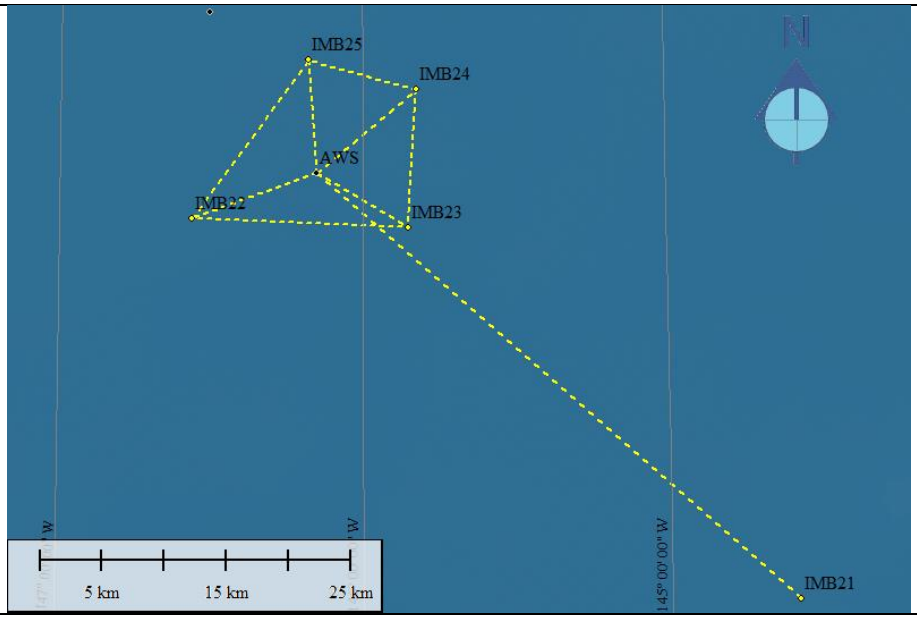

Fig.11.6. Location of five IMBs on 14 August 2014, 02:00 UTC. The center of the buoy array is the location of AWS 05.

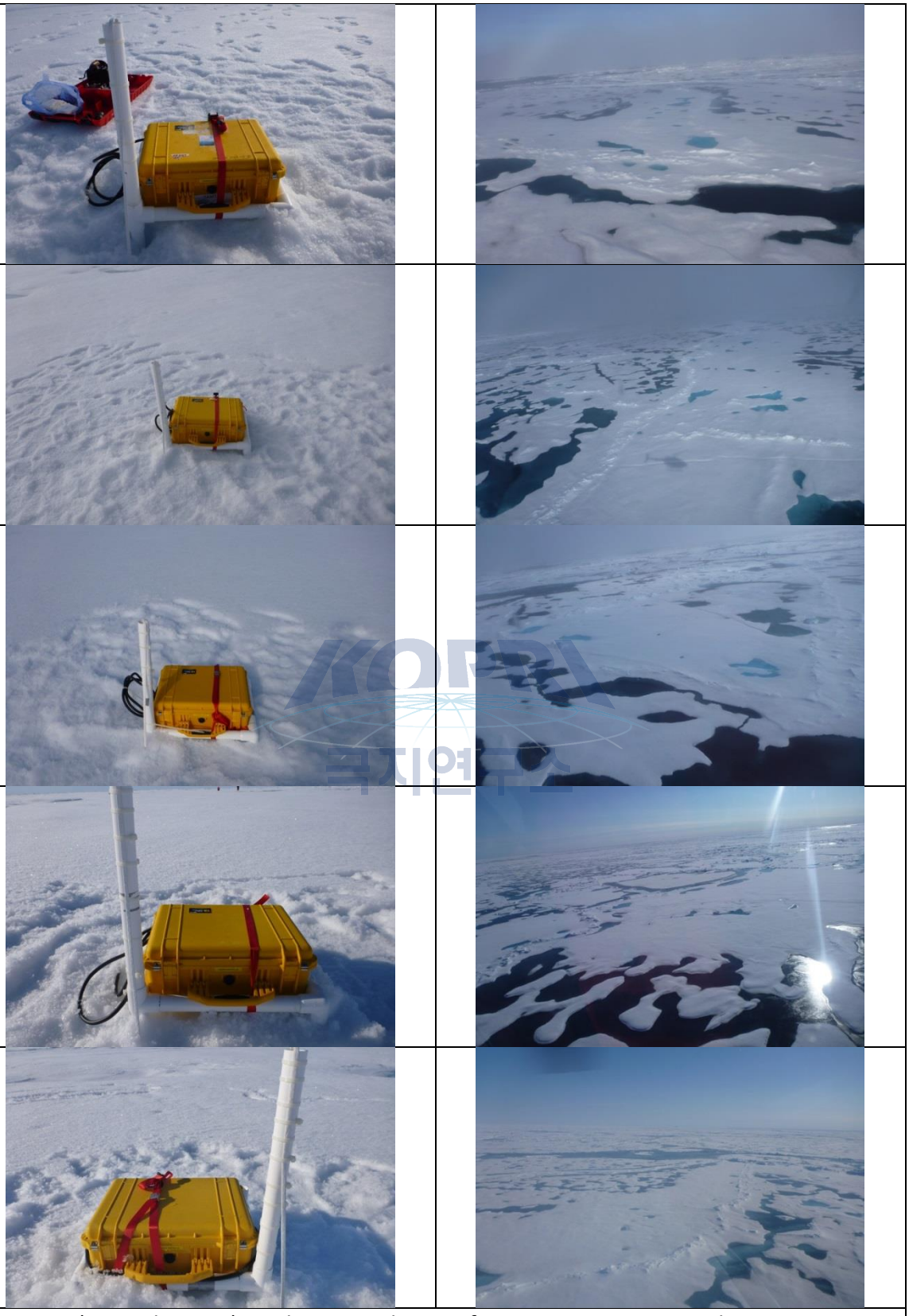

Fig. 11.7. (top to bottom) Deployment photos of IMBs 21, 22, 23, 24 and 25.

Fig. 11.8. A Seismic Wave Buoy (234) installed 1.2 km NW of Araon.

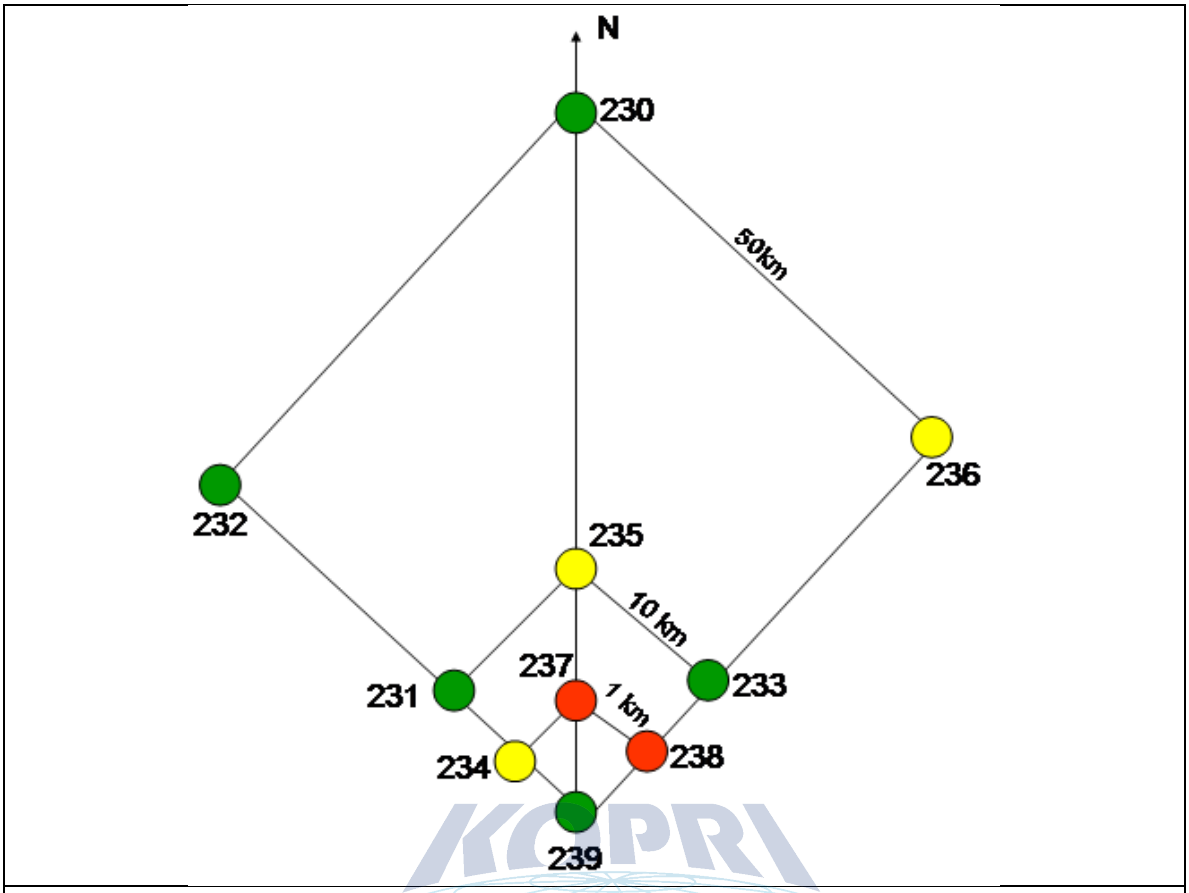

Fig. 11.9. Layout of the SWB array. The ice camp is at the bottom apex (239), and the numbers refer to the SWB IDs (230-239). Colours refer to activation status of the Iridium SIM cards installed in the modems.

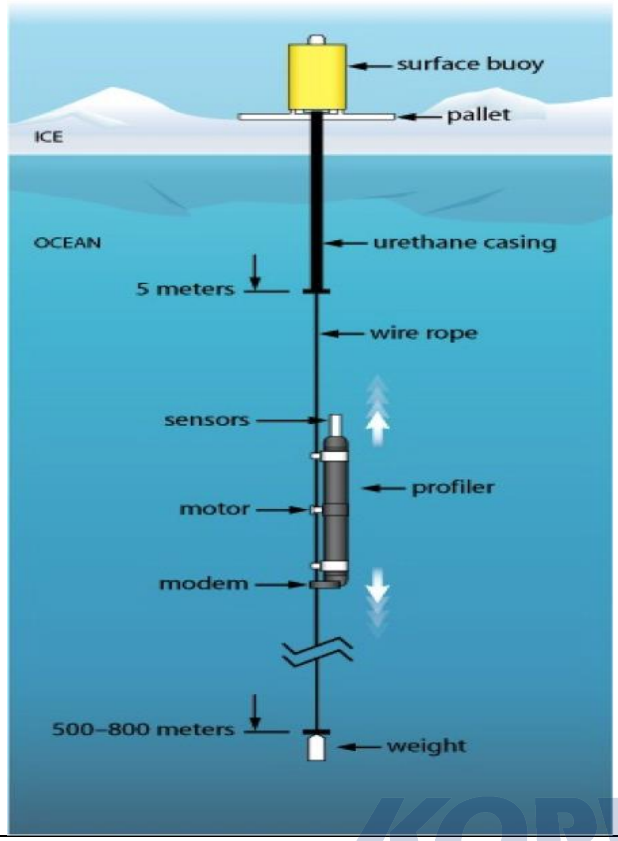

Fig. 11.10. Schematic of an ITP system.

Fig. 11.11. Preparing to lower ITP-V 80 into the 24” diameter hole.

Fig. 11.12. Jeff Pietro (WHOI) using a custom WHOI yale grip to stop the mooring off before transferring the load from the ITP winch to the chainfall.

Fig. 11.13. Final deployment of ITP 86 with the Maritime Helicopter and IBRV Araon in the background.

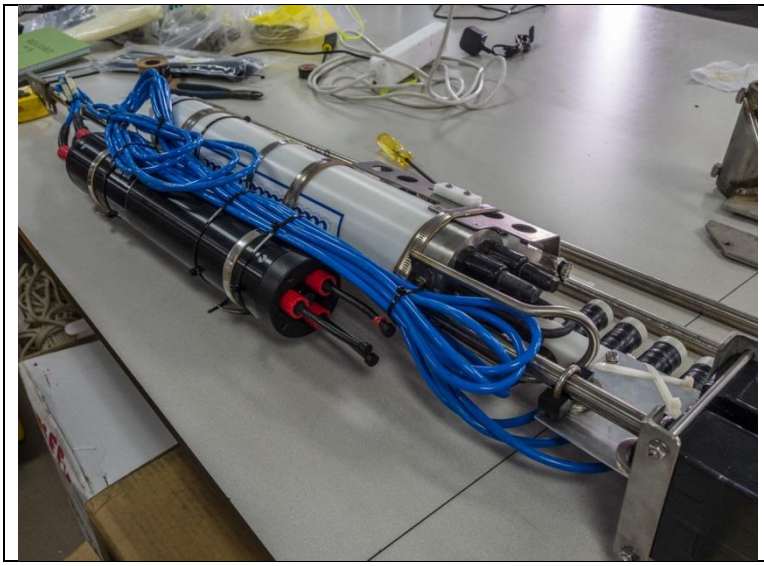

Fig. 11.14. The Aquascat unit mounted on the NPS turbulence string.

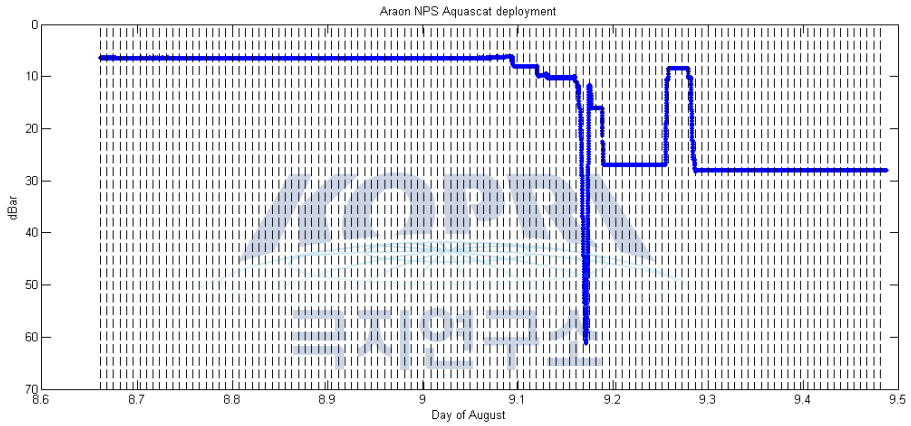

Fig. 11.15. Aquascat pressure record for the deployment. One profile to 60m and several hours' data at the parking depth were obtained before the unit shut down prematurely.

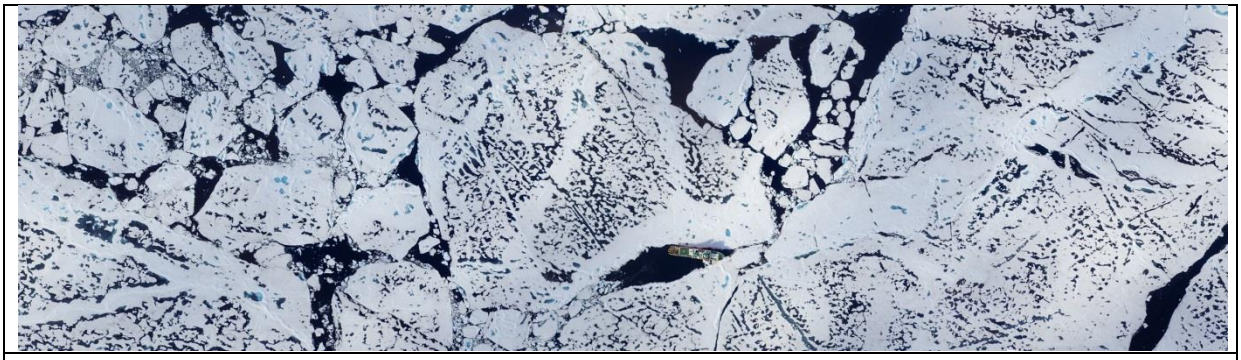

Fig. 11.16. Mosaic of five image frames over the ship and ice camp.

Table 11.1. Wind direction (WD) from AWS 05 and ship, and the heading of the ship. Wind direction from the ship (DADIS) is relative to the ship's heading. 'Corrected Ship WD' contains wind direction corrected for the ship's heading. 'AWS WD-Corrected' contains the difference between AWS 05 wind direction and corrected ship wind direction.

Date	AWS WD	Ship WD	Ship Heading	Corrected Ship WD	AWS WD-Corrected
12/08/2014 18:59	10.5	335.0	32.0	7.0	3.5
12/08/2014 19:58	3.3	312.0	32.1	344.1	19.2
12/08/2014 20:58	348.8	301.0	31.8	332.8	16.0
12/08/2014 21:59	21.8	327.0	31.7	358.7	23.1
12/08/2014 22:58	13.5	331.0	31.6	2.6	10.9
12/08/2014 23:58	19.7	331.0	31.8	2.8	16.9
13/08/2014 01:58	357.5	307.0	31.7	338.7	18.8
13/08/2014 02:58	5.0	313.0	31.7	344.7	20.3
13/08/2014 03:58	356.7	308.0	31.9	339.9	16.8
13/08/2014 04:59	359.5	311.0	32.0	343.0	16.5
13/08/2014 05:58	348.6	304.0	31.9	335.9	12.7
13/08/2014 06:58	317.5	284.0	31.7	315.7	1.8
13/08/2014 07:59	352.7	306.0	31.5	337.5	15.2
13/08/2014 08:58	333.0	295.0	31.3	326.3	6.7
13/08/2014 09:58	342.8	297.0	31.4	328.4	14.4
13/08/2014 10:59	313.2	284.0	31.4	315.4	-2.2
13/08/2014 11:58	331.0	292.0	31.4	323.4	7.6
13/08/2014 12:58	293.1	251.0	31.4	282.4	10.7
13/08/2014 13:59	308.7	251.0	31.4	282.4	26.3
13/08/2014 14:58	302.7	246.0	31.3	277.3	25.4
13/08/2014 15:58	270.2	237.0	31.2	268.2	2.0
13/08/2014 17:58	319.8	279.0	31.1	310.1	9.7
13/08/2014 18:58	335.8	286.0	30.8	316.8	19.0
13/08/2014 19:59	327.7	288.0	30.8	318.8	8.9
13/08/2014 20:58	340.0	299.0	30.7	329.7	10.3
13/08/2014 21:58	331.3	287.0	30.6	317.6	13.7
13/08/2014 22:59	347.0	299.0	30.4	329.4	17.6
13/08/2014 23:58	347.9	295.0	30.4	325.4	22.5
14/08/2014 00:58	348.0	299.0	30.4	329.4	18.6
14/08/2014 01:59	357.6	324.0	30.6	354.6	3.0

Table 11.2. IMB deployment summary.

ID	Date (UTC) y/m/d	Time (UTC)	Ice thick (cm)	freeboard (cm)	Snow depth (cm)	note
21	2014/08/10	00:59	240	45	8	About 50 km SE from the ice camp location. The ice surface to the top of pipe 76 cm. 77°13.72' N/144°47.39'W.
22	2014/08/09	23:17	244	42	6	About 10 km SW from the ice camp location. 77°30.32'N/146°32.51'W.
23	2014/08/09	22:27	274	44	7	About 10 km SE from the ice camp location. Ice surface the top of pipe 72 cm. 77°28.87'N/145°49.85'W.
24	2014/08/11	00:44	191	18	11	About 10 km NE from the ice camp site. Ice surface to the top of pipe 72 cm. Sang Lee's 1st Melt Pond survey with me. 77°30.16'N/145°52.26'W.
25	2014/08/11	01:40	297	37	12	About 10 km NW from the ice camp site. Ice thickness 297 cm. freeboard 37 cm. snow depth 12 cm. Sang Lee's 2nd Melt Pond survey with me. 77° 33.18' /145°52.31'W.

Table 11.3. Seismic Wave Buoy deployment details.

WB	Array posn	Date UTC	Time UTC	WPs	Frames	Aerial tx?	Comments
230	50 km N	8/8	2045Z	011, 012	M500085-087	Return	Active, initially was WB239. Swapped at 2300Z 10/8
232	50 km NW	9/8	0112Z	014	M500097-110	Return	Active
231	10 km NW	9/8	1935Z	018, 019	M500111-118	Return	Active. Returned to restart at 2208Z
233	10 km NE	10/8	0146Z	023	M500204-211	No	Active
236	50 km NE	10/8	1933Z	029	M500267-274	Return	Inactive (1)
235	10 km N	11/8	0037Z	032	M500275-286	Return	Inactive (1)
237	1 km N	11/8	2315Z	042	M500323-348	No	Inactive (2)
238	1 km NE	12/8	0048Z	None	M500353-371	No	Inactive (2). With SIESTA
234	1 km NW	12/8	0410Z	045	M500378-390	No	Inactive (1). With SIESTA. No seismometer installed.
239	ITP	12/8	2233Z	No	M500455-461	No	Active. With ITP, AOFB.

Table 11.4. Aerial photography.

WB	Date UTC	Time UTC	Cam	Frame No.s	Altitude (ft)	Comments
ICE CAMP SITE						
c:_Projects\MEDEA\Data\AerialPhotos\Araon2014**WB239_return_transect_TG3**						
GPS file: c:_Projects\MEDEA\ ... \GPS\Track_140808_WB239_outNreturn.csv						
239	8/8	1812 - 1827	TG-3	P8100025-123	2000	Part return to ship, 99 frames
c:_Projects\MEDEA\Data\AerialPhotos\Araon2014**WB232_return_transect_TG3**						
GPS file: c:_Projects\MEDEA\ ... \GPS\Track_140808_WB232_outNreturn.csv						
232	9/8	2308 - 2322	TG-3	P8100124-222	2000	Part return to ship, 99 frames
c:_Projects\MEDEA\Data\AerialPhotos\Araon2014**WB236_return_transect_OMD**						
GPS file: c:_Projects\MEDEA\Data\GPS\WB236_outNreturnOMD.csv						
236	10/8	1705 - 1723	OM-D	M500241-266	2000	Part return to ship (shutdown)
c:_Projects\MEDEA\Data\AerialPhotos\Araon2014**WB236_return_TG3**						
GPS file: c:_Projects\MEDEA\ ...\GPS\WB236_outNreturnTG3.csv						
236	10/8	1935 - 1948	TG-3	P800223-321	2000	Part return to ship, 99 frames
c:_Projects\MEDEA\Data\AerialPhotos\Araon2014**WB239_outward_transect_TG3**						
GPS file: c:_Projects\MEDEA\ ... \GPS\Track_140810_WB239_swap.csv						
239	10/8	2047 - 2101	TG-3	P8100322-420	2000	Part outward tx to WB239, 99 frames
c:_Projects\MEDEA\Data\AerialPhotos\Araon2014**WB235_return_tx_and_mosaic_TG3**						
GPS file: c:_Projects\MEDEA\ ...\GPS\Track_140810_WB235_outNmosaic.csv						
235	11/8	0250 - 0305	TG-3	P8100422-520	2000	Return tx to ship and 3-line mosaic
c:_Projects\MEDEA\Data\AerialPhotos\Araon2014**Araon_2x2_survey_TG3**						

GPS file: c:_Projects\MEDEA\ ... \GPS\Track_140811_2x2_survey.csv						
MOS	11/8	2152 - 2207	TG-3	P8100522-620	2000	7-line mosaic over ship
NOT ICE CAMP (ITP 80 DEPLOYMENT)						
c:_Projects\MEDEA\Data\AerialPhotos\Araon2014**Araon_3x3_survey_OMD**						
GPS file: c:_Projects\MEDEA\ ... \GPS\Track_140815_3x3_survey.csv/trk						
MOS	15/8	0241 - 0336	OM-D	M500761-1132	2000	15-line mosaic over ship
24 HOUR ICE CAMP (CAMP 2)						
c:_Projects\MEDEA\Data\AerialPhotos\Araon2014\IceCamp2_2x2_survey						
c:_Projects\MEDEA\ ... \GPS\Track_Camp2_2x2_survey_140822.csv						
MOS	22/8	2228 - 2242	OM-D	M501619-1732	1740	7 line mosaic over ship

Table 11.5. Waypoint list for surveys and wave buoy deployments.

Underlines indicate the end of a (local time) working day. WPs copied from: `c:\_Projects\MEDEA\Data\AerialPhotos\Araon2014\GPS\waypoints.wpt`

WP	Lat (N)	Lon (W)	Height (m)	Date UTC	Time UTC	Comment
SHIP	76° 24.0292398	146° 11.6899494	-3.479004	07-Aug-14	23:00:20	
KOJI	77° 39.7253994	147° 46.574991	-10.688843	08-Aug-14	00:15:20	
K1625Z	77° 39.5933946	147° 47.9165952	133.507812	08-Aug-14	01:32:53	
3	77° 36.106758	146° 4.815492	45.307495	08-Aug-14	12:43:58	recon
4	77° 36.591984	146° 5.035146	3.490479	08-Aug-14	13:37:41	recon
5	77° 37.225212	146° 5.96094	12.622925	08-Aug-14	17:12:32	
6	78° 17.25558	145° 57.886926	1.087158	08-Aug-14	17:49:39	
7	78° 17.235312	145° 57.701694	-4.921021	08-Aug-14	18:00:44	WB239
8	77° 37.386678	146° 5.04912	608.635742	08-Aug-14	18:26:16	
9	78° 16.903824	145° 56.264916	15.747192	08-Aug-14	19:37:11	WB230
10	78° 16.850412	145° 56.140398	2.529175	08-Aug-14	19:49:02	
11	78° 16.558452	145° 55.946514	2.288818	08-Aug-14	20:45:03	S align
12	78° 16.580088	145° 55.997226	-0.11438	08-Aug-14	20:45:29	N align
13	77° 35.978736	146° 4.130184	8.537354	08-Aug-14	22:21:28	ship
14	77° 55.43979	147° 36.70902	8.056641	08-Aug-14	22:50:18	WB232
15	77° 55.069956	147° 39.83604	-7.324341	09-Aug-14	01:12:40	WB232
16	77° 33.575934	146° 12.494412	2.288818	09-Aug-14	18:24:46	WB231
17	77° 38.187078	146° 29.012838	5.653442	09-Aug-14	19:34:19	
18	77° 38.168508	146° 29.053836	3.971191	09-Aug-14	19:35:03	S align
19	77° 38.180436	146° 29.04048	3.730835	09-Aug-14	19:35:41	N align
20	77° 32.39484	146° 9.658932	8.537354	09-Aug-14	22:07:12	ship
21	77° 36.939846	146° 28.084992	12.38269	09-Aug-14	22:29:15	
22	77° 36.665478	145° 36.236136	3.250122	09-Aug-14	22:57:35	NEcache
23	77° 36.056388	145° 39.233706	1.087158	10-Aug-14	00:48:06	WB233
24	77° 31.15686	146° 17.514312	7.816406	10-Aug-14	03:21:34	ship
25	77° 39.166518	146° 14.53947	-15.495361	10-Aug-14	03:38:53	Ncache
26	77° 31.05156	146° 18.655332	15.987549	10-Aug-14	16:22:00	ship
27	77° 49.942884	144° 52.132002	107.071655	10-Aug-14	16:46:06	
28	77° 50.1354	144° 47.372664	52.75769	10-Aug-14	16:48:18	
29	77° 51.307152	144° 44.521752	-6.603394	10-Aug-14	17:01:10	WB236

30	77° 51.32085	144° 42.920352	9.739014	10-Aug-14	18:28:38	
31	78° 9.244794	146° 8.139588	-9999	10-Aug-14	20:35:31	
32	77° 37.892118	146° 10.797606	-4.680786	11-Aug-14	00:37:37	WB235
33	77° 30.01476	146° 12.70479	582.68042	11-Aug-14	00:47:31	
SHIP_D	77° 29.832162	146° 12.9920244	-9999	11-Aug-14	20:24:07	
34	77° 27.307302	146° 11.720856	10.940552	11-Aug-14	20:26:25	
35	77° 27.343248	146° 12.241614	3.730835	11-Aug-14	20:29:48	
36	77° 27.989634	146° 14.508966	8.777588	11-Aug-14	20:43:16	NWcache
37	77° 27.206004	146° 11.783322	34.012085	11-Aug-14	20:53:52	
38	77° 28.231014	146° 11.153328	8.777588	11-Aug-14	21:00:35	Ncache
39	77° 27.561114	146° 8.743644	-8.526001	11-Aug-14	21:13:05	NEcache
40	77° 26.928396	146° 10.377054	3.730835	11-Aug-14	21:38:56	
41	77° 26.931504	146° 10.038714	457.709961	11-Aug-14	21:42:43	ship
42	77° 27.73977	146° 10.075926	3.971191	11-Aug-14	22:21:57	WB237
43	77° 25.740756	146° 12.220794	8.056641	12-Aug-14	03:02:06	
44	77° 26.494674	146° 15.577296	4.692139	12-Aug-14	03:15:57	
45	77° 26.591796	146° 15.708234	-3.719238	12-Aug-14	04:10:17	WB234
46	77° 23.927172	146° 12.698214	28.724976	13-Aug-14	02:38:39	
47	77° 22.85157	146° 11.082216	0.125977	13-Aug-14	16:56:42	
48	77° 22.67727	146° 9.807444	23.677979	13-Aug-14	18:13:41	ship
49	77° 22.492956	146° 8.906592	-9999	15-Aug-14	02:40:57	